Space-Time Green Functions for Diffusive Radiation Transport, in Application to Active and Passive Cloud Probing

Anthony B. Davis

Los Alamos National Laboratory

Space & Remote Sensing Group

Los Alamos, NM 87545, USA

now at:

Jet Propulsion Laboratory

California Institute of Technology

Pasadena, CA 91109, USA

Igor N. Polonsky

Colorado State University

Department of Atmospheric Science

Fort Collins, CO 80523, USA

Alexander Marshak

NASA – Goddard Space Flight Center

Climate & Radiation Branch

Greenbelt, MD 20771, USA

PUBLISHED IN:

Light Scattering Reviews, Vol. 4,
A. A. Kohkanovsky (Ed.),
Chapter 5, pages 169-292,
Springer-Verlag, Heidelberg (Germany),
2009.

LANL LA-UR NUMBER: 08-6908

JPL CLEARANCE NUMBER: 09-1336

ABSTRACT

Over the past decade or so, the utility of multiple scattering Green functions has been demonstrated in a number of applications in cloud remote sensing. In view of (i) the large optical thicknesses observed for several important types of cloud, and (ii) the predominance of scattering over absorption by cloud droplets throughout most of the solar spectrum, the diffusion or "P_1" limit of radiative transfer theory proves to be a productive framework for computing Green functions, as needed, in space and/or time. This is largely because the diffusion approximation leads to analytical expressions in Fourier-Laplace variables that return space-time radiation characteristics in the form of moments or of probability distributions (i.e., normalized Green functions). These characteristics are in turn shown to be quite accurate in comparison with Monte Carlo solutions of the full 3D radiative transfer equation. Moreover, physical insights into non-trivial multiple scattering processes are gained because diffusion has an analog in particle random walk theory that predicts qualitatively correct behavior of remote sensing observables as cloud parameters are varied.

In this review, we cover many aspects of the diffusion-theoretical approach to the calculation of radiation transport Green functions for internal as well as boundary sources, and for in situ detectors as well as remote cloud observations. Homogeneous, stratified and moderately variable stratiform cloud models are examined. Solar as well as pulsed laser sources are considered and closed-form expressions for responses in reflection as well as transmission are computed and validated. Last but not least, we discuss applications to current and futuristic cloud remote sensing technologies from ground-level, airborne and space-based platforms. Both active (lidar) and passive (especially, oxygen A-band spectroscopic) modalities are described. As it turns out, they share a surprising amount of common theoretical background that is best described in terms of multiple scattering Green functions.

Keywords:
planetary atmospheres, three-dimensional radiative transfer, time-dependent radiative transfer, multiple scattering, diffusion theory, random walks, Green functions, slab geometry, stratus clouds, remote sensing, oxygen A-band spectroscopy, lidar

Table of Contents

5 Space-time Green functions for diffusive radiation transport, in application to active and passive cloud probing

Anthony B. Davis, Igor N. Polonsky, Alexander Marshak

5.1 Context, motivation, methodology, and overview

Clouds are a feast for the eye but, when contemplating their fluid beauty, it is important – at least for scientists – to bear in mind that they are also key elements of the Earth's climate system. They are indeed the first-order regulators of the intake in solar energy: What portion goes back to space? What reaches the surface (then warms the ground, drives photosynthesis, etc.)? Clouds also contribute strongly to the vertical distribution of solar heating and, from there, the thermal balance of the atmosphere. These are well-known and relatively well-understood/modeled climate roles of clouds, as can be expected for such *naturally occurring* components of the atmosphere. We note that these roles involve radiative transfer across the electromagnetic spectrum. What is far less understood about clouds is how they interact microphysically, chemically and thermo-hydrodynamically, with other natural *and anthropogenic* constituents, especially aerosols. These are known as cloud feedback mechanisms in the parlance of climate science, and have been identified as the single most resilient roadblock in the way of reducing uncertainty in future climate prediction [1], an enterprise that relies heavily on models to explore various scenarios in global greenhouse gas emissions.

The first order of business in addressing cloud feedback issues is therefore to improve statistics and accuracy in cloud observation, which is prerequisite to the improvement of cloud process models, which are in turn expected to enable the progress we so desperately need in global and regional climate modeling. Policy-makers need and deserve the absolute best climate science deliverables if they are to propose in some ways painful regulations for greenhouse gas emissions in accord with future international treaties. Because cloud systems have regional influence and strong diurnal cycles, communities engaged in the meteorology, air-quality and surface hydrology are also stakeholders in improved cloud science, both in observations and in models.

As soon as we realize that direct airborne probing of clouds is prohibitively expensive on a per datum basis, it follows that improving cloud observations globally is primarily a charge to the cloud remote sensing community. Whether from ground or from space – and these perspectives are in many ways complementary

– we need better coverage (number of satellites, and their swaths),[1] better sampling (spatial and angular resolution), and better retrieval techniques (exploitation of spectral and polarization measurements). This picture is overly simplistic. The notion that we can infer all the cloud properties that matter using only spectral and, with increasing appeal and availability, polarization data follows from the prevailing '1D thinking' behind all current cloud remote sensing products delivered by space agencies world-wide. The operational assumption is indeed that clouds can be represented, for the purposes of the unavoidable radiative transfer, as horizontally infinite plane-parallel slabs at the pixel-scale, irrespective of the size of the pixel. We thus ignore the pixel-to-pixel variations that make satellite cloud imagery so interesting, not to mention the likely presence of sub-pixel variability. This assumption may in fact be justified in view of other uncertainties: there is more than just radiative transfer modeling error to worry about, and a relatively fool-proof way of minimizing its impact is to steer away from cloud boundaries. This makes cloudy- versus clear-column discrimination an important preliminary task.

However, those interesting interactions between clouds and aerosols happen in the (often only partially [2]) cloudy pixels, as well as in those pixels at the cloudyclear interface [3] – precisely where we are sure that neither cloud nor aerosol retrievals are accurate due to unaccounted 3D radiative transfer effects. The emerging paradigm in cloud and aerosol remote sensing is therefore 3D and integrative: multi-spectral and multi-polarization methods are merged with multi-pixel and multi-angle ones and, ultimately, synergies across very different kinds of instrumentation are used to optimize cloud property retrievals.

No one ever said that cloud remote sensing is easy!

This review covers in detail the theory of radiation transport Green functions, as it applies to optical probing of cloud structure by remote observers on both sides of the clouds, as well as *in situ* observers. We are only interested in scattering – and indeed multiple scattering – phenomenology based primarily, but not exclusively, on solar and laser sources. Our focus will be on the more opaque clouds that form in the Earth's atmosphere, since we favor analytical methods based on mathematically tractable problems that arise in the diffusion (small mean-free-path) limit of transport theory at large.[2] Finally, we will make the standard assumption of horizontally extended stratiform cloud geometry.[3]

In spite of this cascade of restrictions, the modeling framework we present sheds new light on a wide variety of radiometric modalities: some active and some passive; some advanced concepts and some well-established ones; some from ground,

[1]From geostationary platforms, one sees the whole visible face of the Earth; however, their distance limits the achievable spatial resolution.

[2]We are thus building on the shoulders of the giants that founded and developed statistical physics: kinetic theory (going at least back to L. Boltzmann), neutron transport theory (going back to J. von Neumann, N. Metropolis, R. Peierls, and others), stellar astrophysics (going back to A. Eddington, A. Milne, V.A. Ambartsumian, V.V. Sobolev, S. Chandrasekhar, and others), and even turbulence (going back to L.F. Richardson, A.N. Kolmogorov, G.I. Taylor, and others).

[3]However, the space-time Green function is a 3D radiative property, and we will revisit the challenging problem of practical (i.e., efficient and targeted) 3D cloud radiative transfer armed with said Green functions in various parts of the paper.

some from space, and yet others from aircraft. The application field is so vast that we have opted to survey the relevant theoretical and observational literatures as we encounter different topics. Our main message is that they all branch away from the same radiation transport theory, namely, the unifying framework of Green functions. We present this body of theory up-front in a hierarchical manner: starting with a very detailed incarnation of radiative transfer[4] in three spatial dimensions and with time dependence, implemented numerically mostly with slow-but-accurate Monte Carlo methods, and ending with simple scaling arguments, implemented with the proverbial back-of-the-envelope algebra. In our individual experiences, it is this multi-tiered modeling toolkit that has enabled the pursuit of instrument development ... even though our training is in applied theoretical and computational physics and mathematics. This solid theoretical background also enabled us to propose new ways to use under-exploited components of existing radiometric signals, some of them considered previously as contamination (for example, 3D adjacency effects in remote sensing at high spatial resolutions) or even as noise (for example, solar background in lidar).

Although no real-world data is used in this paper, we point the reader to numerous publications by ourselves and others that are all about data analysis. They are all success stories that, as a whole, have shored up our now firm belief in balance – as well as intense interaction – between (*i*) theory, (*ii*) computation, and (*iii*) observation/experimentation. Stakes are often much higher for engineering projects than for cloud remote sensing: we can think, for instance, of aircraft or nuclear reactor safety and reliability. It is therefore not surprising to learn that engineering scientists have developed a quite formal choreography for the interaction between these three elements. In the process, the notions of 'verification' and 'validation' have been given precise meanings that Roache [6] has distilled into two fundamental questions: *Are the equations solved right?* (Verification) *Are they the right equations?* (Validation). The first V in 'V&V' leads in particular to code-to-code comparisons, while the second invariably leads to model-to-measurement comparisons. This framework can be adapted to the study of atmospheric radiation transport in the presence of clouds [7,8]. We believe many other communities, remote sensing included, have much to gain by adopting – or at least taking inspiration from – this tested framework.

In the next section, we survey the necessary prerequisites in time-domain 3D radiative transfer theory. In section 5.3, Fourier–Laplace transformation is introduced, which will prove useful in several ways. Sections 5.4 and 5.5 are the core material of the paper: formulation and solution of the diffusive Green function problem. In other words, how do we obtain analytic expressions for the Green function in time and/or space, or for its marginal or conditional moments, for light either reflected or transmitted by clouds? Appendices provide the required technical details as well as heuristic approaches to Green functions, in standard as well as anomalous diffusion regimes, using random walk theory. A comprehensive list of symbols and abbreviations is provided for reference at the end of the paper. Since the analytical expressions are delivered in Fourier and/or Laplace spaces, section 5.6 presents

[4]Radiative transfer has itself been connected to Huygens' scalar wave theory [4], and only quite recently in final form to Maxwell's classic electromagnetic wave theory [5], through rigorous methods of statistical optics.

special cases where inverse transforms can be performed in closed-form. The short section 5.7 on (airborne) *in situ* cloud 'lidar', a new probe of optically thick clouds from the inside, is followed by two longer sections devoted to emerging technologies in cloud remote sensing per se. Both time-domain radiative transfer via O_2 A-band spectroscopy (section 5.8) and multiple-scattering cloud lidar (section 5.9) can be implemented in ground-, aircraft- or space-based configurations. We show in particular that there is additional information to harvest in the spatial domain by lidars if the stand-off distance is not too large. A selection of other theoretical and observational applications of Green functions are described in section 5.10, for the most part based on well-established instrumentation. We offer some closing remarks in section 5.11 with an emphasis on future developments.

Notes on reproducibility and validation

The bulk of the analytic diffusion theoretical computations described in sections 5.5 to 5.10 were performed using a commercially available symbolic mathematics package. We believe that any such product can be used at the reader's convenience for replicating, generalizing and/or applying these results. Although it is possible to derive them by hand, the exercise can prove extremely tedious. We did it ourselves only in the simplest of cases.

Furthermore, diffusion is in essence an asymptotic limit of radiative transfer. Before trusting our diffusion results to give us insights about radiation transport processes in real clouds, we compare them on a regular basis using a numerical time-dependent radiative transfer solver, generally a straightforward Monte Carlo scheme. Is this comparison of model outputs verification and validation? In our view, it would be the former if the very same equations were solved, but that is not the case. One model is higher in the accuracy-based hierarchy than the other, so Monte Carlo can be used to validate diffusion. However, because of their role in validation, our Monte Carlo simulations were designed to follow as closely as possible the assumptions of the diffusion problem: single-parameter phase functions, predictions for fluxes, and so on. This way, we are informed about the range of cloud parameters where a specific diffusion model can be applied, and about the magnitude of associated modeling error.

5.2 Elements of time-dependent three-dimensional radiative transfer

5.2.1 Radiant energy transport

Let $G(t, \boldsymbol{x}, \boldsymbol{\Omega})$ denote radiance at instant t and position $\boldsymbol{x}$ in 3D space propagating into direction $\boldsymbol{\Omega}$ (units are $\mathrm{W/m^2/sr}$). In view of the focus of the present study on Dirac δ-sources introduced in the next subsection, we denote radiances here by G, the usual mnemonic for Green functions, and reserve I for 'at-detector' radiances discussed in various parts of the paper. At-the-detector is indeed where we quite literally leave the realm of radiative transfer and enter that of radiometry.

The flow of Green function radiance, $G(t, \boldsymbol{x}, \boldsymbol{\Omega})$, in its (1+3+2)-dimensional space is determined by the monochromatic time-dependent 3D radiative transfer (RT) equation [9], written succinctly as

$$\mathcal{L}G = \mathcal{S}G + Q. \tag{2.1}$$

On the l.-h. side, we identify the propagation operator

$$\mathcal{L} = c^{-1}\frac{\partial}{\partial t} + \boldsymbol{\Omega}\cdot\nabla + \sigma(\boldsymbol{x}) \tag{2.2}$$

where $\sigma(\boldsymbol{x})$ is the extinction coefficient (in 1/m), assumed to depend only on position. The two last terms in $\mathcal{L}$ represent *losses* for the intensity of the light beam as it crosses an elementary volume aligned with $\boldsymbol{\Omega}$, respectively to advection across boundaries and extinction.[5] We caution here that $\ell = 1/\sigma(\boldsymbol{x})$ may have a popular interpretation as the *local* value of the mean-free-path (MFP); however, it will generally differ from the *actual* MFP, except in strictly uniform media [10].

On the r.-h. side of (2.1), we find the *gains* of the elementary volume aligned with $\boldsymbol{\Omega}$. First comes the in-scattering operator

$$\mathcal{S} = \sigma_{\mathrm{s}}(\boldsymbol{x}) \int_{4\pi} p(\boldsymbol{\Omega}'\cdot\boldsymbol{\Omega})[\cdot]\,\mathrm{d}\boldsymbol{\Omega}' \tag{2.3}$$

where $\sigma_{\mathrm{s}}(\boldsymbol{x})$ is the scattering coefficient. It is also assumed to depend only on position and, for simplicity, in such a way that the single scattering albedo (SSA),

$$\varpi_0 = \frac{\sigma_{\mathrm{s}}(\boldsymbol{x})}{\sigma(\boldsymbol{x})} \tag{2.4}$$

remains constant. The scattering phase function (expressed here in 1/sr) is denoted $p(\boldsymbol{\Omega}_{\mathrm{in}}\cdot\boldsymbol{\Omega}_{\mathrm{out}})$; it is also assumed, for simplicity, uniform in space as well as axisymmetric around the incident direction $\boldsymbol{\Omega}_{\mathrm{in}}$. The local source term, denoted by $Q(t, \boldsymbol{x}, \boldsymbol{\Omega})$ in (2.1), is another net gain for the elementary volume (expressed in $\mathrm{W/m^3/sr}$).

Apart from boundaries, to be examined momentarily, the net losses of radiant energy for the whole medium are determined locally by the absorption coefficient $\sigma_{\mathrm{a}}(\boldsymbol{x}) = \sigma(\boldsymbol{x}) - \sigma_{\mathrm{s}}(\boldsymbol{x}) = (1-\varpi_0)\sigma(\boldsymbol{x})$.

The general RT equation spelled out in (2.1)–(2.3) is usually derived from purely phenomenological considerations grounded in radiant energy conservation [11] or, more formally, by analogy with particle kinetic theory leading to Boltzmann's transport equation, which is narrowed to the case of 'photons' [12], often viewed simply as neutrons without the possibility of multiplication events (that cause the SSA to exceed unity). However, when dealing with electromagnetic radiation, one cannot be satisfied with these derivations since, in particular, they do not make clear the conditions of validity of the transport model. Progress towards a wave-theoretical foundation for radiative transfer was achieved steadily using a scalar wave approach

[5] As far as we know, extinction σ can only be negative inside a lasing medium due to stimulated emission under conditions far from thermal equilibrium.

to physical optics [4]. We refer the interested reader to Mishchenko's recent review [13, and several key references therein], to gain understanding of how the RT equation – without temporal or spatial variability, but plus polarization – follows from Maxwell's equations through the rigorous methods of statistical optics. The three most important lessons from this definitive *microscopic* foundation for RT theory are probably:

1. that the *mesoscopic* 3D RT equation is valid in all 'dilute' optical media, i.e., where inter-particle distances are much larger than the wavelengths of interest;
2. that multiple scattering paths ending in propagation exactly backwards toward a source have a residual wave-theoretical signature in the interesting phenomenon of 'weak localization' (resulting in an enhancement of radiance very near the backscattering direction); and
3. that, in view of the purely classical derivation, 'photons' have nothing to do with the story in spite of the often-used analogy with particle transport, especially by Monte Carlo (MC) practitioners.

As an illustration of the last point, we should probably talk about e-folding distances rather than MFPs, a notion inherited from kinetic theory, which is patently about particulate material.

In the following, we will continue to depend on the microscopic description of radiation-matter interactions (Maxwell's equations and, as needed, their quantum mechanical counterparts) only to provide us with transport coefficients (σ's) and phase functions; see, for example, the monographs by Goody and Yung [14] for molecules, Bohren and Huffman [15] for spherical particles, and Mishchenko et al. [16] for nonspherical ones. We will actually be taking a step in the opposite direction: from the above *mesoscopic* 3D RT equation to the *macroscopic* picture where scattering dominates to such a degree that angular details are smoothed down to just two spherical harmonics. That is the 'diffusion' (a.k.a. 'P_1') limit of RT theory. In this asymptotic (small MFP) approximation to RT, the analogy between light (highly scattered) and particles (in Brownian motion) regains some usefulness, bearing in mind the caveat in the above lesson #3; cf. Appendix E.

Strictly speaking, the new microphysical derivation of the RT equation [5] is for spatially uniform, although not necessarily plane-parallel, media under steady and uniform illumination by a collimated beam. Mishchenko [17] extended his derivation to media with fluctuations at scales that are small with respect to the MFP; specifically, one neglects the contributions of electromagnetic wave interactions between particles inside the same (randomly placed) 'inclusion'. However, extensions of this rigorous framework to pulsed and/or narrow beams and/or larger-scale fluctuations – all topics of interest here – are considered open problems [13]. Pending its derivation from first principles (Maxwell's equations), we will use the time-dependent 3D RT equation in (2.1)–(2.3) as the 'exact' numerical benchmark against which analytical diffusion-based approximations are assessed.

5.2.2 Dirac-δ boundary sources

In view of the potential for spatial variability of $\sigma(\boldsymbol{x})$, no generality is lost by bounding the cloudy medium by two horizontal planes at $z = 0$ and $z = H$. If we

exclude from the definition of G the un-collided part of the radiance impinging on the medium from an external source, then we can subject the 3D RT equation to homogeneous boundary conditions (BCs):

$$G(t, x, y, 0, \mathbf{\Omega}) = 0, \ \mu > 0, \tag{2.5}$$

$$G(t, x, y, H, \mathbf{\Omega}) = 0, \ \mu < 0, \tag{2.6}$$

where we denote direction cosines as

$$\mathbf{\Omega}(\theta, \phi) = \begin{pmatrix} \eta \cos\phi \\ \eta \sin\phi \\ \mu \end{pmatrix}$$

in Cartesian coordinates using polar angles, with $\mu = \cos\theta$ and $\eta = \sqrt{1-\mu^2}$. In this case, nontrivial solutions of the RT equation require a non-vanishing source term Q in (2.1). For boundary-source Green functions, we use

$$\begin{aligned} Q(t, \boldsymbol{x}, \mathbf{\Omega}) = \ & \delta(t - z/c)\delta(x)\delta(y)\, \sigma_{\mathrm{s}}(0, 0, z) p(\mu) \\ & \times \ \exp\left(- \int_0^z \sigma(0, 0, z')\, \mathrm{d}z' \right) \end{aligned} \tag{2.7}$$

where we assume, for the moment, vertical beam alignment (normal to the boundary at $z = 0$). Note from the writing of the first δ-function that the instant $t = 0$ is when the the laser pulse hits the cloud at $z = 0$, precisely at $x = y = 0$ for convenience. Lasers are indeed physical sources that approximate Dirac-δ's extremely well in all the variables that matter here: time, location and directionality. In other applications, their δ-in-wavelength and δ-in-polarization qualities also come in handy.

Alternatively, we can set $Q(t, \boldsymbol{x}, \mathbf{\Omega}) \equiv 0$ in the RT equation and model the source in a revised statement of the BC (2.5) at $z = 0$:

$$G(t, x, y, 0, \mathbf{\Omega}) = \delta(t)\delta(x)\delta(y)\delta(\mathbf{\Omega} - \hat{\mathbf{z}}), \ \Omega_z = \mu > 0, \tag{2.8}$$

where $\hat{\mathbf{z}} = (0, 0, 1)^{\mathrm{T}}$ orients the positive z-axis. In this case, the radiance field contains both direct and diffuse components. Apart from this interpretation of what is contained in $G(t, \boldsymbol{x}, \mathbf{\Omega})$ or not, the two ways of modeling the normally incident Dirac-δ source at a boundary are equivalent.

Figure 5.1 offers a comprehensive view of the spatial Green function excited by a steady narrow beam normal to the upper boundary of a uniform non-absorbing cloud assumed to be between altitudes 1 km and 2.2 km. Mean radiance, averaged over all directions, is plotted. We immediately notice that the multiple-scattering Green function permeates the whole optically thick ($\tau = 36$) cloud. In view of the logarithmic scale, we notice the exponential-type decay of the light field with distance from the beam inside the cloud. This contrasts with the much slower decay of overall light levels with distance to the cloud boundaries (viewed as sources for remote observers), which is based on a $1/r^2$ law in the absence of any significant scattering or absorption. Let us assume we have a single laser pulse with $\sim 10^{18}$ photons (for example, a 532 nm solid-state device with 5 W in cw power pulsing

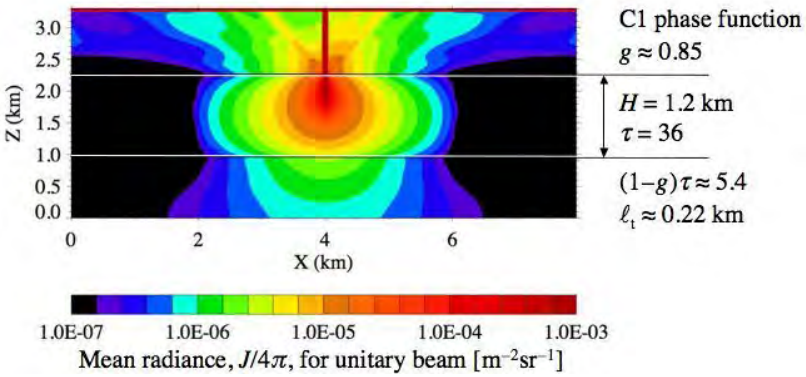

Fig. 5.1. *Mean radiance for the search-beam problem in a finite homogeneous slab.* The steady-state version of the RT problem defined in (2.1)–(2.7) was solved with the Spherical Harmonic – Discrete Ordinate Method (SHDOM) [18, 19] for a uniform non-absorbing ($\varpi_0 = 1$) cloud with thickness $H = 1.2$ km and uniform extinction $\sigma = 30$ km^{-1}, hence optical thickness $\tau = \sigma H = 36$. The phase function is for a 'C1' distribution of droplet size [20] in a Mie scattering computation [15] for $\lambda = 532$ nm, which yields asymmetry factor $g \approx 0.85$ in (2.21). Mean radiance, $J/4\pi$ from (4.5), is plotted for a domain larger than the cloud itself. The 'rays' emanating from the source region near the top of the cloud are an artifact of the discrete ordinates scheme (in this case, $N_\mu = 12$ and $N_\phi = 24$). This result was graciously contributed by Dr K. Franklin Evans (University of Colorado).

at 10 Hz), and a modest (but highly efficient) detector with a modest aperture of $\sim$1 mm^2 and a 1-sr field-of-view (FOV) corresponding to $\approx$66° from side to side. A typical number of photons detected per pulse by such a sensor in the light shaded zone (for example, ground level, right below the source) is then $\sim 10^{18} \times 10^{-6}/\mathrm{m}^2/\mathrm{sr} \times 1\ \mathrm{sr} \times (10^{-3})^2\ \mathrm{m}^2 = 10^6$, which appears to be enough to spread over, say, several 1000s of bins in space (direction) and/or time before the signal-to-noise ratio (SNR) falls below $\sqrt{10^6/1000\mathrm{s}} \sim 10$s for shot noise alone. This leaves plenty of room for a different FOV, reduced optical throughput, quantum efficiency, and so on.[6]

For oblique illumination along $\mathbf{\Omega}_0(\theta_0, \phi_0)$, the internal source formulation with (2.7) becomes

$$Q(t, \boldsymbol{x}, \mathbf{\Omega}) = \delta\left(t - \frac{z/c}{\mu_0}\right) \delta\left(x - \eta_0 \cos\phi_0 \frac{z}{\mu_0}\right) \delta\left(y - \eta_0 \sin\phi_0 \frac{z}{\mu_0}\right) \sigma_\mathrm{s}(x, y, z) \times p(\mathbf{\Omega}_0 \cdot \mathbf{\Omega}) \exp\left[-\int_0^z \sigma\left(\eta_0 \cos\phi_0 \frac{z'}{\mu_0}, \eta_0 \sin\phi_0 \frac{z'}{\mu_0}, z'\right) \frac{\mathrm{d}z'}{\mu_0}\right], \quad (2.9)$$

while the BC source model in (2.8) becomes simply

$$G(t, x, y, 0, \mathbf{\Omega}) = \delta(t)\delta(x)\delta(y)\delta(\mathbf{\Omega} - \mathbf{\Omega}_0), \quad (2.10)$$

[6] If it dominates the shot noise, background noise (sun- or moonlight) can be dealt with by appropriate filtering and time integration [21].

where $\mu, \mu_0 > 0$. Although we will focus primarily on uniform and slant (solar) or pointwise and normal (lidar) illumination geometries, the above model for the boundary source is general enough to cover all possible spatial, temporal and angular distributions of sources by using straightforward space-time translations and linear superposition (i.e., convolutions).

A final type of unitary source we are highly interested in is *isotropic* boundary-point-sources, which can be expressed as

$$G(t, x, y, 0, \mathbf{\Omega}) = \delta(t)\delta(x)\delta(y)/\pi, \tag{2.11}$$

for all $\mu > 0$ in the BC (2.5) at $z = 0$.

All of the *primary* sources of radiation, in the bulk or at the boundary of the optical medium, have now been accounted for. In the same way that the in-scattering operator in (2.3) produces a *secondary* source of radiance for a given beam, boundaries can become secondary sources via partial reflection, as opposed to the systematic absorption/escape described in (2.5)–(2.6). This process of boundary scattering is formalized in a revised r.-h. side for the BC (2.6) at $z = H$ for incoming radiance $G(t, x, y, H, \mathbf{\Omega})$ with $\mu < 0$. Specifically, we introduce in analogy with (2.3),

$$\mathcal{S}_\mathrm{s} = \alpha_H(x, y) \int\limits_{\mu'>0} p_\mathrm{s}(\mathbf{\Omega}' \to \mathbf{\Omega})[\cdot]\, \mathrm{d}\mathbf{\Omega}', \tag{2.12}$$

which is applied to the local G; $\alpha_H(x, y)$ is the local albedo of the boundary and $p_\mathrm{s}(\mathbf{\Omega}' \to \mathbf{\Omega})$ is the surface phase function (in 1/sr).[7] If necessary, we could similarly define a reflective BC for the illuminated boundary at $z = 0$; this would only mean a change of sign in μ and μ'. Two contrasting examples of surface scattering/reflection are the isotropic (a.k.a. Lambertian) case, $p_\mathrm{s}(\mathbf{\Omega}' \to \mathbf{\Omega}) = |\mu'|/\pi$, and the specular (a.k.a. Fresnel) case, $p_\mathrm{s}(\mathbf{\Omega}' \to \mathbf{\Omega}) = \delta(\mu' + \mu)\delta(\phi' - \phi)$.

We have now defined all the components of the RT equation, its BCs, and the boundary δ-sources of primary interest here. This completes the determination of the multiple-scattering Green function in the spirit of Bell and Glasstone [23], who introduced it as a powerful modeling tool in nuclear reactor design and analysis. The remainder of this section narrows our interest to outgoing boundary radiances and their properties.

5.2.3 Remotely observable fields

In remote sensing applications, we use detectors *outside* the medium. We can therefore access only the outgoing radiance fields at cloud boundaries, which echo the boundary conditions in (2.5)–(2.6) but with z-axis direction cosines of opposite sign: $G(t, \overrightarrow{\rho}, 0, \mathbf{\Omega})$, when $\Omega_z = \mu < 0$, for reflection; $G(t, \overrightarrow{\rho}, H, \mathbf{\Omega})$, when $\Omega_z = \mu > 0$, for transmission. We denote here

$$\overrightarrow{\rho} = \begin{pmatrix} x \\ y \end{pmatrix}, \text{ hence } \boldsymbol{x} = \begin{pmatrix} \overrightarrow{\rho} \\ z \end{pmatrix}.$$

[7] To connect with the popular 'bidirectional reflection distribution function' (BRDF) [22]: $\rho(\mathbf{\Omega}' \to \mathbf{\Omega}) = \alpha_H p_\mathrm{s}(\mathbf{\Omega}' \to \mathbf{\Omega})/|\mu'|$.

More precisely, we assume an imaging detector is measuring this radiance at some finite stand-off distance $d_{\rm obs} > 0$ from the cloud boundary of interest: the sensor is thus positioned at $\boldsymbol{x}_{\rm obs} = (\overrightarrow{0}, -d_{\rm obs})^{\rm T}$ or $(\overrightarrow{0}, H + d_{\rm obs})^{\rm T}$. See schematic in Fig. 5.2.

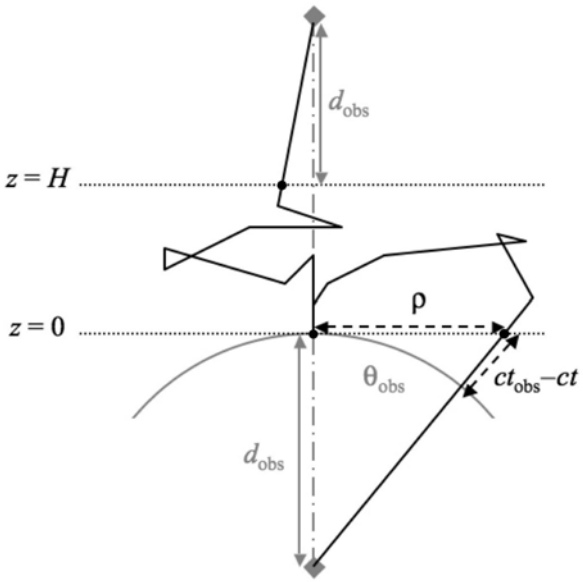

Fig. 5.2. *Schematic of boundary-source/boundary-detector Green function problem.* We illustrate the case of normal incidence and an observer along the incident beam.

Notice that we assume geometric alignment with the normally incident collimated beam. For reflected light, this is tantamount to modeling a monostatic lidar (i.e., transmitter and receiver collocated). For transmitted light, the detector is looking straight at the point-source on the opposite boundary of the optical medium, a typical configuration in imaging and visibility studies. In the latter case, the proportion of the emitted light *directly* transmitted from the collimated source in (2.7) or (2.8) to the detector is $\exp[-\tau(\overrightarrow{0})]$. More generally, we define

$$\tau(\overrightarrow{\rho}) = \int_0^H \sigma(\overrightarrow{\rho}, z)\, {\rm d}z \tag{2.13}$$

as the optical thickness of the medium at horizontal position $\overrightarrow{\rho}$. The interesting questions, however, are about the *diffuse* component generated by one or more scatterings. We are thus restricting ourselves to coaxial source–detector geometry ($\overrightarrow{\rho}_0 = \overrightarrow{\rho}_{\rm obs} = \overrightarrow{0}$), simply because of the applications treated in the present study; if necessary, generalization to $\overrightarrow{\rho}_{\rm obs} \neq \overrightarrow{0}$ is straightforward.

We denote the radiance recorded by the time-resolving/imaging detector as $I_{\rm obs}(t_{\rm obs}, \boldsymbol{\Omega}_{\rm obs})$. From this vantage point, we just sub-sample the Green function for boundary illumination, $G(t, \overrightarrow{\rho}, 0, \boldsymbol{\Omega})$ or $G(t, \overrightarrow{\rho}, H, \boldsymbol{\Omega})$ is equated with

$G(t, \overrightarrow{\rho}, \cdot, \mathbf{\Omega}_{\rm obs}(\overrightarrow{\rho}))$. In the time-domain, t refers to the time interval from entry at the $z = 0$ boundary to escape from anywhere; however, unless the point of escape is the closest to the detector, an observer at finite distance will see an extra delay illustrated in Fig. 5.2. So we have

$$t = t_{\rm obs} - \left(\frac{1}{\cos\theta_{\rm obs}} - 1 \right) \frac{d_{\rm obs}}{c}. \tag{2.14}$$

In the case of monostatic lidar observations (in reflection, when the detector is near the source), one might use $t_{\text{round-trip}} = t_{\rm obs} + 2d_{\rm obs}/c$. To equate 'at detector' and 'at cloud' radiances in the spatial domain, we must also factor into the independent variables the finite distance to the observation point:

$$\rho(\theta_{\rm obs}) = \sqrt{x^2 + y^2} = d_{\rm obs} \tan\theta_{\rm obs},$$

hence,

$$\theta_{\rm obs}(\rho) = \tan^{-1}(\rho/d_{\rm obs}),$$

and

$$\mathbf{\Omega}_{\rm obs}(\overrightarrow{\rho}) = \mp \begin{pmatrix} \cos\phi_{\rm obs}\ \sin\theta_{\rm obs}(\rho) \\ \sin\phi_{\rm obs}\ \sin\theta_{\rm obs}(\rho) \\ \cos\theta_{\rm obs}(\rho) \end{pmatrix}, \tag{2.15}$$

where $-$ is for reflection and $+$ is for transmission.

In the limit $d_{\rm obs} \to \infty$, a reasonable approximation for an orbital detector, the connections in (2.14)–(2.15) still make sense by taking simultaneously the limit $\theta_{\rm obs} \to 0$, but keeping ρ constant. We thus denote the detector response as $I_{\rm obs}(t, \rho)$, after accounting for the large but finite time delay; the last connection in (2.15) simplifies to $\mathbf{\Omega}_{\rm obs}(\rho) = (0, 0, \mp 1)^{\rm T} = \mp\hat{\mathbf{z}}$.

5.2.4 Flux-based spatial and temporal moments

To summarize, we are interested in computing and measuring the time-dependent *equivalent* reflectance (or albedo) field

$$R_{\rm obs}(t, \overrightarrow{\rho}) = \pi G(t, \overrightarrow{\rho}, 0, \mathbf{\Omega}_{\rm obs}(\overrightarrow{\rho}))/\mu_0 \tag{2.16}$$

normalized by total source energy, and its counterpart in transmittance

$$T_{\rm obs}(t, \overrightarrow{\rho}) = \pi G(t, \overrightarrow{\rho}, H, \mathbf{\Omega}_{\rm obs}(\overrightarrow{\rho}))/\mu_0. \tag{2.17}$$

These are just alternatives to boundary-leaving radiance using

1. a Lambertian assumption about outgoing directions other than $\mathbf{\Omega}_{\rm obs}$ (hence the factor π), and
2. normalization by total incoming flux integrated over space, time and direction (hence the $1/\mu_0$ factor that accounts for the reduction in flux when illumination is unitary but oblique).

Temporarily ignoring angular sampling and truncation issues in real measurements, we define

$$R(t,\overrightarrow{\rho}) \;=\; \frac{1}{\mu_0}\int\limits_{-\pi}^{+\pi}\int\limits_{\pi/2}^{\pi} \mid \cos\theta | G(t,\overrightarrow{\rho},0,\mathbf{\Omega}(\theta,\phi))\,\sin\theta\,\mathrm{d}\theta\,\mathrm{d}\phi, \tag{2.18}$$

$$T(t,\overrightarrow{\rho}) \;=\; \frac{1}{\mu_0}\int\limits_{-\pi}^{+\pi}\int\limits_{0}^{\pi/2} \cos\theta\, G(t,\overrightarrow{\rho},H,\mathbf{\Omega}(\theta,\phi))\,\sin\theta\,\mathrm{d}\theta\,\mathrm{d}\phi, \tag{2.19}$$

as the local time-dependent reflected and transmitted *flux* fields, respectively. The equivalent and actual reflectance and transmittance fields displayed above are *by definition* ratios of outgoing-to-incoming hemispherical fluxes, estimated or actual. Lastly, we note that (2.19) is either diffuse or total transmittance depending on the adopted formulation of the 3D RT equation. If we only have the diffuse transmittance, then the total one is obtained by adding $\exp[-\tau(\mathbf{\Omega}_0)]/\mu_0$ where

$$\tau(\theta_0,\phi_0) = \int\limits_0^H \sigma\left(\eta_0\,\cos\phi_0\,\frac{z}{\mu_0},\eta_0\,\sin\phi_0\,\frac{z}{\mu_0},z\right)\frac{\mathrm{d}z}{\mu_0}$$

is the optical path across the whole medium along the incident beam. It coincides with (2.13) only when $\mu_0 = 1$ here and $\overrightarrow{\rho} = \overrightarrow{0}$ there.

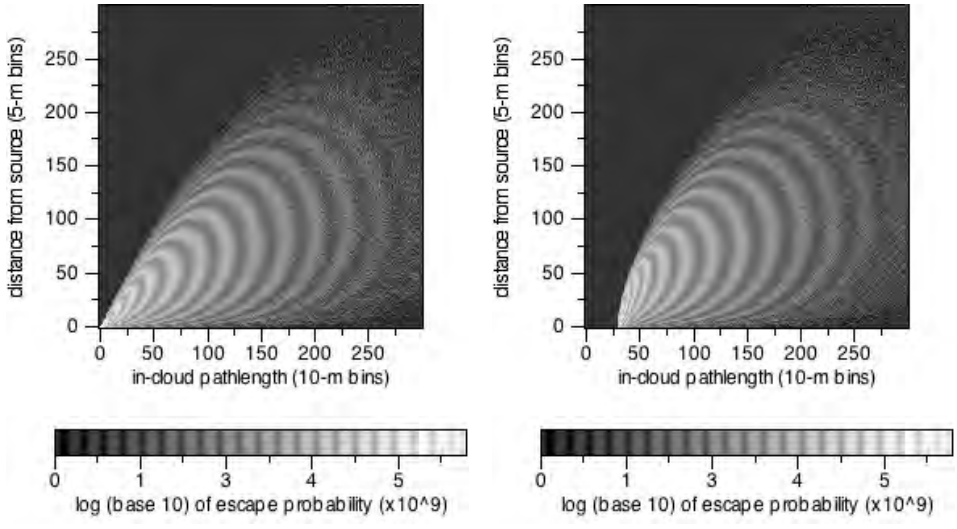

Fig. 5.3. *Space-time boundary Green functions of a uniform cloud under diffuse pointwise illumination for reflection (left) and transmission (right).* These responses in flux were estimated numerically using a MC simulation with 10^9 histories that resulted in reflection with probability $R = 0.557$ and transmission with probability $T = 1 - R$. The logarithmic grayscale is the same for both panels. Lateral transport distance ρ runs vertically from 0 to 1.5 km while in-cloud path ct runs horizontally from 0 to 3 km. Reproduced from Ref. [24] with permission. More details in text.

Figure 5.3 displays numerical (hence binned) estimates of $R(ct, \rho)$ and $T(ct, \rho)$ for a *uniform* cloud, using the convenient units of in-cloud path ct rather than transit time per se. The pointwise illumination is isotropic: boundary condition at $z = 0$ from (2.11) and $Q \equiv 0$ in (2.1). The cloud has $H = 0.3$ km and $\tau = 16$; there is no absorption ($\varpi_0 = 1$) and scattering is according to the Henyey–Greenstein (H–G) model [25]:

$$p(\mu_s) = \left(\frac{1}{4\pi}\right) \frac{1 - g^2}{(1 + g^2 - 2g\mu_s)^{3/2}}, \tag{2.20}$$

where μ_s is the cosine of the scattering angle, i.e., $\mathbf{\Omega}' \cdot \mathbf{\Omega}$. The new parameter g, the well-known 'asymmetry factor', is critical to this study of diffusion regimes. In general, it is defined as

$$g = \int\limits_{4\pi} \mathbf{\Omega}' \cdot \mathbf{\Omega} p(\mathbf{\Omega}' \cdot \mathbf{\Omega}) \, \mathrm{d}\mathbf{\Omega}' = 2\pi \int\limits_{-1}^{+1} \mu_s p(\mu_s) \, \mathrm{d}\mu_s. \tag{2.21}$$

In this case, we used[8] $g = 0.85$.

The most striking difference between the two radiative responses in Fig. 5.3 for a localized and pulsed excitation is that reflectance happens immediately, thanks to low orders of scattering, while transmittance occurs only for $ct \geq H$, with '=' being very unlikely since it calls for a direct transmission (at the $\mathrm{e}^{-16} \approx 10^{-7}$ probability level). Supports of both responses are inside the causality cone ($\rho \leq ct$) dictated by shallow quasi-ballistic lateral propagation away from the isotropic source followed by a reflection. At large ct and ρ, the two responses are indistinguishable since after a large number of scatterings escape is equally probable through either boundary. Also, for fixed $ct \gtrsim H$, we see that the value of ρ that maximizes the Green function (where the tangent to the isophote is vertical in the panels of Fig. 5.3) follows a roughly parabolic trend ($\rho_{\max}(ct) \sim \sqrt{ct}$). This is typical of diffusive radiation transport, as we will see further on.

Figure 5.4 focuses on spatial Green functions. The l.-h. panels are the axisymmetric fields $F(\overrightarrow{\rho}) \equiv F(\rho)$, $F = R, T$, from (2.22) for a uniform cloud with $\tau = 13$ and conservative $g = 0.85$ H–G scattering under normal collimated illumination by a narrow beam. As in Fig. 5.3, the main differences between reflection and transmission are in the near-axis region. The top and r.-h. panels are $F(\overrightarrow{\rho})$, $F = R, T$, for a randomly variable cloud with long-range spatial correlations. The fluctuating values of the local optical depth in (2.13) have the same mean optical depth $\overline{\tau} = 13$; vertical structure is assumed uniform.[9] The boundary flux fields for this scaling (a.k.a. 'fractal') stratocumulus (Sc) cloud model of course have no axial symmetry. Closer examination shows that there is less overall reflection and correspondingly more transmission; in both cases, we see a slight increase in the horizontal dispersion quantified by the root-mean-square (RMS) value of $\overrightarrow{\rho}$.

[8] It is notable that phase functions for observed droplet-size distributions in boundary-layer clouds yield $g \approx 0.85$ with remarkably small variability [26].

[9] This stochastic cloud model was generated with a so-called 'bounded cascade' model [27] tuned to have a Kolmogorov-type wavenumber spectrum in $k^{-5/3}$ and an amplitude of variation similar to those observed in marine stratocumulus [28]. More details on this fractal cloud model are provided in section 5.10.6.

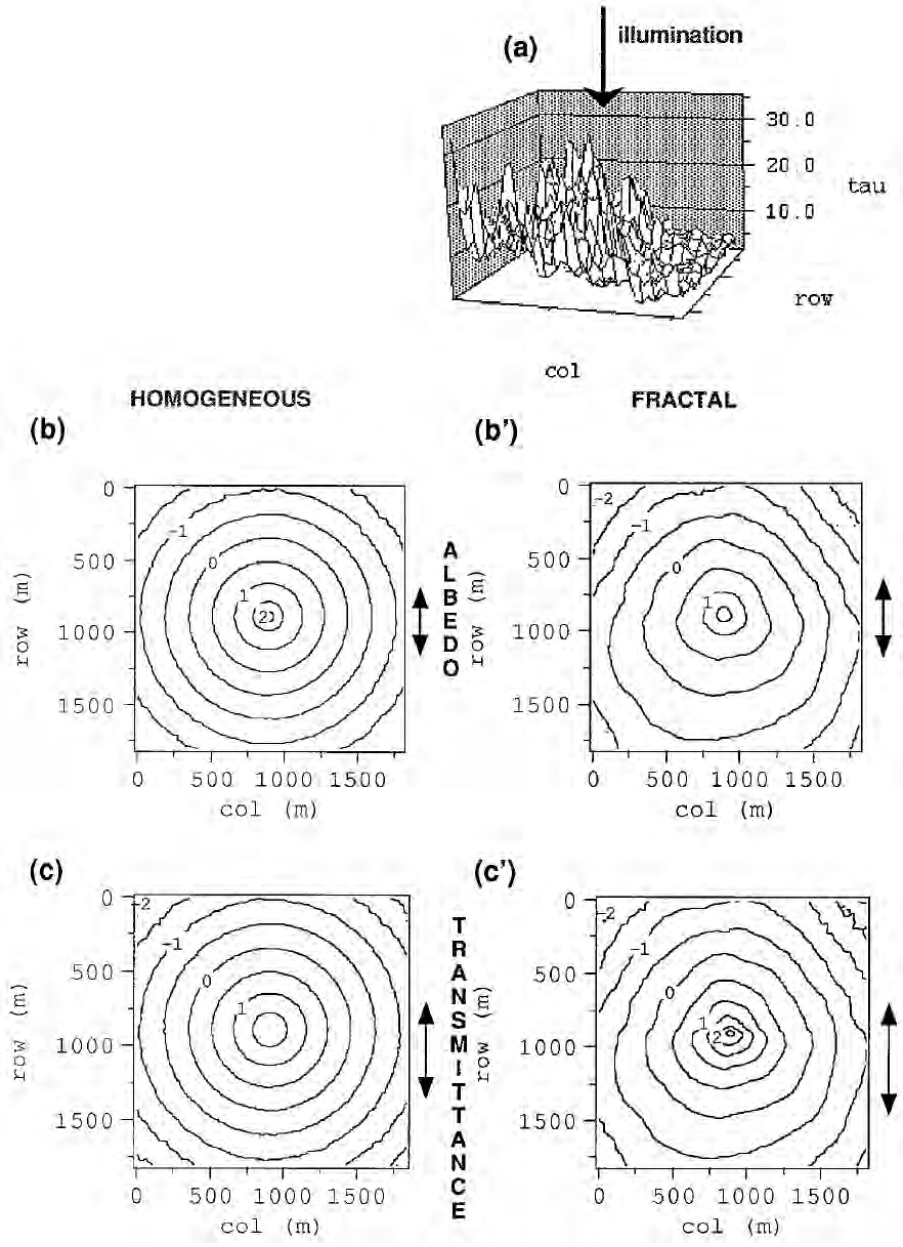

Fig. 5.4. *Spatial Green functions of homogeneous (left) and fractal (right) clouds with the same mean optical depth under steady normal illumination by a narrow beam.* These are the outcome of two MC simulations, each with 10^8 histories; these events resulted in reflection (b,b') with probability $R \approx 0.5$ in the uniform case and ≈ 0.3 in the fractal case, or in transmission (c,c') with probability $T = 1 - R$. A 128×128 grid was used to bin the boundary fluxes $F(\vec{\rho})$ with $F = R, T$. In the fractal case, we notice the systematically larger spread towards rows with high rank, which correspond to the more tenuous region in the top graphic (a) showing $\tau(x, y)$ from (2.13). Reproduced from Ref. with permission. More details in text.

Partly to improve the SNR and partly for conceptual simplicity, we like to use spatial and/or temporal integrals of the observed flux field $F(t, \overrightarrow{\rho})$, for $F = R, T$. We are particularly interested in statistical moments when it is viewed as a probability density function (PDF) for escape in reflection or transmission. In order to normalize the PDFs, we start by estimating

$$F = \int_0^\infty F(t)\,\mathrm{d}t = \iint_{-\infty}^{+\infty} F(\overrightarrow{\rho})\,\mathrm{d}\overrightarrow{\rho}(x,y) = \int_0^\infty \mathrm{d}t \iint_{-\infty}^{+\infty} F(t, \overrightarrow{\rho})\,\mathrm{d}\overrightarrow{\rho}(x,y), \tag{2.22}$$

the cloud's albedo ($F = R$) or transmittance ($F = T$) for steady and uniform illumination, either collimated or isotropic. We can then proceed to compute

$$\langle t^q \rangle_F = \frac{1}{F} \int_0^\infty t^q F(t)\,\mathrm{d}t = \frac{1}{F} \int_0^\infty t^q\,\mathrm{d}t \iint_{-\infty}^{+\infty} F(t, \overrightarrow{\rho})\,\mathrm{d}\overrightarrow{\rho}(x,y) \tag{2.23}$$

for $q = 1, 2$, or more, and

$$\langle \rho^2 \rangle_F = \frac{1}{F} \iint_{-\infty}^{+\infty} \rho^2 F(\overrightarrow{\rho})\,\mathrm{d}\overrightarrow{\rho}(x,y) = \frac{1}{F} \int_0^\infty \mathrm{d}t \iint_{-\infty}^{+\infty} \rho^2 F(t, \overrightarrow{\rho})\,\mathrm{d}\overrightarrow{\rho}(x,y). \tag{2.24}$$

Angular brackets will always denote averages over space and/or time in cloud radiative *responses* while an overscore denotes an average over spatial disorder, i.e., cloud *structure*. Examples of $\langle \rho^2 \rangle_F^{1/2}$ (RMS horizontal transport) for normal illumination are rendered graphically with double-headed arrows in Fig. 5.4.

The above are 'marginal' moments; 'joint' moments $\langle t^q \rho^p \rangle_F$ and 'conditional' moments can also be estimated. Of particular interest in this last class is

$$\langle \rho^2 \rangle_F(t) = \frac{1}{F(t)} \iint_{-\infty}^{+\infty} \rho^2 F(t, \overrightarrow{\rho})\,\mathrm{d}\overrightarrow{\rho}(x,y), \tag{2.25}$$

the mean-square horizontal transport at a fixed time, where $F(t)$ follows from (2.22) without the time integral.

Note that the moment estimations in (2.24)–(2.23) are immune to uncertainties in a multiplicative constant for $F(t, \overrightarrow{\rho})$. From an observational standpoint, and in sharp contrast with the estimation of cloud albedo or transmittance based on (2.22), absolute calibration is not required. The easier task of flat-fielding of the imager's focal-plane array is, however, still necessary.

Of course, real-world observations give us no information on the boundary Green function $G(t, \overrightarrow{\rho}, 0, \mathbf{\Omega}_{\mathrm{obs}}(\overrightarrow{\rho}))$, hence on $R(t, \overrightarrow{\rho})$, outside of the receiver's FOV, i.e., the actual limits of all the above integrals over $\overrightarrow{\rho}(x,y)$ are finite when $F = R$, and similarly for T. Moreover, for each value of $\overrightarrow{\rho}$ we only get one value of θ and ϕ in (2.15). The latter problem is resolved by using an angular model to convert an observed radiance into a boundary flux. The former problem is best addressed by designing instruments with the widest possible FOV, such that it contains at least a couple of the Green function's e-folding distances away from the axis. We can then assume quite safely that the residual truncation errors in both numerator and denominator in (2.24)–(2.23) do not bias the estimates too much.

5.2.5 Vertical variation of scattering coefficient

From this point on, we restrict our interest to stratiform clouds that can be reasonably well represented by plane-parallel slabs of uniform thickness H,

$$\mathrm{M}(H) = \{\boldsymbol{x} \in \mathbb{R}^3; 0 < z < H\},$$

still allowing for some degree of internal structure. In the above, we examined cloud models with fractal behavior in the horizontal plane but uniformity in the vertical. In the following, we will consider two complementary kinds of variability: smooth (convection/radiation-driven) stratification along the z-axis and random (turbulence-driven) 3D fluctuations. Discussion of the latter is postponed until section 5.4.2.3, leaving us until then with $\sigma(\boldsymbol{x}) \equiv \sigma(z)$, and similarly for σ_s and σ_a. The parameters of primary interest for a purely stratified cloud are its physical thickness H and optical depth τ from (2.13), but without the dependence on $\overrightarrow{\rho}(x, y)$.

Basic cloud physics informs us that stratus clouds are expected to be strongly stratified. For instance, liquid water content (LWC) is predicted and widely observed [30] to follow the adiabatic gradient in their 'convective cores', i.e., a linear trend in z over the vertical extent of the cloud.[10] This classic result from the baseline 'rising parcel' theory in cloud microphysics (number density assumed constant) leads to a 2/3 power-law in extinction, from straightforward dimensional analysis. Formally, and depending on what side of the cloud is being illuminated by the δ-source, we can write this as

$$\begin{aligned} \sigma_0(\gamma; z) &= \overline{\sigma} \times (1+\gamma)\,(z/H)^\gamma, \text{ or} \\ \sigma_H(\gamma; z) &= \overline{\sigma} \times (1+\gamma)\,(1-z/H)^\gamma, \end{aligned} \tag{2.26}$$

with $\gamma \geq 0$ (in this case, 2/3) and $\overline{\sigma}$ denoting the mean extinction (obtained, say, from cloud optical depth $\tau = \overline{\sigma} H$).

Instead of the power-law model, it is advantageous to use a linear (constant gradient) model,

$$\sigma_\Delta(z) = \overline{\sigma} \times [1 + \Delta\,(z/H - 1/2)], \tag{2.27}$$

where $|\Delta| \leq 2$ is the relative difference in extinction at the two cloud boundaries with respect to its mean value (invariably crossed at $z = H/2$). To put the linear and power-law models in one-to-one correspondence, we propose to minimize their difference squared (distance in L^2). This exercise leads to

$$\Delta(\gamma) = \pm 6 \times \left(2\,\frac{\gamma+1}{\gamma+2} - 1 \right) \tag{2.28}$$

where $+$ is mapped to $\sigma_0(\gamma; z)$ and $-$ to $\sigma_H(\gamma; z)$. Values of special interest are $\Delta = \pm 3/2$ since they approximate $\gamma = 2/3$, the abovementioned expectations based on parcel theory for a cloud illuminated from below $(+)$ and above $(-)$. Conversely, we have

$$\gamma(\Delta) = 2|\Delta|/(6 - |\Delta|). \tag{2.29}$$

[10] In a broader view of liquid water clouds, the maximum value of LWC is typically reached at a depth of $\approx H/3$ from the top.

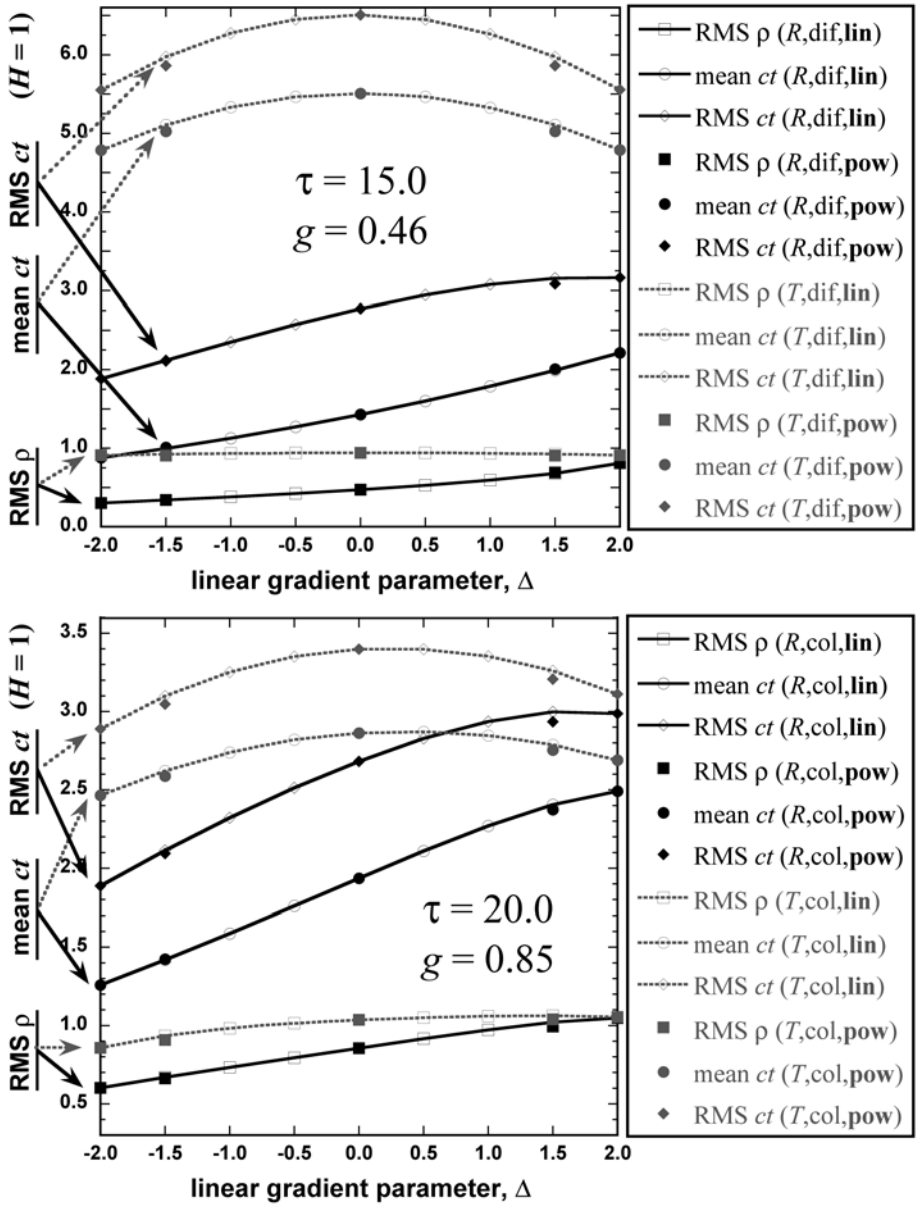

Fig. 5.5. *The impact of internal stratification on space-time cloud responses in flux to an isotropic point-source (top) and a narrow collimated beam (bottom).* These results are from a number of MC simulations ($2 \cdot 10^8$ histories) with H–G scattering (2.20). For simplicity, the maximum cross-section algorithm was used to account for internal structure; see Refs [19, 29]. Moments defined in (2.23)–(2.24) were computed, using their square-root for second-order moments, and normalized to $H = 1$. We used $\tau = 15$ with $g = 0.46$ in the top panel, and $\tau = 20$ with $g = 0.85$ in the lower panel. In spite of the larger optical depth, we notice the smaller spread of results in the latter case (half the vertical range) due to more forward-peaked scattering and a more anisotropic source. More discussion in the main text.

Stratification in $\sigma(z)$, as parameterized in the above, will directly affect the spatial (2.24) and temporal (2.23) observables, even if it has no effect whatsoever on the cloud's albedo ($F = R$) or transmittance ($F = T$) in (2.22). Indeed, the local value of the MFP will be different at the top and bottom of the cloud and, physically, this means that the random walk representing the diffusing light propagation is scaled up (near cloud base) or down (near cloud top). Active and passive instruments are already probing clouds from both sides and will continue to do so; it is therefore imperative to quantify the effect of stratification on the observables.

Figure 5.5 shows numerical MC results for $\sqrt{\langle \rho^2 \rangle_F}/H$, for $\langle ct \rangle_F/H$ and for $\sqrt{\langle (ct)^2 \rangle_F}/H$ ($F = R, T$) using both stratification models. The constant-gradient model in (2.27) is sampled at 0.5 intervals from $\Delta = -2$ to $+2$ for the prescribed clouds and sources. The power-law model in (2.26) degenerates to the linear case when $\gamma = 1$ ($\Delta = \pm 2$), and of course when $\gamma = 0$ ($\Delta = 0$), but it is interesting to seek differences between the $\gamma = 2/3$ cases and the associated values of $\Delta = \pm 3/2$ using (2.28). They are very small compared to the overall effect of stratification. In turn, these effects are significantly larger for reflection than for transmission, especially in the time domain. We also note in the top panel that, when illumination is pointwise but isotropic and the response is for boundary fluxes, the Green functions for transmission depend only on $|\Delta|$ due to source–detector reciprocity and a mirror-symmetry around $z = H/2$.

The qualitative differences between boundary-flux responses R and T we have uncovered can be traced to the fact that *reflected* light is a balanced mix of low- and high-order scattering. The low orders in the observed signal come almost surely from near the source, hence from the illuminated side of the cloud, while the high orders come from radiation that has permeated the whole cloud. In contrast, radiation *transmitted* by optically thick clouds is made almost entirely of highly scattered light.

5.3 Formulation in the Fourier–Laplace domain

Moment integrals in (2.23)–(2.24) are easy to compute by manipulation of transforms in Fourier–Laplace space. In probability theory, the Fourier or Laplace transform of a PDF is called its 'characteristic' function or, more tellingly, 'moment-generating' function [31]. Which transform is used depends on the support of the PDF. In our application, we need both Laplace for time $t \in [0, \infty)$ and 2D Fourier for position $\overrightarrow{\rho}$ in the $z = 0, H$ planes.

We are thus interested in the behavior of

$$\begin{aligned} \tilde{F}(s, \overrightarrow{k}) &= \int_0^\infty \mathrm{d}t \iint_{-\infty}^{+\infty} \exp(-st + \mathrm{i}\,\overrightarrow{k} \cdot \overrightarrow{\rho})\, F(t, \overrightarrow{\rho})\, \mathrm{d}\overrightarrow{\rho}(x, y) \\ &= F \times \langle \exp(-st + \mathrm{i}\,\overrightarrow{k} \cdot \overrightarrow{\rho}) \rangle_F,\ F = R, T. \end{aligned} \tag{3.1}$$

We will apply a similar transformation to other '3+1D' quantities as needed.

5.3.1 Temporal Green functions and pulse-stretching problems

Consider the case of uniform, but still pulsed, illumination ($\overrightarrow{k} \equiv \overrightarrow{0}$). One can show [32] from (3.1) that coefficients of the Taylor expansion of $\tilde{F}(s, \overrightarrow{0})$ at $s = 0$ can be used to estimate temporal moments in (2.23). Specifically, we compute $F = \tilde{F}(0, \overrightarrow{0})$, and then

$$\langle t^q \rangle_F = \frac{1}{F} \left(-\frac{\partial}{\partial s} \right)^q \tilde{F} \Big|_{s=0,k=0} . \tag{3.2}$$

These numbers describe quantitatively how the incoming pulse is stretched out in the responses of the scattering medium.

There is an interesting interpretation of the Laplace conjugate variable s in terms of absorption by a uniformly distributed gas in the otherwise purely scattering medium. Taking the Laplace transform of the general 3+1D RT equation, boundary conditions, and source term in (2.1)–(2.7), we find notable changes, on the one hand, in $\hat{\mathcal{L}}\hat{G} = \mathcal{S}\hat{G} + \hat{Q}$ where

$$\hat{\mathcal{L}} = \boldsymbol{\Omega} \cdot \nabla + \sigma(\boldsymbol{x}) + s/c \tag{3.3}$$

and, on the other hand, in

$$\begin{aligned} \hat{Q}(s, \boldsymbol{x}, \boldsymbol{\Omega}) \; &= \; \delta(x)\delta(y)\, \sigma_{\mathrm{s}}(0,0,z) p(\mu) \\ &\times \; \exp\left(- \int_0^z \sigma(0,0,z')\, \mathrm{d}z' - \frac{s}{c}\, z \right) , \end{aligned} \tag{3.4}$$

and similarly using (2.9) if $\mu_0 < 1$. All is therefore as if the extinction coefficient is boosted everywhere by s/c, but the scattering coefficient is unchanged.

This reading of (3.3)–(3.4) is known as the 'equivalence theorem' that attracted considerable attention in the 1960s and early 1970s [33–39]. It clearly separates absorption and scattering processes in the general RT problem, and states that radiance at an absorbing wavelength can be calculated from the radiance at a non-absorbing one and the attenuation along all possible paths from the sources to the point/direction of interest. It is interesting to note that the earliest numerical investigations (known to the authors) of time-domain RT with multiple scattering (MC-based of course) were performed in the same time period; see Ref. [40].

Most of these early studies of pulse stretching, with or without the Laplace transform, were focused on the $F = R$ scenario. We will exploit it computationally and observationally further on for both $F = R$ and $F = T$, this balance being a recurring theme in this review. We can thus gain access to temporal moments of sunlight ... even though the source is steady and the detection system is passive (cf. section 5.8).

5.3.2 Spatial Green functions and pencil-beam problems

The rotational symmetry acquired in section 5.2.5 for the cloud under already normal/collimated or isotropic illumination conditions in direction space carries over from physical to Fourier space; we therefore have $\tilde{F}(s, \overrightarrow{k}) \equiv \tilde{F}(s, k)$.

Consider now the case of steady illumination ($s \equiv 0$). One can easily show from (3.1) that the Taylor coefficients of $\tilde{F}(0,k)$ at $k=0$ can be used to estimate spatial moments in (2.24). Specifically, we compute $F = \tilde{F}(0,0)$, and then[11]

$$\langle \rho^2 \rangle_F = \frac{-2}{F} \left. \frac{\partial^2 \tilde{F}}{\partial k^2} \right|_{s=0,k=0} . \tag{3.5}$$

RT problems, generally in uniform semi-infinite ($H \to \infty$) media, with localized narrow (collimated) steady beams, are known in the literature as 'pencil-beam' or 'search-light' problems (cf. Figs 5.1 and 5.4). They have attracted quite a lot of attention ever since the very earliest investigations of 3D RT we are aware of [41–47]. Lately, such problems have been proposed as analytical benchmarks for numerical transport code verification [48, 49]. There is not an exact equivalence between horizontal wavenumber $k > 0$ with an effective absorption process, except if we remove the dependence of the source on $\mathbf{\Omega}$ (that controls the direction of the derivative in $\mathcal{L}$) and consequently forgo all but isotropic scattering. At any rate, more effort and creativity is required than in the time-only problem.

5.4 Diffusion approximation for opaque scattering media

In the above, we have established a complete formalism for computing space-time Green functions for scattering media illuminated and observed at a boundary. However, it invariably leads to a numerical implementation, for example, a MC algorithm. This is fine for case studies but impractical for applications in remote sensing. Our goal now is to establish a physically reasonable theory leading to $F(t,\rho)$ or, equivalently, $\tilde{F}(s,k)$ in closed form (section 5.5). We can then use the above definitions and relations that predict analytically the spatial, temporal, joint or conditional moments of the Green functions (sections 5.8 and 5.9), even derive closed-form expressions for the Green functions themselves (sections 5.6 and 5.7).

5.4.1 Derivation from the time-dependent 3D RT equation

Consider dense clouds, say, through which one cannot detect the silhouette and maybe not even the general direction of the sun in the transmitted radiance field. According to Bohren et al. [50], this translates to optical thickness $\gtrsim 9 \pm 1$ (geometrical thickness $\gtrsim 9 \pm 1$ MFPs). We can then safely assume that the transmitted light at least is transported via diffusion, the well-known approximation to RT per se. That statement should carry over to reflected light as long as we focus on higher orders of scattering; in space-time Green function studies, that translates to later times and further distances from the source. In other words, while bearing in mind the caveat in section 5.2.1 about thinking about RT as 'photon' transport, all is as if the radiative fluxes measured in transmission or, for the most part, in reflection

[11] The factor of 2 originates, when the axial symmetry is applied, from the 2D dyadic tensor $\overrightarrow{k}\,\overrightarrow{k}$ used in the multivariate Taylor expansion of $\tilde{F}(0, \overrightarrow{k})$ in (double-dot) combination with the second-order differential tensor operator $\overrightarrow{\nabla}_k \overrightarrow{\nabla}_k$.

were currents of particles executing long convoluted random walks starting at the localized and/or collimated source and ending at a cloud boundary.

Equations for this simplified transport theory can be derived by integrating (2.1)–(2.3) angularly term-by-term over 4π, once directly and once after multiplication by $\boldsymbol{\Omega}$. This leads to [51]:

$$c^{-1}\frac{\partial J}{\partial t} + \nabla\cdot\boldsymbol{F} \;=\; -\sigma_{\mathrm{a}}(\boldsymbol{x})J + q_J(t,\boldsymbol{x}), \tag{4.1}$$

$$c^{-1}\frac{\partial \boldsymbol{F}}{\partial t} + \nabla\cdot\mathsf{K} \;=\; -\sigma_{\mathrm{t}}(\boldsymbol{x})\boldsymbol{F} + \boldsymbol{q}_F(t,\boldsymbol{x}). \tag{4.2}$$

In (4.2), an important new coefficient appears: the 'transport' extinction,

$$\sigma_{\mathrm{t}}(\boldsymbol{x}) = (1-g)\sigma_{\mathrm{s}}(\boldsymbol{x}) + \sigma_{\mathrm{a}}(\boldsymbol{x}), \tag{4.3}$$

equivalently $(1-\varpi_0 g)\sigma(\boldsymbol{x})$, with ϖ_0 from (2.4) and g from (2.21). The associated (local) transport MFP[4, 52] is denoted

$$\ell_{\mathrm{t}}(\boldsymbol{x}) = 1/\sigma_{\mathrm{t}}(\boldsymbol{x}). \tag{4.4}$$

There was been some controversy over the past 15 years about the exact role of σ_{a} (i.e., absorption) in σ_{t}, hence in the diffusivity D, which we define further on as $c\ell_{\mathrm{t}}/3$. In the mid-1990s, the rising importance of biomedical imaging applications of 'photon migration' (diffusion) theory motivated several authors [53–58] to revisit and confirm the idea originated by Furutsu [59] in 1980 that σ_{a} is *not* present in (4.3)–(4.4). Rather, the effect of absorption is added to J after the fact with a multiplicative term in $\exp(-\sigma_{\mathrm{a}}ct)$, assuming a uniform medium. This makes sense from the standpoint of the equivalence theorem discussed in section 5.3.1. Subsequent investigations [60–63], all based on steady-state transport, argued convincingly that absorption *does* impact σ_{t}, although more weakly than in (4.3), for example, Aronson and Korngold [62] give $D = 1/3(\sigma_{\mathrm{s}}+\sigma_{\mathrm{a}}/5)$ when $g = 0$. Cai et al. [64] re-ignited the debate by framing D as dependent on time rather than absorption. We believe that Pierrat et al. [65] have resolved the controversy by distinguishing between the *dynamical* diffusion constant without σ_{a}, and *steady-state* one with it. All this is for uniform media where one can gain insights by way of analytical manipulations, even solutions, of the RT (not just diffusion) equation. In the presence of spatial variability, we further need to distinguish absorption by a *uniform* interstitial gas and by the *clumped* material that produces the scattering. The former case can be treated with the equivalence theorem as stated, but not the latter unless it is extended to include a discrete sum over successive orders of scattering [66].

We also introduced here the zeroth-, first-, and second-order angular moments of Green-function radiance as

$$\begin{aligned} J(t,\boldsymbol{x}) \;&=\; \int\limits_{4\pi} G(t,\boldsymbol{x},\boldsymbol{\Omega})\,\mathrm{d}\boldsymbol{\Omega}, \\ \boldsymbol{F}(t,\boldsymbol{x}) \;&=\; \int\limits_{4\pi} \boldsymbol{\Omega} G(t,\boldsymbol{x},\boldsymbol{\Omega})\,\mathrm{d}\boldsymbol{\Omega}, \\ \mathsf{K}(t,\boldsymbol{x}) \;&=\; \int\limits_{4\pi} \boldsymbol{\Omega}\boldsymbol{\Omega} G(t,\boldsymbol{x},\boldsymbol{\Omega})\,\mathrm{d}\boldsymbol{\Omega}, \end{aligned} \tag{4.5}$$

respectively, the scalar- (a.k.a. actinic-), vector- and (dyadic) tensor-fluxes. We similarly define

$$q_J(t,\boldsymbol{x}) \;=\; \int\limits_{4\pi} Q(t,\boldsymbol{x},\boldsymbol{\Omega})\,\mathrm{d}\boldsymbol{\Omega}, \tag{4.6}$$

$$\boldsymbol{q}_F(t,\boldsymbol{x}) \;=\; \int\limits_{4\pi} \boldsymbol{\Omega} Q(t,\boldsymbol{x},\boldsymbol{\Omega})\,\mathrm{d}\boldsymbol{\Omega}. \tag{4.7}$$

For instance, based on (2.7), we have

$$q_J(t,\boldsymbol{x}) \;=\; \delta\left(t-\frac{z}{c}\right)\delta(x)\delta(y)\,\sigma_{\mathrm{s}}(z)\;\exp\left(-\int\limits_0^z \sigma(z')\,\mathrm{d}z'\right), \tag{4.8}$$

$$\boldsymbol{q}_F(t,\boldsymbol{x}) \;=\; q_J(t,\boldsymbol{x})\,g\,\hat{\mathbf{z}}. \tag{4.9}$$

More generally, (2.9) yields here

$$\begin{aligned} q_J(t,\boldsymbol{x}) \;=\; & \delta\left(t-\frac{z/c}{\mu_0}\right)\delta\left(x-\eta_0\,\cos\phi_0\,\frac{z}{\mu_0}\right)\delta\left(y-\eta_0\,\sin\phi_0\,\frac{z}{\mu_0}\right) \\ & \times\;\sigma_{\mathrm{s}}(z)\;\exp\left(-\int\limits_0^z \sigma(z')\frac{\mathrm{d}z'}{\mu_0}\right), \end{aligned} \tag{4.10}$$

$$\boldsymbol{q}_F(t,\boldsymbol{x}) \;=\; q_J(t,\boldsymbol{x})\,g\,\boldsymbol{\Omega}_0, \tag{4.11}$$

noting that in (2.9) we had not yet assumed that extinction is at most dependent on z; here, the horizontal variations are driven only by the pointwise source distribution.

In analogy with particle transport theory, (4.1)–(4.2) are local expressions of the conservation of radiant energy and momentum respectively [12]. These are the basic ingredients of a *macroscopic* theory of radiation transport where the 3D RT equation describes *mesoscopic* processes involving directional details while Maxwell's equations describe *microscopic* details involving wave phenomena.

As stated, the 'continuity' (or conservation) equations for energy (4.1) and momentum (4.2) are exact. The diffusion approximation follows from making two simplifying assumptions about (4.2): first, the time-derivative is assumed negligible and, second, a natural closure is introduced. The closure statement is that the radiation pressure tensor K/c is isotropic, i.e., off-diagonal components vanish and on-diagonal components are equipartitioned (each one is equal to 1/3 of the radiant energy density J/c) [51]. This is indeed the expectation when radiation – viewed as a monokinetic gas – is in local equilibrium with a dense highly scattering medium. Small deviations from isotropy are then entirely captured by two spherical harmonics, namely, a monopole and a dipole. Specifically, we have[12]

$$G(t,\boldsymbol{x},\boldsymbol{\Omega}) \approx \left[J(t,\boldsymbol{x}) + 3\boldsymbol{\Omega}\cdot\boldsymbol{F}(t,\boldsymbol{x})\right]/4\pi \tag{4.12}$$

[12]We refer to the key paper by King, Radke, and Hobbs [67] for empirical evidence of this representation of in-cloud radiance collected in extensive marine boundary-layer stratocumulus clouds, which are of considerable interest here.

and, accordingly,

$$p(\boldsymbol{\Omega}' \cdot \boldsymbol{\Omega}) \approx [1 + 3g\boldsymbol{\Omega}' \cdot \boldsymbol{\Omega}] / 4\pi \tag{4.13}$$

for the phase function. These two expressions are often used as the point of departure in diffusion (a.k.a. 'P_1') theory.

We notice right away that (4.13) is a rather poor representation of the phase function of real distributions of cloud droplet size [20], most notably, the forward diffraction-induced peak is absent. By the same token, (4.12) is a poor representation of radiance anywhere near the highly collimated beam illuminating the medium, whether localized like a laser source or spread out like the solar source. The latter problem is mitigated by separating the un-collided beam from the diffuse field and thus using internal source terms rather than a source in the boundary conditions. The former problem is addressed in the following subsection.

No matter how one derives the diffusion transport model from the RT equation,[13] we obtain the 'constitutive' equation:

$$\nabla J/3 = -\sigma_{\mathrm{t}}(\boldsymbol{x})\boldsymbol{F} + \boldsymbol{q}_F(t, \boldsymbol{x}), \tag{4.14}$$

a.k.a. Fick's law, especially when the source term is absent ($\boldsymbol{F} = -\nabla J/3\sigma_{\mathrm{t}}$). This defines the diffusion approximation as a first-order closure of the hierarchy of transport equations started in (4.1)–(4.5). In the applications to come, we will focus on wavelengths where the condensed water in cloud particles has negligible absorption: $\sigma_{\mathrm{a}}(\boldsymbol{x}) \equiv 0$, hence $\varpi_0 = 1$ and $\sigma_{\mathrm{s}}(\boldsymbol{x}) = \sigma(\boldsymbol{x})$. The continuity equation (4.1) then simplifies to

$$c^{-1}\frac{\partial J}{\partial t} + \nabla \cdot \boldsymbol{F} = q_J(t, \boldsymbol{x}). \tag{4.15}$$

These coupled partial differential equations (PDEs) encapsulate the diffusion transport model we will exploit in the remainder of this paper.

5.4.2 Directional and spatial enhancements

Diffusion theory can easily be improved in highly relevant ways for cloud remote sensing applications. Among many possibilities, we discuss one well-known approach in previously raised issues in direction space, and two quite recent developments germane to position space.

5.4.2.1 δ-Eddington rescaling for the impact of the diffraction peak in the phase function

As previously mentioned, an inherent weakness of diffusion-based radiation transport modeling is the smooth one-parameter phase function in (4.13) whereas real-world phase functions have prominent forward peaks. We can partially mitigate this

[13] A more contemporary derivation of the 3D diffusion approximation would use asymptotic analysis of the general RT equation where the magnitude of the local MFP $1/\sigma(\boldsymbol{x})$ is small and only large terms are kept; see Refs [68, 69]. Yet another notable derivation [70] makes use of a special limiting case of the discrete-angle phase function in the 'six-flux' model for 3D RT [71].

disconnect by applying the classic δ-Eddington rescaling [72]. The phase function is recast as a combination of a δ-function in the forward direction and a complementary term with two spherical harmonics. In the absence of absorption, this results in a rescaling given by

$$\sigma'(\boldsymbol{x}) = (1-f)\sigma(\boldsymbol{x}),\ (1-g') = (1-g)/(1-f), \tag{4.16}$$

where f is the fraction of 'δ-scattering' (physically, just prolonged ballistic propagation). This operation decreases $\sigma \equiv \sigma_{\rm s}$ (increases the MFP), but leaves $\sigma_{\rm t}$ invariant in (4.3). We will see in the next section that this scaling therefore leaves a large class of diffusion models with isotropic boundary sources unaffected.

A popular choice is $f = g^2$ because it fits the second as well as first spherical harmonic coefficients of the H–G model phase function, hence

$$g' = (g-f)/(1-f) = g/(1+g). \tag{4.17}$$

For liquid water clouds, where $g \approx 0.85$, we get $f \approx 0.72$, hence $\sigma' \approx 0.28\sigma$ and $g' \approx 0.46$. Alternatively, the whole diffraction peak – half of the scattered energy for particles with very large size parameters (Babinet's principle) – can be recast as prolonged propagation in the original direction: $f = 0.5$, hence $\sigma' \approx 0.5\sigma$ and $g' \approx 0.7$.

5.4.2.2 Effects on bulk radiation transport of turbulence-driven random 3D variability of extinction, general considerations

Although not our preferred approach in Green function calculation, $\boldsymbol{F}$ can be eliminated between (4.14) and (4.15), leading to

$$[\partial_t - \nabla\cdot(D\nabla)]\,J = cq_J - D\nabla\cdot\boldsymbol{q}_F \tag{4.18}$$

where

$$D(\boldsymbol{x}) = c/3\sigma_{\rm t}(\boldsymbol{x}) = c\ell_{\rm t}(\boldsymbol{x})/3 \tag{4.19}$$

is the (local) radiative diffusivity.[14] In an arbitrary 3D optical medium with neither sources nor sinks (absorption), apart from boundaries, the local expression for conservation of radiant energy is $[\partial_t - \nabla D\cdot\nabla - D\nabla^2]J = 0$. In the Fokker–Planck interpretation of this boundary-value diffusion problem, $-\nabla D$ is an effective drift velocity. Radiant energy thus flows naturally from low to high diffusivity (high to low extinction) regions.

Dwelling on the no-source/no-sink media, we can use (4.18) to equate the classic operator for diffusion in a uniform medium with a specific variability term: $[\partial_t - D\nabla^2]J = \nabla D\cdot\nabla J$. In the vector-flux picture, this new term on the r.-h. side can be written as $\nabla \ln D\cdot\boldsymbol{F}$, and it formally acts as a pseudo-source/sink term for the mean flow in the hypothetical uniform medium. Davis and Marshak [73] investigated the steady-state ($\partial_t J \equiv 0$) problem in detail, showing systematic

[14] We recall that transport coefficients are the product of particle density and cross-section for scattering, absorption, or both (extinction), per particle. Although there is no compelling rationale for this, we tend to assign the random spatial fluctuations to the particle density and hold the optical properties constant.

effects of any given 3D structure on flux line geometry and, from there, domain-average boundary flux ($T = 1 - R$). The transport mechanisms behind systematic 3D effects observed in absorbing media and time-dependent *deterministic* flows remain open to investigation. For our present purposes, we now tap into a *statistical* approach developed for steady sources to account for 3D effects, be they for temporal characteristics – a conjecture that will eventually call for at least numerical verification.

Barker and Davis [74] survey the two broad classes of models in 3D RT that target large-scale effects of *unresolved* small-scale variability in cloud structure, which is invariably assumed random in nature. Members of one class of such 'mean field' theories lead to *new* transport equations to solve. Members of the other class pursue *homogenization*: redefine coefficients in 1D RT so that the known solutions of that problem capture the main 3D effects, which is clearly the path of least resistance. Among these 'effective medium' approaches to random 3D variability, we favor the rescaling techniques proposed by Cairns et al. [75] and by Larsen [76]. Although one-parameter solutions, they stem from careful treatments of both both 1- and 2-point statistics, i.e., the PDF of $\sigma(\boldsymbol{x})$ and its autocorrelation function respectively.

5.4.2.3 Homogenization via Cairns' rescaling

Starting with the δ-rescaled (primed) quantities in (4.16) that account for the problematic forward-scattering peak in the phase function, Cairns' renormalization theory leads to

$$\sigma''(\boldsymbol{x}) = (1-\epsilon)\sigma'(\boldsymbol{x}),\ (1-g'') = \frac{1-2\epsilon}{1-\epsilon}(1-g'), \tag{4.20}$$

in the case of conservative scattering, where ϵ is the new variability parameter. We see immediately that $1/2$ is a strict upper limit for ϵ, and that it is probably best to not approach too closely in practice, and especially not in diffusion modeling. While δ-Eddington rescaling leaves the product $(1-g)\sigma$ invariant, it decreases here both through σ and through $1-g$ as ϵ increases (since $g'' > g'$). For diffusion models with strict similarity (dependent only on $\sigma_\mathrm{t} = (1-g)\sigma = (1-g')\sigma'$), we have

$$\sigma''_\mathrm{t}(\boldsymbol{x}) = (1-2\epsilon)\sigma_\mathrm{t}(\boldsymbol{x}). \tag{4.21}$$

About the dependence of σ (or σ_t) on $\boldsymbol{x}$, we should bear in mind here that, as soon as we apply this rescaling, we have taken care of all the arguably random small-scale variability – up to a few MFPs (see below). So, implicitly, we are now interested only in cloud scale variations of the extinction, such as the stratification trends discussed in section 5.2.5.

How does one compute ϵ? Recalling that overscores denote averages over the spatial variability, Cairns et al. show specifically that, for moderate-amplitude fluctuations, the 3D RT effects are captured with

$$\epsilon = a - \sqrt{a^2 - v^2} \tag{4.22}$$

where

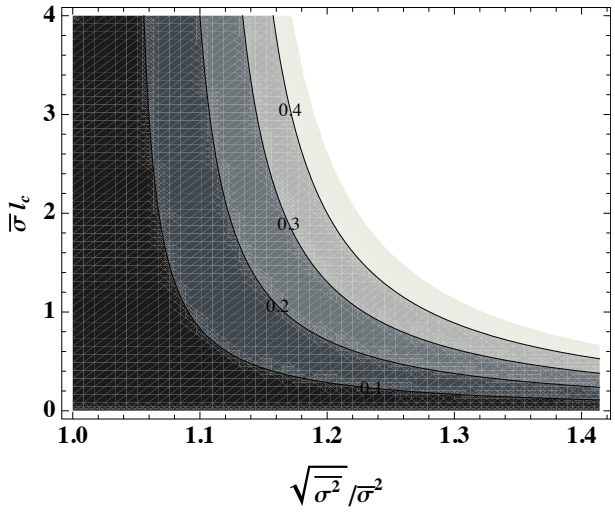

Fig. 5.6. *Cairns' scaling factor ϵ used in (4.20).* The parameter ϵ is plotted as function of $\overline{\sigma^2}^{1/2}/\overline{\sigma}$ and $\overline{\sigma} l_c$ using (4.22)–(4.23). Values up to $\sim 1/3$ can be used with some confidence (this divides $1-g$ at most by 2). Therefore at most moderate 1-point variability ratio (RMS/mean for σ) can be considered (only slightly more than unity), unless the correlations are very short range *vis-à-vis* the MFP (defined here as $1/\overline{\sigma}$, even though this is known to be an underestimation [10]). More discussion in main text.

$$a = \frac{1}{2}\left(1 + \frac{1}{\overline{\sigma} l_c}\right), \; v = \sqrt{\frac{\overline{\sigma^2}}{\overline{\sigma}^2} - 1}. \tag{4.23}$$

Parameter v is the standard deviation to mean ratio, itself expressed with the RMS-to-mean ratio, for σ and we denote here the characteristic correlation scale of the spatial variability by l_c. We see that

- for small-scale fluctuations (i.e., when $l_c \ll \text{MFP} \approx 1/\overline{\sigma}$), we anticipate little effect since $\epsilon \approx (v/a)^2/2 \lll 1$ (irrespective of v) as a becomes very large;
- for fluctuations at larger scales (i.e., when $\overline{\sigma} l_c \gtrsim 1$), we can have a strong impact ($\epsilon \lesssim 1/2$) although this scenario clearly stretches the validity of the model, in particular, amplitude is then limited to cases where $v^2 \lesssim a - 1/4$ ($\overline{\sigma^2}/\overline{\sigma}^2 \lesssim 5/4 + 1/\overline{\sigma} l_c$);
- for fluctuations at the largest scales ($\overline{\sigma} l_c \gg 1$, hence $a \approx 1/2$ and $v \lesssim 1/2$), one should average over macro-scale responses rather than try to find a single effective medium to account for micro-scale variability effects.

Figure 5.6 illustrates this analysis of ϵ. In the last ('slow') variability regime, the large-scale averaging of radiative responses can be computed locally using a strong uniformity assumption, which is the essence of the independent pixel approximation (IPA). See Ref. [74], references therein, and the penultimate section of this paper for applications of the IPA to solar RT (section 5.10.3) and to a related time-dependent problem (section 5.10.4).

The above scale-by-scale breakdown of spatial variability impacts is consistent with the first-principles analysis by two of the present authors [10] who, incidentally,

show that the *actual* MFP is $\approx\overline{1/\sigma}$ in a broad class of variable media with long-range correlations, including clouds. Moreover, that estimate always exceeds $1/\overline{\sigma}$ (they are equal *only* when σ is uniform). This is a direct consequence of Jensen's inequality [77] in probability theory concerning averages of functions with definite convexity (in this case, the exponential).

Those authors come to the same scale-based classification of variability effects in RT from the standpoint of steady-state 3D diffusion theory [73]. The only difference is that the transport MFP in (4.4) replaces the usual MFP used in the present arguments based on propagation between successive scatterings (or, for example, an emission or an absorption).

5.4.2.4 Homogenization via Larsen's rescaling

As competition for Cairns' model, we highlight another notable development in homogenization theory by Larsen [76], who includes a diffusion limit of immediate interest here. It builds on the ideas of Kostinski [78], Davis and Marshak [10] who predict *non*-exponential step distributions between scatterings in randomly variable media: sub-exponential distributions if spatial correlations are positive, super-exponential otherwise [79]. Positive correlations are the norm in clouds, so we anticipate the higher-order moments of to exceed the exponential-based prediction.

Let $P(s)$ be the distribution of steps in the Markovian propagation process of multiply scattered light. Recall that $\ell = \langle s \rangle$ is the well-known MFP. Then the exponential case is completely defined, $P(s) = \exp(-s/\ell)/\ell$, and it leads to $\langle s^q \rangle = \Gamma(q)\ell^q$ (for any real $q > -1$). The sub-exponential laws of interest here will therefore have $\langle s^q \rangle > \Gamma(q)\ell^q$ for $q > 1$ because of the longer tail (slower decay). Dwelling on moments of lowest integer order, we can use

$$r = \frac{\langle s^2 \rangle}{2\langle s \rangle^2} > 1 \tag{4.24}$$

to measure the deviation of $P(s)$ from the exponential case.

By taking a careful asymptotic limit, Larsen finds (in different notations) that, in the case where $\varpi_0 = 1$, homogenized diffusivity is

$$D_{\text{eff}} = D_{\text{exp}} \times [(1-g)r + g], \tag{4.25}$$

which exceeds the classic value of $D_{\text{exp}} = c\ell/3(1-g)$ if $r > 1$, for all $|g| < 1$. Interesting things happen to radiation transport when $\langle s^2 \rangle = \infty$ leading to 'anomalous' diffusion, which is out of the scope of this article; they are briefly discussed in Appendix F and in Refs [80, 81].

To implement this statistical 3D RT correction, we can assign the boost $D_{\text{eff}}/D_{\text{exp}}$ in (4.25) to an effective reduction of σ_{t} in our diffusion models with isotropic boundary or internal sources, hence strict similarity. Before application to models with non-isotropic internal sources, the derivation in Ref. [76] would have to be revisited. In analogy with Cairns' rescaling in (4.21), we can use

$$\epsilon_{\text{L}} = \frac{1}{2}\left(1 - \frac{1}{r-(r-1)g}\right), \tag{4.26}$$

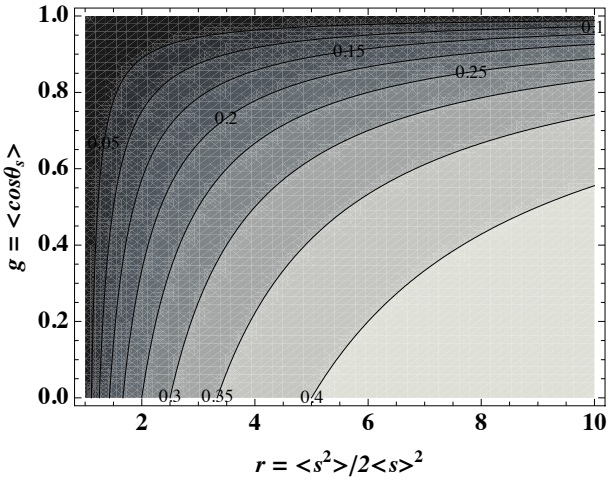

Fig. 5.7. *Larsen's scaling factor* $\epsilon_{\rm L}(g,r)$ *from (4.26).* Parameter $\epsilon_{\rm L}$ is to be used in lieu of Cairns' counterpart in (4.21). It is plotted here as function of asymmetry factor g and the ratio r of the second-order moment of $P(s)$ and its predicted value based on the exponential distribution. As expected from the definition in (4.21), $\epsilon_{\rm L}$ does not exceed 1/2. We believe that values up to $\sim$1/3 can be used with confidence, which would at most divide $\sigma_{\rm t} = (1-g)\sigma$ by 2, hence for $1 < r \lesssim 10$ based on $g = 0.85$.

which of course does not exceed 1/2 for $r \geq 1$ and $|g| < 1$. This homogenization factor is plotted in Fig. 5.7 for the relevant range of its arguments (g, r). Larsen's $\epsilon_{\rm L}$ depends on one local optical parameter, g, and only one variability parameter, r. The later in turn depends however on both 1-point/PDF and 2-point/correlation statistics in ways that are not yet well understood. Indeed, it can be shown that if correlations are only very short range compared to the MFP, then $P(s)$ is very near exponential [10, 17]. Correlations that are very long by the same standard of comparison are better treated by the above-mentioned IPA methods, leaving correlations on the same scales as the MFP as the ones[15] where homogenization theories are truly helpful.

In short, exponential free-path PDFs prevail only in homogeneous optical media. Random-but-correlated media have *wider* step PDFs, in particular, in the sense of the moment inequality in (4.24). Consequently, they can sustain in steady-state systematically larger fluxes thanks to greater effective diffusivity for the bulk of the medium. Guided by the numerical results displayed in Fig. 5.4 for $\langle \rho^2 \rangle_F$ ($F = R, T$), we speculate that the spatial variability will also lead to increased horizontal transport away from a localized source. Although their derivations may need to be revisited for time-dependent transport, we will allow ourselves in the latter sections

[15]The plural is deliberate since, in stochastic optical media, the MFP is itself a random variable dependent on position, direction, and realization. Although a *mean* MFP $\langle s \rangle$ can be defined and investigated, it is no longer the only moment of interest in the step PDF $P(s)$ for the spatial-, directional- and ensemble-average [10]. So scales 'commensurate with the MFP' could cover a wide range, at least going from $\langle s \rangle$ to $\langle s^2 \rangle / 2\langle s \rangle \geq \langle s \rangle$ (where '=' is for the exponential case).

of this paper to use Larsen's or Cairns' homogenizations of $\sigma_{\mathrm{t}}(\boldsymbol{x})$ for time-dependent diffusion.

5.4.3 Boundary conditions, including boundary sources

Bearing in mind that the *local* optical properties that matter in diffusion $\{\sigma(\boldsymbol{x}), \varpi_0, g\}$ can be rescaled to account for unavoidable phase function attributes and 3D random variability, we now need to assign boundary conditions (BCs) to the coupled first-order PDE problem at hand.

If the opaque (radiatively diffusive) cloud is reasonably stratiform, then we can model it with slab geometry $\{\boldsymbol{x} \in \mathbb{R}^3; 0 < z < H\}$. We furthermore recall that, in this plane-parallel framework, cloud optical depth τ is the integral of $\sigma(z)$ from 0 to H. BCs for the above coupled PDEs for J and $\boldsymbol{F}$ must then express hemispherical fluxes crossing a constant-z plane in the $\pm$ directions, namely,

$$F_{\pm} = \int_{-\pi}^{+\pi} \mathrm{d}\phi \int_{0}^{\pm 1} G(\cdot, \boldsymbol{\Omega}) \mu \, \mathrm{d}\mu = \frac{J/2 \pm F_z}{2}, \tag{4.27}$$

obtained from (4.12). The no-incoming-radiance (a.k.a. 'absorbing') BCs for radiance bring us flux-based BCs

$$4F_{+}(t, x, y, 0) \;=\; J(t, x, y, 0) + 2F_z(t, x, y, 0) = 0, \tag{4.28}$$

$$4F_{-}(t, x, y, H) \;=\; J(t, x, y, H) - 2F_z(t, x, y, H) = 0, \tag{4.29}$$

for all x, y, and t.

If we have partial reflectivity at the $z = H$ boundary, which relates outgoing ($\mu > 0$) and incoming ($\mu' < 0$) radiances, as described in (2.12), then the associated BC becomes

$$[1 - \alpha_H(x, y)]\, J(t, x, y, H) - 2\,[1 + \alpha_H(x, y)]\, F_z(t, x, y, H) = 0. \tag{4.30}$$

The precise kind of reflection (for example, Lambertian vs. specular) is of course inconsequential since only fluxes are modeled in diffusion theory.

Alternatively – but no longer equivalently – in the diffusion approximation, one can put the pulsed source in the BC at $z = 0$. In that case, we set $q_J = q_F \equiv 0$ in the r.-h. sides of (4.14)–(4.15) and require

$$J(t, x, y, 0) + 2F_z(t, x, y, 0) = 4q_0(t, x, y) \tag{4.31}$$

for a general distribution of isotropic boundary sources, in lieu of (4.28). The postulated boundary source term $q_0(t, x, y)$ is the μ-weighted angular integral over $\mu > 0$ of the incoming radiance field. The radiance BC at $z = 0$ in (2.8) or in (2.10), irrespective of $\boldsymbol{\Omega}_0$, then yields

$$q_0(t, x, y) = \delta(t)\delta(x)\delta(y), \tag{4.32}$$

as does the expression in (2.11) for an isotropic boundary source; all this while the homogeneous BC at $z = H$ in (4.29) or (4.30) is unchanged. Since flux alone

tells us nothing about directionality, we are now effectively modeling the source as pointwise and pulsed but isotropic in the $\mu > 0$ hemisphere.

Equations (4.28)–(4.29), and their generalizations in (4.30) and (4.31) respectively for secondary and primary sources, express the least usual '3rd-type' of BCs that occur in generic applications of diffusion-type PDE problems, both time-dependent (parabolic) or steady-state (elliptical). They involve the density J at the boundary *and* the boundary-crossing current F_z, equivalently, J and its normal derivative from (4.14). These BCs can be expressed as a *variable* mixture of Dirichlet/first-type (fix J) and Neumann/2nd-type (fix F_z) BCs:

$$\begin{aligned} J(t,\overrightarrow{\rho},0) + 3\chi F_z(t,\overrightarrow{\rho},0) &= 4q_0(t,\overrightarrow{\rho}) \\ [1-\alpha_H(\overrightarrow{\rho})]\,J(t,\overrightarrow{\rho},H) - 3\chi\,[1+\alpha_H(\overrightarrow{\rho})]\,F_z(t,\overrightarrow{\rho},H) &= 0. \end{aligned} \tag{4.33}$$

Although often referred to as 'mixed' BCs,[16] these are known technically as 'Robin' BCs [82]. At any rate, they are the most general BCs we will need to consider in the following applications of diffusion theory to cloud remote sensing.

When $q_0(t,\overrightarrow{\rho})$ does not vanish, the BC mixing factor χ can differ from its 2/3 value used in (4.31), but typically not very much (at least in the most common transport applications). This is basically a tuning parameter that was introduced by early neutron transport theorists to help diffusion models reproduce high-precision solutions of the transport equations in critical applications [52]; this boost in accuracy is naturally applied where diffusion is at its weakest, namely, boundaries. The physical interpretation of χ is that of an 'extrapolation length' measured in transport MFPs. Indeed, in the absence of anisotropic internal sources, Fick's law in (4.14) tells us that $F_z(t,\overrightarrow{\rho},0) = -[\partial_z J/3\sigma_t(z)]_{z=0}$, and similarly at $z = H$. By substitution into (4.33), the l.-h. side reads as a linear extrapolation formula for J, given its derivative along the z-axis, over a distance $\chi/\sigma_t(0)$ into the $z < 0$ region; we have a similar reading of the BC at $z = H$, going into the $z > H$ region. Some values for χ found in the literature are: $1/\sqrt{3}$ ('S_2' model [11]), 2/3 (Marshak flux BCs [51]), $0.7104\cdots$ (Milne half-space problem [52]), $1/n$ (nD 'discrete angle' RT model [70], including 3D 'six-flux' theory [71]), 4/3 (optically thin limit [52]).

This realization in fact opens the possibility of recasting the above Robin BCs as 'extrapolated' Dirichlet BCs:

$$\begin{aligned} J\left(t,\overrightarrow{\rho},-\frac{\chi}{\sigma_t(\overrightarrow{\rho},0)}\right) &= 4q_0(t,\overrightarrow{\rho}) \\ J\left(t,\overrightarrow{\rho},H+\frac{\chi}{\sigma_t(\overrightarrow{\rho},H)}\,\frac{1+\alpha_H(\overrightarrow{\rho})}{1-\alpha_H(\overrightarrow{\rho})}\right) &= 0. \end{aligned} \tag{4.34}$$

We need to assume here that the transport extinction $\sigma_t(\overrightarrow{\rho},z)$ in the bulk and the surface albedo $\alpha_H(\overrightarrow{\rho})$ vary at most rather slowly (almost everywhere finite gradients). The support of the coupled PDE problem at hand has thus been formally extended from $0 < z < H$ to

$$-\frac{\chi}{\sigma_t(\overrightarrow{\rho},0)} < z < H + \frac{\chi}{\sigma_t(\overrightarrow{\rho},H)}\,\frac{1+\alpha_H(\overrightarrow{\rho})}{1-\alpha_H(\overrightarrow{\rho})},$$

[16] In mathematically correct terminology, 'mixed BCs' refers to problems with somewhere Dirichlet and elsewhere Neumann BCs.

which may be between two wavy boundaries. This Dirichlet-type approximation of the exact Robin BCs normally required for diffusion theory is rarely used in atmospheric radiation applications, a notable exception being work by E.P. Zege et al. [83, and references therein]. As demonstrated below, these approximate BCs lead to simpler expressions that in turn enable deeper results, albeit at a cost in accuracy and/or reduction of the applicable parameter space.

Finally, we need to reconsider our parameterizations of internal stratification from section 5.2.5 from a diffusion standpoint. Because g is assumed constant, $\sigma_t(z)$ will have the same behavior as $\sigma_{0,H}(\gamma; z)$ for the presumably superior power-law model. However, the vanishing $\sigma_t(z)$ at either $z = 0$ (source below cloud) or $z = H$ (source above cloud) is problematic for the diffusion model. Indeed, the BCs in (4.33) make necessary the evaluation of $F_z(t, \overrightarrow{\rho}, z)$ in (4.14) for $z = 0$ and $z = H$, one of which contains a division by $\sigma_t(z) = 0$; this problem is even more obvious in the extrapolated BCs in (4.34). Physically, the local transport MFP is divergent at one of the cloud boundaries. Diffusion, as an approximation to RT, is already known to deteriorate near boundaries. However, if the associated extrapolation length is infinite, then the failure is likely to be catastrophic. This is the main reason why we introduced the linear gradient model as a surrogate.

5.4.4 Remote sensing observables

The quantities of interest in cloud remote sensing are local/instantaneous reflectivity and transmittivity, in other words, the outgoing fluxes normalized by total incident energy. This total energy is the space-time integral of $q_J(t, \boldsymbol{x})$ always assumed unitary in Green function analyses. Specifically, we seek:

$$R(t, x, y) = \frac{F_-(t, x, y, 0)}{F_+(0)} = \frac{J(t, x, y, 0)/2 - F_z(t, x, y, 0)}{2\mu_0}, \tag{4.35}$$

$$T(t, x, y) = \frac{F_+(t, x, y, H)}{F_+(0)} = \frac{J(t, x, y, H)/2 + F_z(t, x, y, H)}{2\mu_0}, \tag{4.36}$$

where $F_+(0)$ is the incoming flux (in the hemisphere with $\mu > 0$) integrated over time and the illuminated cloud boundary. Allowing for the possibility of oblique illumination, we have $F_+(0) = \mu_0 \leq 1$. Invoking the BC at $z = 0$ in (4.28), we can express these basic cloud responses simply as

$$R(t, x, y) = J(t, x, y, 0)/2\mu_0, \tag{4.37}$$

$$T(t, x, y) = J(t, x, y, H)/2\mu_0; \tag{4.38}$$

we recall that when, as is the case here, the source is specified internally, then the *diffuse* transmittance in (4.38) does not include the un-collided flux contained in *direct* transmittance.

If the isotropic boundary-source model in (4.33) is used for the BCs, then J and $\boldsymbol{F}$ necessarily contain the incident flux. We must therefore compute the required space-time reflectivity and transmittivity fields in (4.35)–(4.36) from

$$R(t, x, y) = \frac{F_-(t, x, y, 0)}{F_+(0)} = J(t, x, y, 0)/2 - q_0(t, x, y), \tag{4.39}$$

$$T(t, x, y) = \frac{F_+(t, x, y, H)}{F_+(0)} = J(t, x, y, H)/2. \tag{4.40}$$

The outcome in the latter case will contain the contribution of directly transmitted flux, although that should not be a significant contribution in diffusion regimes.

If the extrapolated Dirichlet BCs in (4.34) are used then, in principle, reflectivity $R(t,x,y)$ should be computed as the backward hemispherical flux at $z=0$ (now a point inside the extended domain) combining J and F_z according to (4.27). However, the gain in accuracy is likely to be small compared to the loss incurred by simplifying the BCs; so, for simplicity, it can still be obtained from (4.39). The same remark applies to transmittivity $T(t,x,y)$ from (4.38).

Finally, we recall that diffusion theory only predicts fluxes at cloud boundaries (and, for that matter, elsewhere). A zeroth-order estimate of cloud-leaving radiance is given by $R(t,x,y)/\pi$, a Lambertian assumption that is not unreasonable for highly scattered light. A first-order angular model would make use of (4.12). This radiance-to-flux conversion can be done with better angular models, and should be for actual cloud remote sensing applications; see, for example, Ref. [84].

We have now completed the modeling framework for predicting remote sensing signals originating from internally variable stratiform clouds in the spatial and temporal domains using diffusion theory. Moreover, several options are available to control the degree of fidelity in the model's representation of collimated sources.

5.4.5 Fourier–Laplace transformation for stratified media

In the case of constant coefficients, or simple-enough vertical variability models, Fourier–Laplace transformation of the PDE system in (4.1) and (4.14), with the appropriate boundary conditions, leads to a class of analytically tractable problems for our representations of pulsed laser or solar sources. Equipped with an effective medium approach such as Cairns' or Larsen's for small-scale random 3D variability, we can now restrict ourselves to cloud structure that unfolds only along the z-axis according to the previously introduced stratification models.

We therefore define

$$\tilde{J}(s,\overrightarrow{k};z)=\int_0^\infty \mathrm{d}t \iint_{-\infty}^{+\infty} \exp(-st+\mathrm{i}\overrightarrow{k}\cdot\overrightarrow{\rho})\,J(t,\overrightarrow{\rho},z)\,\mathrm{d}\overrightarrow{\rho}\,(x,y). \tag{4.41}$$

We similarly transform all the components of $\boldsymbol{F}(t,\overrightarrow{\rho},z)$, yielding $\tilde{\boldsymbol{F}}(s,\overrightarrow{k};z)$. We can now think of $(s,\boldsymbol{k})$ as parameters rather than independent variables, hence the deliberate insertion of the ';' separator.

Furthermore, we let $\boldsymbol{F}=(\overrightarrow{F}_h,F_z)^{\mathrm{T}}$, similarly for $\boldsymbol{q}_F$, and we recall that $\nabla=(\partial/\partial\overrightarrow{\rho},\partial/\partial z)^{\mathrm{T}}$ transforms to $(\mathrm{i}\overrightarrow{k},\mathrm{d}/\mathrm{d}z)^{\mathrm{T}}$. Our PDE system in (4.1) and (4.14) then becomes a system of three ordinary differential equations (ODEs):

$$\begin{aligned}(s/c)\tilde{J}+\mathrm{i}\overrightarrow{k}\cdot\overrightarrow{\tilde{F}}_h+\tilde{F}_z' &= -\sigma_{\mathrm{a}}(z)\tilde{J}+\tilde{q}_J\\ \mathrm{i}\overrightarrow{k}\,\tilde{J}/3 &= -\sigma_{\mathrm{t}}(z)\overrightarrow{\tilde{F}}_h+\overrightarrow{\tilde{q}}_{Fh},\\ \tilde{J}'/3 &= -\sigma_{\mathrm{t}}(z)\tilde{F}_z+\tilde{q}_{Fz}.\end{aligned} \tag{4.42}$$

Note that $\overrightarrow{\tilde{q}}_{Fh}\equiv\overrightarrow{0}$ in all of our *laser* source models by axial symmetry, although this is an assumption we can relax when dealing with extended uniform (solar)

sources since it corresponds to the $\overrightarrow{k} = \overrightarrow{0}$ case. From (4.8)–(4.9), Fourier–Laplace transformed internal source terms are

$$\tilde{q}_J(s) = \sigma_{\rm s}(z)\, {\rm e}^{-(s/c)z - \int_0^z \sigma(z')\,{\rm d}z'},\ \tilde{q}_{Fz}(s) = g \times \tilde{q}_J(s), \tag{4.43}$$

independent of k in the case of normal laser-like incidence.

Under these conditions, elimination of $\overrightarrow{\tilde{F}}_h$ between the first and second equations leads to

$$\tilde{F}_z' = -\left[\frac{s}{c} + \frac{k^2}{3\sigma_{\rm t}(z)} + \sigma_{\rm a}(z)\right]\tilde{J} + \tilde{q}_J. \tag{4.44}$$

This last ODE is an expression of energy conservation (with transport) along the z-axis where local time variation and horizontal divergence of J are recast as 'effective' absorption processes:

$$\sigma_{\rm a}^{\rm (e)}(s,k;z) = s/c + k^2/3\sigma_{\rm t}(z). \tag{4.45}$$

This is a key coefficient that, in general, is stratified differently than $\sigma_{\rm x}(z)$ (with x = s,a,t), which all vary together (since ϖ_0 and g are assumed constant).

The general boundary conditions in (4.33) become

$$\tilde{J}(s,k;0) + 3\chi\tilde{F}_z(s,k;0) = 4\tilde{q}_0(s,k), \tag{4.46}$$

$$(1-\alpha_H)\tilde{J}(s,k;H) - 3\chi(1+\alpha_H)\tilde{F}_z(s,k;H) = 0, \tag{4.47}$$

where $\tilde{q}_0(s,k) \equiv 0$ and $\chi = 2/3$ if the distributed internal source model in (4.43) is used. If the boundary point-source model is used instead, $q_0(t,x,y)$ in (4.32) leads to $\tilde{q}_0(s,k) \equiv 1$ in (4.46). For simplicity, the optional surface albedo at $z = H$ is assumed uniform; otherwise, we would need to interpret the product of two functions of $\overrightarrow{\rho}$ as a convolution in $\overrightarrow{k}$-space. Under the same simplifying assumption, treatment of the extrapolated boundary conditions in (4.34) is straightforward.

We recall finally that in remote sensing our interests are limited to

$$\tilde{R}(s,k) = \tilde{J}(s,k;0)/2\mu_0, \tag{4.48}$$

$$\tilde{T}(s,k) = \tilde{J}(s,k;H)/2\mu_0, \tag{4.49}$$

for collimated (possibly oblique) illumination, depending on what side of the cloud the observation is performed. We must bear in mind that the latter expression is restricted to the diffuse (scattered) component of transmission; for total transmittance, we need to add the un-collided component $\exp[-(\sigma + s/c)H/\mu_0]$, which includes the Laplace-space signature of the time-delay going from $z = 0$ to the point of escape. When using the (necessarily isotropic) boundary source option, we instead use

$$\tilde{R}(s,k) = \tilde{J}(s,k;0)/2 - 1, \tag{4.50}$$

$$\tilde{T}(s,k) = \tilde{J}(s,k;H)/2, \tag{4.51}$$

and recall that, in this case, T stands for total transmission.

5.5 Solutions of diffusive Green function problems

Not all of our best representations of the source and of the cloud structure and of the boundary conditions can be used at the same time, even when using computer-assisted algebra. The mathematical complexity becomes intractable. However, boundary-source Green functions can be computed in closed-form for useful regions of the flexible parameter space we have set up in the above diffusion-theoretical framework. In the following, we will move through the models adding and removing capability with specific applications in mind. These applications will be called out here, but described in full detail in the remaining sections of the paper. In particular, we restrict ourselves here to Fourier–Laplace expressions, and move on to PDFs and space-time moments in the two following sections on cloud probing applications, by remote sensing or by *in situ* radiometry.

Throughout, we assume conservative scattering ($\sigma_{\rm a}(z) \equiv 0$, $\varpi_0 = 1$), hence $\sigma_{\rm s}(z) \equiv \sigma(z)$ and $\sigma_{\rm t}(z) = (1-g)\sigma(z)$.

5.5.1 Homogeneous cloud with an isotropic boundary point-source

In this first approach to boundary-source Green function calculus, we do not bother with internal stratification. Moreover, we do not attempt to capture the collimation property of laser beams nor source anisotropy induced by the forward-peaked phase function of cloud droplets (beyond the classic scaling of σ by $1-g$ in $\sigma_{\rm t}$). This is the entry-level model used by Davis, Love and co-workers in their 1999 [85] and 2001 [86] proof-of-concept papers on multiple-scattering cloud lidar (reflected laser light), and by Davis and Marshak in their 2002 paper [24] on transmitted solar light, primarily with ground-based O_2 A-band observations in mind.

The resulting boundary-value problem is quite simple:

$$\tilde{F}'_z = -\sigma_{\rm a}^{(\rm e)}(s,k)\,\tilde{J},\ \ \tilde{J}'/3 = -\sigma_{\rm t}\,\tilde{F}_z, \tag{5.1}$$

subject to boundary conditions

$$\tilde{J} + 3\chi\tilde{F}_z\Big|_{z=0} = 4,\ \ \tilde{J} - 3\chi\tilde{F}_z\Big|_{z=H} = 0, \tag{5.2}$$

leaving χ as an unspecified tuning parameter. By inspection, we see that non-dimensional cloud responses will depend only on the transport or 'scaled' optical depth

$$\tau_{\rm t} = H/\ell_{\rm t} = \sigma_{\rm t}H = (1-g)\tau, \tag{5.3}$$

and of course χ. This means in particular that the δ-Eddington rescaling in (4.16) for forward scattering has no effect on this model. Furthermore, we will have similar behavior between s/c and $k^2/3\sigma_{\rm t}$ since they are interchangeable in the constant coefficient $\sigma_{\rm a}^{(\rm e)}(s,k)$ in (4.45).

This coupled ODE problem can be formally mapped to the simplest version of the well-known two-stream model for solar transport in plane-parallel clouds, with a fixed amount of scattering and a variable amount of absorption; see Ref. [87]. This identification is purely formal because, in spite of their connection in (4.3), $\sigma_{\rm a}^{(\rm e)}$ varies from 0 to ∞ *independently* of $\sigma_{\rm t}$. In practice, this means that the effective

ϖ_0 varies from 1 to $-\infty$. Nonetheless, the analogy can be used if necessary to obtain the solution of (5.1)–(5.2).

We start with the $s/c = k = 0$ case, corresponding to steady/uniform illumination, hence for $\sigma_{\rm a}^{(\rm e)} = 0$. It is easy to show, by direct integration of (5.1)–(5.2), that radiation density decreases only linearly through the medium:

$$\tilde{J}(0,0;z) = 2\left[(1+R) + (1+R-T)\frac{z}{H}\right] \tag{5.4}$$

where we use cloud transmittance T and albedo R given by

$$T(\tau_{\rm t}/2\chi) = \frac{1}{1+\tau_{\rm t}/2\chi},\ R(\tau_{\rm t}/2\chi) = 1 - T(\tau_{\rm t}/2\chi). \tag{5.5}$$

These are the classic results for the two-stream/boundary source model in solar radiation transport at non-absorbing wavelengths, going back to Schuster's landmark 1905 paper [88] about atmospheric RT in the presence of scattering.[17]

Letting

$$L_{\rm D}^{(\rm e)}(s,k) = (3\sigma_{\rm a}^{(\rm e)}\sigma_{\rm t})^{-1/2} = 1/\sqrt{k^2 + 3\sigma_{\rm t}s/c} \tag{5.6}$$

be the so-called diffusion length (in this case, an 'effective' one), the solution we seek is

$$\begin{aligned}\tilde{J}(s,k;z) &= 4\sum_{\{\pm\}} \pm(1\pm X)\,{\rm e}^{\pm(1-z/H)Y} \Big/ \sum_{\{\pm\}} \pm(1\pm X)^2\,{\rm e}^{\pm Y} \\ &= 4\frac{\sinh[(1-z/H)Y] + X\,\cosh[(1-z/H)Y]}{(1+X^2)\,\sinh Y + 2X\,\cosh Y}.\end{aligned} \tag{5.7}$$

We have introduced here the length-scale ratios $X = \chi\ell_{\rm t}/L_{\rm D}^{(\rm e)} = (2\chi/\tau_{\rm t})Y$ where $Y = H/L_{\rm D}^{(\rm e)}$. Expressions for the required boundary fluxes are then

$$\tilde{T}(s,k;H,\tau_{\rm t}/2\chi) = \frac{2X\ \mathrm{cosech}\ Y}{1+X^2+2X\ \coth Y} \tag{5.8}$$

from (4.51), and

$$\tilde{R}(s,k;H,\tau_{\rm t}/2\chi) = \frac{1-X^2}{1+X^2+2X\ \coth Y} \tag{5.9}$$

from (4.50). L'Hôpital's rule can be used to retrieve the above baseline limit where s,k (hence $\sigma_{\rm a}^{(\rm e)}$) $\to 0$, as do X,Y. Figure 5.8 illustrates this Fourier-space solution, $\tilde{F}(0,k;H,\tau_{\rm t}/2\chi)/F(\tau_{\rm t}/2\chi)\,(F = T,R)$ from (5.8)–(5.5), therefore with a focus on steady sources ($s = 0$).

For transmission through a diffusive cloud, we have

$$\frac{\tilde{T}(kH;\xi)}{T(\xi)} = \frac{(kH/\xi)\times(1+\xi)}{[1+(kH/\xi)^2/4]\,\sinh kH + (kH/\xi)\,\cosh kH}, \tag{5.10}$$

[17] For the record, the remarkable result in (5.4)–(5.5) was in fact derived in two earlier but lesser-known papers by Lommel [89] and Chowlson [90].

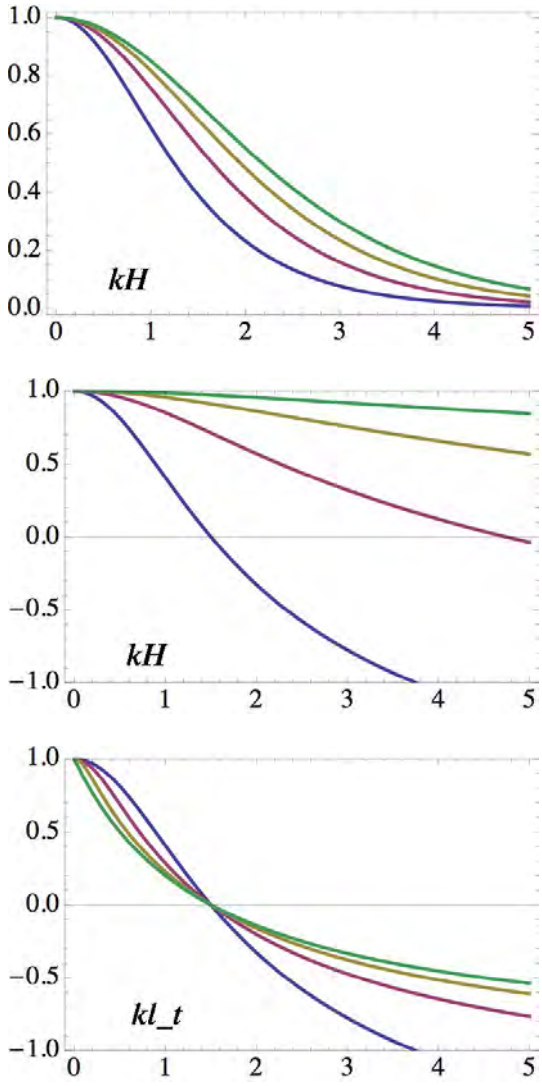

Fig. 5.8. *Flux-based MTFs for similar diffusing clouds.* Top: Fourier space filters $\tilde{T}(k; H, \tau_t/2\chi)/T(\tau_t/2\chi)$ are plotted against non-dimensionalized wavenumber kH for fixed H and $\chi = 2/3$; they determine the loss of definition in imaging (with local flux, not radiance) through clouds with increasing optical depth, from bottom to top: $\tau_t = 1, \sqrt{10} \approx 3.16, 10$, and the somewhat academic case of ∞ (where there is no light left to transmit). The curvature of the MTF at $k = 0$ determines the variance of the lateral transport in transmitted light $\langle \rho^2 \rangle_T$. Middle: Same as top panel but for reflection, and $\tau_t = 31.6$ is used instead of ∞. Bottom: Same as top panel but plotting the reflection MTF versus $k\ell_t$ rather than kH; ordering of optical depth (modulated here with H) refers to r.-h. side, but we note the increasing curvature on the l.-h. side. More discussion in main text.

where we define

$$\xi = \tau_t/2\chi = R/T, \tag{5.11}$$

using (5.5). This normalized response plotted in the top panel of Fig. 5.8 as a function of kH using $\chi = 2/3$. This is basically a poor-person's solution of the pencil-beam problem, with no attempt at accounting for collimation, only localization. It can also be recognized as the flux-based modulation transfer function (MTF) of the cloud for an isotropic point-source. The MTF has immediate applications in imaging theory as the spatial Fourier filter that the medium applies to any pattern viewed by a sensor through the cloud. We refer to Weinmann and Masutani [91] for an interesting atmospheric application: viewing cities through clouds at night from space.

Notice how the more tenuous clouds have a narrower band-pass: the resulting image is brighter but more blurry. This is counterintuitive and results from the propagation away from the assumed *isotropic* point-source in a medium where the transport MFP ℓ_t is increasing, thus promoting further horizontal transport. However, we see that the MTF is not very sensitive to τ_t as it becomes large: it rapidly approaches the limiting case, $kH/\sinh kH$, for $\xi \propto \tau_t \to \infty$. Since the negative curvature of $\tilde{T}(kH;\xi)/T(\xi)$ at the origin becomes asymptotically constant, (3.5) tells us immediately that $\langle\rho^2\rangle_T$ will be $\propto H^2$ (and somewhat larger at finite τ_t). This last prediction will be verified and made quantitative in the next section; see also Appendix E.

For reflection from a diffusive cloud, we have

$$\frac{\tilde{R}(kH;\xi)}{R(\xi)} = \frac{(1-(kH/\xi)^2/4)\times(1+\xi)/\xi}{[1+(kH/\xi)^2/4]+(kH/\xi)\coth kH}, \tag{5.12}$$

with the same definition for ξ in (5.11). This normalized response is plotted in the middle and lower panels with the same value for χ. As in the top one, the middle panel uses kH as the non-dimensional independent variable. By comparison with the case of transmission, we see that curvature at the origin decreases as τ_t increases, and so will $\langle\rho^2\rangle_R$; the size of the reflected spot on a very opaque/reflective non-absorbing medium (such as this sheet of paper!) is hardly bigger than the laser beam (as is easy to verify with a laser pointer).

Another asymptotic limit of interest is when $\xi \propto \tau_t \propto H \to \infty$ with $H/\xi = 2\chi\ell_t$ held constant; the limiting form of the reflected counterpart of the MTF is $(1-\chi|k|\ell_t)/(1+\chi|k|\ell_t)$. The bottom panel re-plots $\tilde{R}(kH;\xi)/R(\xi)$ versus wavenumber non-dimensionalized as $k\ell_t$. Recalling that we are dealing with a necessarily symmetric function of k ($R(\overrightarrow{\rho})$ is axisymmetric), we see that the curvature at the origin is infinite. In other words, $\langle\rho^2\rangle_R$ for semi-infinite non-absorbing media is infinite.

5.5.2 Stratified cloud with an isotropic boundary point-source

The above bare-bones model for a pulsed point-source was recently generalized [92] to include stratification according to the constant gradient parameterization from section 5.2.5.[18]

We thus wish to solve both the space-domain ($s = 0$) problem,

$$\tilde{F}'_z = -[k^2/3\sigma_{\mathrm{t},\Delta}(z)]\,\tilde{J},\ \tilde{J}'/3 = -\sigma_{\mathrm{t},\Delta}(z)\,\tilde{F}_z, \tag{5.13}$$

and its time-domain ($k = 0$) counterpart,

$$\tilde{F}'_z = -(s/c)\,\tilde{J},\ \tilde{J}'/3 = -\sigma_{\mathrm{t},\Delta}(z)\,\tilde{F}_z, \tag{5.14}$$

in both cases, subject to boundary conditions in (5.2) with χ as an floating parameter. By inspection, we see that non-dimensional cloud responses can only depend on Δ and $\tau_{\mathrm{t}} = \overline{\sigma}_{\mathrm{t}} H$ (and χ). This again implies that δ-Eddington rescaling will have no effect on the results. In contrast with the previous $\Delta = 0$ case, however, we will not have similarity-induced behavior between s/c and $k^2/3\sigma_{\mathrm{t}}$ since they are interchangeable in $\sigma_{\mathrm{a}}^{(\mathrm{e})}(s,k)$ only when σ_{t} is constant.

The spatial diffusion problem in (5.13) and (5.2) for $\tilde{J}(0,k;z)$ is solvable in the Fourier domain in terms of Bessel functions of the second kind ($Y_n(x)$, $n = 1,2$) and modified Bessel functions of the second kind ($I_n(x)$, $n = 1,2$); see Appendix A for details. The temporal diffusion problem in (5.14) and (5.2) for $\tilde{J}(s,0;z)$ is solvable in the Laplace domain in terms of Airy functions and their derivatives, which are in turn related to modified Bessel functions with 1/3-integer orders. In both cases, the expressions are too complex to be reproduced here from the computer-assisted symbolic math tool and, at any rate, they are only used after setting $z = 0$ or $z = H$. This leads to somewhat simpler expressions for $\hat{F}(s) = \tilde{F}(s,0)$, $F = R,T$, in terms of (regularized) confluent hypergeometric functions ${}_0F_1(a,x)/\Gamma(a)$; see Appendix B for details.

Boundary fluxes $\tilde{F}(s,0)$ and $\tilde{F}(0,k)$ are obtained as above for $F = R,T$ and, at zeroth order in both k and s, we retrieve (again using L'Hôpital's rule) the standard result in (5.5) for cloud transmittance $F = T$ and albedo $F = R$. As expected, they are insensitive to internal structure since optical properties ϖ_0 and g are held constant with respect to z.

5.5.3 Homogeneous cloud with normally incident illumination at a point

Rather than an isotropic point-source specified in the boundary conditions, we now move to a more accurate representation of the pulsed laser beam formalized in (4.8)–(4.9), hence (4.43) in Fourier–Laplace variables, as an exponential distribution of anisotropic internal sources along the z-axis. However, to achieve analytical results, we must abandon the cloud-scale internal structure we just addressed; we can still apply the Cairns rescaling to correct for the effect of small-scale turbulence.

[18] For another solvable diffusion model (with a steady isotropic point-source) that features exponential stratification, we refer to Section 6.2.2 in Zege et al.'s monograph [83]. Like here, Bessel functions arise; see Appendix A.

Following Ref. [92], we solve this space-domain ($s = 0$) problem,

$$\tilde{F}_z' = -[k^2/3(1-g)\sigma]\,\tilde{J} + \sigma\,\mathrm{e}^{-\sigma z},\ \ \tilde{J}'/3 = -(1-g)\sigma\,\tilde{F}_z + g\sigma\,\mathrm{e}^{-\sigma z}, \tag{5.15}$$

and its time-domain ($k = 0$) counterpart,

$$\tilde{F}_z' = -(s/c)\,\tilde{J} + \sigma\,\mathrm{e}^{-(s/c+\sigma)z},\ \ \tilde{J}'/3 = -(1-g)\sigma\,\tilde{F}_z + g\sigma\,\mathrm{e}^{-(s/c+\sigma)z}, \tag{5.16}$$

subject to the Fourier–Laplace version of (4.28)–(4.29):

$$\tilde{J} + 2\tilde{F}_z\Big|_{z=0} = 0,\ \ \tilde{J} - 2\tilde{F}_z\Big|_{z=H} = 0. \tag{5.17}$$

We anticipate here that non-dimensionalized responses will depend on both τ and g, not just on $(1-g)\tau$. Consequently, δ-Eddington rescaling can improve the accuracy of the model by reducing the impact of forward-peaked phase functions, which we recall is detrimental to diffusion. Also, we notice that s/c enters the exponential source term, as an effective σ_a should since it participates in overall extinction, but $k^2/3(1-g)\sigma$ does not. This transformed 3D time-dependent problem is therefore not formally identical to any known solar two-stream problem, at least when $k \neq 0$.

The desired solution $\tilde{J}(0,k;z)$ of (5.15), with (5.17), can be expressed as a lengthy rational function of k, $\mathrm{e}^{\pm kH}$, $\mathrm{e}^{\pm kz}$ and $\mathrm{e}^{\pm\sigma z}$ with coefficients containing σ, g, and $\mathrm{e}^{\pm\sigma H}$. The diffuse boundary fluxes are now computed from (4.48)–(4.49) with $\mu_0 = 1$; details are provided in Appendix C. The counterpart $\tilde{J}(s,0;z)$ for (5.16), with (5.17), can similarly be expressed as an even lengthier rational function of s/c, $\mathrm{e}^{\pm\sqrt{3s/c(1-g)\sigma}H}$, $\mathrm{e}^{\pm\sqrt{3s/c(1-g)\sigma}z}$, $\mathrm{e}^{\pm(s/c)H}$ and $\mathrm{e}^{\pm(\sigma+s/c)z}$ with coefficients containing σ, g, and $\mathrm{e}^{\pm\sigma H}$; details are given in Appendix D with $\mu_0 = 1$.

The zeroth-order result in both k and s, yet again calling for L'Hôpital's rule, yields the known expressions [87] for total (direct plus diffuse) cloud transmittance,

$$T = \frac{5 - \mathrm{e}^{-\tau}}{3(1-g)\tau + 4}, \tag{5.18}$$

and its albedo $R = 1 - T$, leading to

$$R = \frac{3(1-g)\tau - 1 + \mathrm{e}^{-\tau}}{3(1-g)\tau + 4}, \tag{5.19}$$

for normal solar incidence, this is as expected when the source becomes steady ($s = 0$) and uniform ($k = 0$). Following Meador and Weaver [87], we note that for very small optical depths T can slightly exceed unity (hence R becomes slightly negative) if $g > 2/3$. Although we do not expect to use diffusion theory for such optically thin clouds, this underscores the need to use δ-Eddington rescaling in (4.16), which maps $g = 0.85$ to $g' = 0.46$ (thus crossing the critical $2/3$ threshold for obtaining physical values of R and T for all values of τ).[19]

[19] Since Cairns' rescaling in (4.20) goes in the wrong direction of larger g-values, it is better not to stretch the diffusion model toward media with insufficient opacity.

5.5.4 Homogeneous cloud with normally incident illumination at a point from above and a reflective surface below

This scenario could apply to a down-looking lidar probing fog, low-level arctic clouds, or turbid coastal water. However, to represent accurately the later situation one would need to add: (*i*) a flexible combination of collimated (normal) and diffuse (isotropic) illumination to account for roughness of the air–water interface; (*ii*) partial reflection at the illuminated boundary determined by total internal reflection; (*iii*) the related conservation of flux when crossing a discontinuity in index of refraction, another Brewster-angle effect [93]; and (*iv*) some level of absorption in the optical medium. We explore here the simple version.

In this case, we activate the boundary albedo α_H in the boundary condition at $z = H$. We thus need to solve the space- and time-domain problems in (5.15) and (5.16) subject to (4.46)–(4.47) with $q_0 = 0$ and $\chi = 2/3$, specifically,

$$\tilde{J} + 2\,\tilde{F}_z\Big|_{z=0} = 0, \;\; \tilde{J} - 2\,\frac{1+\alpha_H}{1-\alpha_H}\,\tilde{F}_z\Big|_{z=H} = 0, \tag{5.20}$$

assuming $0 < \alpha_H < 1$ (and $\tilde{F}_z(H) = 0$, a Neumann boundary condition, when $\alpha_H = 1$). There is no new or fundamental difficulty in this enhanced version of the previous problem. The analytical expression of the solution will of course be more complex. Rather, we have here the opportunity to demonstrate a superposition principle of 3+1D RT in $(s, \overrightarrow{k})$-space using a physical argument.

If $\alpha_H = 0$, we already know what happens: some light is reflected, some is transmitted spread over space and time, and we know the Laplace and Fourier transforms of these distributions. Since the surface at $z = H$ is partially reflective, each point on it becomes a secondary source for the medium with a space- and time-dependent intensity determined by the problem with $\alpha_H = 0$. We know from section 5.5.1 how the homogeneous medium responds to each isotropic point-source on a boundary.

Let $\tilde{F}_{\rm col}$ and $\tilde{F}_{\rm iso}$ $(F = R, T)$ be the boundary fluxes for the two problems in $(s, \overrightarrow{k})$-space and let us focus on the remote sensing signal $\tilde{R}(s,k)$, hence $R(t,\rho)$, accessible from above the scene.

The zeroth-order contribution, in the sense of lower surface reflections, is $\tilde{R}_{\rm col}(s,k)$. The first-order contribution to the signal is $\tilde{T}_{\rm col}(s,k)\alpha_H\tilde{T}_{\rm iso}(s,k)$. Indeed, if we think of t and ρ as random variables with PDFs $P_F(t,\rho) = F(t,\rho)/F$, then the associated $\tilde{P}_F(s,k) = \tilde{F}(s,k)/\tilde{F}(0,0)$ are their characteristic functions. In probability theory, addition of two independent random variables calls for a convolution of their PDFs, but just a simple product of characteristic functions. Consequently, we can read

$$\tilde{T}_{\rm col}(s,k)\alpha_H\tilde{T}_{\rm iso}(s,k) = T_{\rm col}\,\tilde{P}_{T,{\rm col}}(s,k) \times \alpha_H \times T_{\rm iso}\,\tilde{P}_{T,{\rm col}}(s,k)$$

as the properly composed probability of three sequential but independent random events: (1) transmission from $z = 0$ to $z = H$ and dispersion according to $P_{T,{\rm col}}(t,\rho)$; (2) isotropic reflection by the uniform surface; (3) re-transmission back to $z = 0$ and dispersion according to $P_{T,{\rm iso}}(t,\rho)$.

Generalization to the next order is straightforward. Rather than transmission back to $z = 0$ the once surface reflected light is reflected back to the surface by

the cloud/fog, surface reflected again and then transmitted: $\tilde{T}_{\rm col}\alpha_H\tilde{R}_{\rm iso}\alpha_H\tilde{T}_{\rm iso}$. By induction, the contribution for $n \geq 1$ surface reflections is $\tilde{T}_{\rm col}[\alpha_H\tilde{R}_{\rm iso}]^{n-1}\alpha_H\tilde{T}_{\rm iso}$. By summing up all the contributions, we have for the requested flux

$$\tilde{R}(s,k) = \tilde{R}_{\rm col}(s,k) + \tilde{T}_{\rm col}(s,k) \times \sum_{n=0}^{\infty} \Big[\alpha_H \tilde{R}_{\rm iso}(s,k)\Big]^n \times \alpha_H \tilde{T}_{\rm iso}(s,k),$$

hence

$$\tilde{R}(s,k) = \tilde{R}_{\rm col}(s,k) + \tilde{T}_{\rm col}(s,k)\,\frac{\alpha_H\,\tilde{T}_{\rm iso}(s,k)}{1-\alpha_H\tilde{R}_{\rm iso}(s,k)}. \tag{5.21}$$

When working in a software environment for symbolic math, it is easy to implement this expression once we have solved the two coupled ODEs problems with different types of source and stored the results.

5.5.5 Homogeneous cloud with uniform oblique illumination

We do not foresee the immediate need to investigate the axially asymmetric spatial patterns of reflected (and even less transmitted) light that would result from oblique illumination by a narrow laser beam.[20] However, it is of interest to understand the impact of slant illumination on the temporal properties (path-length distributions and moments) of reflected and diffusely transmitted light. This is largely because of the emerging capability of measuring such properties from ground and space using sunlight and differential absorption spectroscopy in the oxygen A-band (to be discussed in detail in section 5.8).

As always with diffusion, we only obtain responses in flux, at the cloud boundaries in particular. However, one can invoke optical reciprocity to find new applications. In this case, we have spatially and angularly integrated but time-resolved observation of a pulsed collimated source. This situation can be transposed to a large-scale single-direction (i.e., radiance) observation of an isotropic burst of light, which may or may not be localized at a single point (there is no attempt at imaging). This scenario is directly applicable to light-curve analysis, for example, for optical detection of cloud-to-ground lighting [95–98].

Referring back to (4.10)–(4.11) as needed, with $\phi_0 = 0$, it is straightforward to generalize to $\mu_0 < 1$ the source terms in the time-domain problem in (5.16) for normal ($\mu_0 = 1$) illumination. We thus need to solve

$$\begin{aligned} \hat{F}'_z &= -(s/c)\,\hat{J} + \sigma\,\mathrm{e}^{-(s/c+\sigma)z/\mu_0}, \\ \hat{J}'/3 &= -(1-g)\sigma\,\hat{F}_z + \mu_0 g\sigma\,\mathrm{e}^{-(s/c+\sigma)z/\mu_0}, \end{aligned} \tag{5.22}$$

subject to boundary conditions similar to those in (5.17). However, this is only for Laplace-transformed variables, so we use $\hat{\cdot}$ rather than $\tilde{\cdot}$ symbols, referring back to section 5.3.1. The sought solution $\hat{J}(s;z)$ is a nontrivial generalization of the already complex expression for $\tilde{J}(s,0;z)$ obtained in section 5.5.3; see Appendix D for details.

[20] See Section 6.3 in Zege et al.'s monograph [83] and the paper cited therein by Zege, Polonsky and Chaikovskaya [94] where this problem is addressed in steady state to obtain the non-axisymmetric MTF.

From $\hat{J}(s;z)$ we derive $\hat{R}(s)$ and $\hat{T}_{\rm dif}(s)$ using (4.48) and (4.49), ignoring the horizontal wavenumber k. When $s \to 0$, along with the effective absorption, we retrieve classic formulas from, for example, Ref. [87], for *total* cloud transmittance,

$$T = T_{\rm dif} + \mathrm{e}^{-\tau/\mu_0} = \frac{(2+3\mu_0) + (2-3\mu_0)\,\mathrm{e}^{-\tau/\mu_0}}{3(1-g)\tau + 4}, \tag{5.23}$$

and albedo

$$R = 1 - T = \frac{3(1-g)\tau + (2-3\mu_0)(1-\mathrm{e}^{-\tau/\mu_0})}{3(1-g)\tau + 4}, \tag{5.24}$$

resulting from slant illumination by the (steady) solar beam. Here also there are caveats about unphysical outcomes if $g > 2/3\mu_0$ and τ is too small. The same remedy as above is recommended, namely, to use δ-Eddington rescaling and also to steer away from grazing solar zenith angles (SZAs) if τ is small.

As demonstrated in the previous case, we can easily add surface reflectivity to the model without going through the whole derivation. Indeed, since each term in (5.21) has a physical meaning, it is not hard to transpose it to a different problem. For instance, what if we were to remotely observe an isotropic point-source on a reflective surface ($0 \le \alpha_0 \le 1$) with a non-imaging but time-resolving radiometer through a cloud layer? This could be a cloud-to-ground lightning stroke viewed from satellite. Either way, we need to partition what time-dependence belongs to the source and what 'pulse stretching' was added by the intervening scattering medium. The Laplace transform of the radiance time evolution for a unitary δ-source viewed at an angle $\theta = \cos^{-1}\mu \ge 0$ (away from nadir) is predicted to be

$$\hat{I}_{\rm obs}(s) \approx \frac{1}{\pi} \times \frac{\hat{T}_{\rm col}(s;\mu)}{1 - \alpha_0 \hat{R}_{\rm iso}(s)}, \tag{5.25}$$

where we have used reciprocity and emphasized that the $\hat{T}(s)$ computed here is for a slant illumination ($\mu_0 < 1$) by a uniform collimated beam or, by reciprocity, remote observation ($\mu < 1$) with a large footprint.

As in all of the previous cases, we postpone discussion of higher-order terms in the Taylor expansion of $\hat{R}(s)$ and $\hat{T}(s)$ around $s = 0$ (in this case, moments of path-length ct) until we address specific applications to cloud remote sensing in the following sections. In the interim, we describe what can be done about the challenge of inverse Fourier–Laplace transformation.

5.6 Inverse Fourier–Laplace transformation

We now face the difficult task of performing inverse Fourier and/or Laplace transforms of analytical (but not simple) expressions to obtain explicit expressions for cloud remote sensing signals. Or else we need to look for other ways of exploiting the diffusion models in remote sensing applications, a route we explore in sections 5.8 and 5.9. Since none of the above models have known analytical inverse transforms, we show here (1) the outcome of a numerical approach and (2) how a somewhat degraded representation of the laser beam source enables the inverse transforms to be performed analytically.

5.6.1 Uniform clouds with an isotropic boundary point-source in (5.1), using exact boundary conditions in (5.2)

It is highly desirable to validate the diffusion model for Green functions using numerical solutions of the 3D RT equation, say, by way of Monte Carlo techniques. It is possible to compute Fourier and/or Laplace transforms of radiative responses using MC, i.e., characteristic functions of the MC random variables. However, it is more compelling to see the diffusion predictions and MC benchmarks in physical space.

Unfortunately, not even the simplest of the above models, isotropic boundary point-sources in (5.1)–(5.2), has analytical inverse transforms, so we need to implement them numerically. Figure 5.9 shows an example using the *normalized* spatial Green function for transmission $P_T(\rho)$ obtained from $\tilde{P}_T(k) = \tilde{T}(0,k)/T$ in (5.10), itself plotted in Fig. 5.8(a). In imaging terminology, we are deriving the cloud's point spread function (PSF) from its MTF via inverse 2D Fourier transformation.

In axial symmetry, the 2D Fourier transform in (4.41) morphs into the Hankel transform:

$$\tilde{P}_T(k) = 2\pi \int_0^\infty P_T(\rho) J_0(k\rho) \rho \, \mathrm{d}\rho \leftrightarrow P_T(\rho) = \frac{1}{2\pi} \int_0^\infty \tilde{P}_T(k) J_0(k\rho) k \, \mathrm{d}k, \tag{6.1}$$

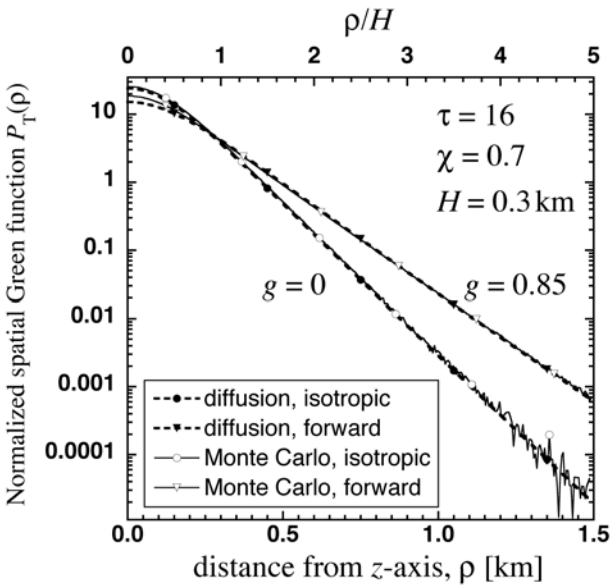

Fig. 5.9. *Normalized spatial Green function for transmitted light according to analytical diffusion theory and numerical transport theory.* The cloud optical depth was set to $\tau = 16$ and illumination was isotropic from a point; the outcome is the PSF for this diffusive medium. The extrapolation length parameter was set to $\chi = 0.7$ for the diffusion expression in Fourier space, which was inverted numerically. Other details about the MC transport simulation are as in Fig. 5.3, which was replicated here for isotropic as well as forward (H–G) scattering. Adapted from Ref. [24].

where $J_0(x)$ is the zeroth-order Bessel function of the first kind. Agreement between transport (MC results) and diffusion theories is excellent for the prescribed $\tau = 16$ cloud, especially for isotropic ($g = 0$) scattering, when $\chi = 0.7$. As is appropriate for a validation exercise, the MC scheme mimicked the isotropic boundary source used in the diffusion model. The only noticeable difference is for the near-axis field when $g = 0.85$.

5.6.2 Uniform clouds with an isotropic internal point-source, using extended boundary conditions in (4.34)

The above numerical approach to inverse Fourier or Laplace transformation is viable for case studies, but not for routine application to remote sensing signal analysis. So we still need an analytical predictor for space-time Green functions, especially for the multiple-scattering cloud lidar application where both dimensions are exploited. Since none of the models in the previous section are amenable to analytic inversion, we first need to modify the diffusion model.

Polonsky and Davis [99] revisited the way the pulsed laser-type sources for the Green function are represented. Following the path blazed by Zege, Katsev and Sherbaf [100] for weakly absorbing semi-infinite media and Bushmakova, Zege and Katsev [101] for finite media, they proposed to compute the radiative Green function at $z = 0$ (the illuminated boundary) and $z = H$ (the opposite boundary) using an *isotropic* source concentrated at a single point *inside* the cloud, but judiciously positioned. For the moment, however, we will denote this roaming position as $z_0 \in (0, H)$. With the 3D RT equation in mind, we write this as[21]

$$Q(t, \boldsymbol{x}, \boldsymbol{\Omega}) = \delta(t)\delta(x)\delta(y)\delta(z - z_0)/4\pi \tag{6.2}$$

in the RT equation, which translates to

$$q_J(t, \boldsymbol{x}) = \delta(t)\delta(x)\delta(y)\delta(z - z_0),\ \boldsymbol{q}_F(t, \boldsymbol{x}) = \boldsymbol{0}, \tag{6.3}$$

for the diffusion model. In Fourier–Laplace space, this translates simply to $\tilde{q}_J(z) = \delta(z - z_0)$ and $\tilde{q}_{Fz} = 0$ (hence no attempt at capturing internal source anisotropy in this particular diffusion model).

We now need to solve[22]

$$\tilde{F}'_z = -\sigma_{\rm a}^{(\rm e)}(s, k)\,\tilde{J} + \delta(z - z_0),\ \tilde{J}'/3 = -\sigma_{\rm t}\,\tilde{F}_z, \tag{6.4}$$

which we subject to homogeneous extended Dirichlet boundary conditions,

$$\tilde{J}(-\chi/\sigma_{\rm t}) = 0,\ \tilde{J}(H + \chi/\sigma_{\rm t}) = 0. \tag{6.5}$$

This is a textbook boundary-value problem [103] leading to

[21] For lidar applications at least, causality dictates that we also shift the δ-in-time by z_0/c. However, this only modulates the Laplace-transformed source $\tilde{q}_J(z)$ by a constant, $\exp(\mathrm{i}sz_0/c)$, and the shift itself can be implemented simply in the end-result anyway. By omitting it here, there is thus no loss in generality, but some gain in simplicity.

[22] Incidentally, this model found an application in one of the earliest papers in 3D RT known to the present authors: Richards' 1956 study of point-sources in plane clouds [102].

$$\tilde{J}(s,k;z_0,z) = \frac{\cosh[m(\tau_\mathrm{t}+2\chi-\sigma_\mathrm{t}|z-z_0|)] - \cosh[m(\tau_\mathrm{t}-\sigma_\mathrm{t}(z+z_0))]}{\chi m \sinh[m(\tau_\mathrm{t}+2\chi)]}, \quad (6.6)$$

where we recognize $\tau_\mathrm{t} = \sigma_\mathrm{t} H$ from (5.3) and define[23]

$$m(s/c,k)^2 = \frac{3\sigma_\mathrm{a}^{(\mathrm{e})}(s,k)}{\sigma_\mathrm{t}} = 3\,\frac{s/c}{\sigma_\mathrm{t}} + \left(\frac{k}{\sigma_\mathrm{t}}\right)^2 = \frac{s/D+k^2}{\sigma_\mathrm{t}^2}, \quad (6.7)$$

recalling that $D = c/3\sigma_\mathrm{t}$. This Green function reflects reciprocity, i.e., $z_0 \leftrightharpoons z$ symmetry between the positions of the isotropic source and detector (in this case, a 'J-meter'). It also has space-time similarity in the sense that k^2 is interchangeable with s/D in the expression for m^2; this will translate in physical space to $\rho^2 \leftrightarrow Dt$ maps in, for example, the marginal moments. Most importantly, the analytical expression contained in (6.6)–(6.7) can be inverse Fourier–Laplace transformed.

Details of the inverse 2D Fourier–Laplace (actually, Hankel-Laplace) transformation of $\tilde{J}(s/c,k;z,z_0)$ can be found in Ref. [99]. The most interesting aspect is that the straightforward expansion of the solution into a series (invertible term-by-term) that converges slowly at large times and distances from the source – precisely the regions we are most interested in. Application of Poisson's sum-rule resolves this issue and delivers a series with reasonably fast convergence in the regime of interest. The end-result is:

$$\begin{aligned} J(t,\rho,z;z_0) \;=\; & \frac{2c\sigma_\mathrm{t}}{\tau_\mathrm{t}+2\chi}\left(\frac{1}{\pi}\times\frac{\mathrm{e}^{-\rho^2/4Dt}}{4Dt}\right) \\ & \times \sum_{n=1}^{\infty} \sin\left(\pi n\,\frac{\sigma_\mathrm{t} z+\chi}{\tau_\mathrm{t}+2\chi}\right)\,\sin\left(\pi n\,\frac{\sigma_\mathrm{t} z_0+\chi}{\tau_\mathrm{t}+2\chi}\right) \\ & \exp\left[-\left(\frac{\pi n}{\tau_\mathrm{t}+2\chi}\right)^2 \sigma_\mathrm{t}^2 Dt\right]. \end{aligned} \quad (6.8)$$

A closely related quantity of interest is net flux in the vertical, from Fick's law:

$$\begin{aligned} F_z(t,\rho,z;z_0) \;=\; & -\frac{D}{c}\,\frac{\partial J}{\partial z} = -\frac{1}{3\sigma_\mathrm{t}}\,\frac{\partial J}{\partial z}, \\ & = -\frac{2\pi c\sigma_\mathrm{t}}{3(\tau_\mathrm{t}+2\chi)^2}\left(\frac{1}{\pi}\times\frac{\mathrm{e}^{-\rho^2/4Dt}}{4Dt}\right) \\ & \times \sum_{n=1}^{\infty} n\,\cos\left(\pi n\,\frac{\sigma_\mathrm{t} z+\chi}{\tau_\mathrm{t}+2\chi}\right)\,\sin\left(\pi n\,\frac{\sigma_\mathrm{t} z_0+\chi}{\tau_\mathrm{t}+2\chi}\right) \\ & \exp\left[-\left(\frac{\pi n}{\tau_\mathrm{t}+2\chi}\right)^2 \sigma_\mathrm{t}^2 Dt\right]. \end{aligned} \quad (6.9)$$

In particular, the two above expressions can be combined according to (4.27) to obtain the hemispherical fluxes $F_\pm$ that are directly measured with standard (2π FOV) radiometers.

[23] In the case of real absorption in steady-state asymptotic 1D RT, this key non-dimensional ratio is known as the 'similarity' parameter [104].

At this point, a well-known physical defect of diffusive transport theory becomes apparent: one obtains $J(t,\rho,z;z_0) > 0$ for all $t > 0$, and not just $t > \sqrt{\rho^2+(z-z_0)^2}/c$. For instance, although it is in very small amounts, light reaches the opposite cloud boundary without delay, thus violating basic causality and in sharp contrast with the MC simulation outcome in Fig. 5.3(b). This artifact can be traced back to the choice of neglecting in (4.2) the $\partial_t \boldsymbol{F}$ term. Not dropping that term leaves us with the so-called telegrapher's equation (system). In some applications, it is desirable to enforce causality in signal modeling [105–107]. In our present application, however, we prefer to commit to not use the diffusion results in regions of space-time where the theory has known defects, over and beyond the present issue with infinite propagation velocity. Avoidance of the problematic short times/paths and distances from the source is especially easy when one has an explicit representation in space and/or time. We discuss another advantage at the close of section 5.9.

In principle, the response to the correct distribution of internal sources in can now be reconstructed by linear superposition (integrating over z_0).[24] However, to preserve the relative simplicity of the above expression, we propose to select a single representative value of z_0 rather than integrate over all the sources, i.e., exponentially weight and integrate[25] over z_0 between 0 and H (even if we can safely assume here that the upper limit is ∞).

A physical argument for positioning such an 'effective' isotropic point-source goes as follows. If we were to collapse the axial exponentially decaying distribution of *anisotropic* point-sources in (5.15) or (5.16) into a single *isotropic* point, we would likely place it at $z_0 \sim \ell_t$, hence $\sigma_t z_0 \sim O(1)$, recalling that $\chi \sim O(1)$ as well.[26] Indeed, the basic idea of the transport MFP is to prolong ballistic propagation just far enough for the memory of the original direction to be erased by multiple forward-biased scatterings [108]. In essence, ℓ_t is the medium's effective MPF for an isotropic scattering [80] and, for the same physical reasons, defines the depth of the radiative boundary-layer in the cloudy medium.

5.6.2.1 Transmission properties

For transmission, we evaluate

$$\tilde{T}(s,k) = \frac{\tilde{J}(s,k;H,z_0)}{2} = \frac{\cosh[m(\sigma_t z_0 + 2\chi)] - \cosh[m\sigma_t z_0]}{2\chi m \times \sinh[m(\tau_t + 2\chi)]}, \tag{6.10}$$

and we note that the combined numerator and the $2\chi m$ factor in the denominator are well-approximated by $\cosh'[m(\sigma_t z_0 + \chi)] = \sinh[m(\sigma_t z_0 + \chi)]$ if $2\chi m \ll 1$. In

[24] There is, however, no $\tilde{q}_{Fz} = g\tilde{q}_J$ term here, hence no account of first-scattering source anisotropy.

[25] This superposition of point-source solutions would change the second sine term in (6.8)–(6.9) into a combination of two trigonometric functions, four if the upper bound is set to $H < \infty$.

[26] A closer look at the spatial Green function plotted in Fig. 5.1 reinforces this choice. The assumed cloud has $\tau_t = H/\ell_t = 5.4$. We can see overall light levels decreasing radially with distance from a point at ∼1–2 transport MFPs $\ell_t = 1/\sigma_t \approx 0.2$ km below the upper (illuminated) boundary.

this case, the desired asymptotic ($\tau_t \gg \chi$) behavior when $m \to 0$ is

$$T_{ts}(\tau_t) \approx \frac{2\chi}{\tau_t + 2\chi}, \tag{6.11}$$

from basic two-stream theory (5.5). It is obtained when we set $\sigma_t z_0 = \chi$. It can be shown that this choice also gives the correct leading terms for $\langle \rho^2 \rangle_T$ and $\langle ct \rangle_T$ because the leading term in m^2 has the 'correct' pre-factor for both k^2 and s/c, using as a benchmark the solutions of (5.1)–(5.2). By enforcing correct small (s, k) behavior, we are sure to obtain the correct behavior for large (t, ρ) after inverse transformation.

Rather than using (6.10) in (s, k)-space, we can thus use the somewhat simpler model[27]

$$\tilde{T}(s, k) \approx \frac{\sinh[m(2\chi)]}{\sinh[m(\tau_t + 2\chi)]}. \tag{6.12}$$

Figure 5.10 demonstrates how close this model is to (6.10), with $\sigma_t z_0 = \chi$, and how well these internal point-source models approximate the boundary-source model in (5.8) where it matters, i.e., as $k \to 0$.

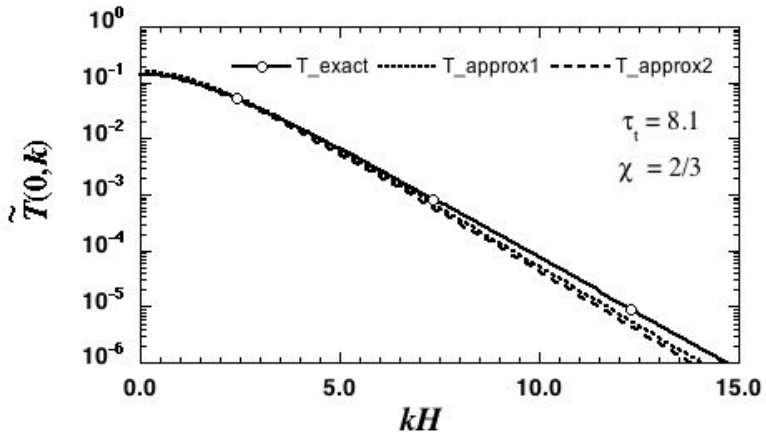

Fig. 5.10. *Three models for* $\tilde{T}(0, k)$. We compare in semi-log axes the 'exact' diffusion model in (5.8) for an isotropic boundary source expressed in Robin BCs, its counterpart in (6.10) based a judiciously positioned internal point-source ($\sigma_t z_0 = \chi$) with extended Dirichlet BCs, and the approximation in (6.12). The first of these MTFs is also plotted in Fig. 5.8 (top panel), but here we use $\tau_t = (1 - g)\tau = 8.1$ and $\chi = 2/3$. Notice the osculating curvatures at $k = 0$, meaning that the predicted value for $\langle \rho^2 \rangle_T$ will be the same; cf. (3.5).

[27] Viewed, like in Fig. 5.10, as a model for the MTF, $\tilde{T}(0, k)$, this expression is adapted from Bushmakova et al.'s 1972 article [46], generalized by the same authors in 1974 to space-time Green functions. However, those studies use $\sigma_t z_0 = (5/4)\chi$ in our notations to achieve slightly better accuracy for a collimated beam at normal incidence. See also Katsev and Zege's 1986 paper [109] and the monograph by Zege et al. [83, Section 4.3.3].

Adapting the Fourier–Laplace inversion procedure in [106], we find

$$T(ct,\rho) \approx \frac{2\pi}{3H}\,\frac{R_{\rm ts}^2}{\tau_{\rm t}}\left(\frac{1}{\pi}\times\frac{3\tau_{\rm t}\,{\rm e}^{-3\tau_{\rm t}\,\rho^2/4Hct}}{4Hct}\right) \times\sum_{n=1}^{\infty} n\,\sin(\pi n R_{\rm ts})\,\exp\left[-(\pi n R_{\rm ts})^2\,\frac{1}{3\tau_{\rm t}}\,\frac{ct}{H}\right]. \tag{6.13}$$

where $R_{\rm ts}(\tau_{\rm t})$ is given by $1-T_{\rm ts}(\tau_{\rm t})$ from (6.11), equivalently, the classic two-stream model outcome in (5.5). We have somewhat rewritten here the Green function to emphasize the two main cloud remote-sensing unknowns, H and $\tau_{\rm t}=(1-g)\tau$. As expected, we see in particular that the outcome of (6.13) does not change, for a given value of H, within a class of similar clouds, i.e., where $(1-g)\tau$ is constant.

We recognize in (6.13) a Gaussian spatial profile of flux with an increasing value of the variance $\langle\rho^2\rangle(t)$ of the lateral transport at each instant t (or path ct); specifically,

$$\langle\rho^2\rangle(t)=\frac{4c}{3\sigma_{\rm t}}\,t. \tag{6.14}$$

This is as expected for $\langle\rho^2\rangle=\langle x^2\rangle+\langle y^2\rangle$ recalling that, for boundary-free *isotropic* diffusion away from a point-source, we have $\langle r^2\rangle=\langle x^2\rangle+\langle y^2\rangle+\langle y^2\rangle=6Dt$ with $D=c/3\sigma_{\rm t}$ [103].

Detailed time-only dependence is obtained from (6.13) by multiplying both sides by $2\pi\rho{\rm d}\rho$ and integrating from 0 to ∞:

$$T(ct)\approx\frac{\pi}{2H}\,\frac{R_{\rm ts}^2}{3\tau_{\rm t}}\times\sum_{n=1}^{\infty} n\,\sin(\pi n R_{\rm ts})\,\exp\left[-(\pi n R_{\rm ts})^2\,\frac{1}{3\tau_{\rm t}}\,\frac{ct}{H}\right]. \tag{6.15}$$

This result can be applied to the monitoring of cloud-to-ground lightning [97] and other rapidly varying time-dependent sources, through dense clouds from space. We see in (6.15) a linear superposition of exponential decays in time, the dominant (slowest, $n=1$) rate being [101]

$$ct^\star = H\times\left(\frac{3}{\pi^2}\right)\times\frac{\tau_{\rm t}}{R_{\rm ts}(\tau_{\rm t})^2}, \tag{6.16}$$

where we continue to emphasize the invariance within similarity classes (constant $\tau_{\rm t}$).

Integrating (6.13) over path ct from 0 to ∞ yields the spatial response to a steady source as observed with an imaging detector:[28]

$$T(\rho)\approx\left(\frac{R_{\rm ts}}{H}\right)^2\times\sum_{n=1}^{\infty} n\,\sin(\pi n R_{\rm ts})\,K_0\left(\pi n R_{\rm ts}\,\frac{\rho}{H}\right). \tag{6.17}$$

where $K_0(\cdot)$ is the zeroth-order modified Bessel function of the second kind. This would apply to the monitoring cloudy regions from space for steady localized sources using imaging sensors; missiles during their boost phase are possible targets.

[28] Use identity $\int_0^\infty \exp[-(at+b/t)]\,{\rm d}t/t = 2K_0(2\sqrt{ab})$.

Although defined above as a sum of Gaussians, the dominant ($n = 1$) term decays radially as an exponential approached from above with a relatively slow power law [110]:

$$T(\rho) \sim \frac{\exp(-\rho/\rho^\star)}{\sqrt{\rho}}, \tag{6.18}$$

where the e-folding radius is

$$\rho^\star = H/\pi R_{\rm ts}. \tag{6.19}$$

As expected from $k^2 \leftrightarrow s/cD$ similarity ($D = c/3\sigma_{\rm t}$), examination of (6.16) shows that we have $(\rho^\star)^2 = (c/3\sigma_{\rm t})\, t^\star$. This connection serves as a reminder that the key space-time variability parameter m defined in (6.7) is $\propto k$ when $s = 0$, but $\propto \sqrt{s}$ when $k = 0$. Consequently, for this class of models cunningly designed to delivery explicit expressions in space end/or time, moment predictions will be accurate for $\langle \rho^2 \rangle$ and $\langle ct \rangle$, but not $\langle (ct)^2 \rangle$.

5.6.2.2 Reflection properties

With reflection in mind, we propose to set $\sigma_{\rm t} z_0 \approx 1$, this time irrespective of χ (although we also have $\sigma_{\rm t} z_0 \approx (3/2)\chi$ since $\chi \approx 2/3$). This leads to

$$\tilde{R}(s,k) = \frac{\tilde{J}(s,k;0,(3/2)\chi/\sigma_{\rm t})}{2} = \frac{\cosh[m(\tau_{\rm t}+\chi/2)] - \cosh[m(\tau_{\rm t}-(3/2)\chi)]}{2\chi m \times \sinh[m(\tau_{\rm t}+2\chi)]}. \tag{6.20}$$

In the asymptotic regime where $\tau_{\rm t} \gg \sigma_{\rm t} z_0 \sim \chi \sim O(1)$, one notes that $\cosh[m(\tau_{\rm t}+\chi/2)] - \cosh[m(\tau_{\rm t}-(3/2)\chi)]$ will be very close to $2\chi m \sinh[m(\tau_{\rm t}-\chi/2)]$ if $2\chi m \ll 1$. The boundary flux at $z = 0$ can therefore be written even more simply as [106]

$$\tilde{R}(s,k) \approx \frac{\sinh[m(\tau_{\rm t}-\chi/2)]}{\sinh[m(\tau_{\rm t}+2\chi)]}. \tag{6.21}$$

The above expression still gives us in the limit $m \to 0$ the correct asymptotic ($\tau_{\rm t} \gg \chi$) form of cloud albedo in (5.19) for the collimated-beam model when the short-lived exponential terms are omitted:

$$R \approx \frac{\tau_{\rm t}/2\chi - 1/4}{1+\tau_{\rm t}/2\chi}. \tag{6.22}$$

Here also, we get the correct leading terms for $\langle \rho^2 \rangle_R$ and $\langle ct \rangle_R$ since the leading term in m^2 has the correct pre-factor for both k^2 and s/c.

Figure 5.11 shows how this coarsest of all representations of the pulsed laser source (in terms of directionality and spatial distribution) compares with our best model for the pencil-beam problem in reflection. Although there are interesting deviations at large wavenumbers,[29] there is no apparent difference at small k (nor

[29] We note that the exact diffusion model in Fig. 5.11 leads to negative values of $\tilde{R}(0,k)$ if $g > 0$; the behavior of this model for $k \gg H$, not plotted here, is $\tilde{R}(0,k) \sim -3g/2k$ (following a single negative minimum). This is unphysical since characteristic functions (Fourier transforms of PDFs) are everywhere non-negative if the PDF is axisymmetric. In this sense, the proposed approximation is more useful than the exact theory in applications where $\tilde{R}(0,k)$ must make physical sense over the full range of k. In our case, its utility is to yield tractable inverse Fourier–Laplace transforms.

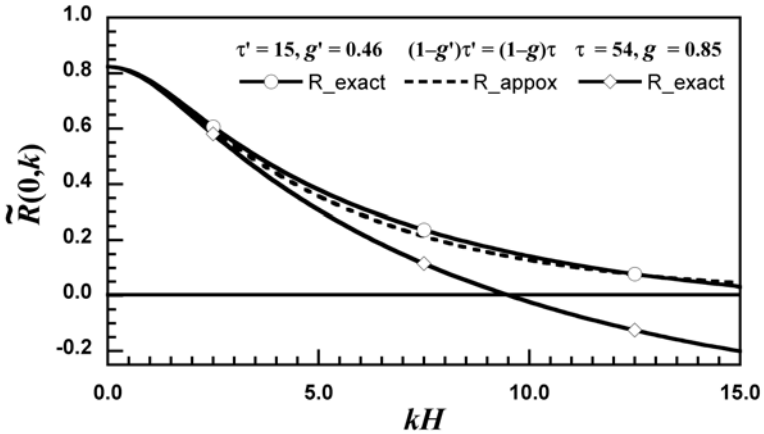

Fig. 5.11. *Two models for* $\tilde{R}(0,k)$. We plot as functions of k (in units of $1/H$) results for both 'exact' diffusion theory that models a collimated incident beam that excites anisotropic sources (details in Appendix C) and a more practical approximation in (6.21) that uses a single judiciously placed isotropic point-source. Two cases with $(1-g)\tau = (1-g')\tau' = 8.1$ are examined. When working with moments and/or long-path and/or far-field properties, only the behavior near $k = 0$ matters. In this case, we have identical behavior up to $O(k^2)$, having set $\chi = 2/3$ in the approximate model.

would there be for small s), where it matters for spatial (temporal) moment estimation as well as long-path and far-field trend analyses.

The end-result of the inverse Fourier–Laplace transform of (6.21) is [106]

$$R(ct,\rho) \approx \frac{2\pi}{3H}\,\frac{R_{\rm ts}^2}{\tau_{\rm t}}\left(\frac{1}{\pi}\times\frac{3\tau_{\rm t}\,{\rm e}^{-3\tau_{\rm t}\,\rho^2/4Hct}}{4Hct}\right) \times\sum_{n=1}^{\infty} n\,\sin\left(\frac{5}{4}\pi n T_{\rm ts}\right)\,\exp\left[-\left(\pi n R_{\rm ts}\right)^2\,\frac{1}{3\tau_{\rm t}}\,\frac{ct}{H}\right], \qquad (6.23)$$

where $T_{\rm ts} = 1 - R_{\rm ts}$ is from (6.11). This result can be applied directly to imaging cloud lidar systems with a wide field-of-view, but maybe not wide enough for robust moment estimation [84].

Integration over space yields

$$R(ct) \approx \frac{\pi}{2H}\,\frac{R_{\rm ts}^2}{3\tau_{\rm t}}\times\sum_{n=1}^{\infty} n\,\sin\left(\frac{5}{4}\pi n T_{\rm ts}\right)\,\exp\left[-\left(\pi n R_{\rm ts}\right)^2\,\frac{1}{3\tau_{\rm t}}\,\frac{ct}{H}\right]. \qquad (6.24)$$

This result can be applied directly to *non*-imaging (for example, space-based) lidar systems with wide-enough footprints [111].

Figure 5.12 shows how well the model in (6.24) performs with respect to the usual 'gold standard' of Monte Carlo simulation. In this case, no effort was made to mimic the actual source used in the diffusion model, namely, an isotropic point-source at about one transport MFP from the observed cloud boundary; as in real cloud lidar, a collimated source was used. So deviations at early times are expected and observed, but diffusion-based models are not to be used in this regime anyway.

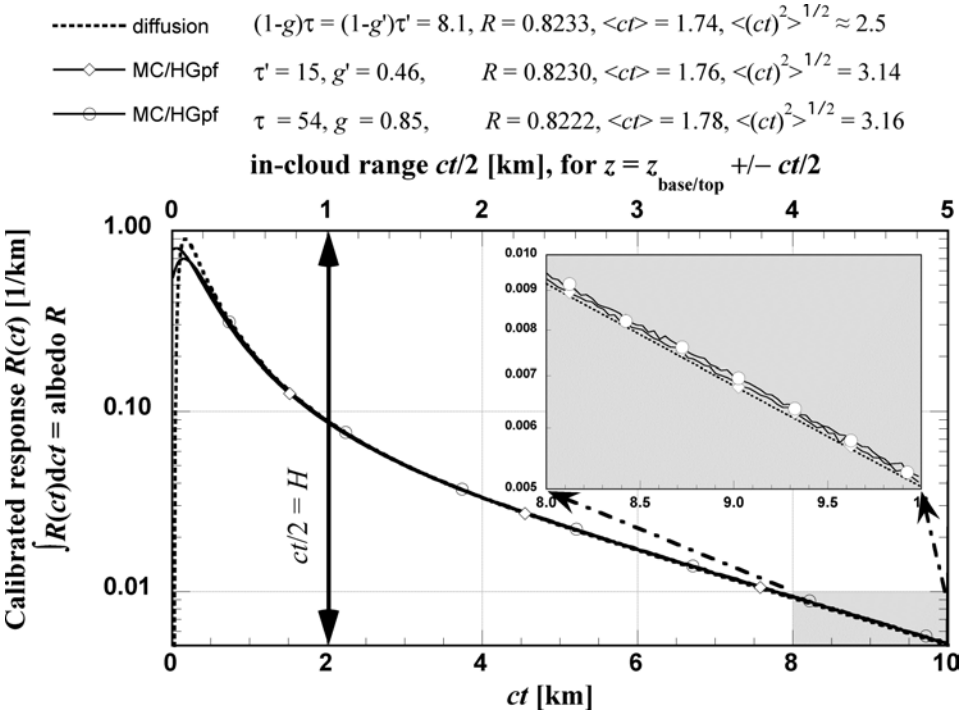

Fig. 5.12. *Diffusion theoretical and MC estimates of the temporal Green function for reflected fluxes.* We have plotted the closed-form expression in (6.24) for the diffusion-based model and two numerical solutions of the basic radiative transfer problem for slab geometry in (2.1)–(2.7). The inset shows the noise level for the adopted MC scheme with $2 \cdot 10^8$ histories. Cloud thickness is $H = 1$ km. The diffusion prediction is the same for all similar clouds, i.e., with the same scaled optical depth $(1 - g)\tau = 8.1$, while slightly different answers are obtained numerically with the RT model (only at early times). All results are normalized to their respective predictions for steady-state albedo, which are quoted to the accuracy of the MC simulations; only ≈2% of the signal lies beyond the cutoff at $ct = 10H$. We see that the diffusion model is an accurate representation of the radiation transport when $ct \gtrsim H$ for the similar cases of H–G scattering with $g = 0.85$ ($\tau = 54$) and $g = 0.46$ ($\tau = 15$).

At long times, the agreement is excellent. The vertical double-headed arrow indicates the range (path $ct/2$) where the single scattering contribution to the signal vanishes. All the signal beyond this point is from multiple scattering only but none of it is in the standard model for backscatter lidar signals. It would be interpreted in classic lidar as a spurious distribution of scattering particles on the opposite side of the cloud.

Integrating (6.23) over path ct yields:

$$R(\rho) \approx \left(\frac{R_{\rm ts}}{H}\right)^2 \times \sum_{n=1}^{\infty} n \ \sin\left(\frac{5}{4}\pi n T_{\rm ts}\right) K_0\left(\pi n R_{\rm ts}\,\frac{\rho}{H}\right). \qquad (6.25)$$

This spatial response would be observable with an imaging detector for a steady narrow-beam source such as a cw laser. An interesting laboratory application is described in Refs [112, 113] targeting oxygen levels in blood.

As noted already for Fig. 5.3, there is no difference in the far-field behavior between reflected and transmitted light in either space or time. So the relations between observables and cloud parameters in (6.14), (6.16) and (6.19) apply to both sides of the cloud [114], and has proven useful in remote sensing applications mentioned previously, but that we now discuss in detail.

5.7 Temporal Green functions applied to *in situ* cloud lidar

5.7.1 Forward model for the radiometric signal

The bulk of this review is about fluxes emerging from cloud boundaries since they are the only ones accessible by remote sensing methods. This section is the exception. We discuss here an interesting new application of forward models for *internal* radiative properties: *in situ* cloud lidar.[30]

In their feasibility study for *in situ* (airborne) cloud lidar, Evans et al. [21] studied the special case $z = z_0 = H/2$ in (6.8) as a first-cut model for a proposed time-resolving wide-FOV radiometry. Notably, they solved the Green function problem directly in the space-time domain using the method of images to satisfy extended Dirichlet BCs (with $\chi = 2/3$). In this highly symmetric situation, the two sine terms reduce to $\sin^2(n\pi/2) = 1$ if n is odd, 0 if even. Thus

$$J(t, \rho, H/2; H/2) = \frac{2c\sigma_t}{\tau_t + 2\chi} \left(\frac{1}{\pi} \times \frac{\mathrm{e}^{-\rho^2/4Dt}}{4Dt} \right) \times \sum_{j=0}^{\infty} \exp\left[-\left(\frac{\pi(2j+1)}{\tau_t + 4/3} \right)^2 \frac{\sigma_t c t}{3} \right]. \tag{7.1}$$

where we recall that diffusivity $D = c/3\sigma_t = c\tau_t/3H$. The authors also argue that, for short times, one can use the classic diffusion Green function for an isotropic pulse at the origin in the absence of boundaries:

$$J(t, \rho, z) = \frac{c}{(4\pi Dt)^{3/2}} \exp\left(-\frac{\rho^2 + z^2}{4Dt} \right), \tag{7.2}$$

where z is now reckoned from the position of the isotropic point-source. For simplicity, Evans et al. assume a monostatic configuration where source and detector are essentially collocated, hence $\rho = 0$ in (7.1) and $\rho = z = 0$ in (7.2). From a cloud characterization perspective, early times can be used to determine a volume-averaged estimate of opacity $\sigma = \sigma_t/(1-g)$ from D, knowing $g \approx 0.85$, and later times to determine $H = \tau_t/\sigma_t$.

[30] Lidar stands for LIght raDAR, or LIght Detection And Ranging, but there is obviously no cloud ranging to be done in this case. The present time-domain signal is entirely about multiple scattering while the conventional ranging application in Lidar assumes necessarily a single scattering or reflection.

This model for *in situ* lidar signals can easily be improved by setting the detector at a horizontal distance $\rho \approx \ell_t = 1/\sigma_t$ from the effective isotropic point-source of light pulses. Instead, Evans et al. moved to qualitatively better forward modeling by using a 3+1D MC code in conjunction with many realizations of a realistic (data-driven) 3D stochastic cloud model [115]. They used this extensive forward modeling to train a neural network to solve the inverse problem at hand: determine from the temporal signal the cloud unknowns $\{\sigma_t, H\}$. Notably, *in situ* lidar retrieval methods must also consider the distance to cloud base (z in our present notation) as an unknown, and its determination calls for estimates of *both* down- and up-welling fluxes that can be modeled (for arbitrary z) using (6.8) and (6.9) combined according to (4.27). The more recent paper by the same authors [116] concludes the proof-of-concept with the successful exploitation of real cloud data gathered from a LearJet operated by the Stratton Park Engineering Company (SPEC), Inc., in Boulder (Colorado).

5.7.2 Illustration with SNR estimation

Figure 5.13 shows $F_\pm(ct) = J(ct, \ell_t, \cdots)/4$, based on (4.27) and (7.1) in this special situation were $F_z \equiv 0$ in (6.9). We upgraded the model only for the radial offset of the effective isotropic source (to the side of the aircraft the laser is pointing away from) and the time-resolving radiometer (looking up or down somewhere on the aircraft). We factored into the result a hypothetical path-bin width of $\Delta ct =$ 20 m, which is easily achievable with laser and detector technology currently used in airborne lidar. The two panels illustrate the sensitivity of this observable as a function of ct for (a) varying H (equivalently, σ) at fixed τ and (b) viceversa. We have high sensitivity to σ at all times. Sensitivity to H increases at later times, which is explained immediately by the dependencies of $ct^\star$ in (6.16). Increasing optical depth (equivalently, extinction) for fixed cloud thickness of course increases the general level of the signal. However, we may not want to depend on absolute calibration of the radiometer as well as accurate monitoring of the laser power; so we should rely only on the shapes of the radiative responses in Fig. 5.13, and not their relative positions on the flux scale.

The positions of the plots in Fig. 5.13 along the vertical (flux) axis can, however, be used for a rough but informative SNR computation for the airborne *in situ* cloud lidar. Lasers used in airborne lidar studies can easily reach 5 W of equivalent cw radiant power, translating to $\approx 10^{18}$ photons/pulse at 532 nm (assuming here a frequency-doubled Nd:YAG solid-state laser with a typical 10 Hz rep rate). The lowest major tick of both plots corresponds to a 10^{-15} probability of detection per laser photon by a (non-imaging) sensor with a reasonable $1\,\mathrm{cm}^2$ aperture. At the 100s of m/s air speed of a jet aircraft, one should not integrate temporally for more than a few pulses, or else cloud structure will not be captured at the natural resolution of multiple-scattering cloud lidar, as determined by $\rho^\star$ in (6.19). This still leaves $N_\gamma \approx 10^3$ multiply-scattered laser photons available for detection. Ignoring background (solar/lunar) and electronic noises, this Poisson count rate yields an estimated SNR of $\sqrt{N_\gamma} \approx 30$: enough leeway for losses by optical throughput, quantum efficiency, an aperture less than 1 cm^2 and/or a FOV reduced from 2π sr. We therefore anticipate all the signals predicted in Fig. 5.13 to be measurable with

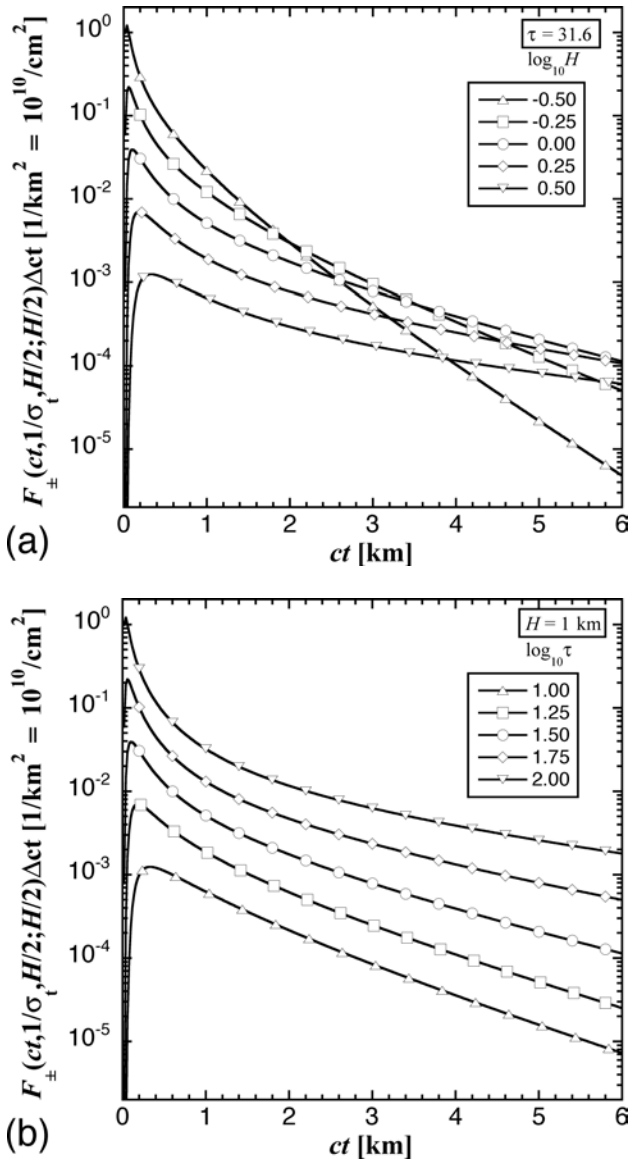

Fig. 5.13. *Sensitivities of in situ lidar signal to changes in cloud thickness H and optical depth τ.* As a surrogate for flux captured by a large (but still practical) FOV, we use here hemispherical fluxes estimated at mid-cloud. Both H and τ are varied over one order-of-magnitude around a typical value: $H = 1$ km in upper panel (a) and $\tau = 31.6$ in lower panel (b). Other parameters used to estimate $F_{\pm} = J/4$ from (7.1) are $\chi = 2/3$ and $g = 0.85$ to compute τ_t, hence σ_t and D; we also assume a finite path bin Δct of 20 m. The presence of a maximum signal at finite time reflects the offset of the detector from the effective origin of the pulse, which is represented here by a effective isotropic point-source. The late-time exponential decay and even the details of the approach to this asymptotic behavior are known to be accurate in the present diffusion model for dense enough clouds, cf. Fig. 5.12.

current lidar technology. Evans et al. [116] did just that (with a detector that had an effective aperture of ≈20 cm^2 and a quantum efficiency estimated to be ≈0.1.) and they successfully inferred cloud thickness and volume-averaged extinction. Validation was conveniently done by executing a 'porpoising' flight pattern where the aircraft goes in and out of cloud base and cloud top.

With variable vertical positions (z, z_0) restored, as in (6.8), plus the possibility of $\rho > 0$ already exercised in Fig. 5.13, this model can be applied to a conceptually simple cloud observation system based on miniaturized (for example, efficient fiber-laser) sources and detectors flying inside the cloud, but now on two or more separate unmanned aerial vehicles (UAVs). This would enable sufficient sampling of the cloud's Green function, in both t and ρ, to retrieve the standard set of *in situ* lidar unknowns $\{z, (1-g)\sigma, H\}$, given $(\overrightarrow{\rho}, z_0 - z)$ from accurate *relative* GPS positioning; cloud base altitude would of course follow from *absolute* GPS estimation of the altitude of the various aircraft. We anticipate that $F_z = F_+ - F_-$, obtained by differencing signals from up- and down-looking radiometers, will be sensitive to z (assuming $z_0 \approx z$); $F_z \approx 0$ would mean near the center of the cloud ($z \approx H/2$), and proximity to the $z = 0$ and $z = H$ boundaries signaled by different signs. Last but not least, these slow-moving platforms would enable longer time-integrations, hence improved SNRs; we indeed expect integration will compensate for the diminished transmitted and received power due to size/weight limitations. Another possibility is to outfit UAVs with stand-alone high-resolution spectrometers dedicated to the A-band of O_2 (dispersive devices can be made very compact).

We now show that this is indeed a passive (no-laser-required) approach to time-domain information. Imagine a uniform pulsed source incident at cloud top with some zenith angle $\cos^{-1}\mu_0 \geq 0$. The basic theory for the absorption spectrum (i.e., uniform gas with variable absorption) is laid out in section 5.5.5 and the associated Appendix D. However, we now broaden our interest from internal fluxes to those at the cloud boundaries, specifically about how they depend on cloud properties.

5.8 Temporal Green functions applied to oxygen A-band spectroscopy of overcast skies

5.8.1 A-band spectroscopy as observational time-domain RT

Oxygen A-band (759–771 nm) spectroscopy has attracted interest in atmospheric remote sensing for at least four and a half decades. The earliest discussions [117–119] were already about using it systematically for cloud observations from space, and the earliest A-band cloud data was indeed collected with a hand-held camera aboard Gemini 5 [120,121]. Multiple scattering effects were considered from very early on, especially in the Former Soviet Union [34,35], first in modeling and eventually in data analysis. Both airborne instruments and spectral models progressed steadily in the United States [122,123], Europe [124,125] Japan [126,127], and FSU [128–147]. The oxygen B-band (c. 687 nm) was also investigated, for example, in Ref. [123].

We are dealing here with a typical differential absorption spectroscopy that tells us how much O_2 was cumulated along the optical path of the light dispersed across

wavelengths. The lower panel of Fig. 5.14 illustrates the fine spectral structure of the A-band with its absorption optical depth across an assumed low-level cloud layer. The upper panel shows examples of simulated spectra for typical clear and cloudy conditions over a dark ocean surface as observed in reflection, normal viewing with a 60° solar zenith angle (SZA); the inset gives the values of the corresponding nadir radiance in the continuum.[31]

What can one do with knowledge of exactly how much of a major gaseous constituent is in the optical path? Some early proposals were to determine atmospheric pressure in remote locales, especially over oceans where there is a dearth of surface stations and radiosonde data, the driving application being numerical weather prediction.[32] It quickly became clear that atmospheric scattering was a wild card in this proposition. The optical path is not always straight down from the sun through an oblique airmass followed by another airmass (say) straight up to a spectral detector. There are both longer and shorter paths because of atmospheric scattering. Details of the line profiles thus depend on the amounts of aerosol, cloud, etc.

It was soon realized that this nuisance could be turned around and exploited to study the scattering components of the atmosphere. One can possibly quantify and qualify the aerosol load, from ground or from space. Concerning clouds, A-band spectroscopy was first thought to be a means of deriving cloud-top pressure using the same logic as for the original idea of measuring surface pressure. This concept also proved problematic because clouds are not optically 'hard' targets. In fact, they are optically speaking very 'soft' in that incident light can permeate the whole cloud before being reflected, i.e., returned from possibly very deep inside the cloud back to the illuminated boundary. Single- and multiple-scattering are of course the mechanism for reflection, as well as for diffuse transmission. Current modeling of reflected A-band signals fully and accurately accounts for multiple scattering [150–155], and more and more includes 3D RT effects [156–158]. As will soon become obvious, the standard retrievals from A-band data are cloud-top pressure and cloud (pressure) thickness.

In this study, we take the standpoint that O_2 A-band spectroscopy at high resolution is a portal to time-domain radiative transfer in clouds, but using steady sources. This powerful connection is encapsulated in the so-called equivalence theorem already discussed in differential form in section 5.3.1. This relation states that, if we know the time-dependent radiance field $G(t, \boldsymbol{x}, \boldsymbol{\Omega})$ resulting from a sudden burst of light in an arbitrary scattering medium, then we can predict the radiance that would be observed at the same point in the presence of a uniform gas with a variable absorption coefficient $\kappa_\nu > 0$.

[31] We note that the A-band sits at the peak of the solar spectrum when reckoned in photons/s/m^2 (as opposed to W/m^2), which is optimal for the SNR.

[32] The competition for cloud-top height retrieval from remote sensing data at large comes (1) from signatures in thermal bands (sometimes called 'CO_2 slicing') [148], but the atmosphere's thermal structure varies far more than its pressure profile, and (2) from direct geometric method using multi-angle imaging [149], which is foolproof as long as the clouds have enough 'texture' for automated stereo matching. Because of the time-delay between the observations of a given cloud at different angles (as the satellite moves along its orbit), the latter method furthermore provides mean wind at the cloud-top altitude.

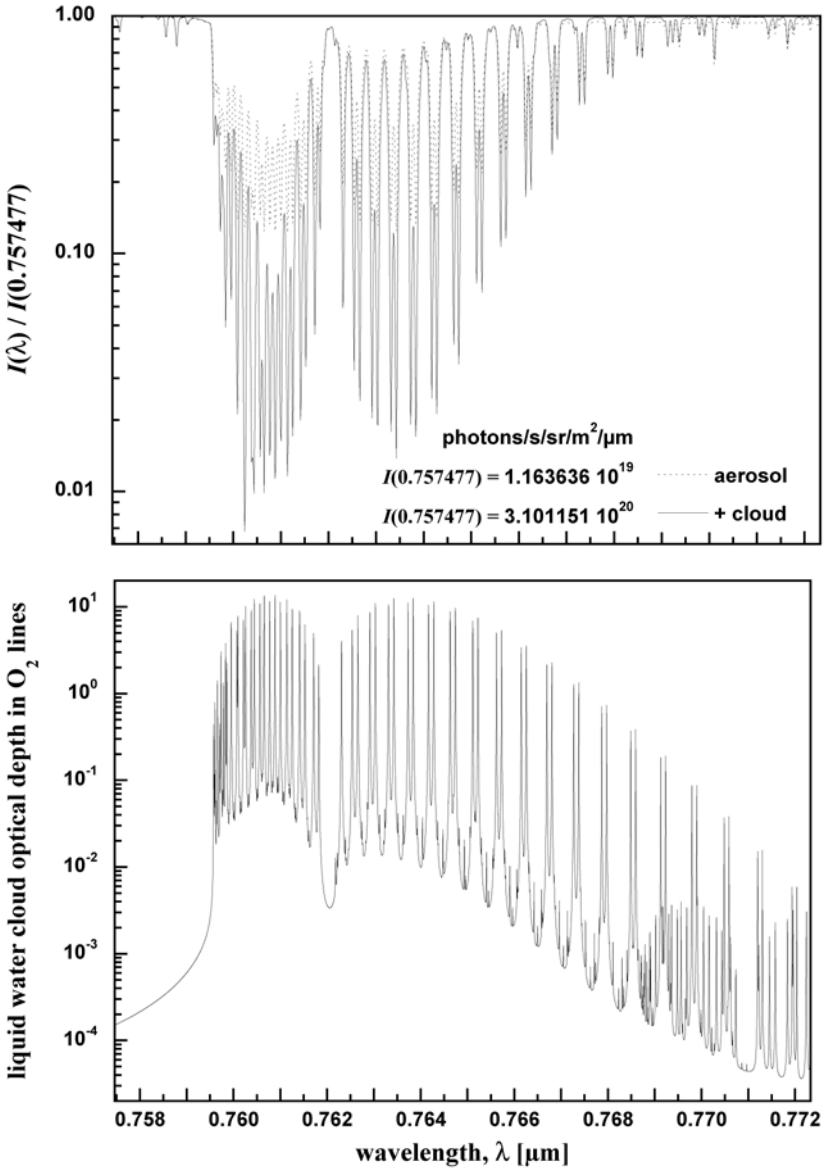

Fig. 5.14. *Simulated O_2 A-band spectra in reflection.* Bottom: Fine structure of the A-band displayed using, as a relevant example, the O_2 optical thickness across a layer from 860 to 911 hPa (c. altitudes 0.85 and 1.3 km), where one could find a typical low-level cloud. Top: The reference spectrum is for a background aerosol atmosphere above an ocean surface (Cox-Munk BRDF for 5 m/s wind speed). The other is for the same situation plus a liquid water (Mie scattering) cloud between 911 and 860 hPa with optical depth 64. Line-by-line computations were coarsened to the 0.0146 nm resolution of the Orbiting Carbon Observatory (OCO) spectrometer. Both spectra were normalized to maximum radiance (given, for reference, in the inset). Computations were kindly provided by Dr Hartmut Bösch (University of Leicester, Dept. of Physics & Astronomy, Earth Observation Science, Space Research Centre).

Formally, we let L denote the *a priori* random path that the light has followed in the medium. Then the optical path for gaseous absorption is $\kappa_\nu L$ and Beer's law of exponential extinction states that light with path L is absorbed with probability $\exp(-\kappa_\nu L)$. In summary, for a fixed κ_ν, radiance is[33]

$$I(\kappa_\nu, \boldsymbol{x}, \boldsymbol{\Omega}) = \frac{1}{c} \int_0^\infty G(L/c, \boldsymbol{x}, \boldsymbol{\Omega})\, \mathrm{e}^{-\kappa_\nu L}\, \mathrm{d}L. \tag{8.1}$$

The different absorption values are realized at different wavelengths λ, equivalently, frequency c/λ or (more conventionally) wavenumber $\nu = 10^7/\lambda$ in cm^{-1} when wavelength is expressed in nm. We have thus assumed up front that the coefficient κ_ν is a function of wavenumber ν, in compliance with spectroscopic tradition. At any rate, we recognize in (8.1) the Laplace side of (3.1) with radiance rather than flux and identifying κ_ν with s/c. So, as in (3.2), we can compute path moments using the spectrometry:

$$\langle L^q \rangle = \frac{1}{I(0, \cdots)} \left(-\frac{\partial}{\partial \kappa_\nu} \right)^q I(\kappa_\nu, \cdots) \Big|_{\kappa_\nu = 0}, \tag{8.2}$$

where the normalizing factor is simply radiance in the continuum near the A-band.

Conveniently, all of our diffusive temporal Green function theory has ended up in Laplace space, or at least used it as a stepping stone. We can therefore obtain, after the usual radiance-to-flux conversion, empirical estimates of $\hat{F}(s) = \tilde{F}(s, 0)$. Identification of observed and theoretical estimates of radiative properties is of course an opportunity for cloud remote sensing: retrieval of cloud parameters, for example, $\{H, \tau\}$, by standard fitting procedures. Once we have a theoretical fit, one can derive other cloud radiative properties such as the temporal/path-length moments in (8.2). Another possibility is to use the observed $\hat{F}(s) = I(\kappa_\nu, \cdots)/I(0, \cdots)|_{\kappa_\nu = s/c}$ in (8.2) to derive the path-length moments directly. In practice, both groups currently engaged in high-resolution A-band spectroscopy from ground (SUNY-Albany [160–163] and University of Heidelberg [159, 164, 165]) use a convenient parameterization of $\hat{F}(s)$ using the first two moments of L, namely,[34]

$$\hat{F}(s) \approx \frac{1}{(1 + \langle L \rangle s/ca)^a}, \text{ where } a = \frac{1}{\langle L^2 \rangle / \langle L \rangle^2 - 1}.$$

Both of these approaches avoid the problem of inverse Laplace transforming noisy data from instruments, a numerical process known to be highly unstable.

A third group, from NOAA, has performed ground-based spectroscopy of oxygen under cloudy skies at somewhat lower resolution and focusing on the γ-band of

[33] We assume in (8.1), purely monochromatic RT. No forward model for A-band spectroradiometry is complete without a convolution of this expression with the spectrometer's 'slit function'. This issue of spectral resolution, as well as out-of-band rejection, is absolutely critical to the *a priori* estimation of how many pieces of path-length/cloud information can be extracted robustly from the radiometric data [159, 160].

[34] This leads back to a Gamma distribution of path-lengths, cf. (10.1)–(10.2) with τ replaced by L. We owe to van de Hulst [166] the original idea of approximating the temporal Green functions with Gamma distributions.

O_2 (c. 628 nm) [167]. Following previous work on low-resolution A-band observations from space, they preferred to directly compare their spectroscopy to a forward 1D RT model (adapted from [168]) with an assumed cloud, which they varied to fit the data. Another interesting development from the NOAA group was to adapt their instrumentation and RT model to work with the spectrally much smoother absorption features of cloud droplets in the near-IR (0.9 to 1.7 μm). Because absorption cross-section (where it exists) is $\propto$ droplet volume, Daniel et al. [169] were able to retrieve liquid water path (LWP).

It is important to bear in mind that a forward model for A-band spectroscopy will have more than just the component for in-cloud multiple scattering we have just described. However, the other contributions are essentially deterministic. Consider a narrow FOV ground-based instrument measuring zenith radiance. The spectrum is formed, on the one hand, by the cloud's temporal multiple-scattering Green function by identifying s with $c\overline{\kappa_\nu}$ (a pressure-weighted average over the cloud layer) in the Laplace transform for transmitted light; on the other hand, this contribution must be convolved with two degenerate (zero-variance) distributions of optical path through the absorbing gas, namely, $\tau_\nu^{(\mathrm{a})}/\mu_0$ and $\tau_\nu^{(\mathrm{b})}$, the absorption optical depths of the above- and below-cloud layers respectively. Now, in Laplace/κ_ν-space, the convolutions translate to simple products and the two δ-like path distributions transform to constants, $T_\nu^{(\mathrm{a})} = \exp(-\tau_\nu^{(\mathrm{a})}/\mu_0)$ and $T_\nu^{(\mathrm{b})} = \exp(-\tau_\nu^{(\mathrm{b})})$. In summary, the forward model for the spectroscopy is

$$I(\kappa_\nu) = I(0) \times \hat{T}(c\overline{\kappa_\nu}) \times \mathrm{e}^{-\left(\tau_\nu^{(\mathrm{a})}/\mu_0 + \tau_\nu^{(\mathrm{b})}\right)}.$$

For light reflected back to an instrument on an aircraft or satellite with oblique viewing capability, the forward model is

$$I(\kappa_\nu) = I(0) \times \hat{R}(c\overline{\kappa_\nu}) \times \mathrm{e}^{-(1/\mu_0 + 1/\mu)\tau_\nu^{(\mathrm{a})}}.$$

Substitution of these models into the expression (8.2) for path moments will of course yield the moment based on $\hat{F}(s)$, for $F = T$ or R, but offset by a known constant. Alternatively, one can correct the data for the spectral offsets before computing the path moments or retrieving cloud properties directly.[35]

In the remainder of this section, we will exploit a subset of our explicit Laplace-space solutions (from section 5.5) for the temporal Green function to assess the cloud information content of O_2 A-band data. Specifically, we will formally identify the random light path L through the absorbing gas with ct, the path covered between emission from a δ-in-time boundary source and escape in transmission ($F = T$) or in reflection ($F = R$). We will then determine the dependence of path moments $\langle (ct)^q \rangle_F$ ($F = T, R$, $q = 1, 2$) on cloud properties, which we have not yet done in framework of diffusion, and we will continue to validate the diffusion model with MC simulations. These are in essence the observables in O_2 A-band spectroscopy. Spatial moments $\langle \rho^2 \rangle_F$ also play a role. Insights from this kind of *a priori* cloud information content analysis are useful in planning for remote sensing mission objectives as well as in the development of retrieval algorithms.

[35] The contributions of multiple reflections between the cloud and the surface can also be added, recalling that green vegetation can have a relatively high albedo at A-band wavelengths; see Scholl et al. [165].

5.8.2 Path-length moments from below

5.8.2.1 Isotropic boundary point-source

Using the same assumptions as in our 2002 paper [24] investigating light transmitted by the cloud to a ground-based sensor, we start with the simple diffusion model based on an isotropic boundary point-source. Applying (3.5) and (3.2) to (5.8) with all ancillary definitions, we find

$$\langle ct\rangle_T/H \;=\; \frac{1}{2}\,\tau_{\rm t} \times \Big[1 + C^{(1)}_{T,ct}(\tau_{\rm t}/2\chi)\Big]\,, \tag{8.3}$$

$$\langle (ct)^2\rangle_T/H^2 \;=\; \frac{7}{20}\,\tau_{\rm t}^2 \times \Big[1 + C^{(2)}_{T,ct}(\tau_{\rm t}/2\chi)\Big]\,, \tag{8.4}$$

$$\langle \rho^2\rangle_T/H^2 \;=\; \frac{2}{3} \times \Big[1 + C^{(2)}_{T,\rho}(\tau_{\rm t}/2\chi)\Big]\,, \tag{8.5}$$

for three low-order moments of interest, all normalized by H. We have highlighted here the asymptotic trends. The pre-asymptotic correction terms are given by

$$\begin{aligned} C^{(1)}_{T,ct}(\xi) \;&=\; C^{(2)}_{T,\rho}(\xi) = (4\xi+3)/2\xi(\xi+1), \\ C^{(2)}_{T,ct}(\xi) \;&=\; (56\xi^3 + (166\xi^2 + 15(10\xi+3)))/14\xi^2(\xi+1)^2, \end{aligned}$$

recalling that $\xi = \tau_{\rm t}/2\chi$. The leading terms made explicit in (8.3) and (8.5) make sense from the random-walk perspective on diffusion exposed in Appendix E wherein the scaling exponents of $\tau_{\rm t}$ are derived. However, in all cases, pre-factors and pre-asymtotic corrections terms in (8.3)–(8.5) call for the PDE-based approach promoted throughout this review.

It is worthwhile to compare these results with those provided by Zege et al. [83]. In their Section 4.8 on pulsed sources, their Eq. (4.8.38) gives, in our notations, the same asymptotic trends for $\tau_{\rm t} \gg 1$ and $\ll 1$ for mean *optical* path $\sigma\langle ct\rangle_T$ as in (8.3): respectively, we find $(1-g)\tau^2/2$ (irrespective of χ) and $(3\chi/2)\tau$ ($= \tau$ when $\chi = 2/3$).[36] Zege et al.'s same equation gives the trend of the st.dev. $\sigma\sqrt{\langle (ct)^2\rangle_T - \langle ct\rangle_T^2}$ of the optical path when $\tau_{\rm t} \gg 1$; in our notations, it yields a pre-factor of 11/20 rather than 7/20 in (8.4). We interpret this discrepancy as the result of requiring only second-order accuracy in $m(s,k)$ for (6.21), on which their temporal moment computations are predicated; to obtain the correct trend for $\langle(\sigma ct)^2\rangle_T$, one needs fourth-order accuracy in $m \sim \sqrt{s}$ when $k = 0$. Finally, Zege et al.'s counterpart of (8.5) is in their Table 4.1 and follows from Ref. [46]. That paper by Bushmakova et al. generalizes to anisotropic scattering the studies by Romanova in Refs [44, 45] that focused on the case of $g = 0$. In our notations, the early prediction is $\langle(\sigma\rho)^2\rangle_T \approx \tau/3$ when $\tau_{\rm t} \gg 1$, irrespective of g and χ. We find twice that value. It is not clear where this systematic difference comes from

[36] The relation $\langle ct\rangle_T \approx H = \tau/\sigma$ for vanishing σ (hence τ) makes intuitive sense: most of the light goes straight through the medium in direct transmission. However, a straightforward *flux*-based estimate of mean path for light transmitted through an optical vacuum of thickness H under isotropic illumination is $2H$ (and, interestingly, the RMS path is divergent). This serves as a reminder (cf. section 5.4.3) that the effective value of χ for optically thin media ($\tau_{\rm t} \ll 1$) is 4/3.

but we will see further on that it occurs again with $\langle(\sigma\rho)^2\rangle_R$, for reflected light, and that our MC simulations agree with our diffusion estimates for both transmission (Fig. 5.15) and reflection (Figs 5.18 and 5.21). We suspect that the factor of 2 in (3.5), which is nontrivial, may have been omitted.

Figure 5.15 shows the low-order moment predictions in (8.3)–(8.5), making RMS values out of second-order moments; this suite is augmented with the zeroth-order transmission term T in (5.5) for the classic two-stream model corresponding to the $s/c, k \to 0$ limit of this case. MC simulations of the same transport problem, including the isotropic boundary point-source, using H–G and isotropic phase functions show excellent agreement with the diffusion model, as long as the proper χ-value is used. We note however that χ is not present in the leading terms of the moments in (8.3)–(8.5).

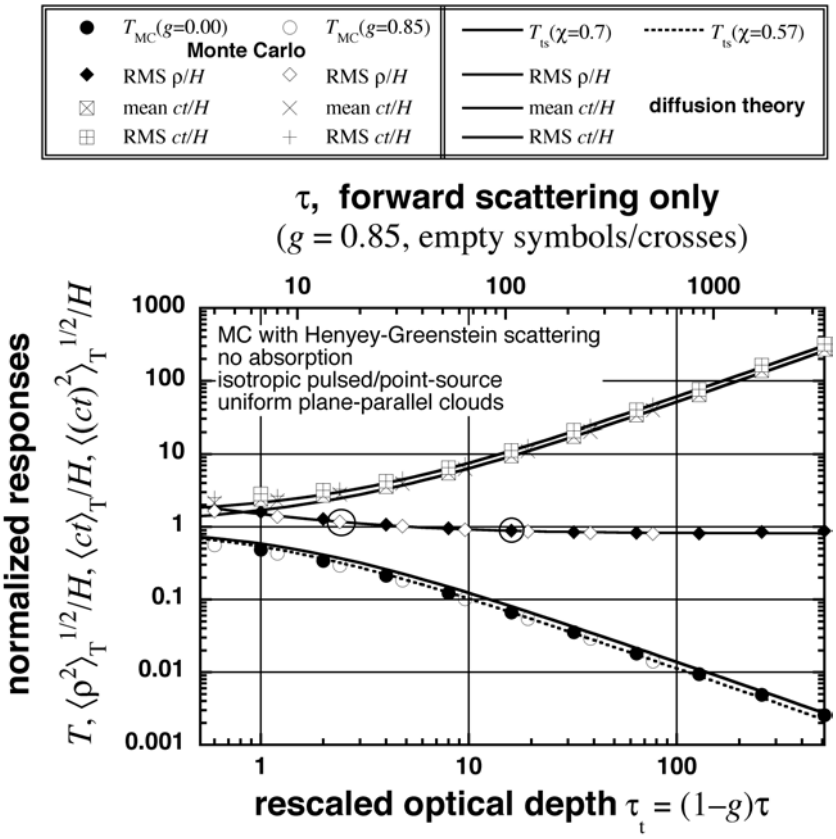

Fig. 5.15. *Cloud responses to a pulsed isotropic point-source in transmission.* Diffusion predictions from (8.3)–(8.5), with correction terms, and (5.5) are in solid lines; MC validation data are plotted with symbols (two values of χ used to reproduce the MC benchmarks). The circled points identify parameters used for the space-only case studies in Fig. 5.9. We note the striking similarity between the two temporal moments. Adapted from Ref. [24].

What do these moments tell us about O_2 A-band spectroscopy from ground? The fact that we have $\langle (ct)^2 \rangle_T \approx (7/5)\langle ct \rangle_T^2$ over the whole range of τ_t, i.e., that one moment predicts the other one, is not good news for cloud property remote sensing with stand-alone O_2 A-band sensors. If we can somehow merge the time-domain A-band data with a spatial methodology that yields $\langle \rho^2 \rangle_T$ (cf. section 5.10.6) or conventional radiometry *with absolute calibration* that yields T, then we are in a far better position. Indeed, the fact that we have different asymptotic scaling exponents for all three observables (including a null exponent for $\langle \rho^2 \rangle_T$) makes it at least theoretically possible to determine τ_t, say, from T and then H from the measured value of, say, $\langle ct \rangle_T$ and the non-dimensional ratio in (8.3).

Even if there is no direct empirical estimate of $\langle \rho^2 \rangle_T$ because the sun is a uniform source, the utility of (8.5) is to inform other retrievals (A-band or radiometric) about their *minimum* effective spatial resolution. It is indeed the fundamental radiative smoothing scale [170] for the transmitted light field [24], below which spatial details are lost for the remote observer due to horizontal radiative transport caused by multiple scattering. In ground-based cloud remote sensing, spatial sampling is determined by temporal sampling Δt and the mean wind $\overline{v}$ at cloud level – Taylor's classic 'frozen turbulence' hypothesis. For instance, if $\overline{v}\Delta t < \sqrt{\langle \rho^2 \rangle_T} \sim H$, then there is redundancy in the spatial sampling.[37] This redundancy can be viewed as desirable or not, depending on circumstances. A case were spatial redundancy is counter-indicated is when compiling statistics that target spatial correlations.

5.8.2.2 Stratification effects

We showed in section 5.5.2 that the above model could be generalized to clouds endowed with internal stratification according to the linear (constant gradient) model in (2.27). Should we worry about this issue in ground-based O_2 A-band spectroscopy?

We are here in the case of $-2 < \Delta < 0$ in the upper panel of Fig. 5.5 (gray curves only), which plots MC results for an isotropic point-source at $z = 0$ and distributed flux detectors at $z = H$, In passing, we note that the converse ($0 < \Delta < +2$) yields the same answer, by optical reciprocity. We see that, for the prescribed cloud ($\tau = 15$, $g = 0.46$), the spatial statistic in (8.5) is essentially unaffected by stratification, but there is a $\sim$10% effect in the time-domain properties of primary interest here in (8.3)–(8.4). In many modeling applications, this level of accuracy is worth pursuing.

Further computer-assisted algebra based on the solution presented in section 5.5.2 (and Appendix A), following the same guidance as above, leads to

[37] This estimate of the smoothing scale is for ground-based *narrow* FOV radiometry. That is indeed how one can access radiance, hence flux, at the lower cloud boundary. In ground-based radiometry with a *wide* FOV (for example, 2π sr, hemispherical flux sensors), the same rule applies but $\langle \rho^2 \rangle_T$ must account for the extensive horizontal transport in the sub-cloud layer. Being about a fundamentally *non*-diffusive transport process, this problem is out of scope for the present review.

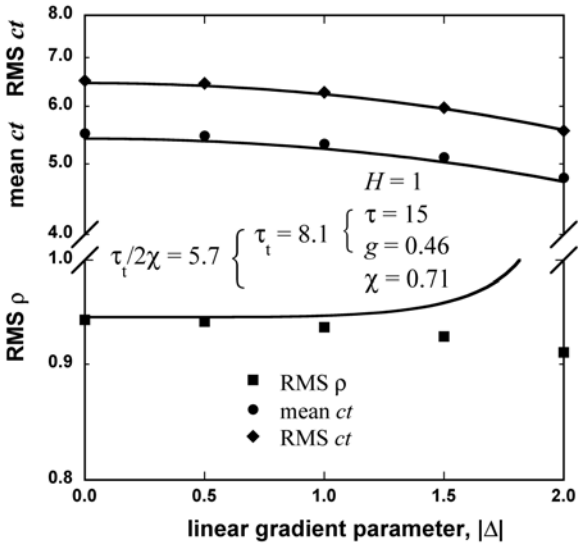

Fig. 5.16. *Effects of stratification on Green functions for transmission.* Diffusion predictions for the prescribed cloud ($\tau_t = 8.1$) are in solid lines; they were obtained from (8.6)–(8.8), including correction terms, with $\chi = 0.71$. MC validation data are plotted with symbols; they are extracted from Fig. 5.5, gray curves in upper panel. We note the nearly flat behavior of $\langle \rho^2 \rangle_T$ away from $|\Delta| = 0$ and up to the onset of the logarithmic singularity at $|\Delta| = 2$ in (8.8), which is discussed in the main text. This is because the prescribed cloud, with $\tau_t/2\chi = 5.7$, happens to be very close to $(5+\sqrt{35})/2 = 5.46\cdots$, the value that cancels the coefficient of Δ^2 in (8.9). For larger values of $\tau_t/2\chi$, the diffusion model for stratification will improve with respect to MC results, and for smaller values it is expected to worsen.

$$\langle ct \rangle_T / H = \left(\frac{1}{2} - \frac{\Delta^2}{40} \right) \tau_t \times \left[1 + C^{(1)}_{T,ct}(\xi, \Delta^2) \right]_{\xi = \tau_t/2\chi}, \tag{8.6}$$

$$\langle (ct)^2 \rangle_T / H^2 = \left(\frac{7}{20} - \frac{\Delta^2(30 - \Delta^2)}{800} \right) \tau_t^2 \times \left[1 + C^{(2)}_{T,ct}(\xi, \Delta^2) \right]_{\xi = \tau_t/2\chi}, \tag{8.7}$$

$$\langle \rho^2 \rangle_T / H^2 = \frac{1}{4} \left(\left[\left(\frac{2}{\Delta} \right)^2 - 1 \right]^2 \frac{\Delta}{2} \ln \sqrt{\frac{1 - \Delta/2}{1 + \Delta/2}} + \left[1 + \left(\frac{2}{\Delta} \right)^2 \right] \right) \times \left[1 + C^{(2)}_{T,\rho}(\xi, \Delta^2) \right]_{\xi = \tau_t/2\chi}, \tag{8.8}$$

which are all symmetric in Δ and lead back to (8.3)–(8.5) in the limit $|\Delta| \to 0$. Figure 5.16 shows how well the full expressions reproduce the MC results from the gray curves in the upper panel of Fig. 5.5. Overall, the diffusion results are just slightly offset from their MC counterparts.

The most remarkable difference between the diffusion and MC predictions in Fig. 5.16 is the logarithmic divergence of $\langle \rho^2 \rangle_T$ at $|\Delta| \to 2$ that is manifest in (8.8). All is as if the *effective* diffusivity constant $\langle \rho^2 \rangle_T / \langle t \rangle_T$, as observed at the cloud boundary (in this case, opposite the δ-source), becomes infinite with the value of the transport MFP at $z = 0$ or $z = H$, for example, $\ell_t(0) = 1/\overline{\sigma}_t(1 - \Delta/2)$.

Diverging ℓ_t is clearly a challenge for diffusion models since trajectories become more ballistic within a transport MFP of cloud boundaries.[38] However, this spatial statistic is only of marginal importance in O_2 A-band observations. We therefore recommend using the uniform cloud ($\Delta = 0$) estimate of $\langle\rho^2\rangle_T$ when and where needed. If more accuracy is needed, one can expand (8.8) in a short series with respect to Δ:

$$\langle\rho^2\rangle_T/H^2 = \left(\frac{2}{3}\right)\frac{\xi(\xi+3)+3/2}{\xi(\xi+1)} - \frac{2\xi(\xi-5)-5}{60\xi(\xi+1)}\Delta^2 + O(\Delta^4), \qquad (8.9)$$

recalling that $\xi = \tau_t/2\chi$. The full variation of $\langle\rho^2\rangle_T$ in diffusive clouds is quite small anyway, cf. MC results in Fig. 5.15. Although there is less and less light to speak of, diffusion becomes quasi-exact deep inside the medium when $\tau_t \gg 1$. In this limit, $\langle\rho^2\rangle_T$ is $\approx 2/3$ when $\Delta = 0$ and using (8.8), with correction term, one can show that this moment becomes $\approx 1/2$ when $|\Delta| = 2$ in the same limit. For a start, the two terms in (8.9) yield 8/15 when $\xi \to \infty$. The range in RMS ρ is even smaller.

5.8.2.3 Uniform oblique collimated illumination

It is of interest to go beyond isotropic sources in A-band transmission studies since solar illumination comes at a specific incidence depending on geographic location, season, and time of day. This can be done for uniform sources using the model introduced in section 5.5.5 (supplemented by Appendix D).

The same steps as in the previous section are followed: obtain $\hat{T}(s)$ from $\hat{J}(s, z = H)/2\mu_0$; expand into a short Taylor series at $s = 0$; estimate low-order moments from coefficients of s^q. We find that the scaling, including pre-factors, for $\tau_t = (1-g)\tau$ in (8.3)–(8.4) is unchanged, but that the pre-asymptotic correction terms are affected. In other words, the simple expression for $C^{(q)}_{T,ct}((1-g)\tau/2\chi)$ becomes a rather complex expression $C^{(q)}_{T,ct}(\tau, g, \mu_0)$ for $q = 1, 2$.

This SZA-independence of the leading terms is not too surprising since we are characterizing light that has filtered through an optically thick medium, and is therefore almost always highly scattered. Recall that memory of the initial direction of propagation is all but forgotten after ∼1–2 transport MFPs. Clouds with diffusive RT regimes have $H \gtrsim 1$ transport MFP, so only a subtle dependence on μ_0 is expected in the transmitted radiation emerging at $z = H$. Figure 5.17 illustrates for $g = 0.46$ the effects of SZA on the first two moments of path ct. These plots show us where in $\{\tau, \mu_0\}$ parameter space and what is the magnitude of the difference with the isotropic source prediction.

5.8.3 Path-length moments from above

To summarize so far, we have established that ground-based O_2 A-band spectroscopy is poised to become a valuable asset in cloud remote sensing as long as

[38] This problem could probably be fixed by introducing an ad hoc parameterization $\chi(\Delta)$ where $\chi \to 0$ as $|\Delta| \to 2$.

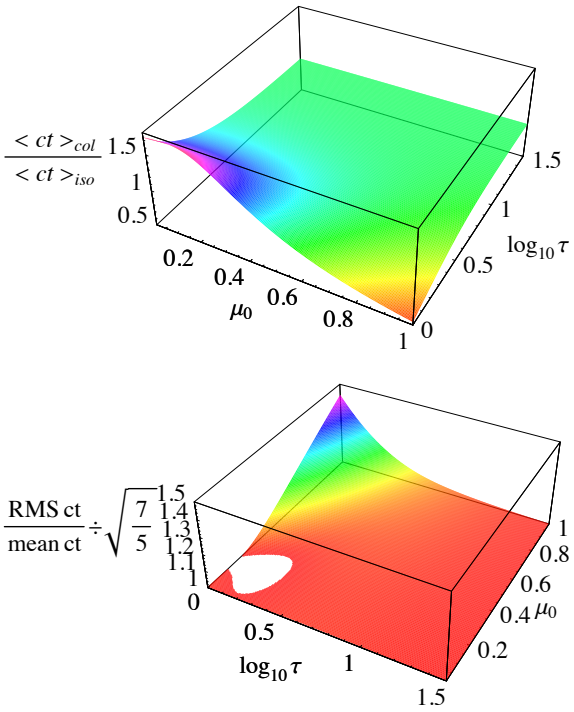

Fig. 5.17. *SZA dependence of temporal moments for light transmitted through diffusive clouds.* Rescaled optical depth τ for such clouds must exceed unity using the rescaled $g = 0.46$ (original τ, for $g = 0.85$, is then 3.6× more); we explore up to $\tau = 10^{1.5}$ (≈114 for $g = 0.85$). The upper panel addresses predictions for mean path $\langle ct \rangle_T$ and ranges from 0.5 to 1.8; we see very little difference between the collimated and isotropic sources for any μ_0 when $\tau \gtrsim 3$ (11 for $g = 0.85$), less if $\mu_0 \approx 1/2$. The lower panel compares the RMS/mean ratio for ct with the quasi-constant prediction for isotropic illumination, namely, $\sqrt{7/5} = 1.183\cdots$ (cf. Fig. 5.15). The variation is only from 1 to 1.5, and we see deviations only when $\tau \lesssim 3$ and $\mu_0 \gtrsim 1/2$ (SZA less than about 60°). The ratio for collimated beams slightly exceeds the isotropic value for all but a small area of low τ under near-grazing incidence angles.

cloud morphology is approximately plane-parallel. When cloud geometry is far from plane-parallel, O_2 A-band spectroscopy can be used in cloud-radiation diagnostics that probe the complex (and highly climate-relevant) process of gaseous absorption in the presence of 3D clouds [161, 163–165]; see Appendix F for a brief description.

At the time of writing, a satellite mission with high-resolution oxygen A-band capability is being prepared for launch in early 2009: the Orbital Carbon Observatory (OCO) [171]. Space-based precursors of OCO with A-band coverage at lower resolutions – but sufficient to initiate cloud studies – are POLDER/Parasol [172], GOME [173], and SCIAMACHY/ENVISAT [174]. There are also opportunities for airborne O_2 A-band at high resolution from above the clouds, for example, the Langley Airborne A-Band Spectrometer (LAABS) instrument. It is therefore timely to hone our predictive skills for A-band products for clouds when observed from above, namely, path-length moments $\langle (ct)^q \rangle_R$ ($q = 1, 2, \ldots$).

We will start our investigation of reflected light, as we did for transmission, with the simple diffusion model for isotropic illumination of a uniform plane-parallel cloud. We will then examine the effects of internal stratification. While the emphasis is on temporal responses, we will keep a tangential interest in spatial properties. Finally, we turn to SZA effects strictly in the time-domain.

5.8.3.1 Isotropic boundary point-source

A bare-bones model for radiative Green functions was introduced in section 5.5.1 using an isotropic pulsed source at a boundary point. Davis et al. [85] and Love et al. [86] developed this model with multiple-scattering cloud lidar in mind – an application to discussed in the next section. However, some of the time-domain signals of this active remote sensing technology and O_2 A-band cloud products are indistinguishable from the Green function perspective. We are thinking here of low-order moments of in-cloud path-lengths for reflected light.

The simple diffusion model predicts the following dependencies on cloud properties:

$$\langle ct\rangle_R/H \;=\; 2\chi \times \left[1 + C^{(1)}_{R,ct}(\tau_t/2\chi)\right], \tag{8.10}$$

$$\langle (ct)^2\rangle_R/H^2 \;=\; \frac{4\chi}{5}\,\tau_t \times \left[1 + C^{(2)}_{R,ct}(\tau_t/2\chi)\right], \tag{8.11}$$

$$\langle \rho^2\rangle_R/H^2 \;=\; \frac{4}{3}\left(\frac{2\chi}{\tau_t}\right) \times \left[1 + C^{(2)}_{R,\rho}(\tau_t/2\chi)\right], \tag{8.12}$$

where

$$C^{(1)}_{R,ct}(\xi) \;=\; C^{(2)}_{R,\rho}(\xi) = (\xi + 3/2)/2\xi(\xi+1),$$
$$C^{(2)}_{R,ct}(\xi) \;=\; (8\xi^3 + 41\xi^2/2 + 75\xi/4 + 1/8)/2\xi^2(\xi+1)^2.$$

We use here the same definition for ξ as in (5.11). Figure 5.18 shows the outcome of the above model, in excellent agreement with MC validation data in the regime that matters ($\tau_t > 1$). Recalling that Monte Carlo simulation is grounded in random walk theory, it is in fact possible to perform a very simple form of MC simulation analytically. We can thus derive the various scaling exponents of the leading terms in (8.10)–(8.12) from heuristic arguments based on random walk (a.k.a. Brownian motion) theory; see Appendix E.

In contrast with the corresponding expressions for transmitted light in (8.3)–(8.5), we see that the idiosyncratic extrapolation length parameter χ in diffusion theory now affects the leading terms directly. We interpret this difference as a reminder that, in the case of optically thick (diffusive) cloud, the main physical difference between reflected and transmitted light is that the latter is almost always highly scattered while the former is a balanced mixture of low- and high-order scatterings. Light that has suffered only a few scatterings originates necessarily from the radiative boundary layer near the source. The present incarnation of diffusion theory uses χ to mitigate its known weakness in the boundary layer. Unsurprisingly, this 'signature' boundary condition parameter of diffusion theory appears in the leading terms of reflected characteristics, but not those of transmitted ones.

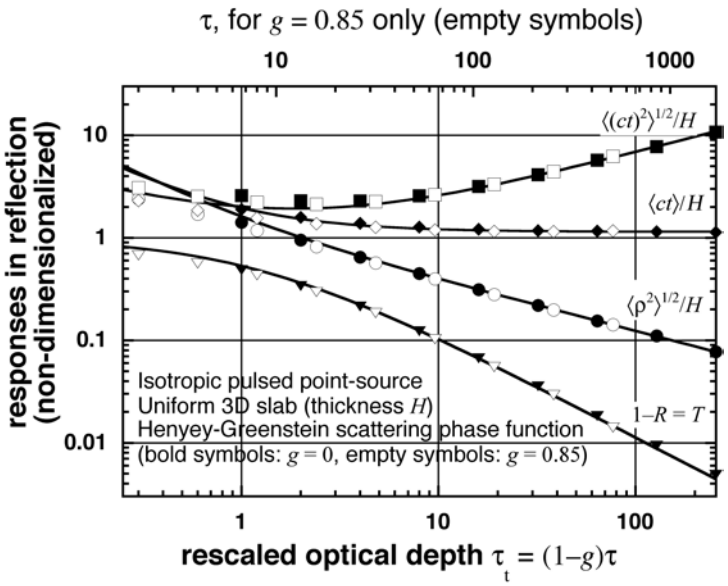

Fig. 5.18. *Cloud responses to a pulsed isotropic point-source in reflection.* Diffusion predictions from (8.10)–(8.12), with correction terms, and (5.5) are in solid lines; MC validation data are plotted with symbols. The best overall fit was obtained for $\chi = 1/\sqrt{3} = 0.577\cdots$. In contrast with the corresponding Fig. 5.15 for transmitted light, we see that the first- and second-order moments of path-length scale differently with τ_t (cf. Appendix E). This turns out to be an opportunity for active as well as passive cloud remote sensing. Adapted from Ref. [86].

As made clear in Appendix E, another consequence of the balanced mixture of low- and high-order scatterings in reflected light is the different scaling exponents for $\langle ct\rangle_R$ and $\langle (ct)^2\rangle_R^{1/2}$ with respect to τ_t. This gives a unique advantage to the cloud remote sensing application of O_2 A-band spectroscopy from above the observed cloud layer. Indeed, without any need for radiometric calibration, a stand-alone O_2 A-band spectrometer can now deliver two pieces of information from the two path-length moments in reflected light. The ratio $\langle (ct)^2\rangle_R / \langle ct\rangle_R^2$ is now a sensitive function of τ_t alone, which can be unambiguously inverted; from there, the known value of τ_t and the observed value of $\langle ct\rangle_R$ can be used in (8.10) to infer cloud thickness H.

As was the case for transmitted light, O_2 A-band spectroscopy alone does not give us access to information on the horizontal transport captured in $\langle \rho^2\rangle_R$. However, the predicted value in (8.12) gives us insight into the spatial resolution of the A-band spectroscopic cloud remote sensing process. We notice that, again because of the non-negligible contribution of lower orders of scattering to reflected light, $\langle \rho^2\rangle_R$ contracts as τ_t increases while $\langle \rho^2\rangle_T$ in (8.5) remains essentially constant, on the order of H^2. On the other hand, since reflected light also has non-negligible contributions from light that has diffused almost down to the non-illuminated boundary and back, the volume of cloud being sampled is effectively $\approx H^3$. We

will therefore retain H^2 as a reasonable estimate of the effective footprint of the A-band approach to cloud property retrieval.

Finally, we notice in Fig. 5.18 that the diffusion prediction for mean path exceeds the one for RMS path for scaled optical depths less than about unity (more precisely, $\tau_t/2\chi < 0.798$); this is a clear violation of Schwartz's inequality, as it applies to statistics, and is of course not observed in the corresponding MC results. This anomaly results ultimately from the fact that solutions of diffusion equations are not constrained by causality; probabilistically speaking, they need not have all the defining properties of characteristic (moment-generating) functions, even though we have used them as reasonable approximations thereof throughout this paper.

Although we have not found predictions for the temporal moments in (8.10)–(8.11) for reflected light in the early literature, we did find one for the variance of horizontal transport distance $\langle \rho^2 \rangle_R$ in Zege et al.'s [83] Table 4.1. That table is compiled from 1972 results by Bushmakova et al. [46] that generalize to cases with $g \neq 0$ results from Romanova's 1971 papers [44, 45] based on isotropic scattering. In our notations, they predict that $\langle (\sigma\rho)^2 \rangle_R \approx (8/9)\tau/(1-g)$ when absorption is weak and $\tau_t \gg 1$. We find precisely twice[39] that value when we set $\chi = 2/3$ in (8.12), 16/9 rather than 8/9. The origin of this factor-of-2 discrepancy is not clear, but our estimate is validated by high-precision MC simulations in Fig. 5.18. Since the same factor-of-2 difference was found for transmitted light in section 5.8.2, we speculate that it originates at a higher level, possibly with the nontrivial factor of 2 in (3.5).

5.8.3.2 Stratification effects

Looking back at the black curves in Fig. 5.5(top), we see that internal stratification matters for reflected light, more than for its transmitted counterpart. In particular, the impact of positive and negative gradients in the extinction (equivalently here, scattering) coefficient away from the illuminated boundary have opposite effects on all the space-time moments. This is sufficient numerical evidence for attempting to capture these effects in the diffusion framework. Moreover, in this observation geometry, we note that the stratification affects multiple-scattering cloud lidar (spatial moment) as well as O_2 A-band (temporal moments only). That is indeed what first motivated two of the present authors to develop in [92] the diffusion model described in section 5.5.2 that generalizes the above results to media with a linear gradient in extinction.

[39] We show further on that the pre-factor of τ_t is actually 20/9 for a *collimated* narrow beam normally incident on the cloud, as opposed to an isotropic boundary point-source, cf. (9.4) and Fig. 5.21. This extra offset is traceable to the term we incorporate in (4.14), hence in (5.15)–(5.16), for the anisotropy of the first-scattering source, i.e., the P_1 in the truncated phase function in (4.13).

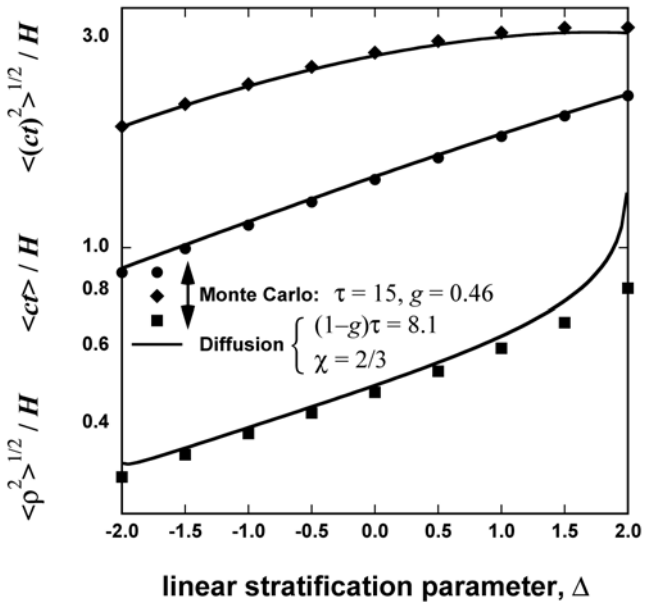

Fig. 5.19. *Effects of stratification on Green functions for reflection.* Diffusion predictions for the prescribed cloud ($\tau_t = 8.1$) are in solid lines; they were obtained from (8.13)–(8.15), including correction terms, with $\chi = 2/3$. MC validation data are plotted with symbols; they are extracted from Fig. 5.5, black curves in upper panel. We note the presence of a logarithmic singularity in $\langle \rho^2 \rangle_R$ at $\Delta = +2$, which is manifest in the leading term written explicitly in (8.15) and discussed in the main text. Adapted from Ref. [92].

Following the usual procedure, we find

$$\langle ct \rangle_R / H = 2\chi \left(1 + \frac{\Delta(10+\Delta)}{40} \right) \times \left[1 + C^{(2)}_{R,ct}(\xi, \Delta) \right]_{\xi=\tau_t/2\chi}, \quad (8.13)$$

$$\langle (ct)^2 \rangle_R / H^2 = \frac{4\chi}{5} \left(1 + \frac{\Delta(80 - \Delta(20 + \Delta(10+\Delta)))}{360} \right) \tau_t \times \left[1 + C^{(2)}_{R,ct}(\xi, \Delta) \right]_{\xi=\tau_t/2\chi}, \quad (8.14)$$

in the time domain, and in the spatial domain,

$$\langle \rho^2 \rangle_R / H^2 = \frac{1}{4} \left(\left[\frac{2}{\Delta} + 1 \right]^4 \frac{\Delta}{2} \ln \sqrt{\frac{1+\Delta/2}{1-\Delta/2}} - \left[1 + 2 \left(2 + \frac{2}{\Delta} \right) \frac{2}{\Delta} \right] \right) \frac{2\chi}{\tau_t} \times \left[1 + C^{(2)}_{R,\rho}(\xi, \Delta) \right]_{\xi=\tau_t/2\chi}. \quad (8.15)$$

These all lead back to (8.10)–(8.12) in the limit $\Delta \to 0$. Figure 5.19 compares the above predictions with the MC results from the black curves in the upper panel of Fig. 5.5. The analytical results for the temporal responses are in very good agreement with the numerical benchmarks.

As was the case for transmission, the most notable discrepancy is the logarithmic divergence in (8.15). However, this now happens *only* at $\Delta \to +2$, i.e., when

the extinction vanishes at the illuminated boundary. We attribute this to the same physical cause we assign to the appearance of χ in all the pre-factors: the extrapolation length (outside the cloud) – as well as the estimated depth of the dreaded radiative boundary layer (inside the cloud) – goes to ∞ as $1/\sigma(z) \propto 1/z$ when $\Delta = +2$ in (2.27). This is a clear harbinger of catastrophic failure of the diffusion model.

In his discussion of multiple-scattering cloud lidar applications, Davis [92] notices that the 'true' MC values for the logarithms of $\langle ct \rangle_R$ and $\langle \rho^2 \rangle_R$ are almost linear in Δ. He therefore suggests using the diffusion model only to predict the response at $\Delta = 0$ from (8.10) and (8.12), or something better, and then use the new model with stratification capability only to estimate the logarithmic partial derivatives $\partial \ln\langle ct \rangle_R / \partial\Delta$ and $\partial \ln\langle \rho^2 \rangle_R / \partial\Delta$ at $\Delta = 0$; then a log-linear extrapolation is performed that will closely follow the MC validation data. For the spatial response in (8.15), one can use the short series expansion

$$\langle \rho^2 \rangle_R / H^2 = \left(\frac{4}{3\xi} \right) \frac{\xi(\xi + 3/2) + 3/4}{\xi(\xi + 1)} + \frac{2}{3\xi} \Delta + O(\Delta^2), \tag{8.16}$$

recalling that $\xi = \tau_t / 2\chi$, to make this estimation. As noted in Ref. [92], the logarithmic derivative for $\sqrt{\langle \rho^2 \rangle_R}$ at $\Delta = 0$, namely, $\xi(\xi + 1)/(4\xi^2 + 6\xi + 3)$, is the same as for $\langle ct \rangle_R$ (cf. Fig. 5.19). Moreover, we note that the useful range for this quantity is rather small: $\approx 2/13$ to $1/4$ for $1 \lesssim \xi \leq \infty$.

5.8.3.3 Uniform oblique collimated illumination

Oxygen A-band spectroscopic observations of clouds from above need to account for the fact that sunlight is collimated and incident under all possible angles. The diffusion model for uniform-but-possibly-slant illumination presented in section 5.5.5 can again be brought to bear, this time, for reflected light. The usual procedure in computer-assisted calculus and algebra leads to

$$\langle ct \rangle_R / H = \frac{1}{3} (2 + 3\mu_0) \times \left[1 + C^{(1)}_{R,ct}(\tau, g, \mu_0) \right], \tag{8.17}$$

$$\langle (ct)^2 \rangle_R / H^2 = \frac{2}{15} (2 + 3\mu_0) (1 - g)\tau \times \left[1 + C^{(2)}_{R,ct}(\tau, g, \mu_0) \right], \tag{8.18}$$

$$\langle (ct)^3 \rangle_R / H^3 = \frac{4}{35} (2 + 3\mu_0) [(1 - g)\tau]^2 \times \left[1 + C^{(3)}_{R,ct}(\tau, g, \mu_0) \right]. \tag{8.19}$$

We notice that μ_0 finds its way into the pre-factor of the dominant power-law relation for each moment. This is a strong dependence in comparison with counterparts for transmission described in the previous subsection, where μ_0 only influences the pre-asymptotic correction terms. Revisiting Fig. 5.17 for quantification of the subtle SZA effects in transmission, using the isotropic source predictions as reference. This difference in sensitivity to SZA between transmitted and reflected fluxes in the time-domain is once again attributable to the fact that reflected light is a mixture of low and high orders of scattering $n_s \approx \sigma ct$. Indeed, all the light observed in reflection originates from some last scattering event within the upper radiative boundary layer of the cloud (i.e., between $z = 0$ and $z \approx \ell_t$); in this mix, the least scattered light will certainly have a memory of its original direction of incidence.

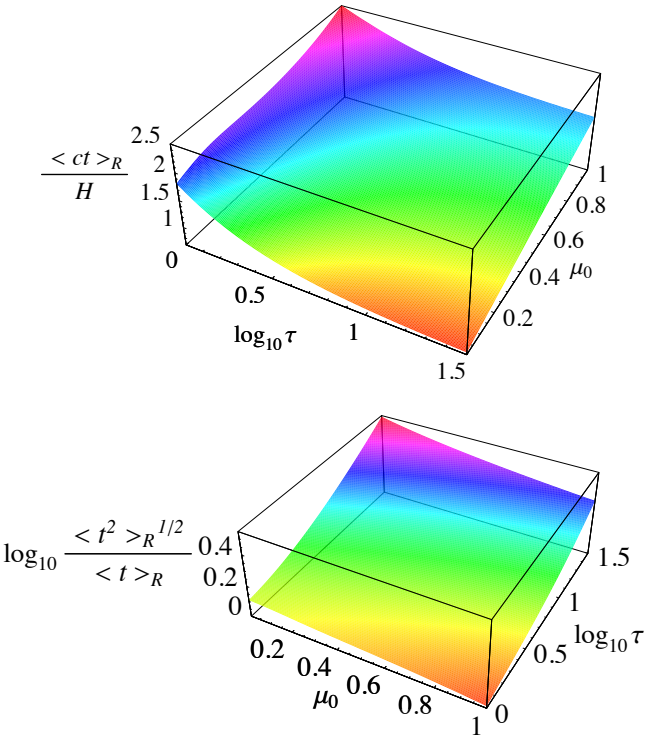

Fig. 5.20. *SZA dependence of temporal moments for light reflected from diffusive clouds.* Upper panel: (8.17) is plotted for $0 < \mu_0 \leq 1$ and $1 \leq \tau \leq 10^{1.5}$ with $g = 0.46$, corresponding to $3.6 \leq \tau \lesssim 114$ for the original $g = 0.85$ if we interpret these values as δ-rescaled (cf. section 5.4.2.1); the vertical range is between 2/3 (limit for $\tau \to \infty$ when $\mu_0 \to 0$) and 2.5. Lower panel: $(1/2)\log_{10}[\langle (ct)^2 \rangle_R / \langle ct \rangle_R^2)]$ is plotted for the same range of parameters; the vertical axis ranges only from 0 ($\log_{10}1$, the minimum theoretical value) to 0.544 ($\log_{10}3.5$). Further discussion in the main text.

Figure 5.20 illustrates SZA effects in reflected light, which are easy to show in their own right. (Unlike transmitted light, there is no need here to refer back to the isotropic source model as a baseline.) In the upper panel, (8.17) is plotted over the relevant range of parameters, namely, $0 < \mu_0 \leq 1$ and $1 \leq \tau \leq 10^{1.5}$ for the δ-Eddington rescaled $g = 0.46$ ($3.6 \leq \tau \lesssim 114$ for the original $g = 0.85$). We see that in-cloud path increases significantly with μ_0 at any given τ, which is to be expected since the light is injected deeper into the cloudy medium as μ_0 approaches unity. The lower panel plots the log of the RMS-to-mean path ratio over the same region of parameter space. We see a monotonic dependence of the non-dimensional moment ratio with τ, which confirms our above prediction that cloud optical depth can be retrieved unambiguously from the two observable moments for any given SZA.

5.9 Space-time Green functions applied to multiple-scattering cloud lidar (MuSCL) observations

We now turn to a new active technology for cloud remote sensing in the diffusive regime: Multiple-Scattering Cloud Lidar (MuSCL),[40] that we first proposed in 1996 on purely theoretical grounds [176]. Although developed independently, this cloud-probing technique is a direct extension of Multiple-FOV (MFOV) lidar, which targets aerosols [177–181] as well as clouds [182–184]. MFOV lidar itself extends the standard design of elastic backscatter lidar implemented, for instance, in the eye-safe design of micro-pulse lidars [185]. In the classic lidar equation, the assumption is single scattering through 180° for the most common configuration, so-called 'monostatic' systems, where the transmitter and receiver are collocated. This is indeed the opposite asymptotic limit in RT theory to the diffusion/P_1 approximation used throughout this paper: it is valid only in optically thin media.

In essence, MFOV lidar capitalizes on the strong forward peaked of the scattering phase function for cloud droplets and most aerosol types. To this effect, the small-angle approximation to time-dependent RT with multiple scattering is invoked, and it is known to work well close to the incident beam [83,186,187, among others]. Although the MFOV lidar project brought it to a high level of sophistication and application, the time-dependent[41] small-angle approximation was applied to pulse propagation through turbid media at least going back to Belyantsev et al. in 1967 [193], Romanova in 1970 [194], and Weinman and Shipley in 1972 [195] who all considered a one-way transit, ending in transmission.[42] Investigations of reflected laser pulses in the same approximation soon followed [196–199].

Because of the necessarily narrow FOV used in classic lidar, which only needs to contain the volume illuminated by the highly-collimated laser beam, there is little penetration into opaque media such as the clouds. Even if we could separate the single-scattering signal from *contamination* by multiple-scattering, which we cannot, there would be no photons left to count after two-way propagation to optical depths in the 10–100 range. MFOV does vastly better by indeed *exploiting* the multiple scattering signal coming from relatively near the laser beam. Optical depths up to 8–10 can be reached; after that wide-angle scattering starts to dominate the signal and we therefore enter the realm of MuSCL.

MuSCL signal physics are the same as in the *in situ* cloud lidar discussed in section 5.7 and, to a large extent, also those of the *reflected* O_2 A-band spec-

[40] This obvious and compelling acronym is closely related to, but not to be confused with, MUSCLE (MUltiple-SCattering Lidar Experiments), an on-going series of international workshops; see Ref. [175] for a special section of *Applied Physics – B* that followed from one of them.

[41] In steady-state, application of the small-angle approximation to the pencil-beam problem goes back much further. In charged particle transport, it has been known as the Fermi–Eyges/Fokker–Planck approximation since c. 1950. This modeling framework has recently regained considerable interest, largely motivated by emerging applications to the accurate computation of minimal-yet-effective dosimetry in electron-beam radiation therapy [188–192].

[42] Formally, this is an isotropic diffusion process in the non-Euclidean space of directions, starting from a given initial position and slowly but surely filling the whole unit sphere, one scatter at a time [81,108].

troscopy covered in the previous section. The main difference is that, having a pulsed laser as a source and observing the Green function from a significant stand-off distance to the cloud, MuSCL can access and exploit the signal in the spatial domain ... although not always easily, as we now show, by starting our discussion with past and future space-based MuSCL systems.

5.9.1 Space-based MuSCL systems

If the lidar instrument is at a very great distance to the cloud, as in space-based systems, then there will be limited, if any, information about the horizontal radiation transport away from the beam. We have estimated this span of the spatial Green function to be $\sim H$ ($\sim$km scales). Although imaging technology exists for much smaller scales, it would soon be 'photon-starved' if also required to resolve the rapid time evolution. Furthermore, the laser beam itself will be spread out to a significant diameter, thus diluting the spatial Green function (by convolution). That said about the present and near-future, systems may prove far more capable in the longer term.

Following Miller and Stephens [200], we make the safe assumption that we only have access to time-domain information. But this is exactly what the proposed cloud remote sensing using reflected oxygen A-band spectroscopy is about. The difference is that a lidar system will access the temporal signal directly with fast radiometry, while the spectroscopic technique delivers the path-length moments as 'products' derived from the differential absorption spectroscopy. The only other difference is the in down-looking lidar we have $\mu_0 = 1$ while passive A-band observation can have any incidence angle. So we are in fact looking at a special case of (8.17)–(8.19):

$$\langle ct \rangle_R / H \;=\; \frac{5}{3} \times \left[1 + C^{(1)}_{R,ct}(\tau, g, 1) \right], \tag{9.1}$$

$$\langle (ct)^2 \rangle_R / H^2 \;=\; \frac{2}{3} \, (1-g)\tau \times \left[1 + C^{(2)}_{R,ct}(\tau, g, 1) \right], \text{ and} \tag{9.2}$$

$$\langle (ct)^3 \rangle_R / H^3 \;=\; \frac{4}{7} \, [(1-g)\tau]^2 \times \left[1 + C^{(3)}_{R,ct}(\tau, g, 1) \right], \tag{9.3}$$

where, following Ref. [92], we have returned to the model for normal incidence in section 5.5.3. Figure 5.21 illustrates (9.1)–(9.3) along with MC validation data and the predicted asymptotes using both $g = 0.85$ and its δ-rescaled counterpart $g' = 0.45$. As expected, the later case is more accurate with respect to the MC simulation benchmarks. We see that the higher the order of the moment, the longer it takes to approach the asymptote; this underscores the practical importance of knowing the $C^{(q)}_{R,ct}$ terms with high accuracy.

At present, the prime application of this limited set of results is for the analysis of the nighttime orbit #135 of the Lidar-In-space Technology Experiment (LITE), which flew on Space Shuttle Discovery (STS-64 mission), September 9–20, 1994 [111]. The LITE payload was in essence a standard research lidar system: 5 W laser transmitting at 532 nm (the popular 'doubled Nd:YAG' solid-state technology) with a pulse rep-rate of 10 Hz and a diffraction-limited beam divergence leading to $\approx$0.3 km diameter at cloud level); receiver composed of a $\approx$1-m telescope feeding

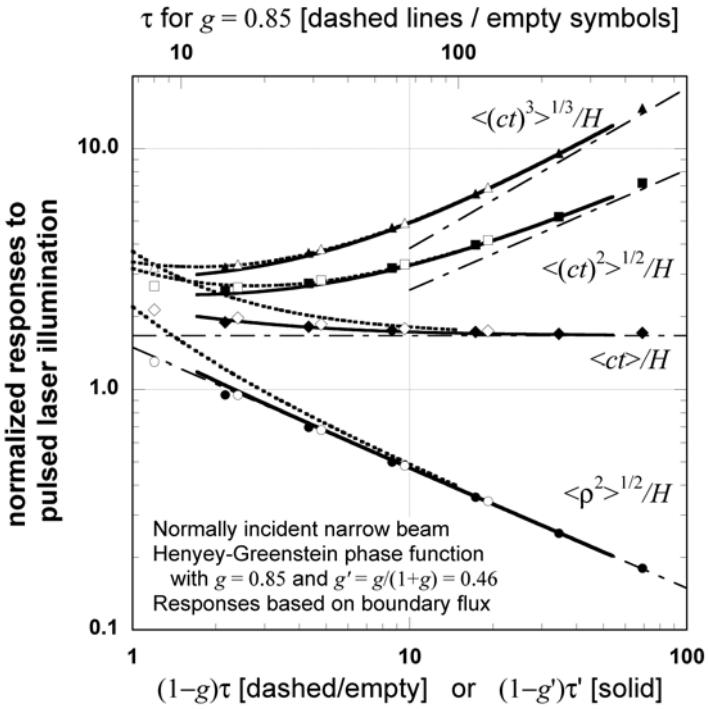

Fig. 5.21. *Spatial and temporal moments of the reflected Green function for normal illumination by a pulsed narrow beam.* From the top down, we have plotted $\sqrt[3]{\langle (ct)^3 \rangle}/H$, $\sqrt{\langle (ct)^2 \rangle_R}/H$, and $\langle ct \rangle_R/H$ from (9.1)–(9.3) and $\sqrt{\langle \rho^2 \rangle_R}/H$ from (9.4) as functions of rescaled optical depth. We note the different results for the canonical $g = 0.85$ value for liquid water clouds and its rescaled counterpart $g = 0.45$. Indeed, when the un-collided and diffuse components of the radiance field are treated separately, we no longer have exact similarity in $(1 - g)\tau$. Adapted from Ref. [92].

a high-efficiency photon-counting detector with a deliberately large FOV, namely, 0.2° (footprint at cloud level with ≈0.9 km diameter (at least during nighttime orbit #135). That data collection targeted a dense marine Sc layer and geometry tells us that the measured light was transported up to 1.2 km horizontally. Since the anticipated spatial Green function for such clouds has RMS-$\rho \sim H \approx 0.3$ km, we can safely assume that very high orders of scattering were present in the LITE signal. We refer the reader to the studies by Davis et al. [114, 201] for quantitative analyses of temporal moments and other time-domain characteristics of the small-but-interesting subset of *non-saturated* LITE returns from this orbit. It suffices to say here that the inferred cloud properties, i.e., $\{H, \tau\}$ pairs, are consistent with what we know about such clouds.

5.9.2 Ground-based and airborne MuSCL systems

We now assume that the MuSCL system is at a finite distance from the cloud. In other words, going back to notation from section 5.2.3 for the distance of the

observer to the closest cloud boundary, we have $d_{\rm obs} \lesssim H, \gtrsim H$, but not $\gg H$ (a case covered in the previous subsection) nor[43] $\ll H$. In short, platforms include those on the ground [84] or in an aircraft (including blimps) flying above the cloud top [202], up to the ≈20 km limit for high-altitude aircraft; as described in the provided references, both kinds of MuSCL system have been deployed and demonstrated. We can then easily measure spatial characteristics such as

$$\langle \rho^2 \rangle_R / H^2 = \frac{20}{9} \frac{1}{(1-g)\tau} \times \left[1 + C^{(2)}_{R,\rho}(\tau, g, 1) \right], \tag{9.4}$$

given here for the same normal/narrow-beam illumination used for the temporal moments in (9.1)–(9.3). The RMS value for ρ obtained from the above is also plotted in Fig. 5.21 with its MC validation data and estimated asymptote. Note that, for consistency, we have reserved in $C^{(2)}_{R,\rho}(\tau, g, 1)$ a slot for the possibility of $\mu_0 < 1$ although there is no longer axial symmetry in that case, and one would need to modify the diffusion model to capture other spatial statistics than the RMS horizontal transport. At present, however, we have no practical reason to take the diffusion transport modeling to that level of complexity. But that is only because of the limited scope of our applications; we refer the interested reader to Zege et al. in Ref. [83, Section 6.3, and citations therein] who address this steady-state problem in order to derive the non-axisymmetric MTF that controls off-axis imaging through a turbid medium.

The random-but-correlated variability of extinction in clouds driven by turbulence affects all aspects of the 3+1D RT, and we have promoted in section 5.4.2.3 a straightforward homogenization approach developed by Cairns et al. [75] to cope with this issue. We recall that in homogenization theory we simply use new values of optical properties σ and g dependent on original values – possibly already δ-rescaled (to account for the anisotropic source and phase function) – and variability parameters. Although all the time-domain responses in (9.1)–(9.3) are affected, we choose to illustrate with the RMS ρ. Figure 5.22 shows the relative effect (in %-difference) of Cairns rescaling for ϵ up to 0.4 on $\sqrt{\langle \rho^2 \rangle_R}$. It is systematic and positive: turbulence makes the RMS horizontal transport larger.

For a more quantitative validation of this prediction, we can turn back to Fig. 5.4 where we see that, going from the uniform to the fractal stratus cloud, the RMS ρ increases by ≈15–20%. That simulation was for a mean cloud optical depth $\tau \approx 13$, hence $\tau' \approx 3.6$ after δ-Eddington rescaling ($\log_{10} \tau' \approx 0.56$). This is about in the middle of Fig. 5.22 where we see that a 15–20% effect is obtained for $\epsilon(\overline{\sigma^2}/\overline{\sigma}^2, \overline{\sigma}' l_{\rm c}) \approx 0.1$–$0.15$. Looking at Fig. 5.6, we see that this magnitude is delivered by a variety of values of the one-point PDF parameter $\overline{\sigma^2}/\overline{\sigma}^2 = \overline{\sigma'^2}/\overline{\sigma'}^2$ and of the two-point correlation parameter $l_{\rm c}$ (knowing that $\overline{\sigma'} = \tau'/H \approx 3.6/0.3 = 12\ {\rm km}^{-1}$). Fractal clouds have, by definition, long-range correlations: horizontally, the variability spectrum observed for marine Sc goes from tens of meters to tens of

[43] For $d_{\rm obs} = 0$, the detector is at the cloud boundary, so no imaging (discrimination between different values of $\rho > 0$) is possible, at least in monostatic systems where source and detector are collocated. This is in fact a limiting case of *in situ* cloud lidar covered in section 5.7, corresponding to the occurrence of dense fog for a ground-based system. Recalling the source/detector geometry for that technique, it may prove useful to decouple the axis of the receiver FOV from the laser beam.

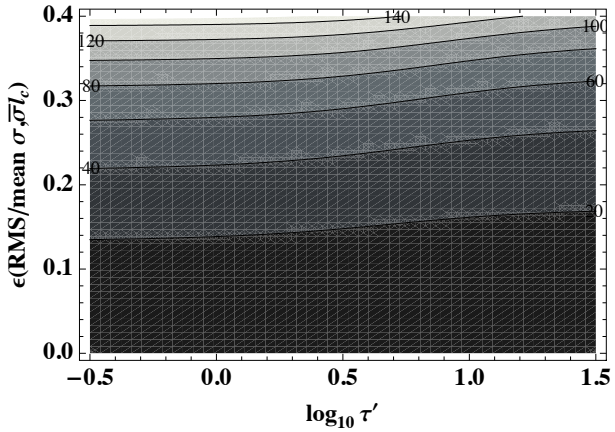

Fig. 5.22. *The impact of random internal variability on* $\langle\rho^2\rangle_R^{1/2}$ *in %.* We have plotted $100 \times ([\langle\rho^2\rangle_R(\epsilon)/\langle\rho^2\rangle_R(0)]^{1/2} - 1)$ where ϵ, obtained from (4.22)–(4.23), is used in (4.20) to change both σ' and g'. In turn, this rescaling of optical properties changes the outcome of (9.4) for $\langle\rho^2\rangle_R$, as an example. We see that over the useful range of ϵ the parameterized impact of turbulence-driven variability is significant, but only weakly dependent on optical thickness.

kilometers [203–205]. However, we are only interested here in the spatial correlations over the horizontal extent of the spatial Green function, which is $\sim H$; so we can take $\overline{\sigma}' l_c \sim \tau' \approx 3.6$. Similarly, we are only interested in the relative one-point variability, as captured by the RMS/mean ratio, over the horizontal extent of the spatial Green function; this implies that $\overline{\sigma'^2}/\overline{\sigma'}^2$ is only slightly more than unity. For this combination of $(\overline{\sigma'^2}/\overline{\sigma'}^2, \overline{\sigma}' l_c)$, we indeed find that ϵ has the right magnitude in Fig. 5.6.

In summary, we have presented upfront (Fig. 5.4) numerical evidence that, for the moderate variability found in Sc cloud layers at scales $\sim H$, we can expect a boost in $\sqrt{\langle\rho^2\rangle_R}$ on the order of ≈15–20% with respect to strictly uniform clouds with the same (domain-average) optical depth. Furthermore, this observation is consistent with our implementation of Cairns' parameterization for small-scale variability effects in the spatial Green function.

Finally, it is important to compare quantitatively the impacts of random turbulence and of deterministic stratification (sections 5.2.5, 5.5.2 and 5.8.3) on the characteristics of reflected light. We summarized the latter effect by estimating the relative effect of a change in relative gradient $|\Delta|$ of unity on either $\langle\rho^2\rangle_R^{1/2}$ or $\langle ct\rangle_R$: it varies between 2/13 (≈15%) and 1/4 (25%) as $(1-g)\tau$ goes from ≈1 to ≫1. We therefore retain that, under typical circumstances, the two effects are of the same order of magnitude.

5.9.3 Moment-based methods for MuSCL

Figure 5.23 illustrates how a hypothetical MuSCL retrieval of cloud thickness H and optical depth τ would proceed, including error propagation. We assume here an observational technology that can deliver one spatial and two temporal moments.

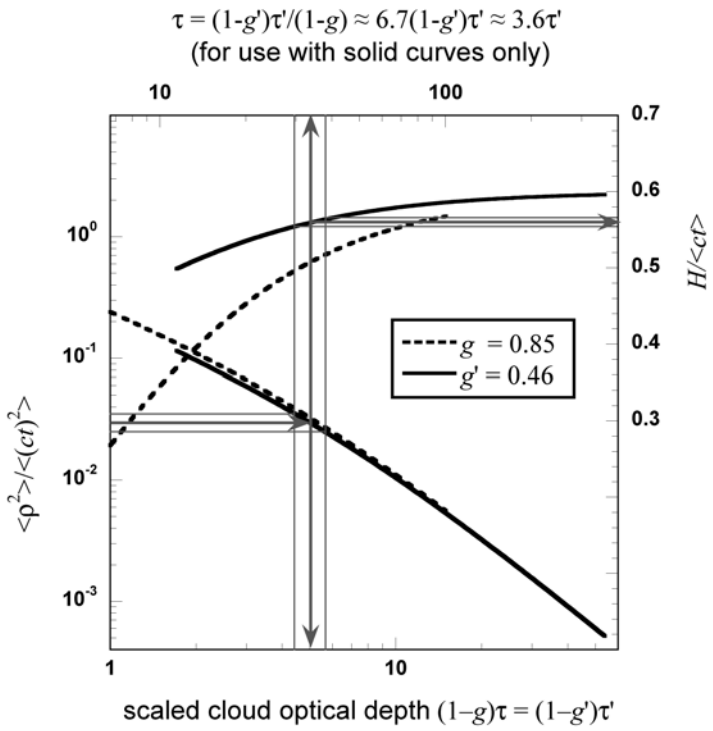

Fig. 5.23. *A typical moment-based cloud remote sensing algorithm for MuSCL data processing.* The lower curves show the non-dimensional ratio of observable moments $\langle\rho^2\rangle_R/\langle(ct)^2\rangle_R$ as a function of rescaled cloud optical depth $(1-g)\tau$ for $g = 0.85$ and the related value of $g' = 0.46$. Although not very different, the curve for g' is favored, and gives us τ, via scaled optical depth τ' (upper axis). We then use the corresponding prediction for $H/\langle ct\rangle$ in the upper curves to determine cloud thickness H. The numerical example uses rescaled $g' = 0.46$, which is expected to be the more accurate. A ratio of second-order moments of $(3.0 \pm 0.5)\,10^{-2}$ is assumed, and yields $\tau \approx 34 \pm 4$ (12% uncertainty) and, from there, $H \approx (0.560 \pm 0.005)\times$ the mean in-cloud path $\langle ct\rangle$ (whatever that may be). Note that the observational error on this first-order moment will very likely overwhelm the ≈1% error on the multiplier (associated with ≈12% on τ, resulting itself from the hypothetical ≈17% on the ratio of second-order moments). Adapted from Ref. [92].

As already suggested in our discussion of cloud remote sensing based on A-band spectroscopy, the non-dimensional property τ is determined from a non-dimensional ratio of moments, and then the dimensional cloud property H is determined from any one of the dimensional observables. Here, we opt for the mean in-cloud path.

Hogan and Battaglia [107] recently developed a time-dependent two-stream model, which is akin to the diffusion model, but with better performance at early times (in terms of causality in particular). Their model furthermore features an improved representation of the source of diffuse radiation by embedding a propagation-with-dispersion model by Hogan [187] for the pulsed laser beam (in the small-angle approximation). This idea was pioneered by Dolin [206] and Zege et al. [207] 20–25 years ago with analytical methods, but Hogan and Battaglia designed

their model from the start as a numerical tool. In particular, *arbitrary* vertical structure can be accommodated. In view of the alternation between physical-space modeling (requiring inverse Fourier and Laplace transforms) and moment-based methods in the present study, they offer an interesting middle road. The temporal signal is modeled in detail (as straightforward outcome of the numerical PDE solution) and, for space, they predict the conditional moment $\langle \rho^2 \rangle_R(ct)$ (basically by assuming, as in diffusion theory, that the instantaneous profile is Gaussian). This framework should prove very fruitful for all future MuSCL-type probes, and especially those in space from whence information about horizontal transport will necessarily be limited.

5.9.4 Deeper mining of MuSCL observations for cloud information

Can we use Cairns' parameterization of internal variability from section 5.4.2.3 in cloud remote sensing with MuSL? When using moment-based retrievals, there is certainly no harm in improving the fidelity of the forward model by prescribing a value of $\epsilon(\overline{\sigma^2}/\overline{\sigma}^2, \overline{\sigma} l_c)$ from the climatology of cloud variability; see Fig. 5.22 for the impact in the ρ-domain. However, if we wish to determine ϵ (hence a metric of internal cloud variability) empirically, we would have to start with at least three moments. We can thus form two or more dimensionless ratios and we include here, along with moments, cloud albedo R; albedo is indeed the zeroth-order moment, but also the ratio of overall reflected flux to incoming flux. These data in principle enable us to determine simultaneously the twice-rescaled τ'' and g'' using the full nonlinear dependence on both parameters (rather than simply prescribe the asymmetry factor); see Fig. 5.24 for an illustration. Then one can derive $\epsilon = 1 - 1/[2 - (1 - g'')/(1 - g')]$ from (4.20) for known $g' = 0.46$; from there, we work back to τ' and τ. Knowing τ (and τ') and having prescribed g (and g'), any predicted moment from (9.1)–(9.4) continues to give us H along the way by comparison with the corresponding observed value.

In the same spirit, a three-moment retrieval scheme can be devised that targets Δ (on top of H and τ) using the parameterizations of stratification impact in (8.13)–(8.15). In principle, a four-moment scheme could target all four cloud parameters. That, however, may be overextending MuSCL capability in cloud remote sensing. Only practice in modeling and in the field with specific implementations will determine how much reliable cloud information can be extracted. Of course, beyond its 'validation-by-intercomparison' phase of development [84, 202], MuSCL can eventually be combined with other cloud remote sensing instruments in optimal multi-modality approaches. We anticipate particularly fruitful integration with millimeter cloud radar and multi-channel passive microwave radiometers. Natural complementarity with thermal and solar radiometers should also be examined carefully and thoroughly.

Proximity of the observer to the cloud will naturally increase the SNR [92]. However, a serious problem arises when the finite FOV of the instrument prevents one from estimating moments reliably – the far-field tail of the spatial Green function is truncated! Although it may not be as obvious, the temporal Green function will be truncated if the spatial one is. If the receiver is a true imager, then it can be tilted with respect to the laser beam, thus gaining theoretically (in the absence of

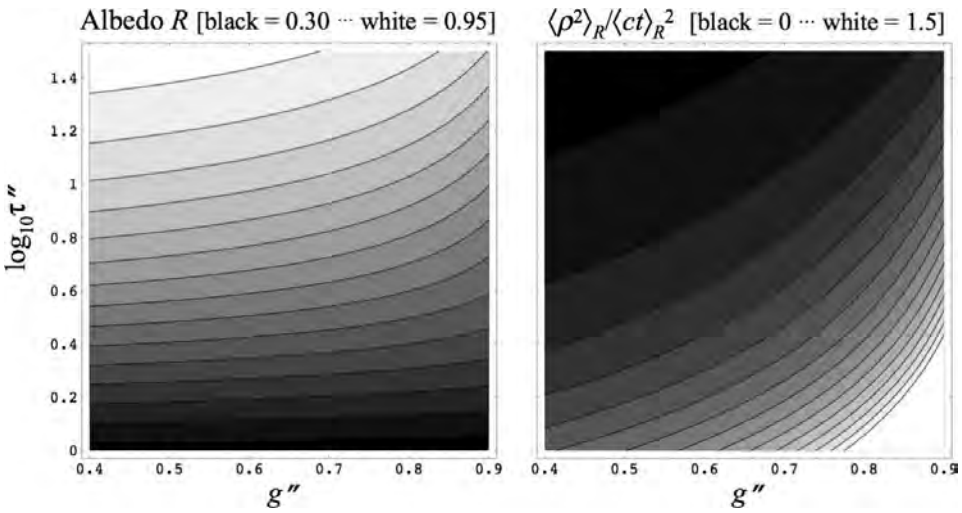

Fig. 5.24. *Feasibility of joint retrieval of the effective τ and g, hence of a metric of random variability, with MuSCL.* Gray-scale plots of cloud albedo R (left) and the non-dimensional moment ratio $\langle\rho^2\rangle_R/\langle ct\rangle_R^2$ (right) as functions of $\log_{10}\tau''$ and g'', the twice rescaled cloud parameters in (4.20). Observational determination of R, which requires absolute calibration, $\langle ct\rangle_R$ and $\langle\rho^2\rangle_R$ can lead to physical and optical thickness as well as the internal variability parameter. As explained in the main text, $\epsilon(g', g'')$, $\tau'(g', g'', \tau'')$ and $\tau(g, g', \tau')$ are determined in that order, assuming we can take $g = 0.85$ and the associated $g' = 0.46$ for granted. However, visual inspection of the two panels reveals that joint retrievals of τ'' and g'' (hence Cairns' ϵ) – the cloud's physical thickness H being determined later – will not be easy in general because isophotes and 'iso-moment-ratio' lines are more parallel than perpendicular. The most favorable region is where τ'' is low (reinforcing the importance of δ-Eddington rescaling as an intermediate step) especially when g'' (hence ϵ) is large.

noise) up to a factor of 2 in off-beam distance at the focal plane. A radical solution is, however, to return to the models that express the Green function in space and time, i.e., the PDFs that lead to the moments, cf. section 5.6 and Refs [84, 99].

5.10 Further applications to passive solar observations of clouds

Having covered in detail the application of radiative Green functions to two emerging cloud remote sensing technologies in the previous sections, we now survey briefly their application to more tested approaches.

5.10.1 Operational cloud remote sensing in the solar spectrum

Reflected and transmitted sunlight has always been a resource in cloud remote sensing in the solar spectrum, as long as absolute radiometric calibration is maintained. The standard model for retrieving cloud properties is, like here, the plane-

parallel slab treated at various levels of accuracy in the RT ranging from a two-stream/diffusion model (with separation of direct and diffuse components) from section 5.5.5 to a full multi-stream 1D RT model such as DISORT [168]. In the latter case, the computational burden is heavy enough that the forward modeling is done ahead of time and used to generate extensive look-up tables used to map cloud properties to radiances and vice versa [208–210].

Excluding O_2 A-band, cloud thickness H is not accessible by passive remote sensing since all one has is steady-state reflected (R) or transmitted (T) radiances[44] at one or more wavelengths, both being functions of τ, ϖ_0 and[45] g, as well as of μ_0 and the viewing angle coordinates $\mu, \phi - \phi_0$. The targeted cloud properties are invariably optical depth τ and the effective radius of the droplet size distribution $r_e = \overline{r^3}/\overline{r^2}$. The latter is obtained indirectly, via an estimate of the SSA, $\varpi_0(r_e)$, at a wavelength where liquid water has non-negligible absorption. This joint retrieval is based on the fact that, to a first approximation, $\sigma \sim \overline{r^2}$ and $\sigma_a \sim \overline{r^3}$, hence $1 - \varpi_0 \sim r_e$ for the co-SSA.

5.10.2 Opacity-driven 3D radiation transport

The question of how applicable 1D RT is to remote sensing of real (3D) cloud has been investigated quite thoroughly; see Ref. [211] for a recent survey. Since 1D RT is applied irrespective of the pixel scale, one must distinguish two qualitatively different kinds of modeling error:

1. if the pixel size is somewhat greater than the characteristic scale of the spatial Green function (namely, $\sim H$), then there is a high probability that there is significant sub-pixel variability and, because of the nonlinear dependence of radiance on cloud properties (τ and r_e), the retrieved values will be biased with respect to their mean values;
2. if the pixel size is $\lesssim$ than H, then the observed radiance is surely 'contaminated' (in the 1D RT sense) by horizontal fluxes coming from adjacent pixels.

In the former case (problem #1), so-called 'plane-parallel' biases occur, which are generally systematic in sign [212]; in the latter case (problem #2), so-called 'independent pixel approximation' biases occur, which are of both signs (depending on structural details) [213–215]. Solutions adapted to both of these situations are discussed in the remainder of this section.

5.10.3 The independent pixel approximation for steady/uniform illumination

The above problem #1 (sub-pixel variability) can be addressed simply by averaging (linearly mixing) the radiances predicted in 1D RT over an assumed variability in cloud properties. We can anticipate nontrivial results because radiances are

[44] It is conventional to normalize the observed radiance by estimating the effective Lambertian reflectivity, $R(\mu, \phi; \mu_0, \phi_0) = \pi I(\mu, \phi; \mu_0, \phi_0)/\mu_0 F_0$, where F_0 is the spectral solar flux integrated over the band of interest, and similarly for T.

[45] In this context of multi-stream 1D RT, we understand 'g' to symbolize the whole phase function representation, in whatever space that may be ($\mathbf{\Omega}$ or P_n).

nonlinear functions of all the cloud optical properties. This procedure is known in 3D RT as the independent pixel approximation (IPA) [212]. It is natural and convenient to choose a model for the variability that leads to analytical treatment.

In stratiform clouds, τ is by far the most variable property in comparison with H, g and r_e (or ϖ_0). The preferred variability model for τ has been the two-parameter Gamma distribution:

$$P_a(\tau) = \frac{1}{\Gamma(a)} \left(\frac{a}{\overline{\tau}}\right)^a \tau^{a-1} \, \mathrm{e}^{-a\tau/\overline{\tau}}, \tag{10.1}$$

where

$$a = \frac{1}{\overline{\tau^2}/\overline{\tau}^2 - 1}. \tag{10.2}$$

Its popularity follows from the ease of integrating rational functions over arbitrary combinations of power laws and exponentials, resulting at most in exponential integral functions and/or incomplete Gamma functions (possibly infinite series thereof).

In the context of radiation budget parameterization for the large-scale domain-averages required in GCMs, Barker [216] worked out the integrals

$$\overline{F}_a(\overline{\tau}, \varpi_0, g; \mu_0) = \int_0^\infty P_a(\tau) F(\tau; \varpi_0, g, \mu_0) \, \mathrm{d}\tau \tag{10.3}$$

for boundary fluxes $F = R, T$ (hence also cloud absorptance $A = 1-R-T$) resulting from uniform collimated illumination in the Eddington/diffusion-based version of the two-stream approximation [87]. This 'Gamma-Weighted Two-Stream' model was later generalized to multiple partially cloudy layers by Oreopoulos and Barker [217], thus calling for the same computations for the R and T responses to a uniform isotropic source, which depend only on $1 - \varpi_0$ and $\tau_\mathrm{t} = (1 - \varpi_0 g)\tau$. For instance, at non-absorbing wavelengths ($\varpi_0 = 1$), they use the simple expression for transmittance in (5.5) and obtain

$$\overline{T}_a(\overline{\tau}_\mathrm{t}) = \int_0^\infty \frac{1}{1 + \tau_\mathrm{t}/2\chi} P_a(\tau_\mathrm{t}) \, \mathrm{d}\tau_\mathrm{t} = X \, \mathrm{e}^X \mathrm{E}_a(X)\big|_{X=2\chi a/\overline{\tau}_\mathrm{t}}, \tag{10.4}$$

although in a different notations; here, $\mathrm{E}_a(X)$ is the exponential integral of (any real) order $a > 0$, and we note that $X = a/\xi$ from (5.11). This leads to the systematic positive bias observed in Fig. 5.25(a) of $\overline{T}_a(\overline{\tau}_\mathrm{t})$ with respect to $\overline{T}_\infty(\overline{\tau}_\mathrm{t}) = 1/(1 + \overline{\tau}_\mathrm{t}/2\chi)$. This is a well-known result in 3D RT: structured clouds transmit more than their homogeneous counterparts *with the same mean* τ. This is an immediate consequence of Jensen's [77] inequality in the case of a convex function like $T(\tau_\mathrm{t}/2\chi)$. Kokhanovsky [218, 219] performed similar computations, with satellite remote sensing in mind, using the asymptotic 1D RT [166,220] expressions for reflected radiances $I(\tau, \varpi_0, g; \mu_0, \mu)$, which become $I_a(\overline{\tau}_\mathrm{t}, \varpi_0, g; \mu_0, \mu)$.

5.10.4 The independent pixel approximation for space/time Green functions

There is no reason why the same averaging procedure cannot be performed on the spatial or temporal Green functions or associated moments obtained in the previous sections, as need be. This computation would apply, as for the above steady-state RT, to solar O_2 A-band spectroscopy at coarse scale. In that respect, it complements the homogenization approaches based on Cairns (section 5.4.2.3) or Larsen (section 5.4.2.4) rescaling, which applies primarily to small-scale variability. At any rate, that is precisely how Davis and Marshak [24] preemptively approached the problem of spatial variability for the spatial dimension in transmitted light, without considering homogenization. They used (10.3) with $\overline{\tau} = 10$ and $a = 4.5$, typical values found by Barker et al. [221] for stratocumulus, to average $T \times \langle \rho^2 \rangle_T$ from (5.5) and (8.5), and then normalized by $\overline{T}$ in (10.4). Davis and Marshak thus captured quantitatively the ≈10–15% difference in RMS ρ clearly visible in Fig. 5.4 between uniform and fractal plane-parallel clouds.

Here is another example, this one in the time-domain hence directly applicable to passive (solar) remote sensing of clouds based on O_2 A-band spectroscopy. We apply (10.3) with $F(\tau; \varpi_0, g, \mu_0)$ replaced by $\langle ct \rangle_T$ from (8.3) times the corresponding $T(\tau_t)$ from (5.5). After dividing by $\overline{T}$ from (10.4), we obtain for the mean path in variable clouds:

$$\overline{\langle ct \rangle}_T / H = \frac{\overline{T \langle ct \rangle}_T}{\overline{T} \times H} = \frac{\chi}{2} \left[1 + a + X + (2 - X)/\overline{T}_a(X) \right] \Big|_{X = 2\chi a/\overline{\tau}_t}, \qquad (10.5)$$

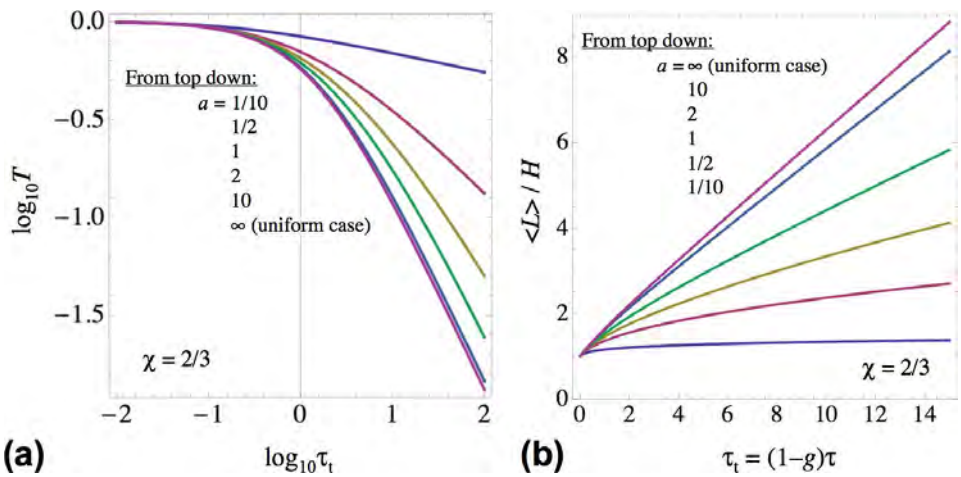

Fig. 5.25. *Transmittance and mean path-length for a Gamma-weighted two-stream model.* (a) The expression in (10.4) is plotted versus $\overline{\tau}_t$ for selected values of a in log-log axes; we note the increasing transmission as the unresolved variability increases (a decreases) at fixed $\overline{\tau}_t$. (b) Mean path-length, in units of H, from (10.5) versus $\overline{\tau}_t$ for the same values of a as in panel (a); we note that paths decrease on average as variability increases (a decreases) at fixed $\overline{\tau}_t$. See text for more explanation.

where $\overline{T}_a(X)$ is expressed in (10.4). Figure 5.25(b) shows $\overline{\langle ct \rangle}_T/H$ for representative values of a over a relevant range of $\overline{\tau}_t$. We see that, for a given H, the unresolved variability reduces the observed mean path with respect to the prediction for a uniform cloud with the same optical depth. The physical reason for this outcome is the same dominance of high transmission values (low τ_t) that affect $\overline{T}$ in Fig. 5.25(a). Indeed, the whole variation of flux-weighted mean path, $T \times \langle ct \rangle_T = \chi(\tau_t^2 + 6\chi\tau_t + 6\chi^2)/(\tau_t + 2\chi)^2$, is between $\chi \lesssim 1$ and $3\chi/2 \approx 1$ for all choices of χ near its canonical value[46] of 2/3.

We note that, if the application is ground-based O_2 A-band spectroscopy of clouds, then the Gamma- or otherwise-weighted averaging should actually be performed on the prediction of the forward RT model in Laplace space, namely, $\tilde{F}(s, 0, \tau_t, \chi)$ from (5.8), or (5.9) for space-based, since that is the quantity observed at a scale so coarse that sub-pixel variability needs to be accounted for. That is a harder computation yielding the same expressions for the path-length moments, but it can be used directly with A-band observations.

5.10.5 Landsat-type observations of clouds from space, and the nonlocal IPA

How can we address the above problem #2 of pixel 'adjacency' effects? In this case, the pixel scale is too small for 1D RT to be realistic. More precisely, the pixel footprint is so small that, even if it were internally homogeneous, net horizontal fluxes coming from denser or more tenuous neighboring pixels would affect the observed radiance at cloud top. With their 30 m pixels, NASA's series of Landsat/Thematic-Mappers are by far the most popular assets delivering imagery that fall in this category. To the best of our knowledge, the first systematic attempt to go beyond quantification and actually attempt to mitigate this inescapable 3D RT effect was by Marshak et al. [222] who proposed the 'nonlocal IPA' (NIPA).

NIPA is based on the intuitive idea that multiple scattering processes cause an *apparent smoothing* of the cloud structure, as observed in the remotely sensed radiance field [170, 223–225]. Rather than run a full 3D RT simulation with an expensive MC code, or even a more efficient grid-based solver such as SHDOM [18], one can simply apply a low-pass filter (smoothing kernel) to the IPA prediction. This approximate 3D RT method works well, at least for stratiform clouds under near-normal illumination. At more oblique illumination, brightening/shadowing effects produce a radiative *roughening* in the sense of enhanced amplitudes in Fourier space [226, 227] at scales $\gtrsim H$.

We note that what is required here is the Fourier transform $\tilde{P}(\overrightarrow{k})$ of the smoothing kernel $P(\overrightarrow{\rho})$ since we wish to perform the convolution product of P and the 2D IPA-derived radiance field $I_{\mathrm{IPA}}(\overrightarrow{\rho})$:

$$I_{\mathrm{NIPA}}(\overrightarrow{\rho}) = \int\int_{-\infty}^{+\infty} P(\overrightarrow{\rho}') I_{\mathrm{IPA}}(\overrightarrow{\rho} - \overrightarrow{\rho}')\, \mathrm{d}\overrightarrow{\rho}', \tag{10.6}$$

[46] We note that $\overline{\langle ct \rangle}_T/H = 3\chi/2$ at $\tau_t \to 0 (X \to \infty)$ in (10.5), which is unity when $\chi = 2/3$, for all values of a (cf. Fig. 5.25(b)). As remarked earlier (in section 5.8.2), this limit should yield 2 (the mean μ-weighted value of $1/\mu$) and, accordingly, we should be using $\chi = 4/3$ for optically thin media, as suggested in section 5.4.3.

which becomes a simple product in Fourier space, $\tilde{I}_{\mathrm{NIPA}}(\overrightarrow{k}) = \tilde{P}(\overrightarrow{k})\tilde{I}_{\mathrm{IPA}}(\overrightarrow{k})$. Any one of the Fourier-space reflected Green functions computed in section 5.5 for illumination can be used. They depend parametrically on H, τ_{t} and g or Δ. Depending on whether local albedo or nadir radiance is targeted, we would choose a spatial Green function for isotropic or normal illumination.

Marshak et al. [222] had an even more empirical approach, however. Eschewing normalized solutions from section 5.5 in Fourier space, they used a convenient two-parameter expression like (10.1) but for ρ instead of τ and averages based on cloud radiative Green functions (in $\langle\cdot\rangle$'s) instead of averages over cloud structural disorder (indicated with $\bar{\cdot}$). The 2D Fourier–Hankel transform in (6.1) of a Gamma-shaped radial Green function (normalized with the appropriate $2\pi\rho$ weighting) can be expressed as an Euler hypergeometric function:

$$\tilde{P}(k) = {}_2F_1\left(\frac{1+a}{2}, \frac{2+a}{2}, 1; -\left(\frac{\langle\rho\rangle k}{a+1}\right)^2\right). \tag{10.7}$$

However, the authors did their proof-of-concept computations with cloud models having optical depth variability in a single horizontal direction, say, x. The required 1D Fourier transform of (10.1), with $\tau \mapsto |x|$ and division by 2 (to cover the new support, all of $\mathbb{R}$), is a simpler expression:

$$\tilde{P}(k) = \frac{\cos\left[a\tan^{-1}\left(\frac{\langle|x|\rangle k}{a}\right)\right]}{\left[1+\left(\frac{\langle|x|\rangle k}{a}\right)^2\right]^{a/2}}. \tag{10.8}$$

Just like the diffusion-based MTFs for reflections presented in section 5.5.1 (Fig. 5.8), these smoothing kernels act in Fourier space as low-pass filters; however, they feature gentle power-law cutoffs in k^{-a} at wavenumber $k_{\mathrm{c}} \approx 1/\langle\rho\rangle_R$ (2D) or $1/\langle|x|\rangle_R$ (1D).[47]

Power-law tails in $\tilde{P}(k)$ are a natural choice to reconcile the spatial correlations observed in satellite images of extensive stratocumulus [225] with those observed with airborne *in situ* probes [204] for the same type of cloud system. The latter have scale-invariant (power-law) internal structure (obviously driven by turbulence); specifically, one finds extinction (actually, liquid water content) fluctuations in $k^{-5/3}$, typically over scales from ∼tens of kilometers down to ∼tens of meters. Satellite (nadir-looking) radiances also have this trend, which follows from the IPA (a nonlinear but one-to-one mapping of local τ to local radiance), but only down to a scale found by numerical simulation to be $\approx \sqrt{\langle\rho^2\rangle_R}$ [170]. Above the associated cut-off wavenumber, a trend approaching k^{-3} is found, which translates to a function at least once differentiable.[48] Noting that the low-pass filtered NIPA radiance goes as $k^{-(5/3+a)}$ when $k \to \infty$. This sets a to a value $\lesssim 4/3$. Only slightly smaller

[47] Recall that this substitution of Gamma-type functions for Green functions derived from transport physics was also done in the time-domain, in particular, for practical data exploitation in O_2 A-band spectroscopy of cloudy skies [159, 160]. This is largely because, as for Fourier transformation, it has a closed-form Laplace transform.

[48] This level of smoothness is quite remarkable since the 3D RT equation puts no constraints on gradients perpendicular to the beams (which, in this situation, are vertical).

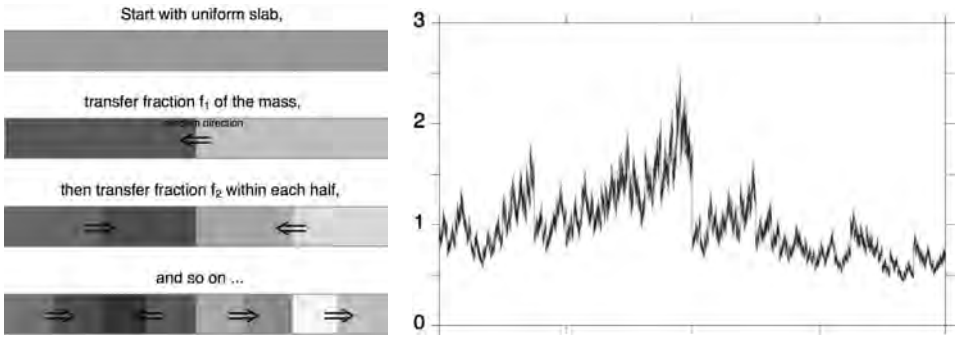

Fig. 5.26. *A simple and convenient stochastic cloud model for radiative smoothing studies.* Left: In the first step, a fraction f_1 of cloud 'mass' is transferred in a random horizontal direction from one half to the other. For every step after that, a fraction f_n is similarly transferred at scale $1/2^n$ such that $f_n/f_{n-1} = \cdots = f_2/f_1$. Right: The outcome for one realization at $n = 14$ when the parameters are $f_1 = 1/4$ and $f_1/f_2 = 2^{1/3}$. This so-called 'bounded cascade' model [27, 228] has been tuned to yield a 1-point st.dev. of 1/3 of the (unit) mean and 2-point correlations reflecting a Fourier spectrum in $1/k^{-5/3}$. These values are typical of the observed variability of local optical thickness for real marine stratocumulus clouds [28]. Both panels are reproduced with permission from Ref. [229].

values ($a \lesssim 1$) are required for consistency between the Landsat observations [225] and the near-field behavior of simulated [170] and observed [85] spatial Green functions for reflected laser light. In short, the anticipated range for a is quite narrow and, in any event, its precise value is not as important as that of $\langle|x|\rangle$ (or $\langle\rho\rangle$) that determines the spatial extent of the running average.

Figures 5.26 and 5.27 illustrate the NIPA procedure for a fractal cloud model. The stochastic 'bounded cascade' model used to generate horizontal cloud structure for a stratocumulus is explained graphically in the l.-h. panel of Fig. 5.26 while the resulting transect of cloud variability normalized to yield a unit mean is plotted in the r.-h. panel; its wavenumber spectrum is prescribed to be $\propto k^{-5/3}$, as observed in real stratocumulus layers. This model is illustrated for 1D and used here as such, but it is readily generalized to 2D [230]. Figure 5.27 exemplifies the differences between MC, IPA and NIPA. The upper panel shows, on the one hand, $\tau(x)$ for a 2-km portion of the synthetic fractal cloud that extends to 12.8 km (and is periodically replicated beyond that). On the other hand, both MC and IPA predictions are plotted for the local albedo: we see how the IPA responds immediately to the fractal variability while the MC results are much like a running mean over several pixels. The lower panel shows MC, IPA and NIPA predictions for the local value of nadir radiance over the same portion of cloud. By comparing the two registered panels, we see that the MC radiance field is not as smooth as its counterpart for albedo, patently because there is no longer angular averaging. The NIPA computation used the smoothing kernel in (10.8) with $a = 0.5$, $\langle|x|\rangle = 0.1$ km (eight pixels). Finally, we see how much the prediction error with respect to MC 'truth' is reduced by going from the IPA to the NIPA.

That completes the description of the *forward* NIPA where we improve the realism of the IPA by introducing scale-specific smoothness. The *inverse* NIPA

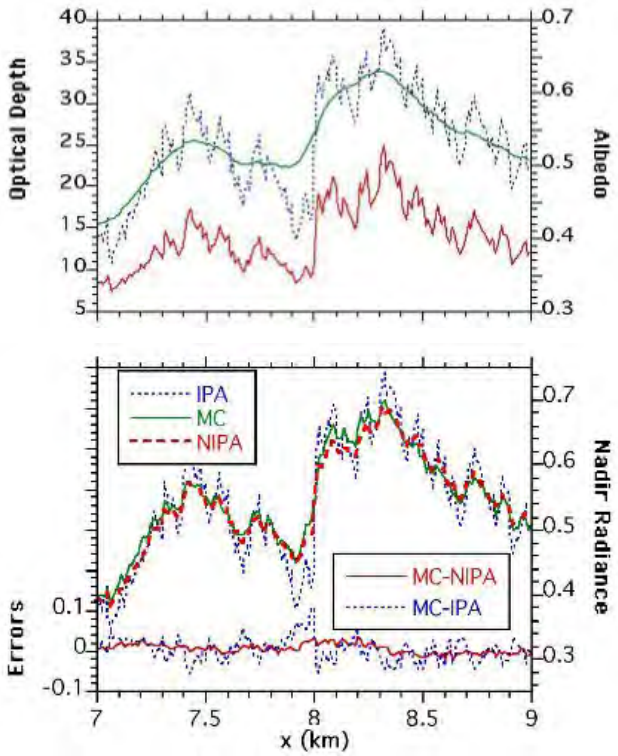

Fig. 5.27. *Comparison of simulated reflectivity fields using MC, IPA and NIPA for a portion of a 1D fractal stratoculmulus cloud.* Top: On the l.-h. axis, we read the 1D horizontal variation in x of the local optical depth $\tau(x)$ (lower curve); the vertically uniform cloud is generated with a 10-step bounded cascade process from Fig. 5.26 with $\overline{\tau} = 13$ and $H = 0.3$ km (pixel/grid-scale = 12.5 m). The upper curves (r.-h. axis) in the same panel show the associated fluctuations of albedo $R(x)$, the normalized up-welling flux in (2.18) for steady and uniform illumination, using both IPA and MC schemes; SZA is 22.5° and scattering is according to a Deirmendjian C1 phase function for a red wavelength for simplicity (both water- and land-surface albedo is negligibly small). Bottom: The r.-h. axis is the same as in the top panel but for normalized nadir radiance in (2.16) rather than hemispherical flux, under the same conditions of spatially uniform and steady illumination, and the computational NIPA scheme is added. The lower curves (l.-h. axis) highlights the reduced error with respect to MC when NIPA is used instead of IPA. Both panels are reproduced, with permission, from Ref. [229].

consists in taking actual cloud radiances and applying the corresponding roughening filter to restore the IPA and, from there, perform straightforward retrievals of (say) the cloud optical depth field. Formally, that amounts to solving (10.6), viewed as an integral equation, for $I_{\rm IPA}(\overrightarrow{\rho})$ knowing $I_{\rm NIPA}(\overrightarrow{\rho})$ from observation or 3D RT computation.

In an ideal (infinite-accuracy, noiseless) world, one only needs to perform the inverse FFT of $\tilde{I}_{\rm IPA}(\overrightarrow{k}) = \tilde{I}_{\rm NIPA}(\overrightarrow{k})/\tilde{P}(\overrightarrow{k})$. However, $1/\tilde{P}(\overrightarrow{k})$ is a high-pass filter that will amplify any noise or small-scale numerical error. This is a classic ill-posed

(i.e., numerically unstable) inverse problem. Marshak et al. [222] demonstrate on 'observations' obtained with a MC code (where the 'truth' is known), that careful Tikhonov-type regularization [231] can be used to estimate $I_{\mathrm{IPA}}(\overrightarrow{\rho})$ even in the presence of considerable noise from the MC scheme itself and, from there, obtain reasonable estimates of the local value of τ from a pre-computed inverse map of τ to nadir radiance from 1D RT.

While the inverse NIPA can be applied to inject more realism into retrieved values of τ for stratocumulus-type clouds, the prerequisite determination of the critical wavenumber k_{c} where the scale break occurs is an opportunity for cloud remote sensing in its own right. Specifically, it can be used to infer H, knowing the mean value of τ. Indeed, the reflected MTF used to inverse filter the quasi-nadir radiance data can only be a function of kH and dimensionless cloud or modeling parameters (τ, g, maybe χ, maybe a for Gamma-weighting, etc.). So, if we know k_{c} in 1/km from observations and the suite of cloud parameters, we can estimate H in km.[49] This idea is pursued using physical- rather than Fourier-space methods in the next example.

5.10.6 Zenith radiance reaching ground, and the nonlocal IPA

Ground-based narrow-FOV radiometers that capture down-welling radiance from zenith have proven at once quite simple to build/maintain and extremely useful in cloud probing. One monospectral approach uses the solar background from the sensitive and well-calibrated detector in an operational ground-based micro-pulse lidar system [185] to infer optical depth of stratiform clouds by comparison with the predictions of 1D RT models for spectral zenith radiance at the laser wavelength [232].[50]

From the 3D RT standpoint, narrow-FOV observations from ground (or space) complement the more classic flux-based measurements from ground (and at least moderately large pixels in MODIS-type instruments): the latter have the above 3D problem #1 while the former present #2. Another application of zenith cloud radiance measurements proposed by Marshak et al. [235] works around the 3D RT effects by using a bi-spectral technique for inference of cloud optical depth *above green vegetation*; the method works even for a field of broken clouds and, moreover, does not require absolute calibration.

Viewed as a time-series, rapidly sampled zenith radiance from an overcast sky contains information about the spatial correlations in the radiance field in essentially the same way high-resolution satellite imagery does. The only difference is

[49] The simplest approach is to equate $1/k_{\mathrm{c}}$ with the RMS value for ρ, which appears parametrically in Gamma-approximated MTFs, since the ratio of $\langle \rho^2 \rangle_R$ and H^2 is a known function of known dimensionless cloud parameters.

[50] This same calibration-based technique was proposed almost a decade ago [233] for the ultra-narrow FOVs in space-based lidar systems, but just recently applied to the Geophysical Lidar and Altimeter System (GLAS) lidar onboard the current ICESat (Ice, Cloud, and land Elevation Satellite) mission. In this time configuration, a comparison with 1D RT predictions for nadir reflected radiance at the laser wavelength is performed [234].

the nontrivial but standard time-to-space conversion using Taylor's frozen turbulence hypothesis: just use the mean wind at cloud altitude to account for advection across the instrument's FOV.

In this context, the transmitted spatial Green function can be used in both forward and inverse NIPA, applied respectively

- to approximate a rigorous 3D RT computation of zenith radiance, given the cloud's detailed structure, and
- to derive the column optical thickness from a time-series of zenith radiance observations.

Recall that the transmitted spatial Green function required for NIPA work has the same exponential decay in the far-field as its reflected counterpart, but it is flat rather than quasi-singular in the near-beam region. That implies in particular that the only reasonable Gamma-based parameterization of this Green function is for the special value of $a = 1$, yielding a simple exponential for the radial profile in (10.1); this choice is equivalent to stating that the RMS-to-mean ratio for ρ is $\sqrt{2}$.

There is, however, the possibility of directly exploiting the outcome of the spatial correlation analysis to derive a key cloud property, namely, the physical thickness H of the (unbroken) layer. Beyond the Fourier wavenumber spectrum invoked in

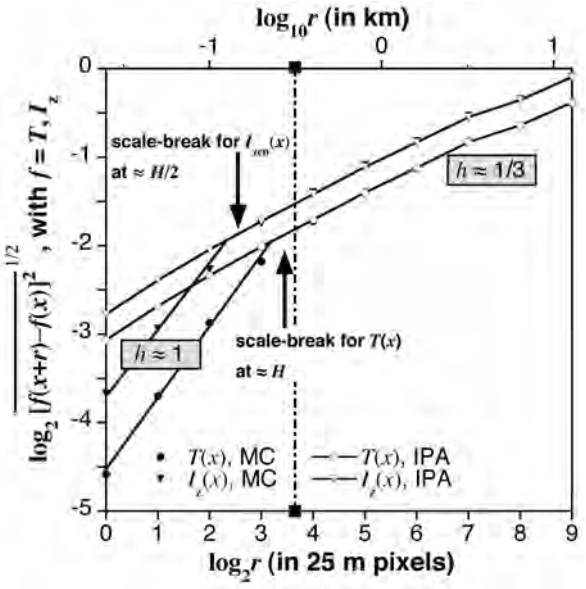

Fig. 5.28. *Simulated structure functions for local transmittance and zenith radiance.* Scale breaks between smooth ($h \approx 1$) and turbulent ($h \approx 1/3$) behaviors are clearly visible, respectively at $\approx H$ and $\approx H/2$. The ensemble of 10 simulated realizations of cloud optical depth were generated using a 10-step 1D bounded cascade model from Fig. 5.26 with the same parameters. Other cloud parameters of interest are mean optical depth $\overline{\tau} = 13$ and the constant physical thickness $H = 0.3$ km (indicated with a vertical dash-dotted line). Scattering follows the usual H–G model (2.20) with $g = 0.85$. SZA is 30°. This plot is adapted from Ref. [24].

the previous subsection, a popular statistical characterization of spatial correlation is the (second-order) 'structure function': $\mathrm{SF}(r) = \overline{[I_{\mathrm{zen}}(x+r) - I_{\mathrm{zen}}(x)]^2}$ for a one-dimensional horizontal transect of zenith radiance, assumed to be along the x axis; r is a given scale parameter and the average is over a large interval in x. As for the Fourier spectrum, one naturally seeks power-law behaviors in r:

$$\sqrt{\mathrm{SF}(r)} = \overline{[I_{\mathrm{zen}}(x+r) - I_{\mathrm{zen}}(x)]^2}^{1/2} \sim r^h, \tag{10.9}$$

where h is the 'Hurst' exponent (a.k.a. the *global* Hölder–Lipschitz exponent).[51] Recognizable scaling behaviors are $h = 0$ for all stationary processes (i.e., that are decorrelated over the associated range of r), $h = 1/3$ for turbulence-like variability (corresponds to a Fourier spectrum in $k^{-5/3}$, as for the fractal model in Fig. 5.26), and $h = 1$ for all smooth (i.e., differentiable) fields.

One can of course find different values of h in (10.9) over different ranges in r. Indeed, von Savigny et al. [236,237] found that the *time*-averaged structure function of ground-based zenith radiance at a non-absorbing (red) wavelength went from $h \approx 1$ scaling to $h = 1/3$ and ended with $h = 0$ at very long time lags, in excess of 1/2 to 1 hour or so (translating to 5–10 km for a nominal 5 m/s wind speed). Their sampling rate was 2 Hz and the longest records covered ≈4 hours. The authors found the predicted transition from smooth behavior to turbulence-like behavior at time lags that translated (via Taylor's hypothesis) to scales commensurate with the thickness of the cloud deck (known through collocated mm-wavelength radar).

Another way to 'calibrate' this simple method of estimating H from zenith radiance records (without a cloud radar present) is to use 3D RT simulations for stochastic cloud models tuned to reproduce the amplitude and scaling of real-world stratus. Figures 5.26(a) and (b) showed how to generate such a model in one horizontal direction and the outcome for one realization. Figure 5.28 shows SFs for both the simulations of zenith radiance field and of the local flux field transmitted at cloud base. Recall from (8.5) and Fig. 5.15 that the RMS radius of the Green function $T(\rho)$ for transmitted steady-state flux is $\approx H$ over the full range of interest in transport optical depths. We see in Fig. 5.28 that the scale break for flux is, as expected, at $\approx H$. In contrast, the numerics show on the same figure that the scale-break for zenith radiance – the *remotely* observable quantity – is at $\approx H/2$. As was just noted for reflected light, this smaller value (favoring roughness) is understandable since, unlike oblique views (let alone the angular integration for flux), a zenith radiance characteristic (i.e., a vertical beam) does not average by propagation over spatial variability unfolding in the horizontal.

This is clearly an opportunity for a remote-sensing retrieval of H using very simple ground-based instrumentation described in Ref. [236]. Only a single non-absorbing wavelength is required; it could be from a few spectral pixels in the continuum of an O_2 A-band spectrometer. Knowing H, one can look back at the cloud information contained in the main cloud product anticipated from ground-based A-band spectrometers, namely, the mean in-cloud path-length $\langle ct \rangle_T$. The ratio with the estimated values of $\langle ct \rangle_T$ and H can then be used to infer $\overline{\tau}$ from

[51] A variant of the Weiner–Khintchin theorem for non-stationary processes with stationary increments relates the Fourier spectrum and the second-order structure function. In particular, if the spectrum scales as $k^{-\beta}$ with $1 < \beta < 3$ then $\beta = 2h + 1$.

a consistently randomized diffusion-theoretical result, such as (10.5), given g, χ and[52] a, or a homogenization approach.

5.10.7 Green functions at work in the adjoint perturbation approach to 3D radiation transport effects

Finally, we briefly describe here another approach altogether to the above problem #2 (traced to pixel adjacency effects) that is also grounded in Green function formalism. Adjoint perturbation theory is very general and can therefore be applied to many aspects of atmospheric RT [238–241], estimation of 3D transport effects is just one example [238, 242–244].

Focusing on steady sources, we start by recasting the 3D RT problem in formal operator language:

$$\begin{aligned} \Lambda I &= Q \text{ where} \\ \Lambda &= \mathcal{L} - \mathcal{S}, \end{aligned} \tag{10.10}$$

is the linear transport (i.e., propagation *and* scattering) operator; it is obtained from (2.2), without the time derivative, and (2.3). In this application, we think of Q as a general distribution of sources over $(\boldsymbol{x}, \boldsymbol{\Omega})$. We also define the adjoint 3D RT problem

$$\begin{aligned} \Lambda^+ I^+ &= Q^+ \text{ where} \\ \Lambda^+ &= \mathcal{L}^+ - \mathcal{S}^+. \end{aligned} \tag{10.11}$$

The general definition of adjoint transport system is that, for all 'reasonable' test functions g and h of $\boldsymbol{x}$ and $\boldsymbol{\Omega}$, we have $(g, \Lambda h) = (\Lambda^+ g, h)$ where

$$(f_1, f_2) = \iiint\limits_{\mathrm{M}(H)} \int\limits_{4\pi} f_1(\boldsymbol{x}, \boldsymbol{\Omega}) f_2(\boldsymbol{x}, \boldsymbol{\Omega}) \, \mathrm{d}\boldsymbol{x} \, \mathrm{d}\boldsymbol{\Omega} \tag{10.12}$$

is the scalar product in the function space of interest. In cases of interest here, the optical medium is $\mathrm{M}(H) = \{\boldsymbol{x} \in \mathbb{R}^3; 0 < z < H\}$.

In particular, we require that the response of a detector with a response function $D(\boldsymbol{x}, \boldsymbol{\Omega})$ is the functional

$$E = (D, I) = (I^+, Q). \tag{10.13}$$

With these definitions, it can be shown [245] that

- $\mathcal{L}^+$ is $\mathcal{L}$ with $\boldsymbol{\Omega} \mapsto -\boldsymbol{\Omega}$,
- $\mathcal{S}^+$ is $\mathcal{S}$ with $\boldsymbol{\Omega} \mapsto -\boldsymbol{\Omega}'$ and $\boldsymbol{\Omega}' \mapsto -\boldsymbol{\Omega}$,
- $Q^+(\boldsymbol{x}, \boldsymbol{\Omega})$ is $D(\boldsymbol{x}, \boldsymbol{\Omega})$.

Furthermore, the applicable boundary conditions for (10.11) at $z = 0, H$ express that no adjoint radiance I^+ *escapes* the medium M.

In other words, when going from the direct to adjoint transport problems, light sources and detectors reverse their roles and, correspondingly, the direction

[52] The Gamma-weighting parameter $a = 9$ for the model in Fig. 5.26, generally less in real Sc.

of propagation is reversed in space and in scattering. While the response in (10.13) describes how an arbitrary sensing device samples the radiance field, it also describes how the adjoint radiance samples an arbitrary distribution of sources. Consequently, adjoint radiance is often called 'importance' (of any localized source for a given detector).

Now suppose we are interested in the nadir radiance generated by reflected sunlight, as can be observed from space, at a horizontal position $\overrightarrow{\rho}_{\mathrm{obs}}$. We then have $Q(\boldsymbol{x}, \boldsymbol{\Omega}) = F_0 \delta(z) \delta(\boldsymbol{\Omega} - \boldsymbol{\Omega}_0)$ and $D(\boldsymbol{x}, \boldsymbol{\Omega}) = \delta(z) \delta(\overrightarrow{\rho} - \overrightarrow{\rho}_{\mathrm{obs}}) \delta(\boldsymbol{\Omega} - \hat{\mathrm{z}})$, noting that both distributions at $z = 0$ can also be expressed in the boundary conditions. This means that (10.11) is the adjoint counterpart of the defining RT equation for the spatial Green function. Therefore, $I^+ \equiv G^+$ in the present problem.

Adjoint perturbation theory seeks to determine the deviation δE of E in (10.13) with respect to some known 'base case' when Λ goes from Λ_{b} to $\Lambda_{\mathrm{b}} + \delta\Lambda$ (and similarly for the adjoints). In the present problem of 3D RT effect quantification, we naturally take Λ_{b} as the uniform plane-parallel case, while $\delta\Lambda$ captures deviations from uniformity in the extinction and scattering coefficients and the ensuing horizontal gradients. Assuming uniform scattering properties (only extinction varies), this operator perturbation is

$$\delta\Lambda = \eta \frac{\partial}{\partial \overrightarrow{\rho}} + \delta\sigma(\boldsymbol{x}) \left(1 - \varpi_0 \int\limits_{4\pi} p(\boldsymbol{\Omega}' \cdot \boldsymbol{\Omega})[\cdot] \, \mathrm{d}\boldsymbol{\Omega}' \right), \tag{10.14}$$

where $\delta\sigma(\boldsymbol{x}) = \sigma(\boldsymbol{x}) - \overline{\sigma}$.

A general result from perturbation theory is that [241]

$$\delta E = -(I_{\mathrm{b}}^+, \delta\Lambda I_{\mathrm{b}}) \tag{10.15}$$

to a first-order approximation. For the present problem in remote sensing of heterogeneous clouds, we have $I_{\mathrm{b}}^+ = G_{\mathrm{b}}^+$, the adjoint Green function for an adjoint source at a roaming point on the illuminated boundary. The above expression (10.15) therefore reads in (x, y)-space as the convolution product of G_{b}^+ with $\delta\Lambda I_{\mathrm{b}}$. We note immediately that the horizontal gradient term in (10.14) contributes nothing to $\delta\Lambda I_{\mathrm{b}}$ since the base-case radiance field is invariant under arbitrary horizontal translation.

Such convolutions are of course best done in Fourier space, which is precisely where we can obtain closed-form expressions for Green functions in the diffusion/P_1 approximation. Assuming a non-absorbing wavelength in the example of the nadir-viewing satellite imager probing an heterogeneous cloud layer, we could determine G_{b}^+ in Fourier space from the following system of ODEs

$$\begin{aligned} -\tilde{F}_z^{+\prime} &= -[k^2/3(1-g)\overline{\sigma}] \, \tilde{J}^+ + \overline{\sigma} \, \mathrm{e}^{-\overline{\sigma} z}, \\ -\tilde{J}^{+\prime}/3 &= -(1-g)\overline{\sigma} \, \tilde{F}_z^+ + g\overline{\sigma} \, \mathrm{e}^{-\overline{\sigma} z}, \end{aligned} \tag{10.16}$$

subject to

$$\tilde{J}^+ - 2\tilde{F}_z^+ \Big|_{z=0} = 0, \;\; \tilde{J}^+ + 2\tilde{F}_z^+ \Big|_{z=H} = 0. \tag{10.17}$$

Note the changes in sign with respect to (5.15) and (5.17) that are dictated by the time-reversal implicit in adjoint transport. The solution of this problem has about the same complexity as the one presented in Appendix C.

Since the receivers in the direct problem in section 5.5.3 measure radiation density J inside the medium and hemispherical boundary fluxes $F_{\pm z}$, the easiest sources to model here are isotropic, either internal or at a boundary. The expression for $I_{\rm b}$ has to take this into account. It can of course also be estimated within the same diffusion approximation. In that case, we would turn to the solution of (5.1), when $\sigma_{\rm a}^{(\rm e)} = 0$, subject to (5.2), with $\chi = 2/3$, for a uniform boundary source at $z = 0$; for an internal source distributed evenly over a horizontal plane at $z = z_0$, we would use (6.4)–(6.5), with the same restrictions.[53]

Recalling that the angular integral implicit in (10.15) is easily carried out in the diffusion limit, cf. (4.12)–(4.13), the beginning-to-end computation of the 3D RT effect captured by δE can be done analytically. This is unique in the 3D RT literature, which is dominated by numerical techniques.

For a glance at computational recipes for higher-order perturbations in 3D RT, we refer to Box et al. [243]. It is instantly clear that Green functions play a central role, much like propagators in perturbation expansions used in quantum mechanics. Incidentally, for domain-average 3D RT effects, the first-order estimate in (10.15) is zero because the integrated contribution of the second term in (10.14) vanishes identically. Thus, according to adjoint perturbation theory, large-scale 3D RT effects are second-order at best. This is corroborated by countless numerical experiments: the domain-average impact of 3D RT is accurately captured by the IPA. Physically, the local horizontal fluxes will indeed lead to both positive and negative deviations from the 1D RT prediction that tend to cancel upon spatial integration.

This leads us to the idea of using the IPA as the base case instead of the strictly uniform plane-parallel medium. Details for this approach are out of the scope of the present review; we refer to Polonsky et al. [244]. However, the three panels of Fig. 5.29 illustrate the power of the IPA-based adjoint perturbation approach to 3D RT using a cloud model adapted from the two-dimensional 'Case 2' stratus cloud of the Intercomparison of 3D Radiation Codes (I3RC) project [246]. Rather than the boundary-leaving radiance of interest in cloud remote sensing, this computation was for the redistribution of the solar heating inside the cloud due to 3D RT, namely, $J(x, z)$. Both perturbation and 3D RT results are reduced to the uniform plane-parallel result based on the mean optical depth. Being based on an implementation in code of closed-form expressions, the perturbation estimate is instantaneous in comparison with the full 3D RT estimate. At the same time, most of the 3D RT effect is reproduced in the right locations.

5.11 Summary and outlook

Our primary goal in this review was to establish the sweeping utility of radiative Green functions in both passive and active cloud remote sensing, extended to in-cloud radiometry and used to retrieve cloud properties. We naturally pursue those

[53] More sophistication is required to account for slant illumination, not for the base-case radiance (where the diffusion solution for a slant uniform collimated beam is well-known), but for the adjoint Green function (where a superposition of spatially distributed isotropic *and* anisotropic detectors along a narrow line is in order).

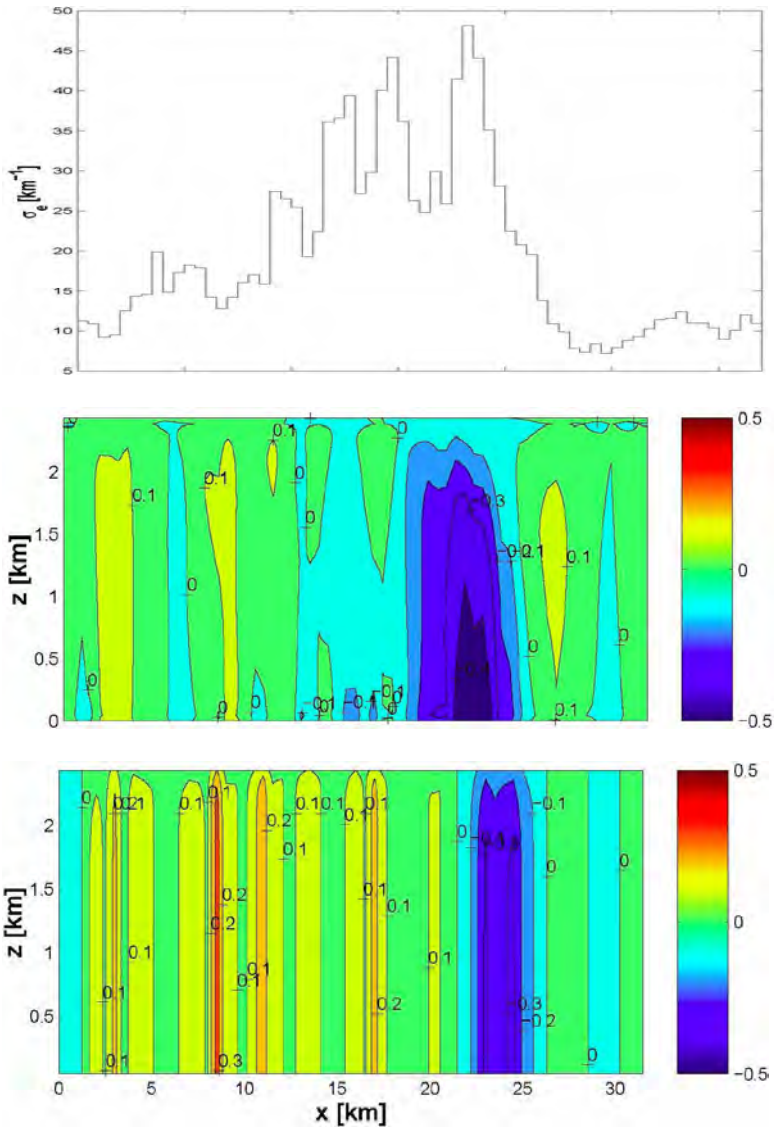

Fig. 5.29. *Adjoint perturbation approach to 3D RT.* Top: Cloud model structure varies only in one horizontal (x) direction, from $x = 0$ to $x = 32$ km (periodic replication beyond and before); the local value of the extinction plotted here is uniform in the vertical (z) direction, from $z = 1$ km to $z = 2.2$ km hence $H = 1.2$ km (the rest of the $0 < z < 2.5$ km domain is empty). Middle: $J(x, z) - J_{1D}(z)$ is plotted for the SHDOM estimate. Bottom: Same as above, but for the adjoint perturbation estimate. These panels are reproduced with permission from Ref. [244].

properties of importance in climate science. The parameters of an opaque stratiform cloud of primary interest here are therefore, beyond the cloud's altitude, its physical thickness H and optical thickness τ (equivalently, its volume-averaged extinction coefficient $\overline{\sigma} = \tau/H$). Properties of secondary interest address internal variability of the cloudy medium, both cloud-scale stratification and small-scale random fluctuations driven respectively by radiation/convection processes and inescapable turbulence.

For the remote sensing of cloud particle size, also an essential quantity in climate and precipitation studies, we point the interested readers to the appropriate passive and active techniques. These methods capitalize either on polarization [247] or wavelengths where condensed water has non-negligible absorption (sensitive to particle effective radius) [210], primarily in passive approaches, or on the multiple-scattering lidar signal coming from short times/ranges and, therefore, from very near the laser beam. In the latter active approaches, that early/near-beam signal is indeed dominated by the phase function, especially the forward diffraction peak (itself sensitive to the particle size distribution) [184]. Neither polarization (a means of selecting low orders of scattering), nor strong particle absorption processes, nor small-angle scattering are amenable to diffusion-based modeling presented here for conservative scattering. They are all serviced, however, by Green function theory in the broader framework of radiative transfer, including diffusion in the presence of weak absorption; see, for example, [248] on polarization, [249] on absorption, [250] on forward scattering.

Our focus has been exclusively on optical wavelengths in the visible and near-IR where one can confidently assume that absorption by cloud particles is small and often negligible. Scattering therefore dominates the radiation transport and, consequently, the physics of radiometry signals. Indeed we soon made the safe assumption for sufficiently opaque clouds – when it is all but impossible to see where the sun comes from in transmission ($\tau \gtrsim 9$) – that diffusion theory can be used to model the multiple scattering. The main benefit of this classic approximation is that, in many relevant situations, the Green functions can be computed analytically; either in closed-form for direct comparison with observations, or else their space-time moments can be expressed analytically and compared with observational estimates. In this respect, we have simply opened new space-time dimensions in radiative transfer models that have already served the GCM community very well for uniform and steady sources, namely, the solar flux.

Another one of our goals was to show that the diffusion-theoretical approach to Green function estimation provides a powerful signal modeling framework, built largely with computer-assisted symbolic math, that unifies very diverse modalities in the remote sensing of clouds. There are at least two emerging technologies that directly target the Green functions in space and/or time: (1) multiple-scattering cloud lidar with a very wide FOV, and (2) high-resolution differential absorption spectroscopy in the oxygen A-band. We have discussed implementations of these techniques from ground, space, and aircraft, each platform having its own particularities. In airborne systems, we include those designed to work from inside the cloud itself. The signal from so-called 'in situ' cloud lidar – and probably *in situ* O_2 A-band spectroscopy as well – contains information to glean about the macroscopic cloud structure, thus complementing the usual microphysics instrumentation car-

ried by aircraft into the depths of clouds to sample particle sizes, composition, and so on.

It is not common, at least in atmospheric science, that the kind of advanced radiative transfer theory surveyed herein influences major thrusts in instrument development. Yet that is precisely what happened in the case of multiple-scattering cloud lidar, as well as for the cloud remote sensing application of oxygen A-band spectroscopy. We wish to reinforce this theory-driven approach to innovation in the design of actual instruments and/or algorithms for data exploitation. To this effect, we have (1) revisited better-established methodologies in cloud remote sensing, showing them to rely implicitly on Green function formalism, and (2) pointed out throughout this review a number of avenues yet to be explored. Some of these proposed optical observation techniques target unknown sources below or imbedded in clouds, for example, lightning strokes. Others simply look for cloud-like media in Nature: turbid coastal waters, snow packs, sea-ice floes [251], dense vegetation canopies [252], etc. We have no doubt that, some day, lidars with multiple scattering capability will probe Europa's ice cover, Titan's thick haze, and worlds beyond.

Meanwhile, back on planet Earth, there are applications of atmospheric optics that are not driven by meteorology or climate science. Visibility studies come to mind. It has been shown that a large proportion of small aircraft crashes – too often with fatalities – are due to pilot error that could be avoided with better knowledge of the prevailing low-visibility conditions. Multiple-scattering lidars are not expensive compared to both the cost of even a single accident and that of the competing technology in active cloud probing, mm-wave radars.[54] So small airports, including aircraft carriers, will eventually be outfitted with such instruments that reliably deliver immediately actionable diagnostics on low clouds and fog. First responders on all-weather rescue missions can also benefit from real-time quantitative knowledge of reduced visibility conditions. And what if that approaching aerosol cloud is transporting a toxin?

For this potentially life-saving diagnostic, we can take a clue from recent developments in medical optics. Multiple-scattering cloud lidar was developed simultaneously and independently of optical tomography (OT), although they share a large amount of signal physics. OT [255] uses light diffusely transmitted through soft tissue, which is highly scattering in the near-IR, to locate and gauge anomalous (absorbing or vacuous) inclusions indicative of pathology, for example, aneurysms and tumors. This is made possible by fast and widely available numerical solvers for Laplace's equation with a given, although nontrivial, outer geometry and arbitrary internal boundaries; the latter are varied until the forward model fits the radiometric (Green function) data from as many source and sensor positions as necessary.[55] OT has made tremendous progress as a low-resolution but inherently

[54]The strategy in mm-wave cloud radar is to retain the single-scattering radar/lidar equation, and therefore to seek a wavelength in the electromagnetic spectrum where its assumptions are valid [148,253]. This leads to ∼mm wavelengths, with the extra burden on theory to connect radar reflectivities from cloud droplets ($\propto \overline{r^6}$) to properties of interest in the radiation budget ($\overline{r^2}$) and hydrology ($\overline{r^3}$) [254].

[55]In this picture, multiple-scattering cloud lidar determines the unknown distance of the *absorbing* cloud boundary opposite the laser source, as well as the unknown opacity of the cloud in between. With very restricted Green function sampling by OT standards,

non-invasive medical imaging technique. A relatively recent development, reviewed in this volume by Klose [256], is inspirational for our problem of detecting toxic material in an optically thick cloud of scattering particles from a safe stand-off distance: we can excite fluorescence with the laser light scattered throughout the cloud, and tune the detectors to the tell-tale fluorescence wavelengths.

Finally, the scope of this survey was limited to 'normal' diffusion modeling, i.e., amenable to classic PDEs and closely related to standard random-walk theory (used, for example, in Appendix E to derive a coarse but insightful characterization of Green functions based on their asymptotic scaling behavior). Furthermore, cloud structure was limited to horizontal plane-parallel slabs with random 3D opacity fluctuations around a deterministic stratification in the vertical. Although the climatically and hydrologically important class of single-layer stratocumulus clouds can be represented in this framework, many other cloud types require full-blown 3D radiative transfer with time-dependence. Yet Green functions can still be brought to bear on this more complex cloudiness, and analytical results (supported by real-world observations) are achievable using 'anomalous' diffusion; a brief overview is provided in Appendix F.

In conclusion, we strongly advocate systematic exploitation of multiple-scattering Green functions, particularly for boundary sources and boundary fluxes, which apply most directly to remote sensing. In the case of the dense clouds that have so far been our foremost concern, they have proven useful far beyond the effort invested in a refresher in mathematical physics. We are confident that many other insights and applications will follow. We also advocate hierarchical modeling frameworks in any application area. In our case, the fact that we have approaches to Green function computation that range from back-of-envelope estimations to detailed numerical simulations of radiation transport physics has enabled us to advance with confidence into quite foreign territory, for instance, completely new instrument concepts.

Acknowledgments

This research was supported largely by the Office of Biological and Environmental Research of the U.S. Department of Energy as part of the Atmospheric Radiation Measurement Program. The authors also acknowledge financial support from NASA's Radiation Sciences Program and from Los Alamos National Laboratory's Lab-Directed Research & Development (LDRD) Programs. Publication of this paper was supported by the JPL, Caltech, under a contract with the National Aeronautics and Space Administration. We thank Howard Barker, Luc Bissonnette, Craig Bohren, Hartmut Bösch, Michael Box, Bob Cahalan, Brian Cairns, Christine Chiu, Dave Crisp, Ed Eloranta, Frank Evans, Nicolas Ferlay, Philip Gabriel, Barry Ganapol, Mike Hall, Lee Harrison, Robin Hogan, Yongxiang Hu, Yuri Knyazikhin, Alexander Kokhanovsky, Ed Larsen, Paul Lawson, Jim Liljegren, Steve Love, Matt McGill, Qilong Min, Michael Mishchenko, Dennis O'Brien, Lazaros Oreopoulos, Klaus Pfeilsticker, Gilles Roy, Christian von Savigny, Jim Spinhirne, Graeme Stephens, Tamas Várnai, Jim Weinman, Dave Winker, Warren Wiscombe, Yuekui Yang, and Eleonora Zege for many fruitful discussions.

one has to make assumptions about inner and outer cloud structure, as described in the main text.

A Responses $\tilde{T}(k)$ and $\tilde{R}(k)$ for horizontal transport away from an isotropic boundary source in stratified clouds

A.1 Definitions

We recall from Bessel function theory [110] that

$$I_n(x) = \mathrm{i}^{-n} J_n(+\mathrm{i}x),$$

and we define by analogy

$$X_n(x) = \mathrm{i}^{+n} Y_n(-\mathrm{i}x),$$

as an alternative modified Bessel function of the second kind; like $I_n(x)$, it is a real-valued function for real-valued x. We also define

$$\begin{aligned} f(x, y; z) &= xI_0(z) + yI_1(z), \\ g(x, y; z) &= xX_0(z) + yX_1(z). \end{aligned}$$

Finally, we define

$$\begin{aligned} D_F(kH; \tau_\mathrm{t}/2\chi, \Delta) = {} & f(+kH, (2+\Delta)\tau_\mathrm{t}/2\chi; (2/\Delta+1)kH/2) \\ & \times g(-kH, (2-\Delta)\tau_\mathrm{t}/2\chi; (2/\Delta-1)kH/2) \\ & + f(-kH, (2-\Delta)\tau_\mathrm{t}/2\chi; (2/\Delta-1)kH/2) \\ & \times g(-kH, (2+\Delta)\tau_\mathrm{t}/2\chi; (2/\Delta+1)kH/2). \end{aligned}$$

A.2 Transmitted light

As required in section 5.5.2, the definition in (4.51) leads to

$$\tilde{T}(kH; \tau_\mathrm{t}/2\chi, \Delta) = \frac{8}{\pi} \times \frac{\Delta\, \tau_\mathrm{t}/2\chi}{D_F(kH; \tau_\mathrm{t}/2\chi, \Delta)}. \tag{A.1}$$

A.3 Reflected light

Similarly, the definition in (4.50) leads to

$$\tilde{R}(kH; \tau_\mathrm{t}/2\chi, \Delta) = \frac{N_R(kH; \tau_\mathrm{t}/2\chi, \Delta)}{D_F(kH; \tau_\mathrm{t}/2\chi, \Delta)}, \tag{A.2}$$

where

$$\begin{aligned} N_R(kH; \tau_\mathrm{t}/2\chi, \Delta) = {} & f(-kH, (2+\Delta)\tau_\mathrm{t}/2\chi; (2/\Delta+1)kH/2) \\ & \times g(+kH, (2-\Delta)\tau_\mathrm{t}/2\chi; (2/\Delta-1)kH/2) \\ & + f(+kH, (2-\Delta)\tau_\mathrm{t}/2\chi; (2/\Delta-1)kH/2) \\ & \times g(+kH, (2+\Delta)\tau_\mathrm{t}/2\chi; (2/\Delta+1)kH/2). \end{aligned}$$

B Responses $\hat{T}(s)$ and $\hat{R}(s)$ for pulse stretching for an isotropic boundary source in stratified clouds

B.1 Definitions

For a given cloud (τ_t, Δ) and χ, we define the following eight functions of $s' = s/c$, i.e., the Laplace conjugate variable for path ct (expressed in 1/m):

$$A_n^{\pm}(s'H; \tau_t, \Delta) = \frac{1}{\Gamma(n/3)}\, {}_0F_1\left(\frac{n}{3}; \frac{\tau_t\, s'H}{3\Delta^2}\,(1 \pm \Delta)^3\right),\ n = 1, 2, 4, 5,$$

where $\Gamma(a)$ is Euler's Gamma function and ${}_0F_1(a, x)$ is the confluent hypergeometric function. We also define

$$\begin{aligned} D_F(s'H; \tau_t, \chi, \Delta) \;=\; & \left(A_1^- - [\chi s'H(1-\Delta/2)/\Delta]A_4^-\right) \\ & \times \left(A_2^+ + [\tau_t(1+\Delta/2)^2/3\chi\Delta]A_5^+\right) \\ & + \left(A_1^+ + [\chi s'H(1+\Delta/2)/\Delta]A_4^+\right) \\ & \times \left(A_2^- - [\tau_t(1-\Delta/2)^2/3\chi\Delta]A_5^-\right). \end{aligned}$$

B.2 Transmitted light

As required in section 5.5.2, the definition in (4.51) leads to

$$\hat{T}(s'H; \tau_t, \chi, \Delta) = \frac{\sqrt{3}}{\pi} \times \frac{1}{D_F(s'H; \tau_t, \chi, \Delta)}. \tag{B.1}$$

B.3 Reflected light

Similarly, the definition in (4.51) leads to

$$\hat{R}(s'H; \tau_t, \chi, \Delta) = \frac{N_R(s'H; \tau_t, \chi, \Delta)}{D_F(s'H; \tau_t, \chi, \Delta)}, \tag{B.2}$$

where

$$\begin{aligned} N_R(s'H; \tau_t, \chi, \Delta) \;=\; & \left(A_1^- + [\chi s'H(1-\Delta/2)/\Delta]A_4^-\right) \\ & \times \left(A_2^+ - [\tau_t(1+\Delta/2)^2/3\chi\Delta]A_5^+\right) \\ & + \left(A_1^+ - [\chi s'H(1+\Delta/2)/\Delta]A_4^+\right) \\ & \times \left(A_2^- + [\tau_t(1-\Delta/2)^2/3\chi\Delta]A_5^-\right). \end{aligned}$$

C Responses $\tilde{T}(k)$ and $\tilde{R}(k)$ for steady illumination by a normally incident pencil-beam

C.1 Definitions

It is of interest to compare the system of ODEs at hand in (5.15) with the classic two-stream model (cf. Appendix D). Indeed, if one can find an analogous choice

of parameters, even allowing for an alternative choice of g and (more formally) for $\mu_0 \neq 1$, then one would have a solution. However, no such choice of ODE parameters exists because our *effective* absorption coefficient, $\sigma_{\mathrm{a}}^{(e)} = k^2/[3(1-g)\sigma]$, contributes neither to the inverse of the diffusivity constant, which multiplies F_z in the constitutive equation (the lower one), nor to the extinction coefficient in the exponential source terms. Thus, there are too many constraints, and we therefore need solve the stated ODEs directly.

We are brought to define

$$\begin{aligned} D_F(kH;\tau,g) \,=\, & \left[\tau^2 - (kH)^2\right] \\ & \times \left[(3(1-g)\tau + 2kH)^2 - (3(1-g)\tau - 2kH)^2\ \mathrm{e}^{-2kH}\right]. \end{aligned}$$

C.2 Transmitted light

Define

$$\begin{aligned} N_T(kH;\tau,g) \,=\, & \tau \times \\ & \Big[-\ (\tau + kH)(3(1-g)\tau + 2kH)(3(1-g)\tau + gkH) \\ & \quad +\ 2kH(3(5 - g(7-2g))\tau^2 + 2(kH)^2)\ \mathrm{e}^{-kH} \\ & \quad +\ (\tau - kH)(3(1-g)\tau - 2kH)(3(1-g)\tau - gkH)\ \mathrm{e}^{-(\tau+kH)}\Big]. \end{aligned}$$

Applying the definition in (4.49), as required in section 5.5.3, with $\mu_0 = 1$ (and $s = 0$), for diffuse transmittance then leads to

$$\tilde{T}(kH;\tau,g) = \mathrm{e}^{-\tau} + \frac{N_T(kH;\tau,g)}{D_F(kH;\tau,g)} \tag{C.1}$$

for total (direct + diffuse) transmittance.

C.3 Reflected light

Define

$$\begin{aligned} N_R(kH;\tau,g) \,=\, & \tau \times \\ & \Big[-\ (\tau - kH)(3(1-g)\tau - 2kH)(3(1-g)\tau + gkH) \\ & \quad +\ (\tau + kH)(3(1-g)\tau - 2kH)(3(1-g)\tau - gkH)\ \mathrm{e}^{-kH} \\ & \quad +\ 2kH(3(1 - g(3-2g))\tau^2 - 2g(kH)^2)\ \mathrm{e}^{-(\tau+kH)}\Big]. \end{aligned}$$

The definition in (4.48), as required in section 5.5.3, with $\mu_0 = 1$ (and $s = 0$), then leads to

$$\tilde{R}(kH;\tau,g) = \frac{N_R(kH;\tau,g)}{D_F(kH;\tau,g)} \tag{C.2}$$

for reflectance.

D Responses $\hat{T}(s)$ and $\hat{R}(s)$ for pulsed normal or oblique uniform illumination

D.1 Definitions

The 'Eddington' (diffusion-based) version of the classic two-stream model for steady-state solar radiation transport in uniform plane-parallel clouds is, at first glance at least, a resource. This is especially attractive since we have easy access to Meador and Weaver's definitive treatment. In our notations, this problem is described by this system of first-order ODEs:

$$\begin{aligned} F_z' &= -\sigma_\mathrm{a} J + \sigma_\mathrm{s}\, \mathrm{e}^{-(\sigma_\mathrm{s}+\sigma_\mathrm{a})z/\mu_0}, \\ J' &= -3[(1-g)\sigma_\mathrm{s} + \sigma_\mathrm{a}]F_z + 3\mu_0 g\sigma_\mathrm{s}\, \mathrm{e}^{-(\sigma_\mathrm{s}+\sigma_\mathrm{a})z/\mu_0}. \end{aligned}$$

They are subjected to the same boundary conditions in (5.17) as our model from section 5.5.3, bearing in mind that Meador and Weaver's cloud optical depth $\tau' = \tau + \sigma_\mathrm{a} H$. The case of normal incidence ($\mu_0 = 1$) is of particular interest in the application covered in section 5.9.

Comparison of the above classic two-stream problem and the system of present interest in (5.22) shows that there is no simple analogy to be made because $s' = s/c$, the *effective* absorption coefficient, does not contribute to the inverse of diffusivity that multiplies F_z in the constitutive equation (the lower one). A formal analogy can nonetheless be made, but at the cost of recasting the asymmetry factor as $g^\star$ in Meador and Weaver's expressions. We would then use $\sigma_\mathrm{a} = s'$ and $\sigma_\mathrm{s} = \sigma$, hence SSA (in Meador and Weaver's notation) $\omega_0 = 1/(1 + s'/\sigma) \le 1$, with $g^\star = g/(1 - gs'/\sigma) \ge g$ (its magnitude can exceed unity!) and $\tau' = \tau + s'H$. We can exploit this approach, or solve the stated ODEs directly.

In the end, we define

$$\begin{aligned} D_F(s'H;\tau,g,\mu_0) &= \sqrt{3(1-g)\tau s'H} \\ &\times \left(\tau^2 + \tau s'H(2 - 3(1-g)\mu_0^2) + (s'H)^2\right) \\ &\times \Big[(3(1-g)\tau + 4s'H)(1 - \mathrm{e}^{-2\sqrt{3(1-g)\tau s'H}}) \\ &+ 4\sqrt{3(1-g)\tau s'H}(1 + \mathrm{e}^{-2\sqrt{3(1-g)\tau s'H}})\Big]. \end{aligned}$$

D.2 Transmitted light

Applying the definition in (4.49), as required in section 5.5.5, with $\mu_0 \le 1$ (and $k = 0$), for diffuse transmittance then leads to

$$\hat{T}(s'H;\tau,g,\mu_0) = \mathrm{e}^{-\tau'/\mu_0} + \frac{N_T(s'H;\tau,g,\mu_0)}{D_F(s'H;\tau,g,\mu_0)} \tag{D.1}$$

for total (direct + diffuse) transmittance, where

$$
\begin{aligned}
N_T(s'H;\tau,g,\mu_0) \;=\; & 3\tau s'H \times \Big[((1+2\mu_0-3g\mu_0^2)(1-g)\tau \\
& -\; (2g\mu_0)s'H-(1-g)\tau^2) \\
& \times\; \sqrt{3(1-g)\tau s'H}(1-\,\mathrm{e}^{-2\sqrt{3(1-g)\tau s'H}})\,\mathrm{e}^{-(\tau+s'H)/\mu_0} \\
& -\; [(2+3\mu_0)\tau+(2+3g\mu_0(1+2\mu_0))s'H]\times(1-g)\tau \\
& \times\; ((1+\,\mathrm{e}^{-2\sqrt{3(1-g)\tau s'H}})\,\mathrm{e}^{-(\tau+s'H)/\mu_0}-2\,\mathrm{e}^{-\sqrt{3(1-g)\tau s'H}})\Big].
\end{aligned}
$$

D.3 Reflected light

The definition in (4.48), as required in section 5.5.5, with $\mu_0 \le 1$ (and $k = 0$), leads to

$$
\hat{R}(s'H;\tau,g,\mu_0) = \frac{N_R(s'H;\tau,g,\mu_0)}{D_F(s'H;\tau,g,\mu_0)} \tag{D.2}
$$

for reflectance, where

$$
\begin{aligned}
N_R(s'H;\tau,g,\mu_0) \;=\; & 3\tau \times \Big[\sqrt{3(1-g)\tau s'H}[(1-g)\tau^2-g\mu_0 s'H] \\
& -\; \tau s'H[(1-g)\tau(3\mu_0-2) \\
& +\; \sqrt{3(1-g)\tau s'H}(2\mu_0-(1-g)(1+3g\mu_0^2))] \\
& \times\; \left(1+\,\mathrm{e}^{-2\sqrt{3(1-g)\tau s'H}}\right) \\
& -\; (1-g)\tau(s'H)^2[2+3g\mu_0(2\mu_0-1)] \\
& \times\; \left(1-\,\mathrm{e}^{-2\sqrt{3(1-g)\tau s'H}}\right) \\
& -\; 2(1-g)\tau s'H[2-3g\mu_0(2\mu_0-1)+(2-3\mu_0)\tau] \\
& \times\; \mathrm{e}^{-\sqrt{3(1-g)\tau s'H}}\Big].
\end{aligned}
$$

E Scaling exponents for diffusive Green function moments from the random walk approach

In this extensive survey of diffusion theory in application to multiple-scattering Green function estimation, we have systematically used Monte Carlo simulation to validate numerically the radiative transfer approximation leading to convenient closed-form results. It is informative to go to the other extreme of this hierarchy of Green function modeling and perform a highly simplified version of MC simulation analytically, namely, estimate statistical properties of random (a.k.a. drunkard's) walks. This approach reveals the physical essence of the problem of transport in dense clouds. In particular, one can derive the scaling exponents for $\tau_\mathrm{t} = (1-g)\tau$ in all the dominant terms of the expressions we have derived for Green function moments, viz. (8.3)–(8.5) for transmitted light and (8.10)–(8.12) for reflected light. The same scaling appears in all other such groupings based on more sophistication in the cloud or source representation: the novelty affects only pre-factors and pre-asymptotic corrections.

We note that in random walk theory τ_t is the ratio of the only two scales that matter:

– H, the outer scale (size of the domain bounding the stochastic process);
– $\ell_{\rm t}$, the inner scale (one MFP for an effectively isotropic scattering).

The latter scale defines diffusivity $D = c\ell_{\rm t}/3$ in three spatial dimensions.

E.1 Caveat about photons as 'particles' of light

The term 'photon' was coined by Gilbert Lewis in 1926 to describe the quantum of the electromagnetic field, of which light is a prime example. Even if this so-called 'second quantification' assigns energy $E = h\nu$, momentum $\boldsymbol{p} = \boldsymbol{\Omega}h/\lambda$, and spin $S = \pm h$ to photons, it is fundamentally incorrect to think of them as either classic or quantic particles traveling through space-time at velocity c. For instance, by definition, it is not the same photon that is incident and re-emitted by a scattering entity. Photons can populate energy levels in, for example, thermal sources and laser cavities; they can also be detected using photoelectric materials. In between, it is light – not photons – that propagates in optical media according to the laws of radiative transfer theory, which is a nontrivial construct from *statistical* optics [5]. The radiance field predicted by the radiative transfer equation, and associated boundary conditions, is only a probability of detecting a photon (per photon emitted at the source) with a roaming virtual instrument.

In Monte Carlo computation, it is very tempting to talk about the 'photons' launched in a simulation. This should be avoided, proper terminology is 'histories' or 'trajectories' or 'realizations'. Recall that Monte Carlo is only a random quadrature approach for estimating integrals over radiances. The random walk theory presented here is basically a poor person's Monte Carlo: too poor to own a computer, and only has some elements of probability theory to work with. So, although strongly reminiscent of wandering particles, we are dealing with light intensities, to be interpreted as probability densities for detection events.

E.2 Elements of Brownian motion theory

In boundary-free homogeneous 3D space, an isotropic source at $x = y = z = 0$ emits a diffusing 'wavefront' of particles propagating at a decreasing 'velocity' such that the mean distance from the origin, $\approx\sqrt{\langle \boldsymbol{r}^2\rangle}$, grows only as $\sqrt{Dt}$. This is just a reading of the classic unbounded diffusion relation [257]

$$\langle \boldsymbol{r}^2\rangle = 6Dt, \tag{E.1}$$

which results directly from the well-known Green function for the basic diffusion equation for particle density $n(t,\boldsymbol{r}) = J(t,\boldsymbol{r})/c$: $[\partial_t + D\nabla^2]n = \delta(t)\delta(\boldsymbol{r}) \Leftrightarrow n(t,\boldsymbol{r}) = {\rm e}^{-r^2/4Dt}/(\pi 4Dt)^{3/2}$, as stated in (7.2) for the short-time/near-field *in situ* cloud lidar signal.

In the statistical physics of Brownian motion, a lesser known but extremely useful result is the 'law of first returns' [258]. Focusing, for simplicity on 1D random walks (where $D = c\ell_{\rm t}$) along the z-axis, we seek the PDF of $t > 0$, the random epoch when the coordinate of Brownian particle (that left $z = 0$ at $t = 0$) first changes sign. It can be shown [31, 259], that

$$\Pr\{t,\,\mathrm{d}t\} = \frac{c}{\sqrt{\pi}\ell_\mathrm{t}}\left(\frac{\ell_\mathrm{t}}{ct}\right)^{3/2}\mathrm{e}^{-\ell_\mathrm{t}/2ct}\,\mathrm{d}t$$
$$\sim \frac{\mathrm{d}t}{t^{3/2}}, \tag{E.2}$$

if we ignore the exponential cutoff at early times. This is an interesting PDF associated with the gambler's ruin problem: How long does it take a person who comes to the roulette table with $1, and always bets on 'red', to walk away with nothing. There is no mean time – it is divergent – and that may go a long way in explaining why gambling is addictive, and why casinos should never close. Before loosing everything in time with probability one to this casino with an infinite reserve, gains can be considerable.

The corresponding RT problem in this review is that of reflection from a semi-infinite ($H \to \infty$) non-absorbing medium, where $\langle ct\rangle$ is indeed infinite, as are all higher moments. Fractional-order moments of order $q < 1/2$ are, however, finite.

E.3 Transmitted light

Now $\boldsymbol{r}^2 = x^2 + y^2 + z^2$ and, by symmetry, all three components are equal in magnitude on average. Therefore, since $z = H$ where $\langle\rho^2\rangle_T$ is computed, $\rho^2 = x^2 + y^2 \approx H^2$. This immediately explains the independence of that moment in (8.5) with respect to cloud opacity, i.e., optical depth.

As soon as the diffusing wavefront reaches the opposite boundary, i.e., $t \approx 3H^2/D \sim H^2/c\ell_\mathrm{t} = (H/c) \times \tau_\mathrm{t}$ based on (E.1), we will detect the transmitted Green function. In other words, reinterpreting the fixed t in (E.1) as a random variable, we can anticipate $\langle ct\rangle_T/H \sim \tau_\mathrm{t}$. This expectation is confirmed by 'exact' (PDE-based) diffusion theory in (8.3).

There is no simple argument for the scaling of the second-order moment in time in (8.4). The fact that it goes as $\langle ct\rangle_T^2$ tells us that the distribution of arrival times at the boundary opposite the source of particles is relatively narrow.

It is interesting that we can estimate at least the scaling of Green function moments in transmission without knowledge of the overall probability of transmission for given H and $D = c\ell_\mathrm{t}/3$ (alternatively, $\tau_\mathrm{t} = H/\ell_\mathrm{t}$). This calls for the law of first returns in (E.2). Real clouds have finite physical and optical thicknesses and real casinos have finite banks. We can approximate the probability of transmission – breaking the casino's bank – by truncating the PDF in (E.2) at $\langle t\rangle_T \sim H^2/c\ell_\mathrm{t}$. This leads to

$$T \approx \Pr\{t > \langle t\rangle_T\} = \int\limits_{\langle t\rangle_T}^{\infty} \Pr\{t,\,\mathrm{d}t\}, \tag{E.3}$$

which scales as $\ell_\mathrm{t}/H = 1/\tau_\mathrm{t}$. That is indeed the asymptotic behavior for $T(\tau_\mathrm{t})$ in (5.5) and all other transmission laws we have come across for $\varpi_0 = 1$; see, for example, Fig. 5.15.

E.4 Reflected light

Temporal/path moments for reflected light can be estimated for a finite domain, namely, $0 < z < H$, by defining a *truncated* (and renormalized) version of the

PDF in (E.2) for the first-return process. Allowing time for the particle to return to $z = 0$ from almost being transmitted at $z = H$, we compute specifically

$$I_q = \int_0^{2\langle t\rangle_T} t^q \Pr\{t, \mathrm{d}t\},$$

$$\langle t^q\rangle_R \approx \frac{I_q}{I_0} \sim \left(\frac{\ell_\mathrm{t}}{c}\right)^{1/2} \left(\frac{H}{c\ell_\mathrm{t}}\right)^{q-1/2}, \tag{E.4}$$

where we have neglected the difference between I_0 and unity, namely, T in (E.3). Recalling that $H/\ell_\mathrm{t} = \tau_\mathrm{t}$, this leads to $\langle (ct)^q\rangle_R^{1/q} \sim H \times (\tau_\mathrm{t})^{1-1/q}$, as was found in the limit $\tau_\mathrm{t} \to \infty$ for (8.10)–(8.11) and all other reflection laws.

It is remarkable that the moments $\langle (ct)^q\rangle_R$ all scale differently with τ_t whereas we fully expect that $\langle (ct)^q\rangle_T \sim \langle ct\rangle_T^q$, for $q \geq 2$. We can trace this property to the mixture, made clear in (E.4), of short and long paths. We have emphasized several times in the main text how much this helps the cloud remote sensing enterprise.

As we did for the spatial Green function in transmission, we can roughly estimate the RMS value of ρ for reflection from (E.1), with $D \sim c\ell_\mathrm{t}$ and (E.4) for $q = 1$. We obtain $\langle \rho^2\rangle_R \sim D\langle ct\rangle_R \sim H\ell_\mathrm{t}$. In other words, the RMS ρ for reflected light goes as the harmonic mean of ℓ_t and H, the inner and outer scales of the diffusion problem at hand.

F Scaling exponents for time-domain anomalous diffusion by extending the random walk approach

F.1 Anomalous diffusion

At first glance, the problem of 3D RT through an atmospheric column populated with broken and/or multiple cloud layers seems intractable, except maybe with heavy-duty numerical methods. Depending on what radiative properties are targeted, that first impression may be quite inaccurate. For instance, Pincus, Barker, et al. [260, 261] developed (with GCMs in mind) the McICA model, a numerical but efficient and unbiased method of estimating large-scale boundary fluxes and flux-divergence profiles, hence radiative heating/cooling rates. McICA creatively merges the concepts

- of MC, viewed as a robust method of random quadrature (rather than a numerical solution of the 3D RT equation), and
- of IPA, appropriately renamed ICA (for independent *column* approximation) in this context of radiation energy budget computation where no pixels exist.

Moreover, two of the present authors have explored the alternate theory of 'anomalous' diffusion, which is still far from being well developed, for estimating large-domain/ensemble average fluxes (currently, only at the boundaries).

In their original paper, Davis and Marshak [80] generalized the random-walk approach used in Appendix E to situations where steps are usually small (inside

clouds) but not infrequently very large (between clouds). They assumed distributions of step size s with power-law tails, $\sim 1/s^{1+b}$, such that all moments of an order greater than $b > 1$ are divergent; it indeed seems natural to require that the MFP (average value of s) be finite. We continue to use here the transport MFP $\ell_\mathrm{t} = \langle s \rangle / (1-g)$ as the effective MFP for an isotropic scattering. Davis and Marshak then addressed finite cloudy media with slab geometry (thickness H), showing

1. that transmittance T_α scales as $\tau_\mathrm{t}^{-\alpha/2}$, and
2. that mean path for transmitted light $\langle ct \rangle_T$ goes as $H \times \tau_\mathrm{t}^{\alpha-1}$,

where $\tau_\mathrm{t} = H/\ell_\mathrm{t}$ is the total scaled optical depth of the variable cloudy layer, and $\alpha = \min\{b, 2\}$. These scaling laws revert to our present findings for any $b \geq \alpha = 2$ (cf. Appendix E). Succinct derivations of these generalized scaling laws are as follows:

– First, we need to consider Lévy's generalizations [31, 262, 263] of the central limit theorem. The standard result is that the variance of a sum of independent random variables is the sum of their variances, and it becomes normally distributed as the length of the sum increases without bound. But what if the variances are infinite? Then other cumulants than variance are additive, and the PDF of the (normalized) sum becomes asymptotically close to a class of distributions known as 'Lévy-stable'. These PDFs are parameterized in particular by the Lévy 'index' $\alpha < 2$, which is the order of the smallest diverging moment. Let z_n be the coordinate of a 1D random-walking Lévy particle after n isotropic scatterings, starting at $z_0 = 0$. In the absence of boundaries, it obeys

$$\langle (z_n/\ell_\mathrm{t})^\alpha \rangle \sim n. \tag{F.1}$$

  where $\alpha = \min\{b, 2\} \in (1, 2)$ (restricted here to cases where the MFP ℓ_t is finite). The angular brackets have a somewhat different meaning here: the above relation can be interpreted as an attempt to estimate the lowest (logarithmically) diverging moment of the symmetric (randomly oriented) steps $\pm s$ when $b < 2$ (step variance is then ∞), viz. $z_n/n = \sum_{i=1}^n \pm s_i/n$. This replaces $\langle z_n^2 \rangle =$ (variance of $\pm s$) $\times n$ in classic diffusion, the 1D equivalent in discrete time of $\langle z(t)^2 \rangle = \langle \boldsymbol{r}(t)^2 \rangle / 3 = 2\ell_\mathrm{t} ct$ from (E.1). Noting that $n \approx ct/\ell_\mathrm{t}$ if sufficiently large, we can now obtain from (F.1) the scaling of $\langle ct \rangle_T$ for a finite medium of thickness H and scaled optical depth τ_t: $H^\alpha \sim \ell_\mathrm{t}^\alpha \times (\langle ct \rangle_T / \ell_\mathrm{t})$, hence $\langle ct \rangle_T / H \sim \tau_\mathrm{t}^{\alpha-1}$. QED.

– Second, we need to update the continuous law of first returns in (E.2) for path ct in a semi-infinite domain with a discrete version for n:

$$\Pr\{n \geq N\} \sim N^{-1/2}, \tag{F.2}$$

  where n is the number of scatterings suffered by a light beam before crossing the $z = 0$ plane where it departed from. This expression is far more general than (E.2), which assumes Gaussian steps: (F.2) only only requires that the distribution of algebraic steps ($\pm s$) to be symmetric, i.e., $\pm$ with equal probability [264, 265]. By definition, transmittance is then $T_\alpha \sim \Pr\{n \gtrsim \langle ct \rangle_T / \ell_\mathrm{t}\}$, which equals $\tau_\mathrm{t}^{-\alpha/2}$. QED.

It is interesting to note that, in order to estimate a steady-state transport property like T_α, we need to go through the framework of time-dependent transport. Transport unfolds in time, even for steady sources.

F.2 Observational validation, and evolution toward anomalous transport

Surprisingly – or maybe not – empirical evidence has cumulated over the past decade that supports anomalous diffusion theory [161, 164, 165]. It is based on estimates of $\langle ct \rangle_T$ from ground-based O_2 A-band spectroradiometry collected under all kinds of cloudy skies; see section 5.3.1 and, for the special case of uniform clouds, section 5.8.2. Although that theory was first inspired by research in contemporary statistical physics [266], it was later justified by investigations of light propagation in random-but-correlated media[56] [10, 78, 79, 267, 268].

Further justification of the $P(s) \sim 1/s^{1+b}$ ansatz for RT in cloudy atmospheric columns comes in retrospect from the 1996 paper by Barker et al. [221]. Their finding of Gamma distributions for the optical depth in a wide variety of Landsat cloud fields can indeed be interpreted as an observation of Gamma-distributed optical paths across a *fixed* distance that happens to be H and happens to be along the vertical. Recall from section 5.10.3 that the Gamma distribution's parameters are the mean $\overline{\tau}$ and the variability parameter $a = 1/(\overline{\tau^2}/\overline{\tau}^2 - 1)$. We then find for mean *direct* transmittance

$$T_{\rm dir}(\overline{\tau}, a) = \overline{T_{\rm dir}(\tau)} = \int_0^\infty \exp(-\tau)\, \Pr\{\overline{\tau}, a; \tau, \mathrm{d}\tau\}$$
$$= \frac{1}{(1 + \overline{\tau}/a)^a}.$$

It is easy to verify that $T_{\rm dir}(\overline{\tau}, a) \to \exp(-\overline{\tau})$ as $a \to \infty$. The transmission law in (F.3) can in turn be interpreted as a new propagation kernel with a power-law tail that can be used in a mean-field 1D RT model. As shown by the first author in Ref. [81] using the more recent observational evidence [165], this anomalous *transport* model supersedes the older anomalous *diffusion* model where the steps are effectively Lévy stable; it is however, only a numerical recipe at present.

Interestingly, Barker et al.'s original goal was to motivate Barker's [216] Gamma-weighted two-stream model, which develops in the opposite logic: first solve the multiple-scattering 1D RT problem for cloud optical depth τ, then randomize the result and determine the domain average (cf. section 5.10.3). Here, we start by averaging the propagation kernel over the spatial disorder, then formulate

[56] Three of these papers were by Kostinski, Shaw, and Lanterman [78, 79, 267] who start from very general considerations in discrete-point statistics; these authors challenge the ability of 3D radiative transfer, a theory grounded in a continuum representation of optical media, to account for the likely deviations from Poissonian behavior that they speculate about. The last one in the chronological series is by two of the present authors [10] who pick up the challenge, and leave only media with the intriguing possibility of 'super-homogeneity' (i.e., negatively correlated particle positions discussed in Ref. [79]), as an open frontier for radiative transfer theory.

and solve the resulting new 1D RT equation that targets domain average fluxes, radiances, etc.

As competition for the anomalous diffusion/transport models in explaining the emerging cloudy-sky climatology of $\langle ct \rangle_T / H$ from O_2 A-band (it decreases as variability increases), we offer the Gamma-weighted diffusion model described in section 5.10.4. Equations (10.4) and (10.5) in the main text yield respectively

$$T \propto \tau_t^{-\min\{a,1\}} \text{ and}$$
$$\langle ct \rangle_T \propto \tau_t^{\min\{a,1\}}$$

in the limit of asymptotically large τ_t. Only future simulations and observations can help decide which is the more accurate representation of Nature's way of propagating solar radiation in the Earth's cloudy atmosphere.

Finally, the importance of pre-factors and pre-asymptotic behavior was amply demonstrated in the present survey. Since it is based entirely on classic diffusion theory, we are of course curious about how to predict them for its anomalous counterpart. The Gamma-weighted time-dependent diffusion model from section 5.10.4 delivers the desired pre-factors and pre-asymptotic corrections; see Fig. 5.25. Scholl et al. [165] propose an ad hoc hybrid of the scaling results from Davis and Marshak [80] and the details they obtained for homogeneous clouds [24]. At present, all we know [81, 269] is that a rigorous approach to anomalous transport theory will involve pseudo-differential equations (fractional-order PDEs [270]) that can be cast as integral equations with singular kernels. This program remains to be implemented.

List of abbreviations

nD	n-dimensional ($n = 1, 2, 3$)
3+1D	three-plus-one-dimensional (i.e., space-time)
BC	boundary condition
BRDF	bi-directional reflection distribution function
cw	continuous-wave (describes steady-source lasers)
FFT	Fast Fourier transform
FOV	field-of-view
GCM	Global Climate Model
GPS	Global Positioning System
H–G	Henyey–Greenstein (scattering or phase function) from Ref. [25]
IPA	independent pixel approximation
LWC	[kg/m^3] (cloud) liquid water content, $(4\pi/3)\overline{r^3}\times$ the density of water (10^3 kg/m^3 = 1 g/cm^3) $\times$ droplet concentration (1/m^3)
LWP	[cm] (cloud) liquid water path, LWC $\times H \approx (2/3)\tau r_e$ in the limit of large size parameters ($2\pi r/\lambda$)
MC	Monte Carlo
MFOV	multiple field-of-view (lidar)
MFP	mean-free-path
MTF	modulation transfer function
MuSCL	multiple-scattering cloud lidar
NIPA	nonlocal independent pixel approximation

ODE	ordinary differential equation
OT	optical tomography
PDE	partial differential equation
PDF	probability density function
PSF	point spread function
RMS	root-mean-square
RT	radiative transfer
Sc	stratocumulus, a frequent cloud formation (especially in the marine boundary layer) with relatively flat top and bottom, but often with quite variable opacity in between (observed to have long-range/fractal-like correlation structures).
SF	second-order structure function
SNR	signal-to-noise ratio
SSA	single scattering albedo
SZA	solar zenith angle
UAV	unmanned aerial vehicle

List of notations

a	[-] characteristic exponent in Gamma PDF, inverse of reduced variance
b	[-] generic exponent for PDFs with 'fat' tails, i.e., decaying in a power law with exponent $1+b$ (hence b for the cumulative probability of the random variable exceeding a given value)
c	[m/s] speed of light in vacuum
ct	[m] path-length of light since emission from pulsed source
$d_{\rm obs}$	[m] distance from remote observer to nearest cloud boundary
D	[m^2/s] radiative diffusivity, $c\ell_{\rm t}/3$
f	[-] fraction of forward vs. P_1 scattering in δ-Eddington rescaling
F	[J/s/m^2] generic for a hemispherical radiative flux, possibly space- or time-integrated
$\boldsymbol{F}$	[J/s/m^2] radiative vector (net) flux
g	[-] asymmetry factor of phase function
G	[J/s/m^2/sr] radiative transfer Green function, almost but not quite always for a boundary source and boundary observation
H	[m] physical thickness of (horizontal) plane-parallel cloud
I	[J/s/m^2/sr] radiance at detector
J	[J/s/m^2] radiative scalar flux (radiant energy density $\times c$)
$\overrightarrow{k}$	[rad/m] horizontal wavenumber (2D Fourier–Hankel conjugate of $\overrightarrow{\rho}$)
K	[J/s/m^2] radiative tensor flux (radiative pressure $\times c$)
ℓ	[m] mean-free-path (MFP), $1/\sigma$
$\ell_{\rm t}$	[m] transport MFP, $\ell/(1-\varpi_0 g) = 1/\sigma_{\rm t}$
m	[-] non-dimensional *effective* similarity ratio in space-time Green function estimation, $\sqrt{(k/\sigma_{\rm t})^2 + 3s/c\sigma_{\rm t}}$
p	[1/sr] (volume) scattering phase function
$p_{\rm s}$	[1/sr] surface scattering phase function, its relation to the BRDF being $p_{\rm s}(\boldsymbol{\Omega}' \to \boldsymbol{\Omega}) = \lvert\mu'\rvert\rho(\boldsymbol{\Omega}' \to \boldsymbol{\Omega})/\alpha_0$
P	[1/(random variable units)] generic for probability density functions
q	[-] integer or fractional order of a statistical (non-centered) moment

$\boldsymbol{q}_F$	[J/s/m^3] anisotropic volume source term (for $\boldsymbol{F}$)
q_J	[J/s/m^3] isotropic volume source term (for J)
q_0	[J/s/m^2] isotropic boundary source term in diffusion theory
Q	[J/s/m^3/sr] radiative transfer volume source term
r	[μm] cloud droplet radius (hence moments $\overline{r^q}$ over the size distribution)
r_e	[μm] effective cloud droplet radius, $\overline{r^3}/\overline{r^2}$
R	[1/s/m^2] local/instantaneous reflectance, or integrals thereof
s	[1/s] Laplace conjugate variable of t
s/c	[1/m] Laplace conjugate variable of ct
t	[s] time, typically starting at the release of a radiant energy pulse
T	[1/s/m^2] local/instantaneous transmittance, or integrals thereof
$\boldsymbol{x}$	[m] position in 3D space $(x, y, z)^\mathrm{T}$, where $\hat{z}$ is vertical (oriented along the direction of source-beam propagation)
α	[-] Lévy index, relating to sums of independent identically distributed (iid) random variables, infimum of 2 and the order of smallest diverging moment of the PDF decaying as a power law with exponent $-(1+\alpha)$
$\alpha_{0,H}$	[-] surface albedo, ground at $z = 0, H$
β	[-] characteristic exponent of power-law wavenumber spectrum in turbulent media, which decays in $1/k^\beta$
γ	[-] exponent for power-law model of internal stratification
Δ	[-] parameter for linear gradient model of internal stratification
ϵ	[-] rescaling parameter for Cairns' or Larsen's homogenization theories of small-scale 3D RT effects
η	[-] $\sin\theta = \sqrt{1-\mu^2}$
η_0	[-] $\sin\theta_0 = \sqrt{1-\mu_0^2}$
θ	[° or rad] zenith angle for propagation direction
θ_0	[° or rad] zenith angle for solar source
κ_ν	[1/m] absorption coefficient for a gas
λ	[nm] wavelength
μ	[-] vertical direction cosine, $\boldsymbol{\Omega}_z = \cos\theta$
μ_0	[-] μ for solar source, $\cos\theta_0$
ν	[cm^{-1}] wavenumber $= 10^7/\lambda$, when wavelength is in nm
ξ	[-] reserved for $\tau_\mathrm{t}/2\chi$ in strictly similar diffusion models
ϖ_0	[-] single scattering albedo, σ_s/σ
$\overrightarrow{\rho}$	[m] position in horizontal plane, typically reckoned from a normally incident laser beam
σ	[1/m] local extinction coefficient, cross-section (in m^2) $\times$ droplet concentration (in 1/m^3), where cross-section $\approx 2\pi\overline{r^2}$ in the limit of large size parameters $(2\pi r/\lambda)$
σ_a	[1/m] local absorption coefficient
σ_s	[1/m] local scattering coefficient
σ_t	[1/m] local transport extinction coefficient
τ	[-] cloud optical depth
τ_t	[-] rescaled or transport optical depth, $(1-\varpi_0 g)\tau$
ϕ	[° or rad] azimuthal angle for propagation direction
ϕ_0	[° or rad] azimuthal angle for solar source

χ [-] extrapolation length in units of transport MFPs $\ell_{\rm t}$
$\mathbf{\Omega}$ [-] direction of propagation
$\mathrm{d}\mathbf{\Omega}$ [sr] infinitesimal solid angle, $\mathrm{d}\mu\,\mathrm{d}\phi$
$\mathbf{\Omega}_0$ [-] propagation direction for source
$\mathbf{\Omega}_{\rm obs}$ [-] direction of observation (opposite of propagation toward instrument)

References

1. S. Solomon, D. Qin, and M. Manning, editors. *Climate Change 2007: The Physical Science Basis*. Intergovernmental Panel on Climate Change, Geneva, 2007.
2. I. Koren, G. Feingold, L.A. Remer, and O. Altaratz. How small is a small cloud? *Atmos. Chem. Phys. Discuss.*, **8**:3855–3864, 2008.
3. I. Koren, L.A. Remer, Y.J. Kaufman, Y. Rudich, and J.V. Martins. On the twilight zone between clouds and aerosols. *Geophys. Res. Lett.*, **34**:L08805, doi:10.1029/2007GL029253, 2007.
4. A. Ishimaru. *Wave Propagation and Scattering in Random Media*. Academic Press, New York (NY), 1978.
5. M.I. Mishchenko. Vector radiative transfer equation for arbitrarily shaped and arbitrarily oriented particles: a microphysical derivation from statistical electromagnetics. *Appl. Opt.*, **41**:7114–7135, 2002.
6. P.J. Roache. *Verification and Validation in Computational Science and Engineering*. Hermosa Publishers, Albuquerque (NM), 1998.
7. D. Sornette, A.B. Davis, K. Ide, K.R. Vixie, V. Pisarenko, and J.R. Kamm. Algorithm for model validation, Theory and applications. *Proc. Nat. Acad. Sci. U.S.A.*, **104**:6562–6567, 2007.
8. D. Sornette, A.B. Davis, J.R. Kamm, and K. Ide. A general strategy for physics-based model validation illustrated with earthquake phenomenology, atmospheric radiative transfer, and computational fluid dynamics. In F. Graziani, editor, *Computational Methods in Transport – Granlibakken 2006*, volume 62 of *Lecture Notes in Computational Science and Engineering*, pages 19–73. Springer-Verlag, New York (NY), 2008.
9. V.V. Sobolev. *A Treatise of Radiative Transfer*. Van Nostrand, New York (NY), 1963.
10. A.B. Davis and A. Marshak. Photon propagation in heterogeneous optical media with spatial correlations: enhanced mean-free-paths and wider-than-exponential free-path distributions. *J. Quant. Spectrosc. Rad. Transf.*, **84**:3–34, 2004.
11. S. Chandrasekhar. *Radiative Transfer*. Oxford University Press, Oxford (UK), 1950. [Reprinted by Dover Publications, New York (NY), 1960.]
12. D. Mihalas. *Stellar Atmospheres*. Freeman, San Francisco (CA), 1979.
13. M.I. Mishchenko. Multiple scattering, radiative transfer, and weak localization in discrete random media: unified microphysical approach. *Rev. Geophys.*, **46**:RG2003, doi:10.1029/2007RG000230, 2008.
14. R.M. Goody and Y.L. Yung. *Atmospheric Radiation Theoretical Basis*. Oxford University Press, New York (NY), 1989.
15. C.F. Bohren and D.R. Huffman. *Absorption and Scattering of Light by Small Particles*. Wiley, New York (NY), 1983.
16. M.I. Mishchenko, J.W. Hovenier, and L.D. Travis, editors. *Light Scattering by Nonspherical Particles: Theory, Measurements, and Applications*. Academic Press, San Diego (CA), 2000.
17. M.I. Mishchenko. Radiative transfer in clouds with small-scale inhomogeneities: the microphysical approach. *Geophys. Res. Lett.*, **33**:L14820, doi:10.1029/2006GL026312, 2006.

18. K.F. Evans. The spherical harmonics discrete ordinate method for three-dimensional atmospheric radiative transfer. *J. Atmos. Sci.*, **55**:429–446, 1998.
19. K.F. Evans and A. Marshak. Numerical methods. In A. Marshak and A.B. Davis, editors, *3D Radiative Transfer in Cloudy Atmospheres*, chapter 4, pages 243–281. Springer-Verlag, Heidelberg, Germany, 2005.
20. D. Deirmendjian. *Electromagnetic Scattering on Spherical Polydispersions*. Elsevier, New York (NY), 1969.
21. K.F. Evans, R.P. Lawson, P. Zmarzly, and D. O'Connor. In situ cloud sensing with multiple scattering cloud lidar: simulations and demonstration. *J. Atmos. Ocean. Tech.*, **20**:1505–1522, 2003.
22. F.E. Nicodemus, J.C. Richmond, J.J. Hsia, I.W. Ginsberg, and T. Limperis. Geometrical Considerations and Nomenclature for Reflectance. Technical Report NBS Monograph No. 160, National Bureau of Standards, Washington (DC), 1977.
23. G.I. Bell and S. Glasstone. *Nuclear Reactor Theory*. Van Nostrand Reinholt, New York (NY), 1970.
24. A.B. Davis and A. Marshak. Space-time characteristics of light transmitted through dense clouds: a Green's function analysis. *J. Atmos. Sci.*, **59**:2713–2727, 2002.
25. L.C. Henyey and J.L. Greenstein. Diffuse radiation in the galaxy. *Astrophys. J.*, **93**:70–83, 1941.
26. H. Gerber, Y. Takano, T.J. Garrett, and P.V. Hobbs. Nephelometer measurements of the asymmetry parameter, volume extinction coefficient, and backscatter ratio in arctic clouds. *J. Atmos. Sci.*, **57**:3021–3034, 2000.
27. A. Marshak, A. Davis, R.F. Cahalan, and W.J. Wiscombe. Bounded cascade models as non-stationary multifractals. *Phys. Rev. E*, **49**:55–69, 1994.
28. R.F. Cahalan and J.B. Snider. Marine stratocumulus structure during FIRE. *Remote Sens. Environ.*, 28:95–107, 1989.
29. G.I. Marchuk, G. Mikhailov, M. Nazaraliev, R. Darbinjan, B. Kargin, and B. Elepov. *The Monte Carlo Methods in Atmospheric Optics*. Springer-Verlag, New York (NY), 1980.
30. H. Pawlowska, J.-L. Brenguier, Y. Fouquart, W. Armbruster, S. Bakan, J. Descloitres, J. Fischer, C. Flamant, A. Failloux, J.-F. Gayet, S. Gosh, P. Jonas, F. Parol, J. Pelon, and L. Schüller. Microphysical and radiative properties of stratocumulus clouds: The EUCREX mission 206 case study. *Atm. Res.*, **55**:85–102, 2000.
31. W. Feller. *An Introduction to Probability Theory and its Applications*, Volumes 1 & 2. Wiley, New York (NY), 1971.
32. I.L. Katsev. The study of some characteristics of a transient field of light. *Zhurnal Prikladnoi Spektroskopii*, **11**:85–91, 1969 [in Russian].
33. W.M. Irvine. The formation of absorption bands and the distribution of photon optical paths in a scattering atmosphere. *Bull. Astron. Inst. Neth.*, **17**:226–279, 1964.
34. L.M. Romanova. Limiting cases of the path distribution function of photons emerging from a thick light-scattering layer. *Izv. Acad. Sci. USSR, Atmos. Oceanic Phys.*, **1**:348–351, 1965.
35. L.M. Romanova. The distribution of photons paths in a plane layer of a turbid medium. *Izv. Acad. Sci. USSR, Atmos. Oceanic Phys.*, **1**:596–602, 1965.
36. L.M. Romanova. Nonstationary light field in the deep layers of turbid medium illuminated by the narrow beam. *Izv. Ak. Nauk SSSR, Fiz. Atm. Okeana*, **5**:463–472, 1969 [in Russian].
37. V.V. Ivanov and Sh. A. Sabashvili. Transfer of resonance radiation and photon random walks. *Astrophysics and Space Science*, **17**:13–22, 1972.
38. D.I. Nagirner. Theory of nonstationary transfer of radiation. *Astrofizika* (English Transl.: *Astrophysics)*, **10**:274–289, 1974.

39. I.L. Katsev and E.P. Zege. On the connection between nonstationary radiation fields in absorbing and nonabsorbing media. *Astrofizika*, **10**:219–225, 1974 [in Russian].
40. G.N. Plass and G.W. Kattawar. Reflection of light pulses from clouds. *Appl. Opt.*, **10**:2304–2310, 1971.
41. S. Chandrasekhar. On the diffuse reflection of a pencil of radiation by a plane-parallel atmosphere. *Proc. Natl. Acad. Sci. U.S.A.*, **44**:933–940, 1958.
42. L.M. Romanova. The light field in deep layers of a turbid medium illuminated by a narrow beam. *Izv. Acad. Sci. USSR, Atmos. Oceanic Phys.*, **4**:175–179, 1968.
43. L.M. Romanova. Light field in the boundary layer of a turbid medium with strongly anisotropic scattering illuminated by a narrow beam. *Izv. Acad. Sci. USSR, Atmos. Oceanic Phys.*, **4**:679–685, 1968.
44. L.M. Romanova. Effective size of the light spot on the boundaries of a thick turbid medium illuminated by a narrow beam. *Izv. Acad. Sci. USSR, Atmos. Oceanic Phys.*, **7**:270–277, 1971.
45. L.M. Romanova. Some characteristics of the light field generated by a point-collimated stationary light source in clouds and fog. *Izv. Acad. Sci. USSR, Atmos. Oceanic Phys.*, **7**:758–764, 1971.
46. O.V. Bushmakova, E.P. Zege, and I.L. Katsev. The distribution of radiation density in the scattering media from a source of limited size. *Izv. Ak. Nauk SSSR, Fiz. Atm. Okeana*, **8**:711–719, 1972 [in Russian].
47. A.P. Odell and J.A. Weinman. The effect of atmospheric haze on images of the Earth's surface. *J. Geophys. Res.*, **80**:5035–5040, 1975.
48. B.D. Ganapol, D.E. Kornreich, J.A. Dahl, D.W. Nigg, S.N. Jahshan, and C.A. Temple. The searchlight problem for neutrons in a semi-infinite medium. *Nucl. Sci. Eng.*, **118**:38–53, 1994.
49. D.E. Kornreich and B.D. Ganapol. Numerical evaluation of the three-dimensional searchlight problem in a half-space. *Nucl. Sci. Eng.*, **127**:317–337, 1997.
50. C.F. Bohren, J.R. Linskens, and M.E. Churma. At what optical thickness does a cloud completely obscure the sun? *J. Atmos. Sci.*, **52**:1257–1259, 1995.
51. K.M. Case and P.F. Zweifel. *Linear Transport Theory.* Addison-Wesley, Reading (MA), 1967.
52. B. Davison. *Neutron Transport Theory.* Oxford University Press, London, UK, 1958.
53. K. Furutsu and Y. Yamada. Diffusion approximation for a dissipative random medium and the applications. *Phys. Rev. E*, **50**:3634–3640, 1994.
54. T. Nakai, G. Nishimura, K. Yamamoto, and M. Tamura. Expression of optical diffusion coefficient in high-absorption media. *Phys. Med. Biol.*, **42**:2541–2549, 1997.
55. M. Bassani, F. Martelli, G. Zaccanti, and D. Contini. Independence of the diffusion coefficient from absorption: experimental and numerical evidence. *Opt. Lett.*, 22:853–855, 1997.
56. D. Contini, F. Martelli, and G. Zaccanti. Photon migration through a turbid slab described by a model based on diffusion approximation, I. Theory. *Appl. Opt.*, **36**:4587–4599, 1997.
57. F. Martelli, D. Contini, A. Taddeucci, and G. Zaccanti. Photon migration through a turbid slab described by a model based on diffusion approximation, II. Theory. *Appl. Opt.*, **36**:4600–4612, 1997.
58. T. Durduran, A.G. Yodh, B. Chance, and D.A. Boas. Does the photon-diffusion coefficient depend on absorption? *J. Opt. Soc. Am. A*, **14**:3358–3365, 1997.
59. K. Furutsu. Diffusion equation derived from space-time transport equation. *J. Opt. Soc. Am.*, **70**:360–366, 1980.

60. D.J. Durian. The diffusion coefficient depends on absorption. *Opt. Lett.*, **23**:1502–1504, 1998.
61. K. Rinzema, L.H.P. Murrer, and W.M. Starr. Direct experimental verification of light transport theory in an optical phathom. *J. Opt. Soc. Am. A*, **15**:2078–2088, 1998.
62. R. Aronson and N. Corngold. Photon diffusion coefficient in an absorbing medium. *J. Opt. Soc. Am. A*, **16**:1066–1071, 1999.
63. R. Graaff and J.J. Ten Bosch. Diffusion coefficient in photon diffusion theory. *Opt. Lett.*, **25**:43–45, 2000.
64. W. Cai, M. Xu, M. Lax, and R.R. Alfano. Diffusion coefficient depends on time, not on absorption. *Opt. Lett.*, **27**:731–733, 2002.
65. R. Pierrat, J.-J. Greffet, and R. Carminati. Photon diffusion coefficient in scattering and absorbing media. *J. Opt. Soc. Am. A*, **23**:1106–1110, 2006.
66. P.T. Partain, A.K. Heidinger, and G.L. Stephens. High spectral resolution atmospheric radiative transfer: application of equivalence theorem. *J. Geophys. Res.*, **D105**:2163–2177, 2000.
67. M.D. King, L.F. Radke, and P.V. Hobbs. Determination of the spectral absorption of solar radiation by marine stratocumulus clouds from airborne measurements within clouds. *J. Atmos. Sci.*, **47**:894–907, 1990.
68. E.W. Larsen. Diffusion theory as an asymptotic limit of transport theory for nearly critical systems with small mean free paths. *Annals of Nuclear Energy*, **7**:249–255, 1980.
69. G.C. Pomraning. Diffusion theory via asymptotics. *Transp. Theory and Stat. Phys.*, **18**:383–428, 1989.
70. S.M. Lovejoy, A. Davis, P. Gabriel, G.L. Austin, and D. Schertzer. Discrete angle radiative transfer, part 1 – scaling, similarity, universality and diffusion. *J. Geophys. Res.*, **D95**:11,699–11,715, 1990.
71. M.C. Chu and W.S. Churchill. Numerical solution of problems in multiple scattering of electromagnetic radiation. *J. Chem. Phys.*, **59**:855–863, 1955.
72. J.H. Joseph, W.J. Wiscombe, and J.A. Weinman. The delta-Eddington approximation for radiative flux transfer. *J. Atmos. Sci.*, **33**:2452–2459, 1976.
73. A.B. Davis and A. Marshak. Multiple scattering in clouds: Insights from three-dimensional diffusion/P_1 theory. *Nucl. Sci. Eng.*, **137**:251–280, 2001.
74. H.W. Barker and A.B. Davis. Approximation methods in atmospheric 3D radiative transfer, Part 2: Unresolved variability and climate applications. In A. Marshak and A.B. Davis, editors, *3D Radiative Transfer in Cloudy Atmospheres*, chapter 6, pages 343–383. Springer-Verlag, Heidelberg, Germany, 2005.
75. B. Cairns, A.W. Lacis, and B.E. Carlson. Absorption within inhomogeneous clouds and its parameterization in general circulation models. *J. Atmos. Sci.*, **57**:700–714, 2000.
76. E.W. Larsen. A generalized Boltzmann equation for 'non-classical' particle transport. In *Proceedings of Joint International Topical Meetings on Mathematics & Computations and Supercomputing in Nuclear Applications (M&C+SNA 2007), Monterey (CA), April 15–19, 2007*. Am. Nucl. Soc., 2007 [available on CD-ROM].
77. J.L.W.V. Jensen. Sur les fonctions convexes et les inégalitiés entre les valeurs moyennes. *Acta Math.*, **30**:175–193, 1906.
78. A.B. Kostinski. On the extinction of radiation by a homogeneous but spatially correlated random medium. *J. Opt. Soc. Amer. A*, **18**:1929–1933, 2001.
79. R.A. Shaw, A.B. Kostinski, and D.D. Lanterman. Super-exponential extinction of radiation in a negatively-correlated random medium. *J. Quant. Spectrosc. Radiat. Transfer*, **75**:13–20, 2002.

80. A. Davis and A. Marshak. Lévy kinetics in slab geometry: scaling of transmission probability. In M.M. Novak and T.G. Dewey, editors, *Fractal Frontiers*, pages 63–72. World Scientific, Singapore, 1997.
81. A.B. Davis. Effective propagation kernels in structured media with broad spatial correlations, illustration with large-scale transport of solar photons through cloudy atmospheres. In F. Graziani, editor, *Computational Methods in Transport – Granlibakken 2004*, volume 48 of *Lecture Notes in Computational Science and Engineering*, pages 84–140. Springer-Verlag, New York (NY), 2006.
82. K. Eriksson, D. Estep, P. Hansbo, and C. Johnson. *Computational Differential Equations.* Cambridge University Press, New York (NY), 1996.
83. E.P. Zege, A.P. Ivanov, and I.L. Katsev. *Image Transfer through a Scattering Medium.* Springer Verlag, Heidelberg (Germany), 1991.
84. I.N. Polonsky, S.P. Love, and A.B. Davis. Wide-Angle Imaging Lidar deployment at the ARM Southern Great Plains site: intercomparison of cloud property retrievals. *J. Atmos. Ocean. Tech.*, **22**:628–648, 2005.
85. A.B. Davis, R.F. Cahalan, J.D. Spinhirne, M.J. McGill, and S.P. Love. Off-beam lidar: an emerging technique in cloud remote sensing based on radiative Green-function theory in the diffusion domain. *Phys. Chem. Earth*, **B24**:177–185 (Erratum 757–765), 1999.
86. S.P. Love, A.B. Davis, C. Ho, and C.A. Rohde. Remote sensing of cloud thickness and liquid water content with Wide-Angle Imaging Lidar. *Atmos. Res.*, **59-60**:295–312, 2001.
87. W.E. Meador and W.R. Weaver. Two-stream approximations to radiative transfer in planetary atmospheres: a unified description of existing methods and a new improvement. *J. Atmos. Sci.*, **37**:630–643, 1980.
88. A. Schuster. Radiation through a foggy atmosphere. *Astrophys. J.*, **21**:1–22, 1905.
89. E. Lommel. Die Photometrie der diffusen Zurüchwerfung. *Sitz. Acad. Wissensch. München*, **17**:95–124, 1887.
90. O. Chowlson. Grunzüge einer mathematischen Theorie der inneren Diffusion des Lichtes. *Bull. Acad. Imp. Sci. St. Petersburg*, **33**:221–256, 1889.
91. J.A. Weinman and M. Masutani. Radiative transfer models of the appearance of city lights obscured by clouds observed in nocturnal satellite images. *J. Geophys. Res.*, **92**:5565–5572, 1987.
92. A.B. Davis. Multiple-scattering lidar from both sides of the clouds: addressing internal structure. *J. Geophys. Res.*, **D113**:14S10, doi:10.1029/2007JD009666, 2008.
93. G. Thomas and K. Stamnes. *Radiative Transfer in the Atmosphere and Ocean.* Cambridge University Press, New York (NY), 1999.
94. E.P. Zege, I.N. Polonskii, and L.I. Chaikovskaya. Peculiarities of the radiation beam propagation at slant illumination of absorbing anisotropically scattering medium. *Izv. Ak. Nauk SSSR, Fiz. Atm. Okeana*, **23**:486–492, 1987 [in Russian].
95. C. Guo and E.P. Krider. The optical and radiation field signatures produced by lightning return strokes. *J. Geophys. Res.*, **87**:8913–8922, 1982.
96. L.W. Thomason and E.P. Krider. The effects of clouds on the light produced by lightning. *J. Atmos. Sci.*, **39**:2051–2065, 1982.
97. W.J. Koshak, R.J. Solakiewicz, D.D. Phanord, and R.J. Blakeslee. Diffusion model for lightning radiative transfer. *J. Geophys. Res.*, **D99**:14,361–14,371, 1994.
98. T.E. Light, D.M. Suszcynsky, M.W. Kirkland, and A.R. Jacobson. Simulations of lightning optical waveforms as seen through clouds by satellites. *J. Geophys. Res.*, **D106**:17,103–17,114, 2001.

99. I.N. Polonsky and A.B. Davis. Lateral photon transport in dense scattering and weakly absorbing media of finite thickness: asymtotic analysis of the space-time Green function. *J. Opt. Soc. Am. A*, **21**:1018–1025, 2004.
100. E.P. Zege, I.L. Katsev, and I.D. Sherbaf. The space-time distribution of the light field in the scattering medium from the pulse source. *Izv. Ak. Nauk SSSR, Fiz. Atm. Okeana*, **9**:937–946, 1973 [in Russian].
101. O.V. Bushmakova, E.P. Zege, and I.L. Katsev. Light field in a layer of finite optical thickness with a pulse source. *Izv. Ak. Nauk SSSR, Fiz. Atm. Okeana*, **10**:250–257, 1974 [in Russian].
102. P.I. Richards. Scattering from a point-source in plane clouds. *J. Opt. Soc. Am.*, **46**:927–934, 1956.
103. P.M. Morse and H. Feshbach. *Methods of Theoretical Physics*. McGraw-Hill, New York (NY), 1953.
104. M.D. King. Determination of the scaled optical thickness of clouds from reflected solar radiation measurements. *J. Atmos. Sci.*, **44**:1734–1751, 1987.
105. D.J. Durian and J. Rudnick. Photon migration at short times and distances and in cases of strong absorption. *J. Opt. Soc. Am. A*, **14**:235–245, 1997.
106. I.N. Polonsky and A.B. Davis. Off-Beam Cloud Lidar: A New Diffusion Model and an Analysis of LITE Returns. Technical Report LA-UR-05-0794, Los Alamos National Laboratory, Los Alamos, NM, 2005.
107. R.J. Hogan and A. Battaglia. Fast lidar and radar multiple-scattering models, Part 2: Wide-angle scattering using the time-dependent two-stream approximation. *J. Atmos. Sci.*, **65**:3635–3651, 2008.
108. M. Lax, W. Cai, and M. Xu. *Random Processes in Physics and Finance*. Oxford University Press, New York (NY), 2006.
109. I.L. Katsev and E.P. Zege. Optical transfer function of an intensely scattering layer. *Zhurnal Prikladnoi Spektroskopii* (English Transl.: *Journal of Applied Spectroscopy*), **44**:552–558, 1986.
110. M. Abramowitz and I.A. Stegun, editors. *Handbook of Mathematical Functions with Formulas, Graphs, and Mathematical Tables*. U.S. Govt. Print. Off., Washington (DC), 1 zeroth edition, 1972. [Reprinted by Dover Publications, New York (NY).]
111. D.M. Winker, R.H. Couch, and M.P. McCormick. An overview of LITE: NASA's Lidar In-space Technology Experiment. *Proc. IEEE*, **84**:164–180, 1996.
112. R.A.J. Groenhuis, H.A. Ferwerda, and J.J. Ten Bosch. Scattering and absorption of turbid materials determined from reflection measurements, 1: Theory. *Appl. Opt.*, **22**:2456–2462, 1983.
113. R.A.J. Groenhuis, J.J. Ten Bosch, and H.A. Ferwerda. Scattering and absorption of turbid materials determined from reflection measurements, 2: Measuring method and calibration. *Appl. Opt.*, **22**:2463–2467, 1983.
114. A.B. Davis, S.P. Love, D.M. Winker, and I.N. Polonsky. Multiple-scattering lidar from both sides of the clouds: ground-based with WAIL, space-based with LITE. In M. Hardesty and S. Mayer, editors, *Proceedings of 2fourth International Conference on Laser Radar (ILRC 24), Boulder (CO), July 23–27, 2008*. NCAR, 2008 [available on CD-ROM].
115. K.F. Evans and W.J. Wiscombe. An algorithm for generating stochastic cloud fields from radar profile statistics. *Atm. Res.*, **72**:263–289, 2004.
116. K.F. Evans, D. O'Connor, P. Zmarzly, and R.P. Lawson. In situ cloud sensing with multiple scattering cloud lidar: Design and validation of an airborne sensor. *J. Atmos. Ocean. Tech.*, **23**:1068–1081, 2006.
117. R.A. Hanel. Determination of cloud altitude from a satellite. *J. Geophys. Res.*, **66**:1300, 1961.

118. G.A. Yamamoto and D.Q. Wark. Discussion of the letter by R.A. Hanel: determination of cloud altitude from a satellite. *J. Geophys. Res.*, **66**:3596, 1961.
119. R.M. Chapman. Cloud distributions and altitude profiles from a satellite. *Planetary and Space Science*, 9:70–71, 1962.
120. F. Saiedy, D.T. Hilleary, and W.A. Morgan. Cloud-top altitude measurements from satellites. *Appl. Opt.*, **4**:495–500, 1965.
121. F. Saiedy, H. Jacobowitz, and D.Q. Wark. On cloud-top determination from Gemini-5. *J. Atmos. Sci.*, **35**:63–69, 1967.
122. M.-L.C. Wu. On cloud-top determination from Gemini-5. *J. Climate Appl. Meteor.*, **24**:539–546, 1985.
123. A. Kuze and K.V. Chance. Analysis of cloud top height and cloud coverage from the o_2 A and B bands. *J. Geophys. Res.*, **99**:14,481–14,491, 1994.
124. J. Fisher and H. Grassl. Detection of cloud-top height from backscattered radiances within the oxygen A band, 1, Theory. *J. Appl. Meteor.*, **30**:1260–1267, 1991.
125. J. Fisher, W. Cordes, A. Schmitz-Pfeiffer, W. Renger, and P. Mörl. Detection of cloud-top height from backscattered radiances within the oxygen A band, 2, Measurements. *J. Appl. Meteor.*, **30**:1245–1259, 1991.
126. A. Hayazaka, T. Nakajima, Y. Fujiyoshi, Y. Ishikaza, T. Takeda, and M. Tanaka. Geometrical thickness, liquid water content, and radiative properties of stratocumulus over the Western North Pacific. *J. Appl. Met.*, **34**:460–470, 1995.
127. S. Asano, M. Shiobara, and A. Uchiyama. Estimation of cloud physical parameters from airborne solar spectral reflectance measurements for stratocumulus clouds. *J. Atmos. Sci.*, **52**:3556–3576, 1995.
128. T.G. Adiks and V.I. Dianov-Klokov. Molecular parameters of the oxygen absorption band at 0.7620 μm and their use in calculating the transmission function. *Izv. Acad. Sci. USSR, Atmos. Oceanic Phys.*, **4**:605–609, 1968.
129. V.I. Dianov-Klokov, E.P. Kropotkina, I.P. Malkov, and O.A. Matveyeva. Absorption-band deformation and the effective path-length of light in clouds. *Izv. Acad. Sci. USSR, Atmos. Oceanic Phys.*, **6**:458–463, 1970.
130. T.G. Adiks, Yu.S. Georgiyevskiy, M.S. Malkevich, and N.S. Filippova. Atmospheric transmission in the 0.76 μm oxygen band. *Izv. Acad. Sci. USSR, Atmos. Oceanic Phys.*, **8**:210–216, 1972.
131. V.I. Dianov-Klokov and L.D. Krasnokutskaya. Comparison of observed and calculated effective photon path-length in clouds. *Izv. Acad. Sci. USSR, Atmos. Oceanic Phys.*, **8**:487–492, 1972.
132. B.A. Kargin, L.D. Krasnokutskaya, and Ye. M. Feygel'son. Reflection and absorption of solar radiant energy by cloud layers. *Izv. Acad. Sci. USSR, Atmos. Oceanic Phys.*, **8**:287–293, 1972.
133. Ye.I. Grechko, V.I. Dianov-Klokov, and I.P. Malkov. Aircraft measurements of photon paths in reflection and transmission of light by clouds in the 0.76 μm oxygen band. *Izv. Acad. Sci. USSR, Atmos. Oceanic Phys.*, **9**:262–269, 1973.
134. V.I. Syachinov and Ye.M. Kozlov. Determination of cloud-top altitude from the Cosmos-320 satellite. *Izv. Acad. Sci. USSR, Atmos. Oceanic Phys.*, **10**:582–586, 1974.
135. M.S. Malkevich, L.U. Chagar, and A.Kh. Shukurov. Corrections for scattering of radiation in clouds in photometric cloud-height determination. *Izv. Acad. Sci. USSR, Atmos. Oceanic Phys.*, **11**:561–564, 1975.
136. Ye.I. Grechko, V.I. Dianov-Klokov, N.A. Yevstratov, and A.P. Ozerenskiy. Calculation of mean and effective photon paths for a two-layer cloud model with consideration of reflection from the underlying surface. *Izv. Acad. Sci. USSR, Atmos. Oceanic Phys.*, **12**:20–24, 1976.

137. V.I. Dianov-Klokov. Determination of effective photon path-lengths from the spectral brightness of clouds. *Izv. Acad. Sci. USSR, Atmos. Oceanic Phys.*, **12**:221–224, 1976.
138. V.I. Dianov-Klokov, N.A. Yevstratov, and A.P. Ozerenskiy. Calculation of radiant energy density and equivalent photon paths for certain cloud models. *Izv. Acad. Sci. USSR, Atmos. Oceanic Phys.*, **13**:217–221, 1977.
139. Ye.I. Grechko. Measuring the difference in effective paths at two wavelengths in the presence of reflection of light by clouds. *Izv. Acad. Sci. USSR, Atmos. Oceanic Phys.*, **14**:479–481, 1978.
140. V.V. Badayev and M.S. Malkevich. On the possibility of determining the vertical profiles of aerosol attenuation using satellite measurements of reflected radiation in the 0.76 μm oxygen band. *Izv. Acad. Sci. USSR, Atmos. Oceanic Phys.*, **14**:722–727, 1978.
141. V.V. Badayev and Ye.M. Kozlov. On a determination of the optical parameters of the atmosphere from reflected radiation measurements in the 0.76 μm oxygen absorption band. *Izv. Acad. Sci. USSR, Atmos. Oceanic Phys.*, **16**:375–377, 1980.
142. Ye.I. Grechko and V.I. Dianov-Klokov. Spectroscopic measurements of the 'additional absorbing mass' in the cloudy atmosphere of the intertropical convergence zone. *Izv. Acad. Sci. USSR, Atmos. Oceanic Phys.*, **17**:153–156, 1981.
143. L.M. Romanova and Ye.A. Ustinov. The generalized transfer equation for the distribution of photon paths and the problem of vertically inhomogeneous gas absorption in the atmosphere. *Izv. Acad. Sci. USSR, Atmos. Oceanic Phys.*, **18**:186–192, 1982.
144. Ye.I. Grechko, S.V. Dvoryashin, and A.Ya. Red'ko. Evaluation of effect of scattering indicatrix on the mean photon ranges in clouds. *Izv. Acad. Sci. USSR, Atmos. Oceanic Phys.*, **18**:854–856, 1982.
145. Ye.I. Grechko and V.I. Dianov-Klokov. Spectroscopic measurements of the 'additional absorbing mass' in solid and broken cloud cover. *Izv. Acad. Sci. USSR, Atmos. Oceanic Phys.*, **19**:117–121, 1983.
146. V.N. Skorinov and G.A. Titov. Mean photon path-lengths for broken clouds. *Izv. Acad. Sci. USSR, Atmos. Oceanic Phys.*, **20**:377–381, 1984.
147. I.S. Gusev and S.V. Dvoryashin. Recovery of the effective photon path-length in cloud from its spectral brightness. *Izv. Acad. Sci. USSR, Atmos. Oceanic Phys.*, **26**:536–539, 1990.
148. G.L. Stephens. *Remote Sensing of the Lower Atmosphere: An Introduction.* Oxford University Press, New York (NY), 1994.
149. C. Moroney, R. Davies, and J.-P. Muller. Operational retrieval of cloud-top heights using MISR data. *IEEE Trans. Geosci. Remote Sensing*, **40**:1532–1540, 2002.
150. D. O'Brien and R.M. Mitchell. Error estimates for the retrieval of cloud top pressure using absorption in the A-band of oxygen. *J. Appl. Meteor.*, **31**:1179–1192, 1992.
151. D. O'Brien, R.M. Mitchell, S.A. English, and G.A. Da Costa. Airborne measurements of air mass from O_2 A-band absorption spectra. *J. Atmos. Oceanic Tech.*, **15**:1272–1286, 1999.
152. G.L. Stephens and A.K. Heidinger. Line absorption in a scattering atmosphere. I: Theory. *J. Atmos. Sci.*, **57**:1599–1614, 2000.
153. A.K. Heidinger and G.L. Stephens. Molecular line absorption in a scattering atmosphere. II: Application to remote sensing in the O_2 A-band. *J. Atmos. Sci.*, **57**:1615–1634, 2000.
154. A.A. Kokhanovsky and V.V. Rozanov. The physical parameterization of the top-of-atmosphere reflection function for a cloudy atmosphere – underlying surface system: the oxygen A-band study. *J. Quant. Spectr. Rad. Transfer*, **85**:35–55, 2004.
155. V.V. Rozanov and A.A. Kokhanovsky. Semi-analytical cloud retrieval algorithm as applied to the cloud top altitude and the cloud geometrical thickness determination

from top-of-atmosphere reflectance measurements in the oxygen A-band. *J. Geophys. Res.*, **D109**:5202, doi:10.1029/2003JD004104, 2004.
156. A.K. Heidinger and G.L. Stephens. Molecular line absorption in a scattering atmosphere. III: Path length characteristics and effects of spatially heterogeneous clouds. *J. Atmos. Sci.*, **59**:1641–1654, 2002.
157. G.L. Stephens, A.K. Heidinger, and P.M. Gabriel. Photon paths and cloud heterogeneity: an observational strategy to assess effects of 3D geometry on radiative transfer. In A. Marshak and A.B. Davis, editors, *3D Radiative Transfer in Cloudy Atmospheres*, chapter 13, pages 587–616. Springer-Verlag, Heidelberg, Germany, 2005.
158. A.A. Kokhanovsky, B. Mayer, V.V. Rozanov, K. Wapler, J.P. Burrows, and U. Schumann. The influence of broken cloudiness on cloud top height retrievals using nadir observations of backscattered solar radiation in the oxygen A-band. *J. Quant. Spectr. Rad. Transfer*, **103**:460–477, 2007.
159. K. Pfeilsticker, F. Erle, O. Funk, H. Veitel, and U. Platt. First geometrical path-lengths probability density function derivation of the skylight from spectroscopically highly resolving oxygen A-band observations, 1. Measurement technique, atmospheric observations, and model calculations. *J. Geophys. Res.*, **D103**:11,483–11,504, 1998.
160. Q. Min and L. Harrison. Joint statistics of photon path-length and cloud optical depth. *Geophys. Res. Lett.*, **26**:1425–1428, 1999.
161. Q.-L. Min, L.C. Harrison, and E.E. Clothiaux. Joint statistics of photon path-length and cloud optical depth: Case studies. *J. Geophys. Res.*, **D106**:7375–7385, 2001.
162. Q.-L. Min and E.E. Clothiaux. Photon path-length distributions inferred from rotating shadowband spectroradiometer measurements at the Atmospheric Radiation Measurment Program Southern Great Plains site. *J. Geophys. Res.*, **D108**:4456–4464, 2003.
163. Q.-L. Min, L.C. Harrison, P. Kiedron, J. Berndt, and E. Joseph. A high-resolution oxygen A-band and water vapor band spectrometer. *J. Geophys. Res.*, **D109**:2202–2210, 2004.
164. K. Pfeilsticker. First geometrical path-lengths probability density function derivation of the skylight from spectroscopically highly resolving oxygen A-band observations, 2. Derivation of the Lévy-index for the skylight transmitted by mid-latitude clouds. *J. Geophys. Res.*, **D104**:4101–4116, 1999.
165. T. Scholl, K. Pfeilsticker, A.B. Davis, H.K. Baltink, S. Crewell, U. Löhnert, C. Simmer, J. Meywerk, and M. Quante. Path length distributions for solar photons under cloudy skies: comparison of measured first and second moments with predictions from classical and anomalous diffusion theories. *J. Geophys. Res.*, **D111**:12,211–12,226, 2006.
166. H.C. van de Hulst. *Multiple Light Scattering (Tables, Formulae and Applications)*, Volumes 1 & 2. Academic Press, San Diego (CA), 1980.
167. R.W. Portmann, S. Solomon, R.W. Sanders, and J.S. Daniel. Cloud modulation of zenith sky oxygen path-lengths over Boulder, Colorado: measurement versus model. *J. Geophys. Res.*, **D106**:1139–1155, 2001.
168. K. Stamnes, S.-C. Tsay, W.J. Wiscombe, and K. Jayaweera. Numerically stable algorithm for discrete-ordinate-method radiative transfer in multiple scattering and emitting layered media. *Appl. Opt.*, **27**:2502–2509, 1988.
169. J.S. Daniel, R.W. Portmann, H.L. Miller, S. Solomon, R.W. Sanders, A.O. Langford, C.S. Eubank, R. Schofield, D.D. Turner, and M.D. Shupe. Cloud property estimates from zenith spectral measurements of scattered sunlight between 0.9 and 1.7 μm. *J. Geophys. Res.*, **D111**:16208, doi:10.1029/2005JD006641, 2006.
170. A. Marshak, A. Davis, W.J. Wiscombe, and R.F. Cahalan. Radiative smoothing in fractal clouds. *J. Geophys. Res.*, **D100**:26,247–26,261, 1995.

171. D. Crisp, R.M. Atlas, F.-M. Bréon, L.R. Brown, J.P. Burrows, P. Ciais, B.J. Connor, S.C. Doney, I.Y. Fung, D.J. Jacob, C.E. Miller, D. O'Brien, S. Pawson, J.T. Randerson, P. Rayner, R.J. Salawitch, S.P. Sander, B. Sen, G.L. Stephens, P.P. Tans, G.C. Toon, P.O. Wennberg, S.C. Wofsy, Y.L. Yung, Z. Kuang, B. Chudasama, G. Sprague, B. Weiss, R. Pollock, D. Kenyon, and S. Schroll. The Orbiting Carbon Observatory (OCO) mission. *Adv. Space Res.*, **34**:700–709, 2004.
172. C. Vanbauce, R. Cadet, and R.T. Marchand. Comparison of POLDER apparent and corrected oxygen pressure to ARM/MMCR cloud boundary pressures. *Geophys. Res. Lett.*, **30**:1212, doi:10.1029/2002GL016449, 2003.
173. V.V. Rozanov, A.A. Kokhanovsky, and J.P. Burrows. The determination of cloud altitudes using GOME reflectance spectra: multilayered cloud systems. *IEEE Trans. Geosc. and Remote Sens.*, **42**:1009–1017, 2004.
174. A.A. Kokhanovsky, V.V. Rozanov, W. von Hoyningen-Huene, H. Bovensmann, J.P. Burrows, and H.K. Baltink. The determination of cloud altitudes using SCIAMACHY onboard ENVISAT. *IEEE Geosc. and Remote Sens. Lett.*, **1**:211–214, 2004.
175. C. Flesia and P. Schwendimann (editors). Special section on MUltiple SCattering in Lidar Experiments (MUSCLE). *Applied Physics B – Lasers and Optics*, **B60**:315–362, 1995.
176. A. Davis, D.M. Winker, A. Marshak, J.D. Spinhirne, R.F. Cahalan, S.P. Love, S.H. Melfi, and W.J. Wiscombe. Retrieval of physical and optical cloud thicknesses from space-borne and wide-angle lidar. In A. Ansmann, R. Neuber, P. Rairoux, and U. Wadinger, editors, *Advances in Atmospheric Remote Sensing with Lidar*, pages 193–196. Springer-Verlag, Heidelberg, Germany, 1997 [selected papers presented at the *18th International Laser Radar Conference (ILRC18)*, Berlin (Germany), 22–26 July, 1996].
177. L.R. Bissonnette and D.L. Hutt. Multiple scattering lidar. *Appl. Opt.*, **29**:5045–5048, 1990.
178. D.L. Hutt, L.R. Bissonnette, and L. Durand. Multiple field of view lidar returns for atmospheric aerosols. *Appl. Opt.*, **33**:2338–2348, 1994.
179. L.R. Bissonnette and D.L. Hutt. Multiply scattered aerosol lidar returns: Inversion method and comparison with *in situ* measurements. *Appl. Opt.*, **34**:6959–6975, 1995.
180. L.R. Bissonnette. Multiple-scattering lidar equation. *Appl. Opt.*, **35**:6449–6465, 1996.
181. L.R. Bissonnette, G. Roy, L. Poutier, S. Cober, and G. Isaac. Multiple-scattering lidar retrieval method: tests on Monte Carlo simulations and comparisons with *in situ* measurements. *Appl. Opt.*, **41**:6307–6324, 2002.
182. G. Roy, L.R. Bissonnette, C. Bastille, and G. Vallée. Estimation of cloud droplet size density distribution from multiple-field-of-view lidar returns. *Optical Engineering*, **36**:3404–3415, 1997.
183. G. Roy, L.R. Bissonnette, C. Bastille, and G. Vallée. Retrieval of droplet-size density distribution from multiple-field-of-view cross-polarized lidar signals: theory and experimental validation. *Appl. Opt.*, **38**:5202–5211, 1999.
184. L.R. Bissonnette, G. Roy, and N. Roy. Multiple-scattering-based lidar retrieval: method and results of cloud probings. *Appl. Opt.*, **44**:5565–5581, 2005.
185. J.D. Spinhirne. Micropulse lidar. *IEEE Trans. Geosc. Remote Sensing*, 31:48–55, 1993.
186. E.W. Eloranta. Practical model for the calculation of multiply scattered lidar returns. *Appl. Opt.*, **37**:2464–2472, 1998.
187. R.J. Hogan. Fast lidar and radar multiple-scattering models, Part 1: Small-angle scattering using the photon variance-covariance method. *J. Atmos. Sci.*, **65**:3621–3635, 2008.

188. D. Jette. Electron dose calculation using multiple-scattering theory: A new theory of multiple scattering. *Med. Phys.*, **23**:459–477, 1996.
189. C. Borgers and E.W. Larsen. On the accuracy of the Fokker-Planck and Fermi pencil beam equations for charged particle transport. *Med. Phys.*, **23**:1749–1759, 1996.
190. G.C. Pomraning. A non-Gaussian treatment of radiation pencil beams. *Nucl. Sci. Eng.*, **127**:182–198, 1997.
191. M. Asadzadeh. Streamline diffusion methods for Fermi and Fokker-Planck equations. *Transp. Theory and Stat. Phys.*, **26**:319–340, 1997.
192. A.J. Prinja. Pencil beam transport in a random medium using the Fermi transport equation. *Transp. Theory and Stat. Phys.*, **27**:667–679, 1998.
193. A.M. Belyantsev, L.S. Dolin, and V.A. Savel'ev. On the propagation of light impulses of small duration in a turbid medium. *Izvestiya Vysshikh Uchebnykh Zavedenii Radiofizika*, **4**:489–497, 1967 [in Russian].
194. L.M. Romanova. Nonstationary light field in the boundary layer of turbid medium with strongly anisotropic scattering illuminated by the narrow beam. *Izv. Ak. Nauk SSSR, Fiz. Atm. Okeana*, **6**:489–498, 1970 [in Russian].
195. J.A. Weinman and S.T. Shipley. Effects of multiple scattering on laser pulses transmitted through clouds. *J. Geophys. Res.*, **77**:7123–7128, 1972.
196. L.S. Dolin and V.A. Savel'ev. Characteristics of back scattering signal at pulse radiation of turbid medium by a narrow directional light beam. *Izv. Ak. Nauk SSSR, Fiz. Atm. Okeana*, **7**:505–510, 1971 [in Russian].
197. I.L. Katsev. The reflection of a narrow light beam from a homogeneous isotropically scattering medium. *Izv. Ak. Nauk SSSR, Fiz. Atm. Okeana*, **10**:425–430, 1974 [in Russian].
198. J.A. Weinman. Effects of multiple scattering on light pulses reflected by turbid atmospheres. *J. Atmos. Sci.*, **33**:1763–1771, 1976.
199. K.E. Kunkel and J.A. Weinman. Monte carlo analysis of multiply scattered lidar returns. *J. Atmos. Sci.*, **33**:1772–1781, 1976.
200. S.D. Miller and G.L. Stephens. Multiple scattering effects in the lidar pulse stretching problem. *J. Geophys. Res.*, **D104**:22,205–22,219, 1999.
201. A.B. Davis, D.M. Winker, and M.A. Vaughan. First retrievals of dense cloud properties from off-beam/multiple-scattering lidar data collected in space. In A. Dabas and J. Pelon, editors, *Laser Remote Sensing of the Atmosphere: Selected Papers from the 2 zeroth International Conference on Laser Radar, Vichy (France), July 9–14, 2000*, pages 35–38, Palaiseau, France, 2001. École Polytechnique.
202. R.F. Cahalan, M.J. McGill, J. Kolasinski, T. Várnai, and K. Yetzer. THOR, cloud THickness from Offbeam lidar Returns. *J. Atmos. Ocean. Tech.*, **22**:605–627, 2005.
203. A. Davis, A. Marshak, W.J. Wiscombe, and R.F. Cahalan. Multifractal characterizations of non-stationarity and intermittency in geophysical fields: Observed, retrieved, or simulated. *J. Geophys. Res.*, **D99**:8055–8072, 1994.
204. A. Davis, A. Marshak, W.J. Wiscombe, and R.F. Cahalan. Scale-invariance in liquid water distributions in marine stratocumulus, Part I, Spectral properties and stationarity issues. *J. Atmos. Sci.*, **53**:1538–1558, 1996.
205. A. Davis, A. Marshak, H. Gerber, and W.J. Wiscombe. Horizontal structure of marine boundary-layer clouds from cm- to km-scales. *J. Geophys. Res.*, **D104**:6123–6144, 1999.
206. L.S. Dolin. Passage of a pulsed light signal through an absorbing medium with strongly anisotropic scattering. *Izvestiya Vysshikh Uchebnykh Zavedenii Radiofizika (Engl. Transl.: Radiophysics and Quantum Electronics)*, **26**:220–228, 1983.

207. E.P. Zege, I.L. Katsev, and A.I. Kolesnik. Integral characteristics of time deformation of a light pulse in a scattering medium. *Izv. Ak. Nauk SSSR, Fiz. Atm. Okeana*, **24**:1163–1169, 1988 [in Russian].
208. T. Nakajima and M.D. King. Determination of optical thickness and effective radius of clouds from reflected solar radiation measurements: Part I: Theory. *J. Atmos. Sci.*, **47**:1878–1893, 1990.
209. T. Nakajima, M.D. King, J.D. Spinhirne, and L.F. Radke. Determination of optical thickness and effective radius of clouds from reflected solar radiation measurements: Part II: Marine stratoculmulus observations. *J. Atmos. Sci.*, **48**:728–750, 1991.
210. S. Platnick, M.D. King, S.A. Ackerman, W.P. Menzel, B.A. Baum, J.C. Riedi, and R.A. Frey. The MODIS cloud products: algorithms and examples from Terra. *IEEE Trans. Geosci. Remote Sens.*, **41**:459–473, 2003.
211. R. Davies. 3D radiative transfer in satellite remote sensing of cloud properties. In A. Marshak and A.B. Davis, editors, *3D Radiative Transfer in Cloudy Atmospheres*, chapter 11, pages 532–541. Springer-Verlag, Heidelberg, Germany, 2005.
212. R.F. Cahalan, W. Ridgway, W.J. Wiscombe, T.L. Bell, and J.B. Snider. The albedo of fractal stratocumulus clouds. *J. Atmos. Sci.*, **51**:2434–2455, 1994.
213. R.F. Cahalan, W. Ridgway, W.J. Wiscombe, S. Gollmer, and Harshvardhan. Independent pixel and Monte Carlo estimates of stratocumulus albedo. *J. Atmos. Sci.*, **51**:3776–3790, 1994.
214. T. Várnai. Influence of three-dimensional radiative effects on the spatial distribution of shortwave cloud reflection. *J. Atmos. Sci.*, **57**:216–229, 2000.
215. T. Várnai and A. Marshak. A method for analyzing how various parts of clouds influence each other's brightness. *J. Geophys. Res.*, **D108**:4706, doi:10.1029/2003JD003561, 2003.
216. H.W. Barker. A parameterization for computing grid-averaged solar fluxes for inhomogeneous marine boundary layer clouds – Part 1, Methodology and homogeneous biases. *J. Atmos. Sci.*, **53**:2289–2303, 1996.
217. L. Oreopoulos and H.W. Barker. Accounting for subgrid-scale cloud variability in a multi-layer, 1D solar radiative transfer algorithm. *Quart. J. Roy. Meteorol. Soc.*, **125**:301–330, 1999.
218. A.A. Kokhanovsky. The influence of the horizontal inhomogeneity on radiative characteristics of clouds: an asymptotic case study. *IEEE Trans. Geosc. and Remote Sens.*, **41**:817–825, 2003.
219. A.A. Kokhanovsky. Statistical properties of light reflected and transmitted by a thick horizontally inhomogeneous turbid layer. *J. Opt. Soc. Am. A*, **22**:2419–2423, 2005.
220. V.V. Sobolev. *Light Scattering in Planetary Atmospheres*. Nauka, Moscow, FSU, 1972.
221. H.W. Barker, B.A. Wielicki, and L. Parker. A parameterization for computing grid-averaged solar fluxes for inhomogeneous marine boundary layer clouds – Part 2, Validation using satellite data. *J. Atmos. Sci.*, **53**:2304–2316, 1996.
222. A. Marshak, A. Davis, R.F. Cahalan, and W.J. Wiscombe. Nonlocal independent pixel approximation: direct and inverse problems. *IEEE Trans. Geosc. and Remote Sens.*, **36**:192–205, 1998.
223. G.L. Stephens. Radiative transfer through arbitrary shaped optical media, Part 1 – A general method of solution. *J. Atmos. Sci.*, **45**:1818–1836, 1988.
224. A. Marshak, A. Davis, W.J. Wiscombe, and G. Titov. The verisimilitude of the independent pixel approximation used in cloud remote sensing. *Remote Sens. Environ.*, **52**:72–78, 1995.

225. A. Davis, A. Marshak, R.F. Cahalan, and W.J. Wiscombe. The Landsat scale break in stratocumulus as a three-dimensional radiative transfer effect: implications for cloud remote sensing. *J. Atmos. Sci.*, **54**:241–260, 1997.
226. P. Zuidema and K.F. Evans. On the validity of the Independent Pixel Approximation for the boundary layer clouds observed during ASTEX. *J. Geophys. Res.*, **D103**:6059–6074, 1998.
227. L. Oreopoulos, A. Marshak, R.F. Cahalan, and G. Wen. Cloud three-dimensional effects evidenced in Landsat spatial power spectra and autocorrelation function. *J. Geophys. Res.*, **D105**:14,777–14,788, 2000.
228. R.F. Cahalan. Bounded cascade clouds: Albedo and effective thickness. *Nonlinear Proc. Geophys.*, **1**:156–167, 1994.
229. A. Marshak and A.B. Davis. Scale-by-scale analysis and fractal cloud models. In A. Marshak and A.B. Davis, editors, *3D Radiative Transfer in Cloudy Atmospheres*, pages 653–663. Springer-Verlag, Heidelberg, Germany, 2005.
230. A.B. Davis, A. Marshak, and E.E. Clothiaux. Anisotropic multi-resolution analysis in 2D, Application to long-range correlations in cloud mm-radar fields. *Proc. SPIE*, **3723**:194–207, 1999.
231. A.N. Tikhonov and V.Y. Arsenin. *Solutions of Ill-Posed Problems*. Scripta Series in Mathematics. V.H. Winston & Sons, Washington (DC), 1977 [translated from Russian, preface by translation editor Fritz John].
232. J.C. Chiu, A. Marshak, W.J. Wiscombe, S.C. Valencia, and E.J. Welton. Cloud optical depth retrievals from solar background signals of micropulse lidars. *IEEE Geosc. Remote Sensing Lett.*, **4**:456–460, 2007.
233. C.M.R. Platt, W.H. Hunt, D.M. Winker, and M.A. Vaughan. Measurement of cloud solar reflected radiance and extinction from space lidar. *Proc. SPIE*, **3504**:542–549, 1998.
234. Y. Yang, A. Marshak, J.C. Chiu, W.J. Wiscombe, S.P. Palm, A.B. Davis, D.A. Spangenberg, L. Nguyen, J. Spinhirne, and P. Minnis. Calibration of solar background signal for retrievals of cloud optical depth from the Geoscience Laser Altimeter System (GLAS). *J. Atmos. Sci.*, **65**:3531–3527, doi:10.1175/2008JAS2744.1, 2008.
235. A. Marshak, Yu. Knyazikhin, A. Davis, W.J. Wiscombe, and P. Pilewskie. Cloud–vegetation interaction: use of normalized difference cloud index for estimation of cloud optical thickness. *Geophys. Res. Lett.*, **27**:1695–1698, 2000.
236. C.v. Savigny, O. Funk, U. Platt, and K. Pfeilsticker. Radiative smoothing in zenith-scattered sky light transmitted through clouds to the ground. *Geophys. Res. Lett.*, **26**:2949–2952, 1999.
237. C.v. Savigny, A.B. Davis, O. Funk, and K. Pfeilsticker. Large-scale stationarity in time series of zenith radiance under cloudy skies. *Geophys. Res. Lett.*, **29**:1825, doi:10.1029/2001GL014153, 2002.
238. M.A. Box, S.A.W. Gerstl, and C. Simmer. Computation of atmospheric radiative effects via perturbation theory. *Beitr. Phys. Atmosph.*, **62**:193–199, 1988.
239. M.A. Box, M. Keevers, and B.H.J. McKellar. On the perturbation series for radiative effects. *J. Quant. Spect. Rad. Trans.*, **39**:219–223, 1989.
240. M.A. Box. Radiative perturbation theory: a review. *Environmental Modelling & Software*, **17**:95–106, 2002.
241. I.N. Polonsky and M.A. Box. General perturbation technique for the calculation of radiative effects in scattering and absorbing media. *J. Opt. Soc. Am. A*, **19**:2281–2292, 2002.
242. I.N. Polonsky, M.A. Box, and A.B. Davis. Radiative transfer through inhomogeneous turbid media: implementation of the adjoint perturbation approach at the first-order. *J. Quant. Spectrosc. Radiat. Transfer*, **78**:85–98, 2003.

243. M.A. Box, I.N. Polonsky, and A.B. Davis. Higher-order perturbation theory applied to radiative transfer in non-plane-parallel media. *J. Quant. Spectrosc. Radiat. Transfer*, **78**:105–118, 2003.
244. I.N. Polonsky, A.B. Davis, and M.A. Box. Radiative transfer in 3D clouds: a perturbation theoretical approach. In *Proceedings of 15th Atmospheric Radiation Measurement (ARM) Program Science Team Meeting, Daytona Beach (Fl), March 14–18, 2005*. US Department of Energy, 2005 [available on-line at http://www.arm.gov/publications/proceedings/conf15/].
245. G.I. Marchuk. *Adjoint Equations and Analysis of Complex Systems*. Kluwer Academic, Norwell (MA), 1995.
246. R.F. Cahalan, L. Oreopoulos, A. Marshak, K.F. Evans, A.B. Davis, R. Pincus, K. Yetzer, B. Mayer, R. Davies, T.P. Ackerman, H.W. Barker, E.E. Clothiaux, R.G. Ellingson, M.J. Garay, E. Kassianov, S. Kinne, A. Macke, W. O'Hirok, P.T. Partain, S.M. Prigarin, A.N. Rublev, G.L. Stephens, F. Szczap, E.E. Takara, T. Várnai, G. Wen, and T.B. Zhuravleva. The international Intercomparison of 3D Radiation Codes (I3RC): Bringing together the most advanced radiative transfer tools for cloudy atmospheres. *Bull. Amer. Meteor. Soc.*, **86**:1275–1293, 2005.
247. F. Parol, J.C. Buriez, C. Vanbauce, J. Riedi, L.C. Labonnote, M. Doutriaux-Boucher, M. Vesperini, G. Sèze, P. Couvert, M. Viollier, and F.-M. Bréon. Capabilities of multiangle polarization cloud measurements from satellite: POLDER results. *Adv. Space Res.*, **33**:1080–1088, 2004.
248. V.V. Rozanov and A.A. Kokhanovsky. The solution of the vector radiative transfer equation using the discrete ordinates technique: selected applications. *Atmos. Res.*, **79**:241–265, 2006.
249. A. Marshak and A.B. Davis. Horizontal fluxes and radiative smoothing. In A. Marshak and A.B. Davis, editors, *3D Radiative Transfer in Cloudy Atmospheres*, chapter 12, pages 543–586. Springer-Verlag, Heidelberg, Germany, 2005.
250. C. Chai, Y. Chen, P. Li, and Q. Luo. Improved steady-state diffusion approximation with an anisotropic point-source and the δ-Eddington phase function. *Appl. Opt.*, **46**:4843–4851, 2007.
251. T. Várnai and R.F. Cahalan. Potential for airborne offbeam lidar measurements of snow and sea ice thickness. *J. Geophys. Res.*, **C112**:12S90, doi:10.1029/2007JC004091, 2007.
252. S.Y. Kotchenova, N.V. Shabanov, Y. Knyazikhin, A.B. Davis, R. Dubayah, and R.B. Myneni. Modeling lidar waveforms with time-dependent stochastic radiative transfer theory for remote estimations of forest biomass. *J. Geophys. Res.*, **D108**:4484, doi:1029/2002JD003288, 2003.
253. P. Kollias, E.E. Clothiaux, M.A. Miller, B.A. Albrecht, G.L. Stephens, and T.P. Ackerman. Millimeter-wavelength radars: new frontier in atmospheric cloud and precipitation research. *Bull. Amer. Meteor. Soc.*, **88**:1608–1618, 2007.
254. E.E. Clothiaux, M.A. Miller, B.A. Albrecht, T.P. Ackerman, J. Verlinde, D.M. Babb, R.M. Peters, and W.J. Syrett. An evaluation of a 94-GHz radar for remote sensing of cloud properties. *J. Atmos. and Oceanic Technol.*, **12**:201–229, 1995.
255. A. Yodh and B. Chance. Spectroscopy/imaging with diffusing light. *Phys. Today*, **48**:34–40, 1995.
256. A. Klose. Radiative transfer of luminescence light in biological tissue. In A.A. Kokhanovsky, editor, *Light Scattering Reviews*, volume 4, chapter 6, pages 293–346. Springer-Praxis, Chichester, UK, 2009.
257. A. Einstein. On the motion, required by the molecular-kinetic theory of heat, of particles suspended in a fluid at rest. *Ann. Phys. (Leipzig)*, **17**:549–560, 1905 [Reprinted

by Dover Publications, New York (NY), in *Investigations on the Theory of the Brownian Movement* (1956).]
258. S. Redner. *A Guide to First-Passage Processes*. Cambridge University Press, Cambridge, UK, 2001.
259. S. Chandrasekhar. Stochastic problems in physics and astronomy. *Rev. Mod. Phys.*, **15**:1–89, 1943.
260. R. Pincus, H.W. Barker, and J.J. Morcrette. A new radiative transfer model for use in GCMs. *J. Geophys. Res.*, **D108**:4376–4379, 2003.
261. P. Räisäsen and H.W. Barker. Evaluation and optimization of sampling errors for the Monte Carlo Independent Column Approximation. *Quart. J. Roy. Meteor. Soc.*, **130**:2069–2085, 2005.
262. P. Lévy. *Théorie de l'Addition des Variables Aléatoires*. Gauthier Villars, Paris, France, 1937.
263. G. Samorodnitsky and M.S. Taqqu. *Stable Non-Gaussian Random Processes*. Chapman & Hall, New York (NY), 1994.
264. E. Sparre Anderson. On the fluctuations of sums of random variables. *Math. Scand.*, **1**:236–285, 1953.
265. U. Frisch and H. Frisch. Universality in escape from half space of symmetrical random walks. In M.F. Shlesinger, G.M. Zaslavsky, and U. Frisch, editors, *Lévy Flights and Related Topics in Physics*, pages 262–268. Springer-Verlag, New York (NY), 1995.
266. M.F. Shlesinger, G.M. Zaslavsky, and U. Frisch, editors. *Lévy Flights and Related Topics in Physics*. Springer-Verlag, New York (NY), 1995.
267. A.B. Kostinski. On the extinction of radiation by a homogeneous but spatially correlated random medium: reply to comment. *J. Opt. Soc. Amer. A*, **19**:2521–2525, 2002.
268. A.G. Borovoi. On the extinction of radiation by a homogeneous but spatially correlated random medium: comment. *J. Opt. Soc. Amer. A*, **19**:2517–2520, 2002.
269. S.V. Buldyrev, M. Gitterman, S. Havlin, A.Ya. Kazakov, M.G.E. da Luz, E.P. Raposo, H.E. Stanley, and G.M. Viswanathan. Properties of Lévy flights on an interval with absorbing boundaries. *Physica A*, **302**:148–161, 2001.
270. K.S. Miller and B. Ross. *An Introduction to the Fractional Calculus and Fractional Differential Equations*. Wiley–Interscience, New York (NY), 1993.